Structural Transitions and Ferroelectric Properties of Chemical Solution Deposition Derived Rare Earth Doped Bismuth Ferrite Films

Jinling Zhou

A thesis in fulfilment of the requirements for the degree of Doctor of Philosophy

School of Materials Science and Engineering

Faculty of Science

University of New South Wales

May 2022

ORIGINALITY STATEMENT

☑ I hereby declare that this submission is my own work and to the best of my knowledge it contains no materials previously published or written by another person, or substantial proportions of material which have been accepted for the award of any other degree or diploma at UNSW or any other educational institution, except where due acknowledgement is made in the thesis. Any contribution made to the research by others, with whom I have worked at UNSW or elsewhere, is explicitly acknowledged in the thesis. I also declare that the intellectual content of this thesis is the product of my own work, except to the extent that assistance from others in the project's design and conception or in style, presentation and linguistic expression is acknowledged.

COPYRIGHT STATEMENT

☑ I hereby grant the University of New South Wales or its agents a non-exclusive licence to archive and to make available (including to members of the public) my thesis or dissertation in whole or part in the University libraries in all forms of media, now or here after known. I acknowledge that I retain all intellectual property rights which subsist in my thesis or dissertation, such as copyright and patent rights, subject to applicable law. I also retain the right to use all or part of my thesis or dissertation in future works (such as articles or books).

For any substantial portions of copyright material used in this thesis, written permission for use has been obtained, or the copyright material is removed from the final public version of the thesis.

AUTHENTICITY STATEMENT

☑ I certify that the Library deposit digital copy is a direct equivalent of the final officially approved version of my thesis.

UNSW is supportive of candidates publishing their research results during their candidature as detailed in the UNSW Thesis Examination Procedure.

Publications can be used in the candidate's thesis in lieu of a Chapter provided:

- The candidate contributed **greater than 50%** of the content in the publication and are the "primary author", i.e. they were responsible primarily for the planning, execution and preparation of the work for publication.
- The candidate has obtained approval to include the publication in their thesis in lieu of a Chapter from their Supervisor and Postgraduate Coordinator.
- The publication is not subject to any obligations or contractual agreements with a third party that would constrain its inclusion in the thesis.

☑ The candidate has declared that **some of the work described in their thesis has been published and has been documented in the relevant Chapters with acknowledgement**.

A short statement on where this work appears in the thesis and how this work is acknowledged within chapter/s:

> The results from "Tuning Phase Fractions and Leakage Properties of Chemical Solution Deposition-Derived Mixed-Phase BiFeO3 Thin Films" in ACS Applied Electronic Materials is contained in Chapter 4, Chapter 5, and Chapter 9. Acknowledgement of the work contained in this thesis is made in Chapter 9. Acknowledgement of the work of the other authors of this paper has been made in the "List of Publications" section as well as my acknowledgements section.

Candidate's Declaration

I declare that I have complied with the Thesis Examination Procedure.

Acknowledgments

I would like to express my sincere gratitude to my supervisor, Professor Nagarajan Valanoor, for enabling me to be one of his group members and guiding me in the exploration of ferroelectric thin films. His critical thinking and enlightening advice provided sparkling ideas for my research. His constant support is the potent backing throughout my Ph.D. life. I also would like to thank my secondary supervisor Dr. Owen Standard for his help.

I would like to express my deepest thanks to my joint supervisor Dr. Qi (Peggy) Zhang, who is not only a mentor but also a close friend on the journey of my Ph.D. studies. Her professional and patient guidance on experiment design, data analysis, and thesis writing keeps my research on the right track. With her gentle and caring personality, I have a warm and pleasant working environment that I really enjoyed and appreciated.

Moreover, I am grateful for the opportunity to collaborate with some of the worldwide outstanding research groups. I would like to thank Professor Ichiro Takeuchi at the University of Maryland for his generous support during my research in the United States, especially during such a tough time as the COVID-19 outbroke. Thanks for his understanding, tolerance, and endless help. Thank Dr. Heshan Yu from Prof. Takeuchi's group for his help with training me in the pulsed laser deposition (PLD) technique. I also wish to thank Professor Jing-Feng Li and Professor Ke Wang for their kindly hosting me for doing my research work at Tsinghua University. Thank Professor Yu Pu and Dr Yanli Jia at Tsinghua University for their help with the access to Radiant and Keithley equipment. Besides, I appreciate Dr. Xuan (Heidi) Cheng at Monash University for her help with transmission electron microscopy (TEM) characterization, assistant Professor Zhijun Ma at Hubei University for his help with data analysis, and assistant Professor Shintaro Yasui at Tokyo Institute of Technology for his help with 2D X-ray diffraction (XRD) test of BSFO/LSMO//LAO (BSFO: $Bi_{1-x}Sm_xFeO_3$, LSMO: $La_{0.67}Sr_{0.33}MnO_3$, LAO: $LaAlO_3$) films. I am thankful to all of them for their great advice and helpful feedback.

I am also very grateful for my friends and colleagues who have given me much care and help during my Ph.D. life. I thank Dr. Daniel Sando for kindly providing thin-film-based XRD techniques and knowledges, and 2D XRD test of BSFO/LSMO//STO (BSFO: $Bi_{1-x}Sm_xFeO_3$, STO: $SrTiO_3$), Mr. Max Summers for training me in film preparation techniques and the fabrication of BSFO/LSMO//STO films, and Ms. Vicki Zhong, Mr. Xihua Chen, and Ms. Christie Lau for their

efforts on bottom electrode preparation. I also thank Dr. Stuart Burns, Dr. Pariasadat Musavigharavi, Dr. Jackson Wong, Dr. Yangyang Zhang, Dr. Tiziana Musso, Dr. Vivasha Govinden, Dr. Richard Winkler, and Mr. Oliver Paull for making me feel at home in the group.

I extend special thanks to Dr. Yu Wang and Dr. Saroj Kumar Bhattacharyya for their help with XRD characterization, Dr Anne Rich for her help with Fourier transformation infrared spectroscopy (FTIR) and Raman analysis, Dr. Karen Louise Privat for her help on scanning electron microscopy (SEM) and wavelength dispersive spectrometer (WDS) operation, Dr. Yin Yao for his help with SEM sample preparation from Mark Wainwright Analytical Centre (MWAC), Dr. Josiah Firth, Ms. Pierrette Michaux, Ms. Joanna Szymanska from ANFF for their help with device preparation, Dr. Rahmat Kartono for furnace maintenance, and Ms. Jane Gao for her IT service support.

I also appreciate the friendship of Ms. Lisha Liu, Mr. Yixuan Liu, Mr. Hualu Zhuang, Ms. Yu Huang, Mr. Liang Shu, Ms. Jingwei Li, Ms. Yueyushan Cheng, Ms. Ziwan Du, Mr. Wei Li, Mr. Geng Li, and Ms. Yanqi Wu in China. I am thankful for their help in lab issues as well as school life.

Last but not the least, I would like to thank my parents and siblings for their endless love and encouragement. It is their unconditional support and understanding that made me pursue my dream without fear.

I would like to offer my sincere words to all of them for giving me a great Ph.D. experience.

Abstract

Over the past two decades, Bismuth ferrite ($BiFeO_3$, BFO) thin films have attracted significant attention on account of their attractive multifunctional properties, ranging from room-temperature multiferroicity to robust high Curie temperature (T_c), large switchable spontaneous polarization (P_s) and enhanced electromechanical response, and ability to generate photovoltaic current etc. In particular, the past decade has seen huge efforts devoted to engineering the phase structure of BFO films to achieve a morphotropic phase boundary -(MPB)-like materials system with excellent ferroelectric properties and high electromechanical response.

In this thesis, strain engineering and site engineering are applied to tailor the phase composition of epitaxial BFO films through a chemical solution deposition (CSD) method. The compressive epitaxial strain provided by the lattice misfit between the film and the lanthanum aluminate ($LaAlO_3$, LAO) substrate can stabilize a tetragonal-like (T') phase. The chemical pressure produced by the A-site substitution of smaller Sm element can induce a ferroelectric rhombohedral (R) to paraelectric orthorhombic (O) phase transition. The coexistence of these diverse polymorphs of BFO is expected to generate an MPB effect, where a maximum electromechanical property usually reports.

The thesis first employs the misfit strain engineering (BFO films grown on LAO substrates) to tune the phase fraction in mixed-phase (rhombohedral-like (R')-T' coexistence) BFO films by altering the synthesis parameters via the CSD method. It shows that the T'-phase fraction ranging from 10% to 35% is achieved by decreasing the spin-coated layers from four to one layer. In a two-layer configuration, the T'-phase fraction is further found that can be varied from 8% to 38% by changing the precursor concentration and heating treatment parameters. The mixed-phase BFO films show a typical polydomain structure with a polarization-orientation dependent conduction behavior whereby poled-up (polarization pointing away from the lower electrode) domains have higher conductivity. An optimized film with a T'-phase fraction of ~ 28% shows the lowest leakage current of <0.1 A/cm^2 up to field strengths of 500 kV/cm. Upon increasing electric field, the mixed-phase film shows an interface-limited Schottky emission to bulk-limited space-charge-limited-conduction (SCLC) mechanism predominate leakage current transition.

The thesis then applies site engineering (A-site substitution with Sm) to tailor the phase structure of BFO films deposited on strontium titanate ($SrTiO_3$, STO, the lattice parameter is similar to that of BFO) substrates. The role of the Sm on the precursor gelation chemistry is first studied. It is found that the electronegativity of the cation species in metal nitrates affects the reaction rate of the hydrolysis reaction and esterification reaction. The structural investigation of the crystalline films shows that the phase transition occurs at x = 0.10 with paraelectric O phase and antipolar phase appearance. The domain contrast of as-grown BFO/BSFO (BSFO: $Bi_{1-x}Sm_xFeO_3$) films reduces gradually with the increase of the Sm composition. More importantly, Sm introduction greatly improves the ferroelectric properties of BFO films. At an Sm ratio of 0.14, a fully developed polarization hysteresis loop is achieved. When the Sm ratio is increased to 0.15, an electric-field-induced distorted double hysteresis loop is observed.

Then strain engineering and site engineering are combined to construct a complex phase configuration in BSFO films. A structural evolution from T'-R' to T'-R'-O, and then to T'-O phases is demonstrated with the increase of the Sm ratio. The synergetic effects of misfit strain and chemical pressure drive the phase transition composition to a higher value of 0.14 compared to that of strain-free BSFO/LSMO//STO (LSMO: $La_{0.67}Sr_{0.33}MnO_3$) films at 0.10. Likewise, Sm doping in the A-site leads to the decrease of the piezoresponse force microscopy (PFM) amplitude. While an enhanced domain switching behavior is attained at MPB. The ferroelectric properties show a transition from a single ferroelectric square-shaped to a slightly distorted double hysteresis loop with the Sm^{3+} doping content increasing from 0.14 to 0.16. The investigation of the resistive switching behavior shows an interesting transition of the current flow under the external bias from "high resistance state (HRS)-> low resistance state (LRS)->HRS->LRS" to "HRS->LRS->LRS->HRS".

This thesis provides a comprehensive understanding of the effects of epitaxial strain or/and chemical pressure on the phase composition of BFO films and their multifunctional properties. The appealing physical properties induced by the structure evolution promote the seeking of novel phase structure of perovskite oxides in thin-film form.

List of Publications

Publications included in this thesis

- **Jinling Zhou**, Daniel Sando, Xuan Cheng, Zhijun Ma, Nagarajan Valanoor, and Qi Zhang, Tuning Phase Fractions and Leakage Properties of Chemical Solution Deposition-Derived Mixed-Phase $BiFeO_3$ Thin Films[J]. *ACS Applied Electronic Materials*, 2020, **2**(12): 4099-4110.

  Author contribution: Jinling Zhou (candidate) initiated all the experiments and drafted the whole manuscript. Xuan Cheng conducted the TEM experiment. Zhijun Ma participated in the IV data analysis. Daniel Sando, Q. Zhang, and N. Valanoor engaged the revision of the manuscript. Q. Zhang and N. Valanoor supervised the study.

Forthcoming articles related to this thesis

- **Jinling Zhou**, Shintaro Yasui, Daniel Sando, Nagarajan Valanoor, and Qi Zhang, Phase Transition and Ferroelectricity of Chemical Solution Deposition Derived Mixed-Phase $Bi_{1-x}Sm_xFeO_3$ Thin Films. (In preparation)

  Author contribution: Jinling Zhou (candidate) initiated all the experiments and will draft the whole manuscript. Shintaro Yasui performed the tests and analysis of 2D XRD. Daniel Sando, Q. Zhang, and N. Valanoor will participate in the revision of the manuscript. Q. Zhang and N. Valanoor supervise the study.

- **Jinling Zhou**, Daniel Sando, and Nagarajan Valanoor, Qi Zhang, Gelation Chemistry and Phase Development of Chemical Solution Deposition-derived Sm Doped $BiFeO_3$ Thin Films: The Role of Sm Dopant. (In preparation)

  Author contribution: Jinling Zhou (candidate) initiated all the experiments except 2D XRD characterization and will draft the whole manuscript. Daniel Sando performed the tests and analysis of 2D XRD. Daniel Sando, Q. Zhang, and N. Valanoor will participate in the revision of the manuscript. Q. Zhang and N. Valanoor supervise the study.

Additional publications during this thesis

- Yihao Wang, Qi Zhang, **Jinling Zhou**, et al. Fowler-Nordheim Tunnelling-Assisted Enhancement of Tunnelling Electroresistance Effect Through a Composite Barrier[J]. Applied Physics Letters, 2020, 116(20): 202901.

  Author contribution: Jinling Zhou (candidate) conducted the piezoresponse force microscopy (PFM) experiments.

- Zhiyin Tu, Ti Xie, Yeonghun Lee, **Jinling Zhou**, et al. Ambient effect on the Curie temperatures and magnetic domains in metallic two-dimensional magnets[J]. npj 2D Materials and Applications, 2021, 5(1): 1-6.

  Author contribution: Jinling Zhou (candidate) conducted the atomic force microscopy (AFM) experiments.

Forthcoming articles prepared during this thesis

- Yi-Xuan Liu, **Jinling Zhou**, Chen-Bo-Wen Li, Jing-Tong Lu, Yicheng Wang, Yijia Du, Ke Wang, Lead-Free Perovskite Piezoelectric MEMS Acoustic Sensors. (In preparation)

  Author contribution: Jinling Zhou (candidate) participated in all the characterizations of structure and properties of films, including XRD θ-2θ scans, reciprocal space mapping (RSM) pole figure measurements, PFM, SEM, TEM, piezoelectric coefficient d_{33} mapping, and P-E loops.

List of Abbreviations

Bismuth ferrite ($BiFeO_3$, BFO)

Sm-doped bismuth ferrite ($Bi_{1-x}Sm_xFeO_3$, BSFO)

Lanthanum aluminate ($LaAlO_3$, LAO)

Strontium titanate ($SrTiO_3$, STO)

Lanthanum strontium manganite ($La_{0.67}Sr_{0.33}MnO_3$, LSMO)

Lead zirconate titanate ($Pb(Zr_xTi_{1-x})O_3$, PZT)

Morphotropic phase boundary (MPB)

Space-charge-limited-conduction (SCLC)

Root-mean-square (RMS)

Out-of-plane (OP)

In-plane (IP)

Polarization-electric field (P-E)

Alternating current (AC)

Direct current (DC)

High resistance state (HRS)

Low resistance state (LRS)

Rhombohedral (R)

Tetragonal (T)

Orthorhombic (O)

monoclinic (M)

Tetragonal-like (T')

Rhombohedral-like (R')

Spontaneous polarization (P_s)

Remanent polarization (P_r)

Curie temperature (T_c)

Coercive field (E_c)

Chemical solution deposition (CSD)

Physical vapor deposition (PVD)

Pulsed laser deposition (PLD)

Molecular beam epitaxy (MBE)

Metal organic chemical vapor deposition (MOCVD)

Radiofrequency (RF)

Hydrothermal method (HM)

Liquid phase epitaxy growth (LPE)

X-ray diffraction (XRD)

Reciprocal space maps (RSMs)

Atomic force microscopy (AFM)

Piezoresponse force microscopy (PFM)

Dual AC resonance tracking (DART)

Switching spectroscopy-PFM (SS-PFM)

Conductive atomic force microscopy (CAFM)

Scanning electron microscopy (SEM)

Transmission electron microscopy (TEM)

Wavelength dispersive spectrometer (WDS)

Fourier transformation infrared spectroscopy (FTIR)

Attenuated total reflectance (ATR)

List of Figures

List of Tables

Table of Contents

Chapter 1. Introduction

1.1 Motivations

Piezoelectric oxides are a class of high-profile functional materials due to their ability to convert mechanical energy into electrical energy and vice versa. Ferroelectric materials, as a subset of piezoelectric materials, have a reversible spontaneous polarization (P_s), which has been exploited in a number of electronic device applications ranging from capacitors, acoustic transducers, and nonvolatile random-access memory devices (FeRAM), resistive-memory switches, pyroelectric thermal imaging etc. Lead zirconate titanate ($PbZr_xTi_{1-x}O_3$, PZT), one of the most distinguished piezoelectric/ferroelectric oxides, has been exploited in the industrial applications for a long time. However, the toxicity of lead has raised several environmental and health concerns.

Bismuth ferrite ($BiFeO_3$, BFO), as one member of the simple perovskite ferroelectric family, possesses large P_s up to 100 μC/cm^2 (the highest one among the ever-known bulk ferroelectrics) and high ferroelectric Curie temperature (T_c, ~ 830 ℃) [6] In particular, the rich phase diagram of the thin-film form of BFO produce a fertile ground for the development of versatile functional properties. For example, in 2008, Kan *et al.* [7, 8] found a large piezoelectric coefficient d_{33} as high as 110 pm/V in BFO thin films because of a rhombohedral-orthorhombic (R-O) phase transition induced by A-site substitution with various rare earth (RE) elements. In 2009, Zeches *et al*. [9] reported a measurable surface displacement in a mixed-phase BFO thin film due to a reversible phase interconversion between tetragonal-like (T-like, T') and rhombohedral-like (R-like, R') phases produced by compressive strain from lanthanum aluminate ($LaAlO_3$, LAO) substrate. These strong electromechanical responses driven by the BFO phase transition among its different polymorphs under external strain or pressure, termed as "morphotropic phase boundary (MPB)" effect, endow them as a promising alternative for toxic lead-based piezoelectric materials.

The so-called MPB is a phase transition region, where the low symmetry phase bridges two different phases with proximal energy. The lower energy barrier between structure transition at MPB can generate an enhanced dielectric constant and piezoelectric response as above. Therefore, by altering the strain state (strain engineering) and the composition of the

A-site substitution (site engineering) in BFO films, novel phase structures are expected to be stabilized. Further, the modification of the leakage current and ferroelectric properties, and, thus, probably exotic physical properties can be achieved at the MPB composition.

Hitherto, the reported high-quality epitaxial BFO films are mainly prepared by the physical vapor deposition (PVD), such as pulsed laser deposition (PLD) [10], molecular beam epitaxy (MBE) [11], and radiofrequency (RF) sputtering [12, 13].

Chemical solution deposition (CSD) method as a common chemical route technique is also widely taken for the fabrication of thin films, especially viable at a commercially scale due to its cost-effectiveness and easy adaptability to large-area wafers. In addition, the CSD method provides an opportunity to precisely tailor the species and composition of the precursors, used for the A-site substitution with RE, thus, enabling tighter control of the MPB compositions. However, it is still a challenge to achieve a CSD-derived BFO film with the properties comparable to PVD-derived one, particularly for oriented or epitaxial structures. Secondary phases, pores or cracks, as well as crystallographic defects during the CSD synthesis process are fatal to the dielectric and ferroelectric properties of the ultimately prepared films.

The aim of the work is to demonstrate a CSD method that can compete with PVD based BFO films and elucidate the relationship between the phase structure variation and the electrical properties transformation.

1.2 Objectives

Misfit strain or/and chemical pressure are utilized to tailor the phase structure and physical properties of BFO films. The specific objectives of the thesis are as follows:

(1) Enhanced electromechanical response has been reported both in PLD- and CSD-derived epitaxial mixed-phase BFO films due to the reversible conversion between T’ and R’ phases under the external electric field. [9, 14] The relatively large and nonvolatile changes in the surface displacement in this mixed-phase system make it an attractive candidate for the application in microelectronic actuators and sensors. Therefore, tailoring epitaxial strain to achieve the alternation of the phase constitution in mixed-phase BFO films is of great significance for adjusting the microstructure and electromechanical properties.

(a) Most of the literatures on the tuning of epitaxial strain in mixed-phase BFO films are focused on films fabricated by PLD. Reports of high-quality epitaxial mixed-phase BFO films fabricated using the CSD method are rare. Especially, a systematic investigation of **the synthesis parameters during the CSD process on the influence of the phase fraction (i.e., the ratio of T'/R') and domain structure** is lacking. A detailed tuning of the phase fraction regarding the factors of the number of the deposited layer, the precursor concentration, and the heating treatment process will be carried out first.

(b) Once realized the tuning of the phase fraction in CSD-derived mixed-phase BFO films, we investigated **the phase fraction on the influence of the conductivity and leakage behavior, as well as the conduction mechanisms of the films**.

(2) The interesting phase transition from ferroelectric rhombohedral (R) phase to paraelectric orthorhombic (O) phase induced by the A-site substitution with Sm has been reported in PLD-derived BFO films. [15] Despite the similar works on the Sm-doped BFO films using the sol-gel method [16], **the typical ferroelectric loop to distorted double hysteresis loop transformation is lacking due to the polycrystalline structure.** In Sm-doped BFO system, the double hysteresis loop originates from the electric-field-induced paraelectric to ferroelectric phase transition. The randomly orientated polarization in each grain of the polycrystalline films makes the observation of double hysteresis loop challenging. **In addition, the Sm introduction on the influence of the gelation chemistry of the BFO precursors is absent**. To obtain the epitaxial Sm-doped BFO films and understand the role of Sm on the structure evolution, the Sm introduction on the influence of the gelation chemistry of the BFO precursors and the Sm doping on phase structure and the ferroelectric properties variation will be conducted.

(3) A comprehensive understanding of the effects of strain engineering or site engineering, separately, on the phase composition and the physical properties are explored as above. **The synergetic effects of both the strain and site engineering will be adopted to construct a complex phase composition in BFO films**. A novel phase transition and physical properties are expected.

(a) **A structural transition as a function of the doped Sm composition** will be investigated methodically. Particularly, the study of the microstructure of the film at the MPB

composition is performed with the purpose to understand the effect of the strain and the chemical pressure on the MPB behavior.

(b) The last objective of this thesis is to **systematically study the evolution of the domain structure, piezoelectric properties, and the electrical properties (including the ferroelectric properties, conductivity, and the resistive switching behavior) induced by the complex phase transition** due to epitaxial strain and Sm substitution.

1.3 Organization of Thesis

The thesis consists of nine chapters presented in the following orders:

Chapter 2: A literature review of the basic introduction of ferroelectricity, the structure of perovskite oxides, and key ferroelectric characteristics, as well as the potential application is first given. Then the concepts of the MPB effect and its origin are summarized. Subsequently, two common methods (i.e., the epitaxial strain effect and the chemical pressure effect, for the design of the phase structure of the research subject BFO films and the modification of their ferroelectric properties) are surveyed in depth. Last, thin-film fabrication techniques, especially the CSD method used in this thesis are introduced.

Chapter 3: The general experimental procedures used in this thesis are summarized. It covers the fabrication process of BFO films and top electrodes, the analytical equipment and methods for the characterization of the gelation chemistry of BFO precursors, and the structure and electrical properties of as-prepared BFO films. Specific details relevant to each experiment are detailed within the working chapters.

Chapter 4: A systematic investigation is conducted by adjusting the synthesis parameters to tailor the phase fraction of mixed-phase BFO films. The number of deposited layers, the concentration of applied precursors, and the heating treatment (temperature and dwell time) process are included. X-ray diffraction (XRD), Raman spectroscopy, and piezoresponse force microscopy (PFM) are used to characterize the phase composition and domain structures. Scanning electron microscopy (SEM) and transmission electron microscopy (TEM) are utilized to study the microstructure of films.

Chapter 5: The domain switching behavior, the leakage current behavior, the

polarization-dependent conductivity behavior, and the conduction mechanisms of the mixed-phase films are comprehensively studied to elucidate the relationship between the phase fraction and the electrical properties in mixed-phase BFO films.

Chapter 6: The first part of this chapter investigates the role of Sm dopant on gelation chemistry. The second part studies the phase and domain structure, the ferroelectric properties, and the resistive switching behavior of two typical Sm-doped BFO films. The outcome of this chapter provides an understanding of the effect of only the chemical pressure (A-site doping with Sm) on the structure and the physical properties of BFO films.

Chapter 7: Strain engineering and site engineering are simultaneously applied to introduce a complex phase configuration in Sm-doped BFO films grown on LAO substrates. The crystal structure evolution as a function of Sm composition is investigated by XRD measurements (2ϑ-ϑ scans, pole figures) and 2D XRD reciprocal space maps. Detailed microstructure investigation of the Sm-doped BFO film with the composition at the MPB is conducted by TEM.

Chapter 8: The evolution of the domain structure and domain switching behavior, the local and global piezoelectric response, the ferroelectric properties, the conductive behavior, and the resistive switching behavior of the Sm-doped BFO films are comprehensively carried out.

Chapter 9: The last chapter summarizes each of the preceding chapters and presents suggestions for future work.

The thesis carries out a comprehensive investigation of strain engineering or/and site engineering on the phase structure evolution and physical properties in BFO films. The outcomes provide insight into the tailoring of the multifunctional properties of BFO films from the view of the structure design. The improved ferroelectric and electromechanical properties at the MPB with Sm doping show a significant promise for the development of microelectronic technology and devices.

Chapter 2. Literature Review

2.1 Ferroelectricity

2.1.1 Definition

Ferroelectricity refers to a property demonstrated in certain materials that show spontaneous polarization and this spontaneous polarization can be switched when subjected to an external electric field. [17] In ferroelectric materials, a spontaneous electric dipole moment, namely spontaneous polarization derives from the uneven charge distribution due to the separation of the positive and negative electric charges. Normally, both the direct displacement of the ions [18, 19] and the deformation of the electron cloud [20] can lead to such a separation. From the principle of crystallographic symmetry, the breakdown of 32 crystal classes can derive to 10 polar pyroelectric materials (10-point groups of *1, 2, m, mm2, 4, 4mm, 3, 3m, 6 and 6mm*) due to the spontaneous polarization. Among these 10 classes, only crystals with the unipolar axis whose spontaneous polarization can be rotated by the externally applied electric field can be classified as ferroelectric. [21] **Figure 2-1** represents the hierarchy diagram of the classification of 32 crystal structures. Due to the crystallographic phase transition at a certain temperature, known as the Curie temperature (T_c), the polar ferroelectric will transform into an isotropic nonpolar paraelectric phase. Thus, normally, ferroelectricity can be observed within a certain temperature range, that is under T_c. The ferroelectric phenomenon was first discovered in a single crystal with hydrogen bonds, Rochelle salt ($NaKC_4H_4O_6 \cdot 4H_2O$) in 1920 by French scientist J. Valesek. [22] After that, more than 250 materials have been found showing ferroelectricity, in which the simple perovskite crystal structure is predominant.

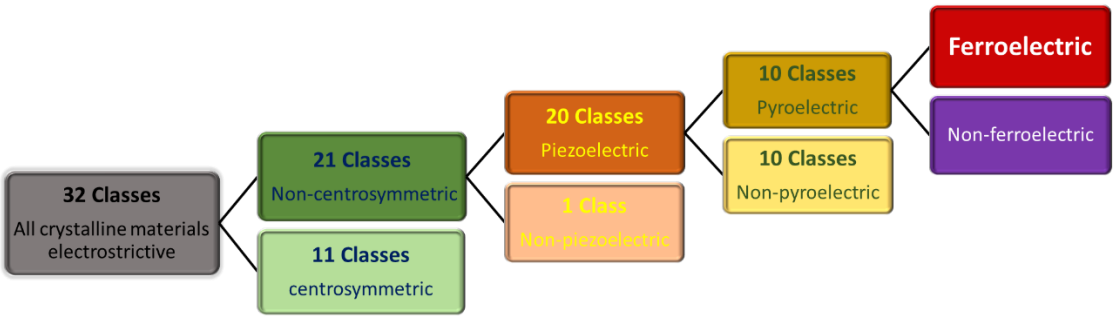

Figure 2-1. Hierarchy classification of 32 crystal classes.

2.1.2 Structure of Perovskite Oxides

In the ideal cubic perovskite crystal, referring to the general formula ABO_3, A-site cations occupy the vertices of the lattice, and face-centered oxygen ions form oxygen octahedra with B-site cations located in the octahedral interstices. [23] In such an isotropic cubic phase, no spontaneous dipole (spontaneous polarization, P_s=0) exists. Most perovskite materials show off-centering movement of B cations [24] due to the rotating or tilting of the corner-shared oxygen octahedra, and thus lead to a non-centrosymmetric crystal structure and yield a spontaneous polarization in a certain direction. As shown in **Figure 2-2(a)**, there are three possible symmetric directions (<111>, <001>, <110>) that the B cations can shift away from their center position. [25] It happens in non-symmetrical systems such as the R, T, and monoclinic (M) phases. Taking barium titanate ($BaTiO_3$) as an example, it is a paraelectric cubic phase above its T_c due to its center of the positive charges coinciding with the center of negative charges. When the temperature is below T_c, a ferroelectric T structure stabilizes as the positively charged cation ions (Ti^{4+}) is deviated from the negatively charged oxygen ions (O^{2-}) octahedra center. Thus, a spontaneous polarization along the <001> direction is yielded due to the formed electric dipoles, as shown in **Figure 2-2(b)**. [17] The ensuing structure-related properties such as dielectric, elastic, and thermal properties are also altered.

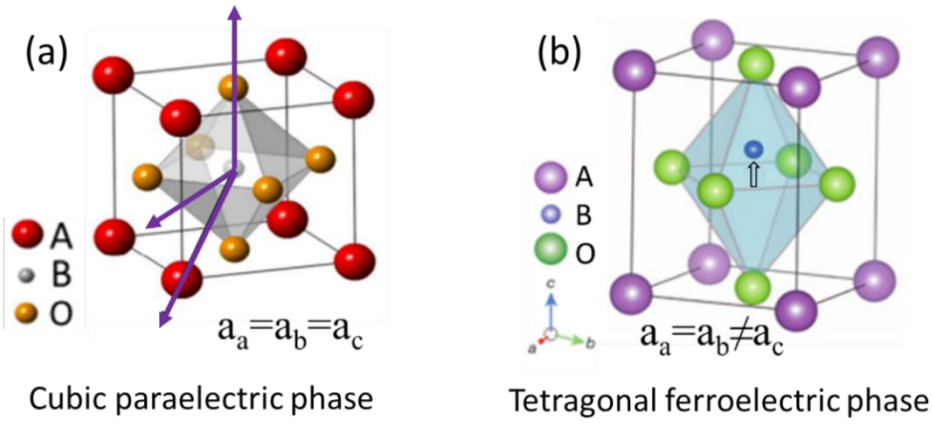

Figure 2-2. Unit cell of perovskite structure (a) cubic paraelectric phase, [26] (b) tetragonal ferroelectric phase. [27]

To evaluate the stability and distortion of the ABO_3 perovskite structure, the Goldschmidt tolerance factor (t) was first introduced by Victor Moritz Goldschmidt in 1926 [28] as

$$t=\frac{R_A+R_O}{\sqrt{2}(R_B+R_O)} \qquad \textbf{Equation 2-1}$$

Where R_A, R_B, and R_O are the radii of the A cation, B cation, and oxygen anion, respectively. The relationship between the t value and the corresponding phase structure is listed in **Table 2-1**.

Table 2-1. Goldschmidt tolerance factor (t) and corresponding phase structures.

Goldschmidt tolerance factor	Structure	Explanation
$t > 1$	Hexagonal/T	Ion A too big or ion B too small
$0.9 < t \leq 1$	Cubic (C)	Ions A and B have ideal size
$0.71 < t \leq 0.9$	Orthorhombic (O)/R	Ion A too small to fit into ion B interstices
$t \leq 0.71$	Different structures	Similar ionic radii of ions A and B

2.1.3 Ferroelectric Properties of Perovskite Oxides

2.1.3.1 Ferroelectric Domains

As mentioned above, reversible spontaneous electric polarization is one of the most important characteristics of ferroelectric materials. Depending on the crystal structure, the polarization direction is different. For example, the polarization directions in T, R, and O phases are along one of the [001], [111], and [110] cubic directions, respectively, as shown in **Figure 2-3**.

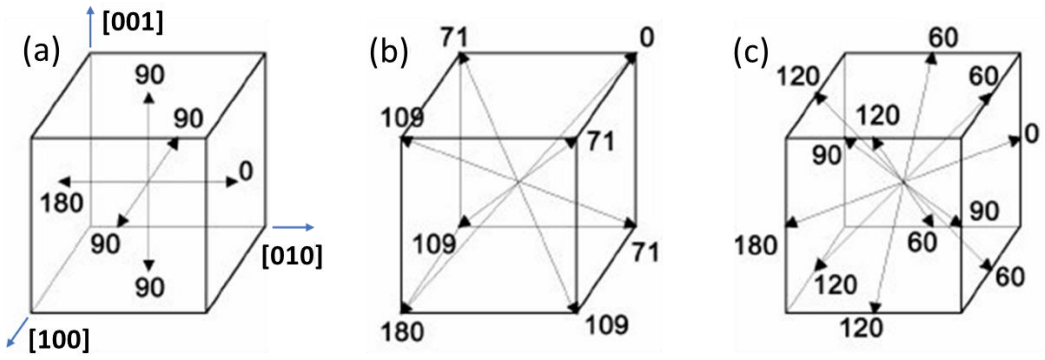

Figure 2-3. Directions of spontaneous polarization in the (a) tetragonal, (b) orthorhombic, and (c) rhombohedral phases with angle reference to 0°. [29]

The regions with uniformly oriented spontaneous polarization in the crystal are ferroelectric domains and the boundary between two different domains is the domain wall, as shown in **Figure 2-4(a)**. [21] The formation of ferroelectric domains can minimize the electrostatic energy of depolarizing fields and elastic energy produced by the mechanical constraints of the material. [30] Under an externally applied electric field, the polarization vectors can be switched to align with the same direction as the electric field, as shown in **Figure 2-4(b)**. In this whole switching process, the concomitant nucleation and growth of new domains, as well as the movement of the domain walls also occurs. [31]

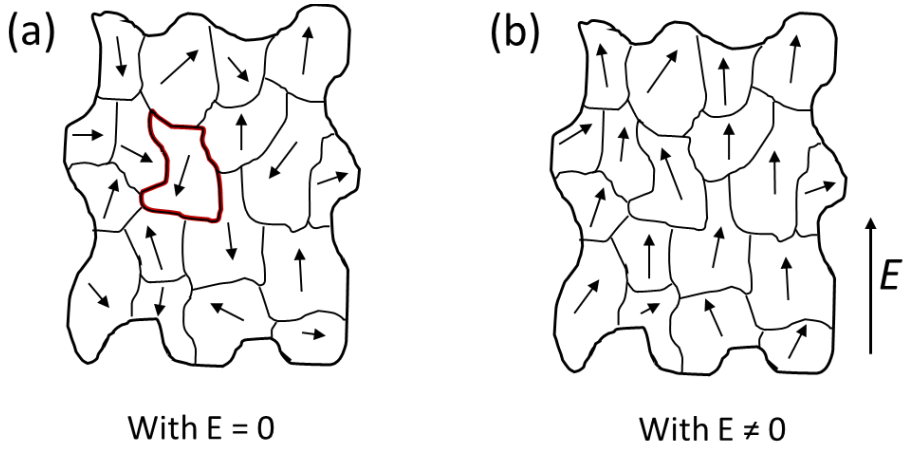

Figure 2-4. Domain structures under the applied electric field of (a) zero and (b) nonzero.

The domain walls can be determined by the angle between the polarization vectors of two adjacent domains. Taking a rhombohedral structure as an example, as stated previously, its ferroelectric polarization is aligned to one of the <111> directions that is the body diagonals of the unit cell. Thus, eight possible domain orientations can occur, which can form three types of domain walls, 71°, 109°, and 180°, as **Figure 2-3(b)**. Here, the [-111] is referred to as 0°. There are (1) three components of the diagonal polar vectors, that is [111], [-11-1], and [-1-11] form 71° domain walls with the reference [-111] polarization vector; (2) another three components, that is [-1-1-1], [1-11], and [11-1] form 109° domain walls with the reference vector; and (3) the [1-1-1] form 180° domain wall with [-111] one. Among them, 71° and 109° domain walls can minimize the elastic energy and be also called ferroelastic domain walls.

2.1.3.2 Ferroelectric Hysteresis Loop

A ferroelectric hysteresis loop, that is polarization-electric field (P-E) hysteresis loop, is a macroscopic description of the motion of the ferroelectric domain under an external electric field, as shown in **Figure 2-5**. The random orientation of the virgin domain shows no net polarization. Under applied electric field, the domains can be switched to align with the direction of the external electric field. As a lower external electric field is applied, the movement of the reversible domain walls plays a dominant role and polarization linearly depends on the electric field. When the external field increases, the nucleation of the new domains occurs, and the movement of the domain walls is irreversible. The polarization increases faster than that of the linear part. When the value of the external field is up to that of the B point, the polarization tends to saturation. When further enhancing the external field, the total polarization keeps increasing (B-C segment). The value of the intercept with the polarization axis by extrapolating the linear B-C segment is the spontaneous polarization. When decreasing the external field, the polarization decreases along the curve of C-B-D. When the field is zero, the net polarization is nonzero, resulting in the remanent polarization (P_r). A reverse electric field is needed to make the polarization zero. This field is called the coercive field (E_c). With increasing the strength of the reverse field continuously, a similar polarization rearrangement occurs in the negative part.

The ability of the polarization direction able to be reversed makes ferroelectric materials a desirable application in a multitude of devices. A hysteresis loop showing a square loop shape, high P_r, as well as low E_c represents a robust ferroelectric that is desired for switching applications. [32] Usually, the ratio of the P_r and P_s (P_r / P_s) is applied to estimate the degree of the square. A high ratio of P_r / P_s indicates this ferroelectric material shows a low leakage current and can be used as an effective capacitor due to its ability to retain charges. A high P_r can guarantee a high strain and electromechanical coupling effect. A low E_c means much lower energy consumption for domain switching of the ferroelectric materials. There are several factors that may deteriorate these properties: (1) the existence of the charged defects, such as oxygen vacancies or electrons; [33] (2) the orientation of the film inconsistent with the direction of spontaneous polarization; [21, 34] (3) the effect of extension stress and residual stress; [35] (4) the resistivity of the electrode,[36] the external electric field and the structure of the ferroelectric domains [21]. Thus, it is necessary to decrease the content of the charged

defects and modify the process conditions to fabricate oriented thin films with highly selective polarization.

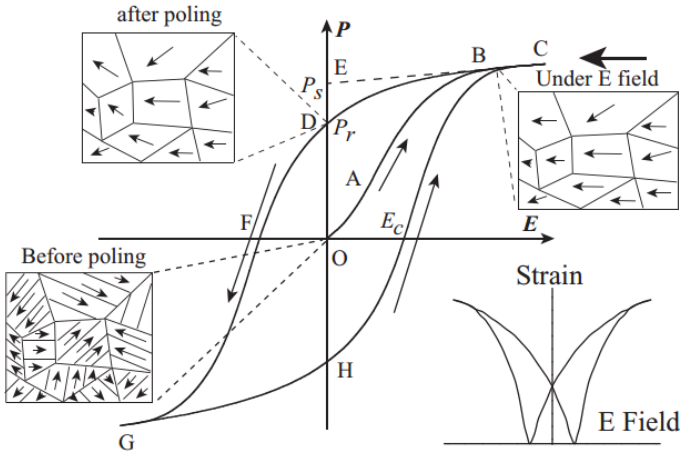

Figure 2-5. A typical hysteresis loop in ferroelectrics and corresponding domain reversal (polarization rotation) and strain-electric field curve. [21]

In addition, there are two other kinds of relationships between electric field and polarization, which are antiferroelectric and paraelectric states. In antiferroelectrics, the adjacent dipoles orient in antiparallel directions and each orientation forms an interpenetrating sublattice. This unique ordered array of electric dipoles gives antiferroelectric materials double hysteresis loops under external electric field, as shown in **Figure 2-6(a)**. There is a linear characteristic between polarization and electric field at a low field. When the electric field reaches a critical value, an electric-field-induced phase transition occurs, which leads to a ferroelectric structure and the appearance of a hysteresis loop. When removing the external electric field, the system reverts back to the original antipolar state with no net polarization. In paraelectrics, a simple proportional relationship between the induced polarization and electric field is observed, as shown in **Figure 2-6(b)**.

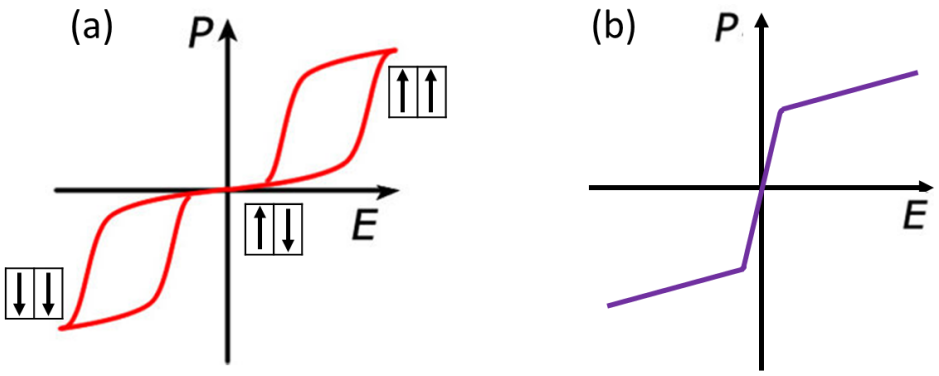

Figure 2-6. Typical hysteresis loops in (a) antiferroelectric and (b) paraelectric states.

2.1.4 Applications

Ferroelectric materials as an important family of functional materials possess piezoelectricity, pyroelectricity, and ferroelectricity simultaneously. The piezoelectricity characteristic endows ferroelectric materials with potential applications in sensors, actuators, and transducers. Its pyroelectricity can be applied in infrared detection, imaging, and thermometry. The "1" or "0" state generated by the reversible spontaneous polarization due to its ferroelectricity makes it a promising binary data storage media. $Pb(Zr_xTi_{1-x})O_3$ (PZT), as a mature commercial material, has been widely used in microelectromechanical systems since 1952 due to its physical strength, chemically stability, and its greater sensitivity, as well as higher operating temperature compared to other piezoelectric ceramics. However, in 2006, the Restrictions of Hazardous Substances issued by the European Community explicitly limits the usage of lead (Pb) in electronic equipment and thus, curbs the usage of PZT, which greatly drives the development of lead-free ferroelectric materials.

2.2 Morphotropic Phase Boundary

2.2.1 Overview

The morphotropic phase boundary (MPB) is a phase transition region, where a low symmetry phase bridges two different phases with proximal energy. At the MPB, ferroelectric materials can often generate an enhanced dielectric constant and piezoelectric response, even under weak external stimulus. [8, 37] These outstanding electromechanical properties are attributed to the lower energy barrier between structure transition and the multiple polarization rotation paths at the MPB. [38-40]

2.2.2 $PbZr_xTi_{1-x}O_3$ Materials

$Pb(Zr_xTi_{1-x})O_3$ or PZT, the most widely utilized piezoelectric material, was found to show maximum dielectric and piezoelectric properties at its MPB composition with $0.45 \leq x \leq 0.52$. The phase diagram was initially established in 1971 by Jaffe *et al*. [41], as shown in **Figure 2-7(a)**. The first report discussing this enhanced MPB effect was published in 1954. The sharp increase of the electromechanical response, d_{31} and d_{33} constants was found near the transition composition between rhombohedral and tetragonal PZT at 45 mole% $PbTiO_3$, as

shown in **Figure 2-7(b)**. [37] For the R structure, Zr is rich, and the B-site cations displace along one of the eight $<111>_{pc}$ directions. For the T phase, Ti is rich, and the B-site cations shift from their center position along one of the six $<100>_{pc}$ directions. This MPB-induced high performance due to the structural transformation greatly promoted the development of the PZT system and made it one of the dominant piezoelectric materials in commercial applications.

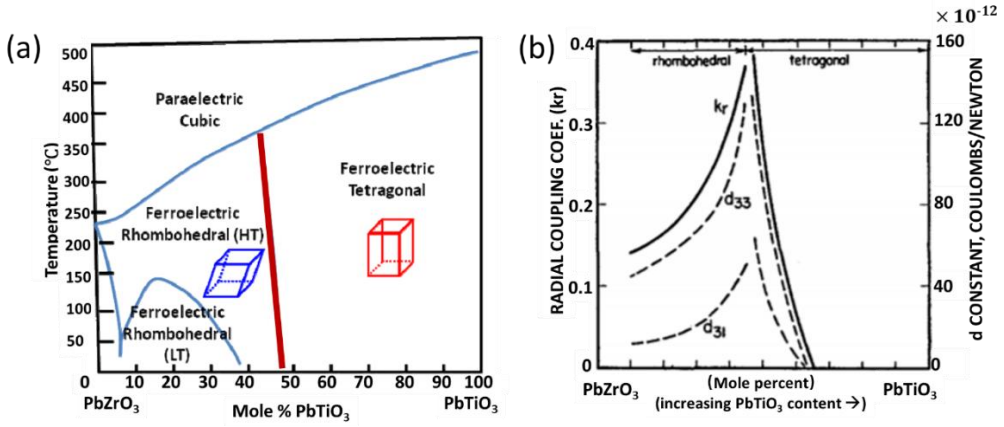

Figure 2-7. (a) Phase diagram [41] and (b) electromechanical coupling coefficient and dielectric constants of $Pb(Zr_xTi_{1-x})O_3$ (the red curve marks the MPB of PZT with $0.45 \leq x \leq 0.52$). [37]

To unveil the underlying mechanism for the origin of the remarkable electromechanical response, many studies have been conducted to investigate the structure characteristics and the possible polarization rotation behavior at MPB composition. There are two major views. One posits that there is a lower symmetry M phase bridging the T and R phases in the MPB region, which provides multiple paths for the rotation of the polarization vector within the monoclinic plane, and, thus, lead to enhanced piezoelectric performance. [42, 43] Another proposes that it is the averaged nano twinned domains of the T and R phases that demonstrates an M phase on the macroscale, also called the adaptive phase model. [44, 45] There are also some other different views about the structural phase composition at the MPB. [40, 46] It is sophisticated and remains controversial.

PZT ceramics have dominated the commercial market for more than 50 years because of their marked piezoelectric effect. However, as mentioned previously, due to the restriction of toxic lead usage, it is critical to search for lead-free materials with properties comparable to those of PZT. Thus, the exploration of lead-free systems that exhibit a PZT-like MPB continue to attract much attention.

2.2.3 Lead-Free Piezoelectric Materials

There are two lead-free systems, simple perovskite (i.e., $BaTiO_3$ (BT)-based, [38, 47] $K_{0.5}Na_{0.5}NbO_3$ (KNN)-based, [48, 49] $Bi_{0.5}Na_{0.5}TiO_3$ (BNT), [50, 51] and $BiFeO_3$ (BFO), [9] etc.) and complex perovskite (i.e., bismuth layer structure ferroelectrics (BLSFs) and tungsten bronze structured compositions, etc.) structures.

The Aurivillius family, (i.e., BLSFs) has a crystal structure with the pseudoperovskite $(A_{m-1}B_mO_{3m+1})^{2-}$ layers interleaved with $(Bi_2O_2)^{2+}$ layers along the *c* axis, as shown in **Figure 2-8(a)**. [52] The A and B sites in pseudoperovskite layers crystal can accommodate a huge compositional flexibility, and thus yield a wide ranging lead-free piezoelectric materials system. These BLSF based materials usually show high T_c (> 500 ℃), [53] while their piezoactivities are relatively low (< 20 pC/N). [54] A typical representative of BLSFs is $Bi_4Ti_3O_{12}$, which shows a piezoelectric coefficient d_{33} value of 8 pC/N. Through co-doping with W and Co, 28 pC/N can be achieved. [55] The tungsten bronze structured composition, $(Sr_{1-x}Ba_x)_2NaNb_5O_{15}$ piezoelectric single crystal with x = 0.7 near the MPB composition has also shown large dielectric and piezoelectric constants. [56]

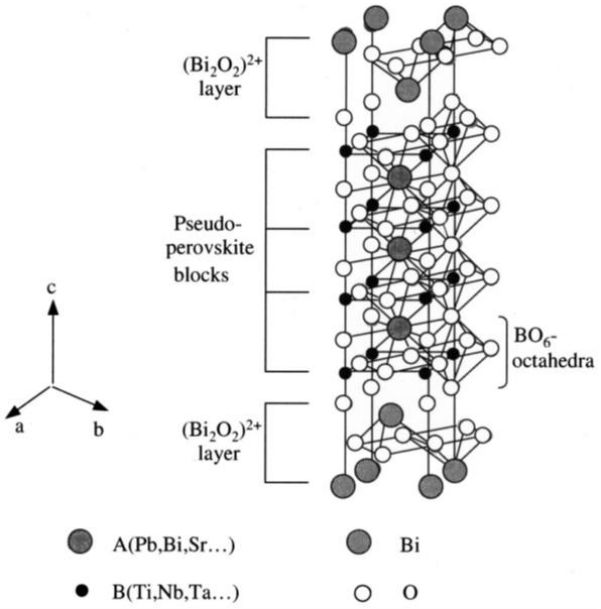

Figure 2-8. Crystal structure of bismuth layer structured ferroelectrics. [52]

Compared to the complex perovskite-type materials, simple perovskite compounds have large piezoelectric properties. [57] $BaTiO_3$ ceramics show a high piezoelectric coefficient d_{33} of 190 pC/N through conventional solid-state processing. However, its low T_c of 120 ℃ limits

its working temperature for practical piezoelectric applications. [57] Alkaline niobates [$(K_{0.5}Na_{0.5})NbO_3$, KNN)] based compounds have been reported to show striking dielectric and piezoelectric properties. [48, 49] However, the sintering density issues of KNN based family is still a major challenge.

2.3 Bismuth Ferrite

BFO, as one member of the simple perovskite ferroelectric materials, shows multiferroic properties. Its high T_c (830 °C) and P_s (as high as 100 μC/cm^2, the largest value known for bulk ferroelectrics) [10, 58] make it a potential candidate for the application in the lead-free piezoelectric field.

2.3.1 Overview

Multiferroics are multifunctional materials that possess at least two ferroic orders: ferroelectricity, (anti-)ferromagnetism, ferroelasticity, and ferrotoroidicity (**Figure 2-9**). [59] BFO, as one of the most intensively investigated multiferroics, possesses ferroelectric (T_C ~ 830 °C) and antiferromagnetic properties (Néel temperature, T_N ~ 370 °C). [58, 60-62]. In BFO, the 6s lone pair electrons of Bi are believed to be responsible for ferroelectricity and the partially filled d orbital of Fe is responsible for magnetic ordering. [63] Magnetoelectric coupling has promising applications in electrically-written and magnetically-read memory devices, [64] in which the switching of ferromagnetic state can be controlled with the changing of the direction or magnitude of the electric field and vice versa. [65]

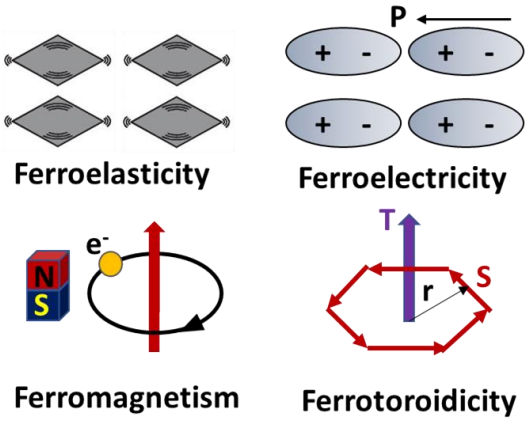

Figure 2-9. Different forms of "ferroic" orders. [59]

2.3.2 Crystal Structure and Phase Composition

Bulk BFO has a rhombohedral (*R*3*c*) distorted perovskite structure at room temperature, [58] which allows for antiphase octahedral tilting and ionic displacements from the center position about and along the $[111]_{pc}$ direction [6], as shown in **Figure 2-10**. The pseudocubic unit cell parameters of BFO are a=b=c=3.965 Å, α=β=γ=89.4°. The oxygen atoms occupy the face-center of the cubic framework comprised of Bi atoms.

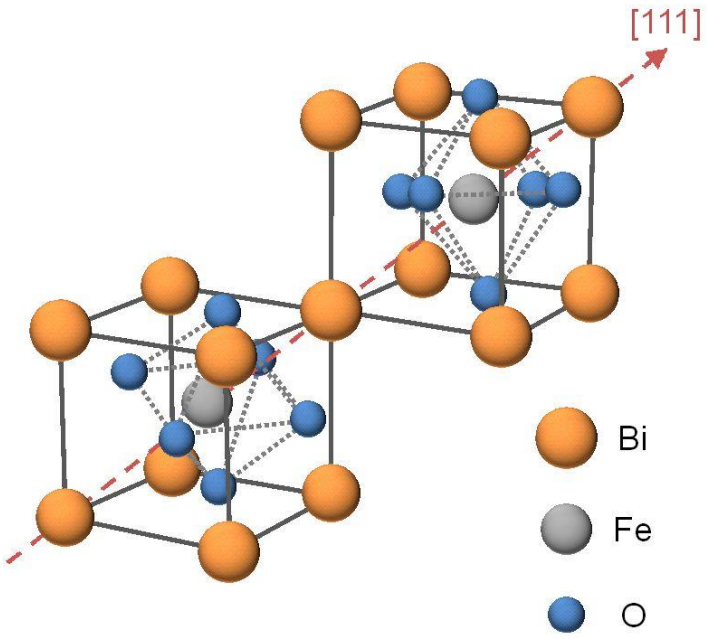

Figure 2-10. *R3c* crystal structure of the BFO. [66]

Figure 2-11(a) demonstrates the binary phase diagram of Bi_2O_3-Fe_2O_3. The stoichiometric ratio of Bi and Fe (Bi: Fe = 1) is usually applied for the synthesis of BFO. Due to the thermodynamic instability of BFO, parasitic phases (such as $Bi_2Fe_4O_9$, $Bi_{25}FeO_{39}$) are prone to form, and at high temperatures, BFO tends to decompose back into starting Bi_2O_3 and Fe_2O_3. The volatile nature of Bi^{3+} ion leads to the reduction of Fe^{3+} to Fe^{2+} ion and the formation of oxygen vacancies. Thus, the initial Bi/Fe ratio of starting materials and the annealing atmosphere are also used to control the synthesis kinetics of BFO.

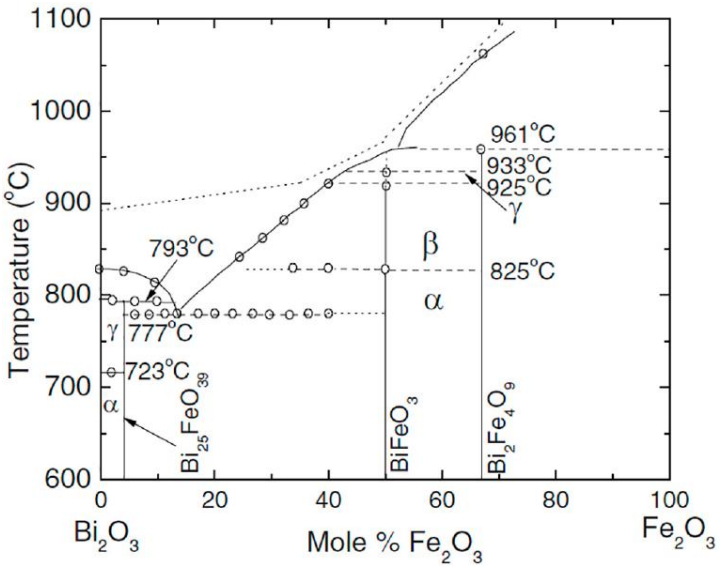

Figure 2-11. Phase diagram of the Bi_2O_3-Fe_2O_3 system. [67]

For bulk BFO ceramics, the sintering temperature of the pure phase is usually high at ~ 800 ℃. Under this temperature, the BFO is considered to be a metastable compound, and easy to decompose and yield secondary phases. While, in thin film form, a lower sintering temperature (≤ 700 ℃) is sufficient for the crystallization of pure-phase BFO due to the heterogeneous nucleation. Importantly, the versatile polymorphs are easily achievable in BFO thin films through the controllable strain magnitude, which provides a large design margin for multifunctional electronic devices.

2.3.3 BFO Thin Films

In 2003, a large P_r of 50-60 μC/cm^2 in epitaxial BFO thin films was realized by Wang *et al.* [10], which at the time was an order of magnitude higher than the best value reported in bulk BFO of 6.1 μC/cm^2 (It wasn't until 2007 that large spontaneous polarization of 100 μC/cm^2 was found in bulk BFO single crystals [68]). Since then, significant interest in BFO films has been raised. The appearance of high-quality ferroelectric thin films is an important revolution for the miniaturization and integration of electronic devices. [6]

More importantly, in film form, the stable crystal structure can be easily altered. The epitaxial strain effect resulting from the lattice mismatch [69, 70] and chemical pressure effect produced by the chemical substitution [8, 71, 72] are two common ways taken to induce the distortion of the perovskite cell and create MPB, and, thus, possibly, a superior electromechanical response.

2.3.3.1 Epitaxial Strain Effect

Epitaxial growth occurs when a film presents in a specific crystallographic orientation that matches with the substrate. Depending on the magnitude of the lattice match between the thin film and substrate, tensile or compressive strain can be imposed, which can result in the in-plane (IP) elongation or contraction and, correspondingly, an out-of-plane (OP) contraction or elongation of the film. This lattice mismatch (σ) is defined as:

$$\sigma = \frac{d_s - d_f}{d_s} \qquad \textbf{Equation 2-2}$$

Where, d_s and d_f are the IP lattice parameters of substrate and film, respectively.

The bulk structure of BFO is rhombohedral (R3c space group). In epitaxial BFO films, the various polymorphs, such as tetragonal-like (T'), R, O, monoclinic (M_C, M_A & M_B), and triclinic, can be stabilized under the specific epitaxial strain. The crystal structures and corresponding strain types are summarized in **Figure 2-12**. As shown, the bulk-like R phase usually forms on (111)-oriented substrates. The M_A monoclinic and the highly distorted *T*-like monoclinic C_m phase can be stabilized at moderate and strong compressive strain, respectively. The tetragonal BFO forms only for very thin films. The orthorhombic and monoclinic M_B forms in tensile strain locations. [6, 73] Therefore, the structural symmetry of BFO films can be artificially designed by tailoring the strain effect.

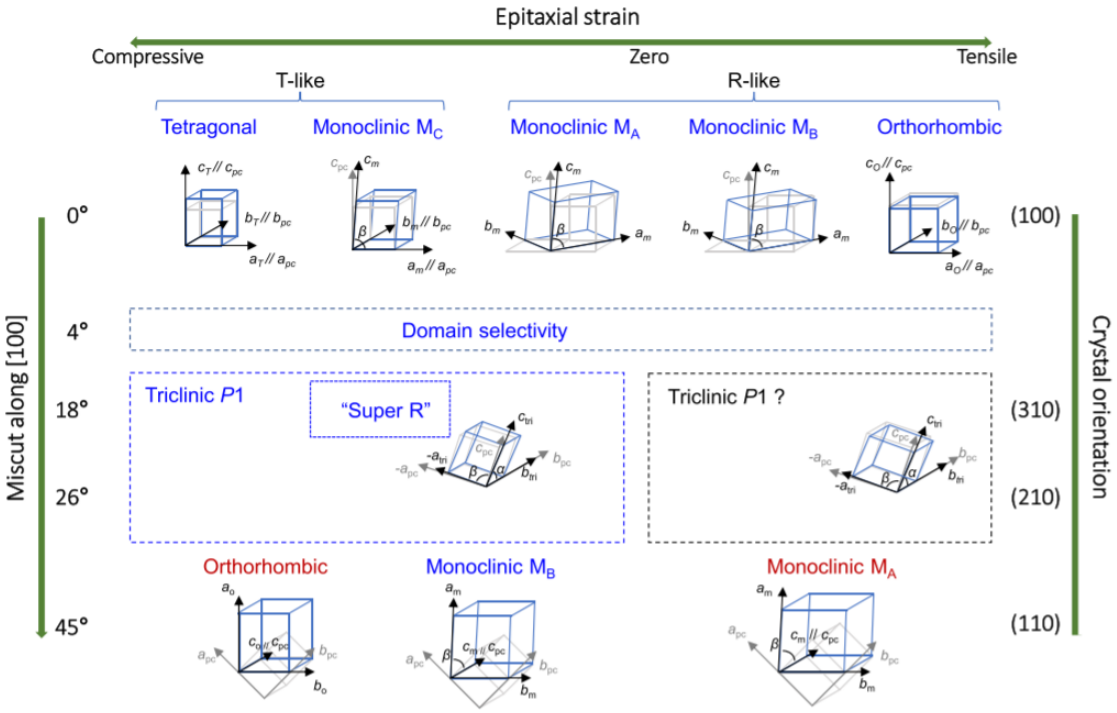

Figure 2-12. Various crystal structures of BFO thin films under different stains. [73]

One effective way to induce different strain effects is by growing the BFO thin films on substrates with different orientations. It has been reported that the epitaxial BFO films on (001), (110), and (111) $SrTiO_3$ (STO) substrates have M_A, M_B, and R structures, respectively, with the polarization constrained to (001), (110) planes and <111> direction. Further, growing BFO on low symmetry orientations of single crystal substrates (i.e., (130) and (120) STO substrates), a triclinic phase was formed. [73, 74]

Another commonly adopted approach is by growing BFO on various substrates. The lattice parameters of the different single crystal substrates are listed in **Table 2-2**. For a clear view of the BFO structure transformation under various strains, a linear relationship between the OP lattice parameters and the IP strain was given by Chen *et al.* [69], as shown in **Figure 2-13**. They systematically studied the epitaxial BFO films on seven different pseudocubic (001) oriented single-crystal substrates ($LaAlO_3$ (LAO), $NdGaO_3$ (NGO), STO, $DyScO_3$ (DSO), $(LAO)_{0.3}$-$(SrAl_{0.5}Ta_{0.5}O_3)_{0.7}$ (LSAT), $TbScO_3$ (TSO) and $KTaO_3$ (KTO)). The lattice mismatches are ranging from -4.4% (BFO/LAO) to +0.6% (BFO/KTO). With the compressive strain increasing from 0 to -4.4%, the $R \rightarrow M_A \rightarrow M_C$ phase evolution was observed. The abrupt increase of the c lattice parameter from M_A to M_C transformation indicates an obvious change of the polarization direction. With the tensile strain increasing from 0 to 0.6%, the $R \rightarrow M_B$ was found. The

polarization direction change induced by the change of the symmetry of BFO structures are described as the inserted picture in **Figure 2-13(a)**. The evolution of the energy and the ratio of the c/a lattice parameter as a function of the IP strain is shown in **Figure 2-13(b) and (c)**. The increase of the strain and the induced structural deformation will lead to an increase in energy. By imparting the epitaxial strain from an underlying substrate, the altering of the stable structure and further tailoring of the physical properties of BFO films can be achieved.

Table 2-2. Lattice parameters of the commonly used substrates for the growth of BFO films. [63]

Substrate materials	Phase structure	Lattice parameters (Å)	Misfit strain (BFO) (%)	Strain types
$NdCaAlO_4$	*T*	3.685(a = b)/12.12(c)	-7.0	
$YAlO_3$	*O*	3.69(a = b = c)	-6.9	
$LaSrAlO_4$	*T*	3.755(a = b)/12.6(c)	-5.2	Compressive strain
$LaAlO_3$	*R*	3.79(a = b = c)	-4.4	
$NdGaO_3$	*O*	5.426(a)/5.496(b)/7.707(c)	-2.8	
$SrTiO_3$	*C*	3.905(a = b = c)	-1.5	
$KTaO_3$	*C*	3.989(a = b = c)	+0.6	
$NdScO_3$	*O*	5.575(a)/5.776(b)/8.003(c)	+1.2	Tensile strain
MgO	*C*	4.216(a = b = c)	+6.3	

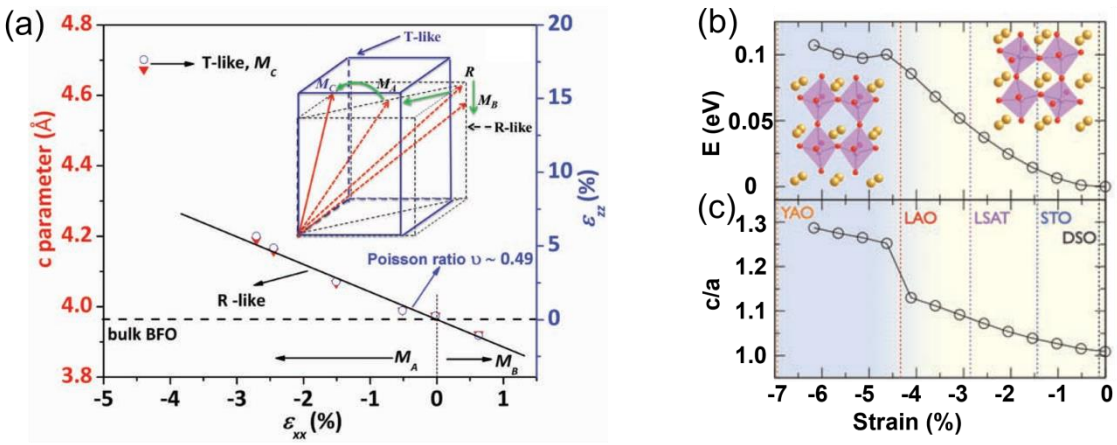

Figure 2-13. (a) Schematic diagram of OP lattice parameters (solid red) and lattice strains ε_{zz} (open blue) plotted as a function of the IP misfit strain ε_{xx} (inset: the possible strain-induced rotation path, red arrows: the polarization directions) [69], The evolution of the energy (b) and the c/a lattice parameter ratio (c) of the BFO structure as a function of IP strain. [9]

In 2009, Zeches *et al.* [9] reported a strain-driven MPB in epitaxial BFO films with a measurable physical height change. High-quality mixed-phase BFO thin films with the T' and rhombohedral-like (R') phases coexistence were fabricated on an LAO substrate. The

reversible conversion from the T phase to a mixture of T and R phases under an applied electric field provided large and nonvolatile changes in surface displacements with an effective strain of up to 2.4%. The high-resolution transmission electron microscopy (TEM) image of the mixed-phase boundaries of the typical stripe-like atomic force microscopy (AFM) image is shown in **Figure 2-14**.

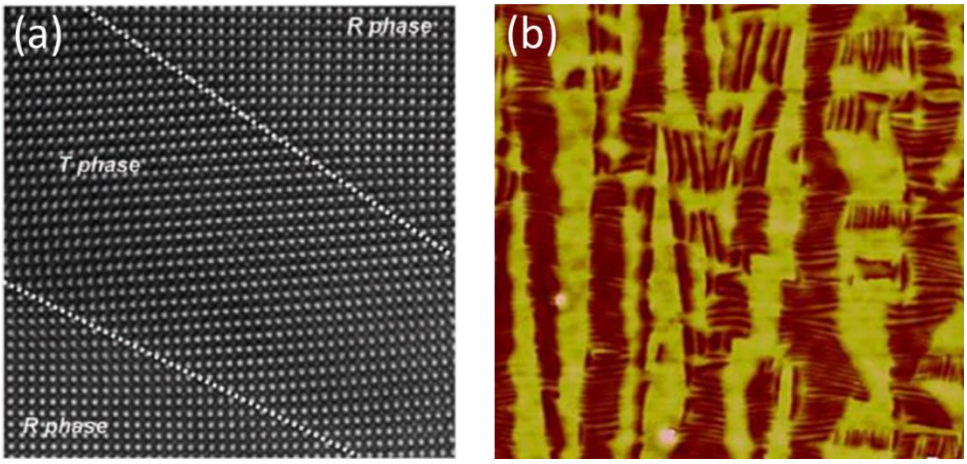

Figure 2-14. (a) High-resolution TEM image of the mixed-phase boundaries and (b) AFM image of the mixed-phase region. [9]

Except for the orientation and the variety of the substrates, the thickness of thin films as well as the synthesis conditions can also alter the strain state. The modulation of strain is also called strain engineering. In the following **Chapter 4 and Chapter 5**, we investigated the influence of the thickness and heating treatment process on the phase fraction and further the conduction behavior of prepared films.

2.3.3.2 Chemical Pressure Effect

Chemical substitution, so-called site engineering, is an effective method to tune the composition and crystal structure of BFO from bulk ceramics to thin films. Here, we focus on films.

Chemical doping, that is by incorporating heteroatoms into the host lattice, can generate an intrinsic pressure to induce the lattice distortion, and thus stabilize a novel crystal structure. In addition, it is accepted that the ferroelectricity of BFO mainly derives from the Bi 6s lone pair of electrons. Thus, the A-site substitution is expected to not only realize the giant piezoelectric properties at MPB but also modify its ferroelectric properties.

A series of A-site doping, including La, Nd, Gd, Ba, Ce, Eu, Sm, Tb, Sr, and Ho, has been

intensively investigated. The improved ferroelectric properties after doping are summarized in **Table 2-3**. Taking La doping as an example, La doping was expected to stabilize the oxygen octahedron of BFO and thus reduce the oxygen vacancies, which is highly related to the leakage behavior of films. High leakage current is one of the most detrimental problems, which greatly hinders the performance of BFO. It will be discussed in the following **Chapter 3.4.2** Yan *et al.* [75] reported a suppressed leakage current and a giant P_r of 102 μC/cm^2 in La-doped BFO thin films on Pt/TiO_2/SiO_2/Si substrates. The leakage current density-electric field (J-E) curves and P-E loops are shown in **Figure 2-15**. The enhanced ferromagnetic properties were also observed in La-doped BFO thin films on Nb-doped STO substrates by pulsed laser deposition (PLD). [76]

Table 2-3. Ferroelectricity characteristics of A-site substitution of BFO thin films.

Material system	Pr (μC/cm^2)	Ec (kV/cm)	Substrate	Techniques	Ref.
$Bi_{0.95}La_{0.05}FeO_3$	90	250	$BaPbO_3$/Pt/ TiO_x/SiO_2/Si	rf magnetron sputtering	[12]
$Bi_{0.95}Sm_{0.05}FeO_3$	82	350	Pt/Ti/SiO_2/ Si(100)	CSD	[77]
$Bi_{0.9}Eu_{0.1}FeO_3$	74	250	Pt/Ti/SiO_2/Si	PLD	[78]
$Bi_{0.9}Nd_{0.1}FeO_3$	60	314	Pt/Ti/SiO_2/Si	PLD	[79]
$Bi_{0.9}Tb_{0.1}FeO_3$	9.4	65	Pt/Ti/SiO_2/Si	Sol-Gel	[80]
$Bi_{0.95}Gd_{0.05}FeO_3$	8.9	108	Pt(111)/Ti/ SiO_2/Si(100)	Sol-Gel	[81]
$Bi_{0.8}Ce_{0.2}FeO_3$	3.12	198	Pt/TiN/Si_3N_4/ Si	Sol-Gel	[82]
$Bi_{0.85}Ba_{0.15}FeO_3$	35	353	Corning 1737 glass	rf magnetron sputtering	[13]
$Bi_{1-x}Sr_xFeO_3$ (x = 0-0.15)	-	-	Pt/TiO_2/SiO_2/ Si	Sol-Gel	[83]
$Bi_{0.9}Ho_{0.1}$ $(Fe_{0.99}Ni_{0.01})O_3$	32	385	Pt(111)/Ti/ SiO_2/Si(100)	CSD	[84]

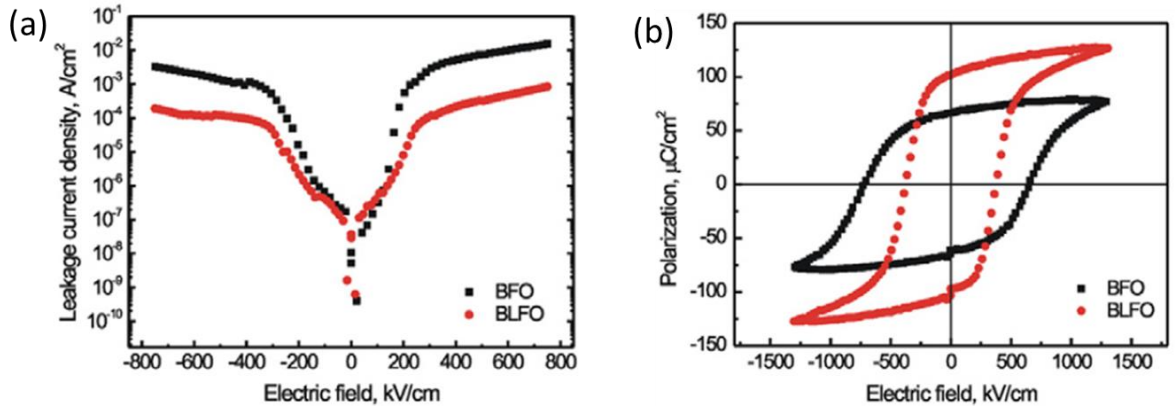

Figure 2-15. (a) leakage current density; (b) ferroelectric hysteresis loops of BFO and $Bi_{0.95}La_{0.05}FeO_3$ (BLFO) thin films at room temperature. [75]

Besides A-site doping, B-site doping is also commonly adopted for improved ferroelectric properties in perovskite oxides. There are several candidates (such as Mn [85, 86], Zn [87], Co [88], Ti [89], Ru [75] and Cr [90]) that have been applied to substitute the Fe ion for better ferroelectric or magnetic properties. A decreased leakage current and high P_r of 100 μC/cm^2 were observed at the 3-5% Mn doping in chemical solution deposition (CSD) -derived BFO thin films. The Mn doping led an R phase towards O or T phase transition due to the induced lattice deformation. [91, 92] Wang *et al.* [87] utilized Zn to substitute Fe by a radiofrequency (RF) sputtering technique. The as-fabricated $BiFe_{0.96}Zn_{0.04}O_3$ thin films showed a low leakage current and dielectric loss, and a high $2P_r$ value of 268.5 μC/cm^2. Meanwhile its magnetic properties deteriorated because of the suppression of Fe^{2+} formation by aliovalent doping with nonmagnetic Zn^{2+}.

In addition, the co-doping in A- and B-site, such as the substitution with La and Mn [93], Sm and Mn [94, 95], Dy and Mn [96], Ca and Mn [97], Ce and Zr [98], In and Co [99], has also been pursued to seek for both the improved ferroelectric and magnetic properties in BFO. That is to suppress the defects formation and modulate the inhomogeneous magnetic spin structure, respectively.

2.3.4 Sm-Doped BFO Thin Films

Compared to the large ionic radii of Bi^{3+} of 1.36 Å, RE dopants with smaller ionic radii. It is expected that this difference in atomic radii can induce a potential octahedra rotation, and further a possible crystal structure change, as well as the novel and improved functional

properties. Sm, one of the lanthanide elements, is the choice of investigation for this work. Therefore, the literature on the effects of Sm substitution in A-site on the BFO films is separately summarized here.

In 2008, Prof. Takeuchi's group [7], reported an MPB in Sm-doped BFO thin films with the Sm composition at 14%, which showed dielectric constant and piezoelectric coefficient comparable to that of epitaxial (001) oriented $PbZr_{0.52}Ti_{0.48}O_3$ films. They found Sm substitution induced a phase transition from ferroelectric R phase to paraelectric O phase. Two years later, they, further, systematically tracked the structure and ferroelectric behaviors of the doping BFO using trivalent ions Sm, Gd, and Dy with the ionic radii of 1.28 Å, 1,27 Å, and 1.24 Å respectively. [8] A universal behavior and a similar structure transition from ferroelectric R phase to paraelectric O phase were discovered, as shown in **Figure 2-16**. It was concluded that the structure and ferroelectric properties transitions were dependent on the average radius of the A-site ionic and not the dopant species. The consequent investigation of the Sm-doped BFO on different substrates, STO and lanthanum aluminate-strontium aluminium tantalate, showed the same phase transition at Sm concentration of 14%. [72] This confirmed that it is the chemical pressure effects rather than the strain effects that lead to the change in structure. Cheng *et al.* conducted a detailed investigation of the microstructure near the MPB composition with selected area electron diffraction patterns (SAEDs). They found that there was a complex nanoscale phase coexistence at MPB with the presence of a competing intermediate antipolar phase with the ferroelectric *R* and nonpolar O phase. [15, 100, 101]

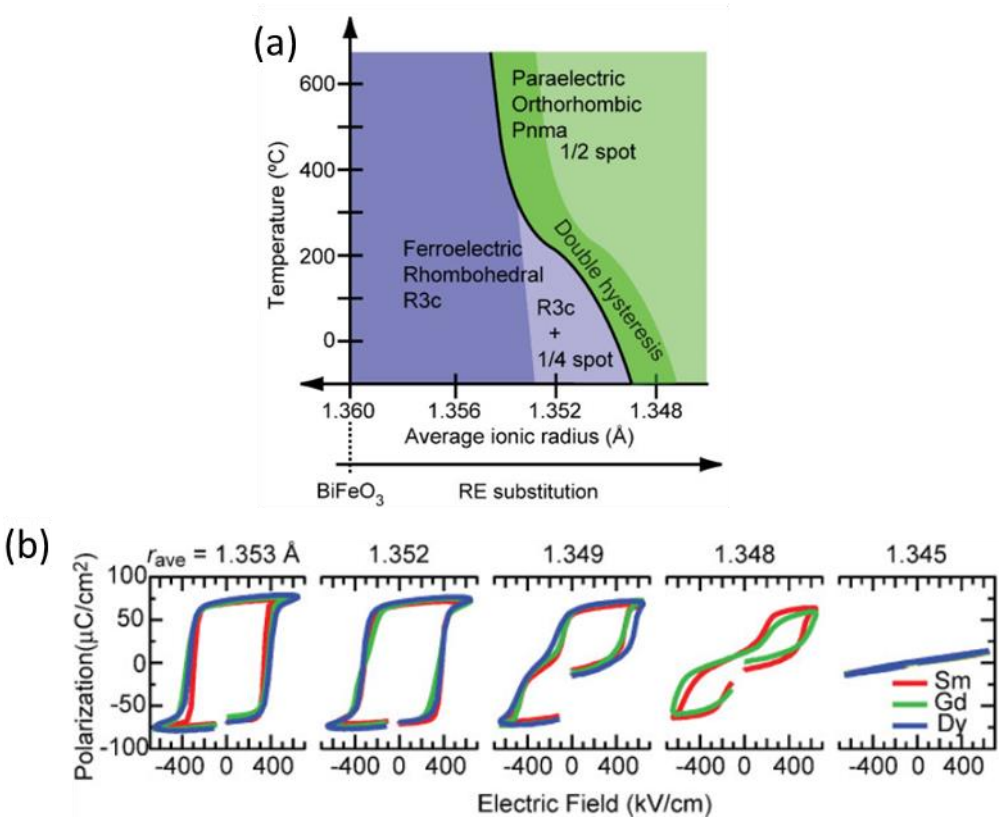

Figure 2-16. (a) Phase diagram and (b) universal behavior in polarization hysteresis loops of $(Bi_{1-x}RE_x)FeO_3$. [8]

The large design margin in film form provides the opportunity for the discovery of novel phases in BFO and thus, huge piezoresponse and improved ferroelectric properties. Strain Engineering or/and site engineering are separately/simultaneously applied in this work.

2.3.5 Leakage Current and Conduction Mechanisms

The leakage issue suffered in BFO is one of the main challenges that impede the detection of its intrinsic ferroelectric properties and limits its use in practical applications. It is commonly accepted that the high leakage current originates from the volatile bismuth and the fluctuation of the valence of Fe ions, which leads to the formation of charge defects (e.g., oxygen vacancies and electrons), as shown in **Equations 2-3 to 2-5**.

$$2Bi_{Bi}+3O_o \rightarrow Bi_2O_3(\text{evaporation})+2V_{Bi}^{'''}+3V_O^{\cdot\cdot} \qquad \textbf{Equation 2-3}$$

$$2Fe_{Fe}+3O_O \rightarrow 2Fe_{Fe}^{'}+V_O^{\cdot\cdot}+\frac{1}{2}O_2+2O_O \qquad \textbf{Equation 2-4}$$

$$2Fe_{Fe}+O_o \rightarrow 2Fe_{Fe}^{'}+V_o^{\cdot\cdot}+\frac{1}{2}O_2 \qquad \textbf{Equation 2-5}$$

Usually, a relatively large electric field is required to trigger the corresponding physical performance for the normal operation of the devices. At such a high electric field, a noticeable conduction current will occur and is detrimental to the performance. That is, to satisfy the specific reliability standard, the conduction current is required to be lower than a certain value. Thus, it is imperative to understand the underlying conduction mechanisms.

There are two types of conduction mechanisms in dielectric films (i.e., electrode-limited (or injection-limited) conduction mechanism and bulk-limited (or transport-limited) conduction mechanism. Electrode-limited conduction, as the name implies, depends on the effects at the electrode-dielectric contact. The barrier height at the electrode-dielectric interface and the effective mass of the conduction carriers in dielectric films are two key parameters in this conduction mechanism. The second mechanism, bulk-limited conduction, depends on the properties of the dielectric itself. The trapped energy level in the dielectric films is the most important factor. **Table 2-4** summarizes these various conduction mechanisms. [102]

Table 2-4. Classification of conduction mechanisms and the defined equations. [102]

Electrode-limited conduction mechanism
(1) Schottky or thermionic emission $J = A^* T^2 exp[\frac{-q(\phi_B - \sqrt{qE/4\pi\varepsilon_r\varepsilon_0})}{kT}]$ J: the current density, A^*: the effective Richardson constant, T: the absolute temperature, q: the electronic charge, $q\phi_B$: the Schottky barrier height, E: the electric field across the dielectric, k: the Boltzmann's constant, h: the Planck's constant, ε_0: the permittivity in a vacuum, ε_r: the optical dielectric constant (i.e., the dynamic dielectric constant).
(2) Fowler-Nordheim tunnelling $J = \frac{q^2E^2}{8\pi h\phi_B} exp[\frac{-8\pi(2qm_T^*)^{1/2}}{3hE}\phi_B^{3/2}]$ m_T^*: the tunneling effective mass.
(3) Direct tunnelling $J = \frac{q^2}{8\pi h\varepsilon\phi_B} C(V_G,V,t,\phi_B) exp\{\frac{-8\pi\sqrt{2m^*}(q\phi_B)^{\frac{3}{2}}}{3hq\lvert E\rvert}\cdot[1-(1-\frac{\lvert V\rvert}{\phi_B})^{\frac{3}{2}}\}$ t: the thickness of the dielectric, V: the voltage across the dielectric.
(4) Thermionic-field emission $J = \frac{q^2\sqrt{m}(kT)^{1/2}E}{8h^2\pi^{5/2}} exp[\frac{-q\phi_B}{kT}] exp[\frac{h^2q^2E^2}{24m(kT)^3}]$
Bulk-limited conduction mechanism
(1) Poole-Frenkel emission $J = q\mu N_C E exp[\frac{-q(\phi_T - \sqrt{qE/\pi\varepsilon_i\varepsilon_0}}{kT}]$ μ: the electronic drift mobility, N_C: the density of states in the conduction band, $q\phi_T$ (= Φ_T): the trap energy level.
(2) Hopping conduction $J = qanvexp[\frac{qaE - E_a}{kT}]$ a: the mean hopping distance (i.e., the mean spacing between trap sites), n: the electron

concentration in the conduction band, v: the frequency of thermal vibration of electrons at trap sites, Ea: the activation energy, namely, the energy level from the trap states to the bottom of the conduction band (E_C).

(3) Ohmic conduction

$$J = nq\mu E$$

(4) Space-charge-limited conduction (SCLC)

$$J_{Ohm}=qn_0\mu E \qquad J_{TFL}=\frac{9\mu\varepsilon_r\varepsilon_0\vartheta}{8d}E^2 \qquad J_{Child}=\frac{9\mu\varepsilon_r\varepsilon_0}{8d}E^2$$

d: the thickness of thin films.

(5) Ionic conduction

$$J=J_0 exp[-(\frac{q\phi_B}{kT}-\frac{Eqd}{2kT})]$$

J_0: the proportional constant, d: the spacing of two nearby jumping sites.

(6) Grain-boundary-limited conduction

$$\Phi_B=q\phi_B=\frac{q^2n_b^2}{2\varepsilon_r\varepsilon_0 N}$$

n_b: the grain boundary trap density, N: the dopant concentration.

Chung *et al*. [103] investigated the leakage current behaviors of CSD-derived polycrystalline Mn-doped, Nb-doped, and pure BFO films, and found that the conduction mechanisms were Ohmic conduction, grain-boundary-limited and space charge limited conduction, respectively. Wang *et al.* [104] studied the influence of the oxygen pressure and annealing effect on the leakage current in PLD fabricated $(Bi_{0.6}Tb_{0.3}La_{0.1})FeO_3$ films. An SCLC-dominant mechanism was found in film grown at higher oxygen pressure and a Poole-Frenkel conduction mechanism at lower oxygen pressure. Pabst *et al.* [105] investigated the influence of the symmetric and asymmetric device structures on the BFO leakage mechanisms and found a Poole-Frenkel emission mechanism in the symmetric structure and no dominant leakage mechanism observed for the asymmetric one. Therefore, the elements doping, processing conditions, and the device structures all have a significant influence on the leakage current behaviors of BFO films.

In this work, by tailoring the strain states of the BFO films, we investigated the leakage behavior and the conduction mechanism variation with the phase fraction. We also studied the conduction behaviors of the Sm dopant composition on BFO films.

2.4 Thin Films Fabrication

2.4.1 Film Deposition Process

Physical methods and chemical methods are two approaches to the synthesis of ferroelectric thin films. [32] The physical method includes PLD, RF-magnetron sputtering, and molecular beam epitaxy (MBE) *etc*. Chemical methods include CSD, metal organic chemical vapor deposition (MOCVD), hydrothermal method (HM), and liquid phase epitaxy growth (LPE), etc. **Table 2-5** lists their pros and cons. Generally, high-quality epitaxial thin films with higher cleanliness, density, and lower surface roughness are achieved via physical method. Among them, PLD is widely used in the lab for high-quality ferroelectric mono/multilayer thin films. These samples usually show outstanding epitaxial crystallographic structures and nearly defect-free microstructures. The ferroelectric properties are also superior. However, PLD is not suitable for large-scale commercial adoption since its time- and labor-intensive and high cost. In comparison, chemical methods are relatively more economically viable. The ease of controlling the film composition by tuning the sol precursor makes it a promising candidate for the industrial field. In this work, the CSD method was adopted for film preparation.

Table 2-5. Pros and cons of different synthesis technologies of thin films.

	Pros	Cons	Ref
PLD	· Suitable for the depositing materials with a high melting point · Accurate control of film thickness and composition · High deposition rate · No high-temperature annealing required · No pollution and easy to exchange targets · Suitable for the synthesis of high purity epitaxial monocrystalline, superlattice and multilayer films	· High equipment and maintenance costs · Not suitable for the preparation of large-scale films and industrial application	[106, 107]
Sputtering	· Suitable for a wide range of materials, especially, with high melting point and low vapor pressure · low deposition temperature · High deposition rate · Suitable for high-quality epitaxial monocrystalline films	· Difficult to control the composition of thin films · Complex equipment required ·High-pressure device required · Susceptible to impurity gases	[12, 108]
MBE	· Accurate control of the element beams in situ · Relatively low substrate temperature · Possible doping in suit · Accurate control of doping concentration · Suitable for preparation of multicomponent films	· Super high vacuum required · Time-consuming · Not suitable for depositing high melting point materials · High equipment and maintenance costs	[109]
MOCVD	· Precise control of film thickness and stoichiometric ratio · High uniformity and repeatability · Low deposition temperature · Higher deposition rate · Suitable for large-scale industrial production	· High flammability, explosibility, and toxicity of the raw materials · Rare species of metal organic sources · Highly cost	[110]
HM	· Easily extendable and inexpensive ·Low-temperature method to grow thin films under autogenous or increased pressure · Good stoichiometry control	· Difficult to grow monocrystalline thin films · Poor repeatability · Hard analysis in suit	[111-113]
LPE	· Simple and reliable devices · Precise control of thin films composition and thickness · Easy to grow high purity monocrystalline layer · High growth rate	· Not suitable for ultrathin single crystal growth · Poor surface morphology of epitaxial layer · Nonuniform composition and doping concentration along the growth direction	[114]

2.4.2 Chemical Solution Deposition (CSD) Technique

CSD, also known as the sol-gel method, consists of five steps to deliver the final oxide thin film protocols. That is the preparation of the precursor solution, deposition on substrates via spin coating, gelation, pyrolysis, and crystallization. [32, 115]

(1) Preparation of precursor solution

Typically, the precursor solution is a mixture of metal salts (metal acetates, nitrates, sulfates, chlorides, or alkoxides), solvent (water or organic solvent) and chelating agent (acetic anhydride, acetic acid, or citric acid). The applied stoichiometric ratios of the metal salts decide the ultimate film's composition. For pure BFO and Sm-doped BFO films, bismuth nitrate pentahydrate [$Bi(NO_3)_3 \cdot 5H_2O$], iron nitrate nonahydrate [$Fe(NO_3)_3 \cdot 9H_2O$], or/and samarium nitrate hexahydrate [$Sm(NO_3)_3 \cdot 6H_2O$] are used. 2-Methoxyethanol (2-MOE) and acetic anhydride are used as solvents and chelating agents. The organic solvent, 2-MOE can offer high solubility of the metal nitrates. Its proper viscosity can provide a suitable surface tension, which is critical for defect-free gel films during the spin coating process. The chelating agent, acetic anhydride can facilitate the gelation process and adjust the viscosity of the precursor. In addition, the use of a chelating agent as a multidentate ligand can induct several bonds to a single metal ion, which ensures the formation of a three-dimensional network structure. This formed polymeric structure can help a film crystalized in a certain direction. Due to the volatilization of Bi, excess bismuth nitrate is usually added to compensate for the loss of Bi during the annealing process. Oversupplied Bi can possibly form bismuth-rich clusters, which is detrimental to films' dielectric and ferroelectric properties. Therefore, proper stoichiometric ratios of metal nitrates and suitable solvents must be weighed and used for the preparation of precursors.

(2) Deposition on substrates via spin coating

Spin coating is one of the most common approaches to depositing thin films on given substrates, which can form uniform films with the thicknesses ranging from nanometers to several microns by controlling the spin speed and holding time at the maximum spin velocity. In addition, the viscosity and vapor pressure of the precursor solution, temperature and the humidity of the environment also determines the final thickness and quality of the thin films.

(3) Gelation

The gelation process is vital in making defect-free gel films with high uniformity and stability. It is always accompanied by polymerization and solvent evaporation. After spin coating, the following drying process will be adopted to vaporize the solvent molecules left in the three-dimensional network structure. At this stage, the thickness will be reduced. The

relatively high specific surface area of films may lead to a large shrinkage of the gel films. The homogeneity of the gel films highly depends on the drying temperature and holding time. Therefore, optimizing the gelation and drying process for a better balance between the relative rates of polymerization and solvent evaporation can help to prevent the appearance of unexpected precipitates and cracks in the gel films.

(4) Pyrolysis and crystallization

Pyrolysis process is used to remove the polymers in the gel films, which undergoes at a relatively lower temperature than that of crystallization. At this step, an amorphous phase will be formed. Then after the crystallization, the amorphous phase can be converted into crystalline oxide film. Due to these two heat treatment processes, substantial shrinkage occurs. It may lead to the formation of defects (e.g., cracks and pores) in the films, which will deteriorate the microstructure and electromechanical properties. Therefore, careful optimization of the heating process is vital for the quality of the ultimate films.

It was in the 1980s that the CSD method was first applied to synthesize perovskite oxide thin films. Fukushima *et al.* [116] and Budd *et al.* [117] prepared PZT ferroelectric films with better properties via metalloorganic deposition (MOD) and sol-gel methods respectively. Afterwards, various perovskite-related compound films were explored using the CSD method. In 1997, Teowee synthesized polycrystalline BFO films on Si(100) substrates via the sol-gel method. [118] In the early stage, the prepared BFO films by CSD were polycrystalline without preferred orientations and usually accompanied by the generation of secondary impurity phases, and thus showed unsaturated P-E loops. To improve the ferroelectric properties, investigations into the composition of the precursor solution [119], the amount of Bi [120, 121], the thickness [122, 123], heat treatment procedure (annealing temperature [124], rate of heating, sintering atmosphere [125, 126]) were carried out to optimize the quality of films. Although this enabled reduced leakage current and the improved ferroelectric properties, the reliable P-E loops could be only obtained at low temperatures. It wasn't until 2007, when Gonzalez [127] and Simoes [128] *et al.* synthesized the pure BFO thin films on Pt/Ti/SiO_2/Si substrates using the soft chemical method that good P-E loops (**Figure 2-17**) were achieved. Subsequently, more BFO films with better ferroelectric properties via CSD were reported in succession.

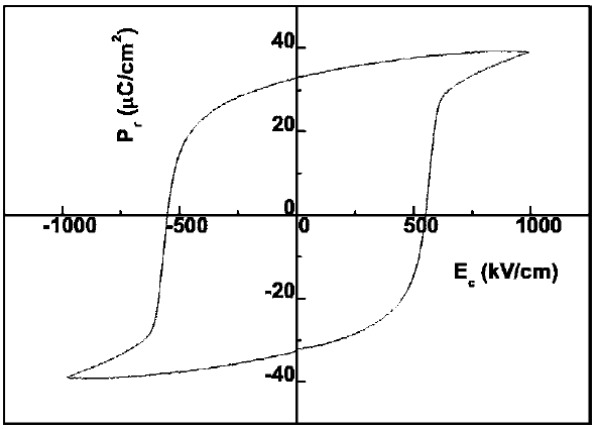

Figure 2-17. P-E loop of soft chemical solution-derived BFO films at room temperature. [127]

In brief, every single step is vital to the composition, microstructure, and properties of the final thin films. The possible secondary phases, pores and cracks defects, and thus induced poor electrical properties are the major barriers to the popularization and application of CSD technology in film preparation. Therefore, optimizing the synthesis conditions to realize a high-quality CSD-derived film with few or even no defects is of great significance.

2.5 Summary

This literature review has given an introduction to the concepts of ferroelectricity and domain structure of perovskite oxides, and the MPB effects, as well as the potential applications of these materials. Particularly, lead-free BFO thin film was systematically introduced due to its appealing structural variety and multifunctional properties. The importance of epitaxial strain effects and the chemical pressure effects on the structure composition and electromechanical properties of BFO films were highlighted. In addition, the fundamental procedures of CSD method are simply summarized. The major points are enumerated as below:

(1) Perovskite-type ferroelectric oxides, possessing both piezoelectricity and ferroelectricity simultaneously, are important materials that have great potential for applications in microelectronic devices, such as sensors, actuators, transducers, and memory devices.

(2) The coexistence of multiple structural phases at the MPB offers superior electromechanical properties, which highly drive the development of lead-free

piezoelectric materials.

(3) BFO has attracted intensive attention due to its room-temperature single phase multiferroic character, which make it an excellent candidate for environmental-friendly and high-temperature applications.

(4) BFO thin films offer a large design range for the tuning of the structure configuration and multifunctional properties due to the possible various polymorphs stabilized by epitaxial strain or/and chemical pressure effects. For example, the reversible phase transition between T' and R' in mixed-phase BFO thin film showed a colossal electromechanical response. The phase transition from the R to O phase in Sm-doped BFO films leads to the ensuing evolution from ferroelectric to paraelectric state. It makes BFO particularly appealing for practical applications. However, the suffered leakage issues have hampered its development.

(5) CSD method is easy to implement both in labs or industrial fields due to its economic and large-scale viability. The easy tuning of the precursor composition offers great flexibility for the introduction of various dopants into the BFO host lattice, and thus constructs an MPB. However, it is still a challenge for the fabrication of high-quality epitaxial thin films due to the small synthesis window of pure phase BFO.

This thesis aims to (1) prepare high-quality epitaxial BFO films with mixed-phase structures (strain engineering), and study the leakage behavior variation with the phase fraction change; (2) substitute the A-site Bi^{3+} with Sm^{3+} (site engineering) to investigate the evolution of the phase and ferroelectric properties with the Sm content; (3) further construct a more complex MPB through both strain engineering and site engineering to seek for novel phase structure and electrical properties. This systematically and step-by-step tailoring of the BFO structures gives a better understanding of the role of epitaxial strain and Sm doping on the phase transition and the physical properties improvement.

Chapter 3. Experimental Procedures

This chapter contains an outline of the basic methodologies of the film preparation and device fabrication processes used in this thesis, as well as the corresponding characterization techniques.

3.1 Thin Film Fabrication Process

3.1.1 Precursor Solution Preparation

The specifications of the starting chemicals utilized for the precursor preparation are listed in **Table 3-1**. All metal nitrates are stored in tightly sealed containers and kept in a ventilated cupboard to prevent water absorption.

Table 3-1. Detailed information about the raw chemicals.

Product name	Chemical formula	Specification	Brand	Supplier
Bismuth nitrate pentahydrate	$Bi(NO_3)_3{\cdot}5H_2O$	ACS 98%	Sigma-Aldrich	Sigma-Aldrich (Australia)
Iron nitrate nonahydrate	$Fe(NO_3)_3{\cdot}9H_2O$	ACS 98%	Alfa Aesar	Bio-Strategy (UK)
Samarium nitrate hexahydrate	$Sm(NO_3)_3{\cdot}6H_2O$	ACS 99.9%	Alfa Aesar	Bio-Strategy (UK)
2-methoxyethanol	$C_3H_8O_2$	ACS 99.3+%	Alfa Aesar	Bio-Strategy (UK)
Acetic anhydride	$C_4H_6O_3$	ACS 99%	Sigma-Aldrich	Sigma-Aldrich (Australia)

The stoichiometric $BiFeO_3$ (BFO) precursor solutions with/without Sm doping (denoted as $Bi_{1-x}Sm_xFeO_3$, BSFO) are prepared by dissolving $Bi(NO_3)_3{\cdot}5H_2O$, $Sm(NO_3)_3{\cdot}6H_2O$, and $Fe(NO_3)_3{\cdot}9H_2O$ in 5 ml 2-MOE organic solvent and stirring for 30 min until fully dissolved, followed by adding 5 ml acetic anhydride ($(CH_3CO)_2O$)). After constant stirring for another one hour, a further 5 ml 2-MOE is added to dilute the solution to the desired concentration. The above process is performed under constant stirring at room temperature to obtain a homogenous precursor, as shown in the flow chart (**Figure 3-1**). Here, the 2-MOE not only provides a medium for the dissolution of the metal nitrates but is also involved in the consequent condensation of the molecular during the gelation chemistry process. [129] Acetic anhydride is added to dehydrate [130] and acted as a chelating agent [131] to adjust the solution viscosity through bonding the ions and molecules to metal ions.

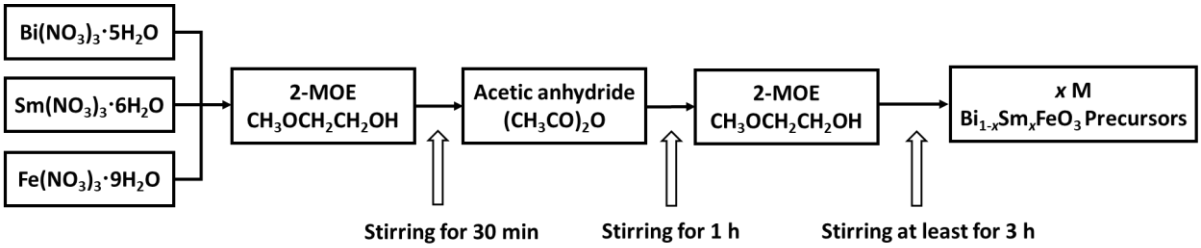

Figure 3-1. Flow chart of the preparation process of BSFO precursor solutions.

3.1.2 Film Deposition

3.1.2.1 Substrate Preparation

The selection of substrate is crucial, which determines both the crystallographic orientation [132] and the crystal structure [133, 134] of deposited films. In this thesis, $LaAlO_3$ (LAO) and $SrTiO_3$ (STO) are used as the substrate for the BSFO films deposition. The detailed information on the used substrates is listed in **Table 3-2**. The large lattice mismatch of –4.3% between LAO and BFO causes a compressive strain in BFO which stabilizes a different crystal structure (i.e., tetragonal-like (T')). [9, 135] STO has lattice parameters more comparable with BFO, which prefers a heterogeneous nucleation and epitaxial rhombohedral-like (R') BFO films. [135] Through tuning the strain state, we can tailor the phase composition of the deposited films, and thus their ensuing physical properties. [6]

In addition, for the measurement of the electrical properties, a conductive buffer layer of lanthanum strontium manganite ($La_{0.67}Sr_{0.33}MnO_3$, LSMO), is deposited as the bottom electrode on the top of the substrate before the deposition of BFO films. **Table 3-3** outlines the corresponding lattice parameters and lattice misfit between substrates and BFO films. In our work, 5 nm thick LSMO is deposited by pulsed laser deposition (PLD) (PASCAL CO., LTD, Japan). The deposition parameters are listed in **Table 3-4**.

Table 3-2. Detailed information about the substrates.

Substrate	Chemical formula	Specification	Supplier
Lanthanum aluminate	$LaAlO_3$	15 mm × 15 mm × 0.5 mm 001-0riented, non-stepped	Shinkosha (Japan)
Strontium titanate	$SrTiO_3$	15 mm × 15 mm × 0.5 mm 001-0riented, non-stepped	Shinkosha (Japan)

Table 3-3. Lattice parameters of perovskite materials and misfit with BFO.

Perovskite materials	Chemical formula	Lattice parameter (Å) (room temperature)	% Misfit with BFO
Bismuth ferrite	$BiFeO_3$	3.960	-
Lanthanum aluminate	$LaAlO_3$	3.790	- 4.3%
Strontium titanate	$SrTiO_3$	3.905	- 1.4%
Lanthanum strontium manganite	$La_{0.67}Sr_{0.33}MnO_3$	3.875	- 2.2 %

Table 3-4. Deposition conditions of LSMO bottom electrode on LAO and STO substrates.

Target	LSMO
Deposition temperature (℃)	750
Deposition pressure (mTorr)	100
Deposition Frequency (Hz)	5
Laser Fluence (J/cm^2)	1-2
Cooling rate (℃/min)	25
Cooling pressure (Torr)	5

The as-grown LSMO/LAO or LSMO/STO is cut into the size of 5 mm × 5 mm and cleaned with an isopropanol-soaked cotton swab. These precleaned substrates are then transferred into a beaker with a moderate amount of isopropanol for a 3-5 min ultrasonic bath. Then the substrates are dried with the compressed house nitrogen in the preparation for the following spin coating.

3.1.2.2 Spin Coating

A spin coater (WS-650-23 Spin Coater, Laurell Technologies Corporation, Pennsylvania, US) is utilized to prepare the BSFO films. This spin coater provides a vacuum specimen stage and digital controlling system for spin velocity and duration. Before the deposition, the substrate is heated to ~ 80 ℃ by placing it on a preheated hot plate for 2 min. Meanwhile, the spin coater is dried using a hair dryer to maintain a certain temperature (i.e., ~ 90 ℃) and humidity (⩽ 30%). Then the preheated substrate is placed and sucked onto a vacuum stage for the following spinning at 4000 rpm for 10 s. Once the deposition is completed, the sample is transferred to another preheated hot plate and heated at ~ 270 ℃ for 5 min. Thus, a homogeneous gel film is prepared. The whole spin coating process is operated inside a fume cupboard.

3.1.2.3 High-Temperature Heat Treatment

Rapid thermal processing for the as-deposited thin films is conducted by using a tube furnace. A refractory holder with a heat resistant metal rod is customized for the high-temperature heat treatment. The whole process is divided into two stages, one for pyrolysis and another for the crystallization of the BSFO films. A pure oxygen atmosphere in the tube is created and maintained by continually flushing oxygen gas. In the first stage, the temperature is raised to 450 ℃. After a 5 min wait to ensure temperature stabilization, the sample is put into the holder and transferred to the hot zone of the tube furnace and held for 30 min. The sample is then quenched to room temperature by withdrawing the holder suddenly. Then the temperature controlling program is started up again to raise the temperature to 640 ℃. Once the temperature is reached and stabilized, the sample is pushed into the furnace again and heated for another 30 min. After that, another quench process is applied. A crystallized film is then achieved and ready for the subsequent characterization. During the whole heating process, the gas flow rate is kept at ~ 100 ml/min for an approximately 1 atm oxygen atmosphere.

The whole film deposition process is shown in the below **Figure 3-2**. In the following research, the deposition techniques and heating process are repeated to obtain multiple layer films.

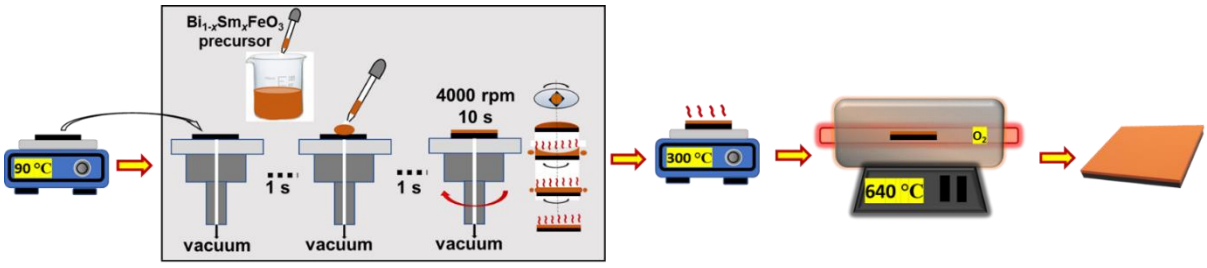

Figure 3-2. Flow diagram of the preparation process of BSFO films.

3.1.3 Top Electrode Preparation

Electrodes are essential for the measurement of electromechanical and ferroelectric properties. The configuration of the ferroelectric thin film device in this thesis is shown in **Figure 3-3**. The LSMO bottom electrode is prepared by PLD as described above. For the top electrodes, platinum is used due to its high conductivity. The top electrodes are deposited using the UV photolithography process and thermal evaporation deposition.

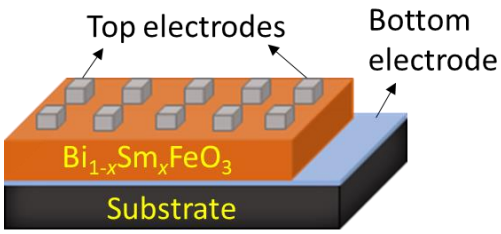

Figure 3-3. Schematic of BSFO film device.

(1) Photolithography

Photolithography is a typical technique used in microfabrication to pattern micro-sized geometry onto a wafer. As shown in **Figure 3-4**, a layer of photoresist is first coated on the sample surface. The photoresist is then exposed to a UV light through a photo mask with the desired pattern. There are two types of photoresists. One is a positive photoresist, which can be degraded by light and thus becomes soluble. The other one is a negative photoresist, which will be strengthened after exposure to UV light and become insoluble. Thus, after a development process, the patterns of exposed areas (positive photoresist) or unexposed areas (negative photoresist) are removed by soaking the samples in a developer solution. [136]

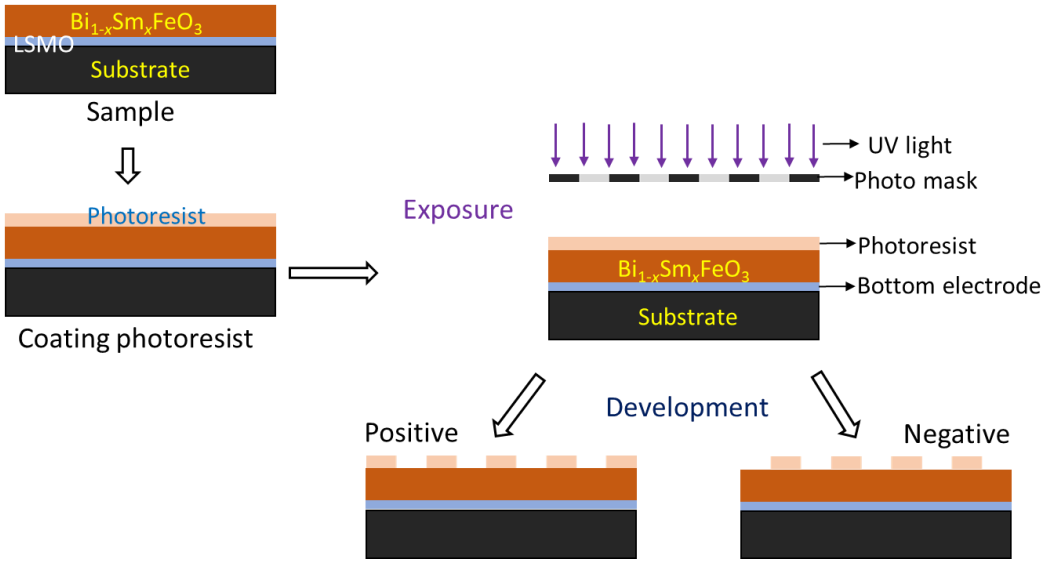

Figure 3-4. Schematic representation of the photolithographic process using positive and negative photoresists.

In our work, a negative photoresist (nLOF202) is chosen for the deposition. Before the photolithography, a continuous flush with acetone and subsequently with isopropanol is applied to clean the BSFO films. Then a spin coating program with two combined spin velocity

and duration processes (3000 rpm for 30 s and 7500 rpm for 5s) is conducted to deposit a layer of nLOF2020 photoresist onto the surface of BSFO films. The sample is then heated on a hot plate at 110 ℃ for 90 s to remove the excess solvent of the photoresist.

Next, a mask aligner (Karl Suss MA6, SÜSS MicroTec, Germany) with the resolution down to 1 μm is utilized for the UV exposure. A mask with a geometry of 23 μm ×23 μm squares is used to pattern the platinum electrode. The film is first put on the sample stage and aligned to the desired mask patterns. Based on the reflectivity of our substrates and the roughness of as-prepared BSFO films, an exposure time of 4.8 s under the light intensity of 10 mW/cm^2 is optimized for the exposure. Once the exposure is completed, the sample is transferred to a preheated hot plate with a temperature of 110 ℃ and held there for 60 s to strengthen the cross-link of the photoresist. Then the sample is soaked into a developer solution (AZ826, TMAH 2.38% in H_2O) and slightly raised up and down for 60 s to remove the unexposed photoresist. Last, the sample is flushed with deionized water and dried with high purity compressed air.

(2) E-beam evaporation deposition

The use of an E-beam evaporator is a common technique for coating a metal layer on a substrate. Compared to the traditional resistive thermal evaporation, the e-beam source can provide a much higher temperature, thus, allowing a very high deposition rate. The metal source (i.e., Pt, Ti in this work) evaporates under a high temperature heating in a high vacuum below 5 × 10^{-6} Torr. The vapor particles are then directed to the substrate and condensed to a solid state to form a thin layer covering the substrate surface.

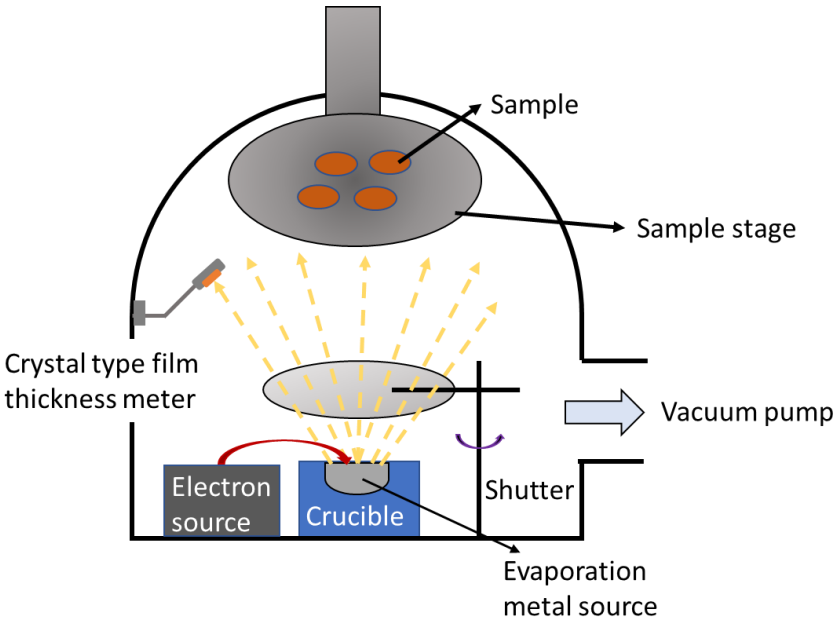

Figure 3-5. Schematic representation of the metal thermal evaporation deposition.

An e-beam evaporator (Lesker PVD75, Kurt J. Leaker company, US) is used in this work to fabricate the top electrodes. A ~ 5 nm thick titanium layer is deposited prior to a ~ 50 nm platinum deposition to strengthen the adhesion between BSFO film and platinum electrode. Here, high purity platinum and titanium ingots are used as the metal sources.

(3) Photoresist lift-off

The lift-off process is the last step for the preparation of top electrodes. The sample is soaked in the N-methyl-pyrrolidone (NMP) and heated to 80 ℃. After 2 hours of soaking, a short ultrasonic for 15 s is applied to help remove the unwanted photoresist and the above metal coating. The sample is then taken out and cleaned by another short ultrasonic (15 s) in an isopropanol liquid. Samples with clear and sharp electrode patterns are obtained after rinsing in deionized water followed by drying with compressed air.

3.2 Analytical Instruments and Methods

3.2.1 Phase Composition Analysis

X-ray diffraction (XRD), Raman spectrometer, and electron microscopy (including field-emission scanning electron microscopy (SEM) and transmission electron microscopy (TEM) techniques are used to investigate the crystalline structure, phase composition, and

microstructure of BSFO films.

3.2.1.1 X-ray Diffraction Analysis

XRD is a powerful non-destructive technique for analyzing crystalline materials. The periodical arrangement of atoms with a long-range order in crystals can be detected using the diffraction techniques. For example, two parallel incident beams with identical wavelength (λ) and phase approach to the atom planes and are scattered off. The lower beam traverses an extra length of 2dsinθ, as shown in **Figure 3-6**. Consecutive interference occurs when this length is equal to an integer multiple of the wavelength of the radiation. That is the Bragg's Law [137]:

$$n\lambda = 2d\sin\vartheta \qquad \textbf{Equation 3-1}$$

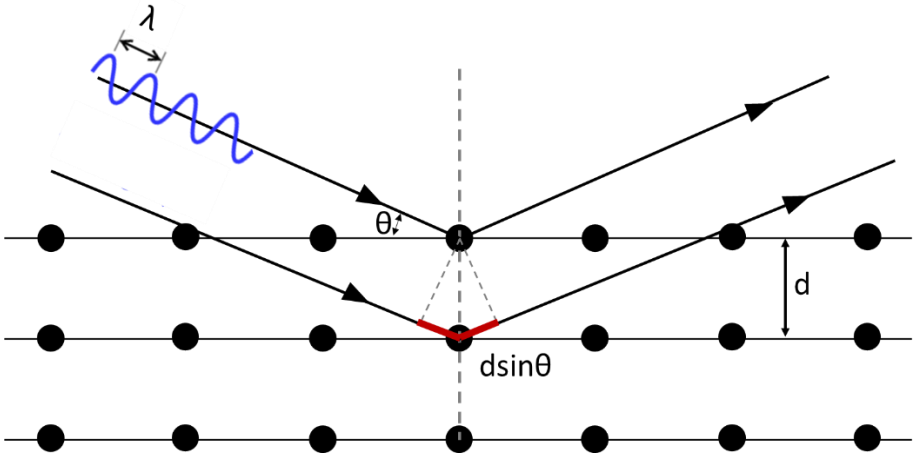

Figure 3-6. Visualization of the Bragg equation.

(1) $\vartheta/2\vartheta$ scan

The $\vartheta/2\vartheta$ scan is a major X-ray scattering technique in thin film analysis. The probing X-ray beam is directed to the sample surface at an angle of ϑ. Meanwhile the detector monitors the scattered radiation. During the whole scan, the angle of the incoming and exiting beam continuously varies and remains $\vartheta_{in} = \vartheta_{out}$ (i.e., the exit angle referring to the extended incoming beam keeps at 2ϑ). In a $\vartheta/2\vartheta$ scan, the scattering vector **Q** is always parallel to the substrate normal. Thus, for single crystals, only the lattice plane *hkl* oriented parallel to the surface plane can contribute to a Bragg reflection. **Figure 3-7** demonstrates the working principle of a $\vartheta/2\vartheta$ scan.

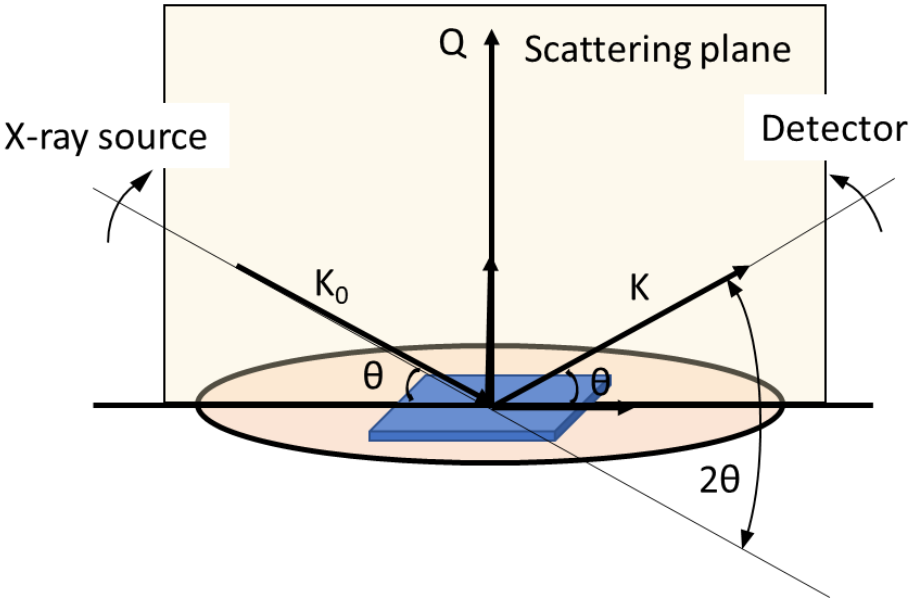

Figure 3-7. Schematic representation of a $\vartheta/2\vartheta$ Scan.

(2) Pole figures

A pole figure is a two-dimensional contour map, which is commonly employed for analysis of the orientation of as-grown films. In a pole figure measurement, the diffraction angle 2ϑ is fixed. By altering two geometrical parameters (i.e., φ and ψ angles), the diffracted intensity is recorded. The φ is the angle of the diffraction vector around surface normal direction, and ψ is the one of the diffraction vectors from the direction of the sample normal. Thus, the diffracted intensity distributes on a curved surface with a constant distance to the coordinate origin in the reciprocal space, as shown in **Figure 3-8(a)**. **Figure 8-3(b)** is the collected XRD pole figure of BFO films with the 2ϑ = 32°, which is attributed to the (101) T'-BFO peak. The clear fourfold symmetric spots indicate an epitaxial growth of BFO films.

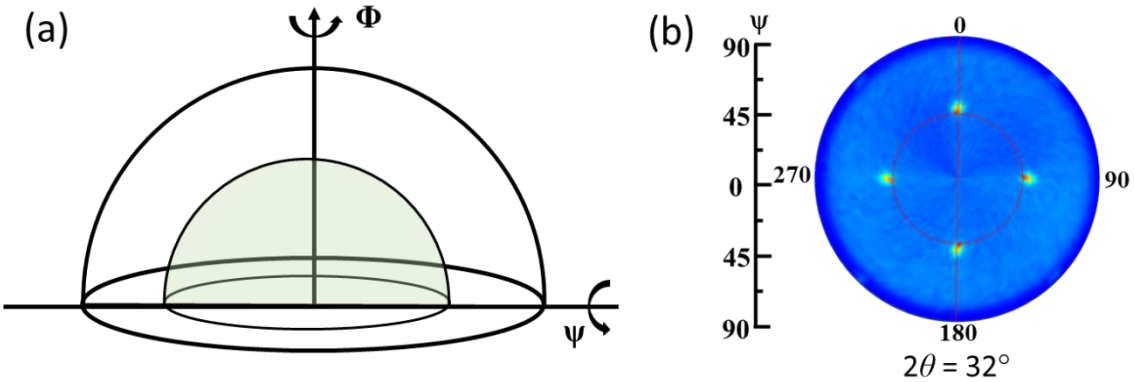

Figure 3-8. (a) Schematic illustration of pole figure measurement and (b) pole figure scan around the (101) reflection of the BFO films on LAO.

(3) Reciprocal space maps (RSMs)

RSMs are typically used to aid the interpretation of the epitaxial nature and crystal structure of thin films. In reciprocal space, the vector ***Q*** can be constructed by two orthogonal vectors (q_x and q_z). [137]

$$q_x = \frac{2\pi}{\lambda}\left[\cos(\vartheta-\omega) - \cos(\vartheta+\omega)\right] \qquad \textbf{Equation 3-2}$$

$$q_z = \frac{2\pi}{\lambda}\left[\sin(\vartheta-\omega) - \sin(\vartheta+\omega)\right] \qquad \textbf{Equation 3-3}$$

The RSMs are plotted by performing multiple scan steps. One way consists in running successive rocking curves with an increasing scattering angle of 2ϑ. Rocking curves (i.e., ω scans) are measured with the detector fixed to the $2\vartheta_0$ of the investigated Bragg peak and sample tilted on the ϑ circle around the ϑ_0 (rocked), as shown in the **Figure 3-9(a)**. In this case, the ϑ and the 2ϑ circles are decoupled (here, the ϑ angle is also called ω). Another one performs subsequent radial scans, where the ω and 2ϑ increase simultaneously by $2\Delta\omega$ and $\Delta\omega$, respectively (the $\vartheta/2\vartheta$ scan is a typical radial scan). The orientation of the probing Q vectors keeps the same tilt with the surface normal during the whole measurement, as shown in **Figure 3-9(b)**. An intensity map of the Q area around the Bragg reflection is then collected. Different from the pole figure whose diffracted intensity is located on a curved surface, the signal intensity in RSM distributes on a flat cross-section plane passing through the coordinate origin, as shown in **Figure 3-9(c)**. The epitaxial nature can be confirmed through the peak position and the peak shape of films and substrates.

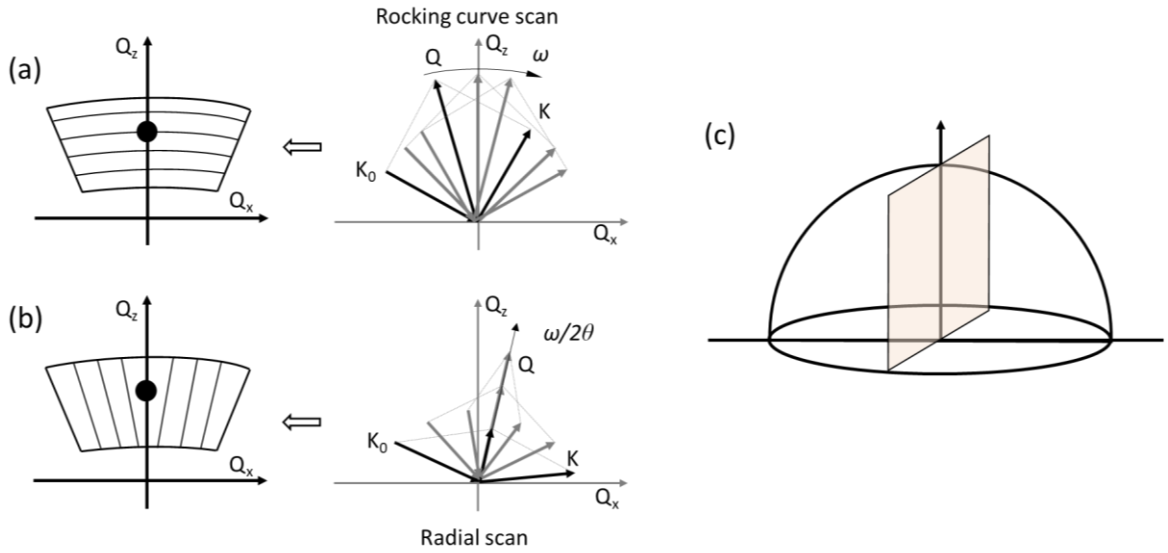

Figure 3-9. Two different ways of collecting RSMs either by (a) subsequent rocking curve measurements or (b) subsequent radial scans, and (c) schematic illustration of RSM. [137]

In this thesis, a smart lab (Rigaku corporation, Japan) is used to inspect the phase composition and crystallographic orientation. Prior to the measurement, film alignments including 2theta, omega, phi, psi angles, and x-axis and y-axis and z axis scans are performed to position the X-ray beam on films and promise a maximum intensity. Once the alignment is completed, $\vartheta/2\vartheta$ scan, pole figure, and RSM are collected using Cu K_α (λ= 1.5406 Å) radiation at 45kV/200mA. In addition, a Pilatus X-ray detector is applied to acquire a large area scan of RSMs with a beam size of 300 μm and measurement area of 2theta from 35° to 55° and chi from -30° to +30°.

3.2.1.2 Raman Spectroscopy Analysis

Raman spectroscopy is a non-destructive analysis technique, which offers the chemical structure, phase, and intrinsic stress/strain information based on the interaction between the incident light and chemical bonds within materials. [138] A Raman spectrum consists of the intensity and wavelength position of the Raman scattered light. The peak position relates to the specific molecular bond vibration. Thus, the strain or element substitution induced structural alternation in films is expected to be detected through Raman spectroscopy.

A Raman spectrometer (Renishaw inVia 2 Raman microscope (532 nm), UK) is used to analyze the phase structure evolution in this thesis. Prior to the sample measurement, a silicon substrate is applied for laser calibration. The sample is then placed on the sample stage

and measured. For every sample, 10 areas are characterized. The whole measurement is conducted in a closed environment.

3.2.2 Chemical Analysis of Fourier Transformation Infrared Spectroscopy (FTIR)

FTIR is a commonly used technique to determine the molecular structure of organics by detecting the infrared spectrum of absorption, emission, and photoconductivity. [139] The mid-infrared energy with the wavenumber between 4000 and 400 cm^{-1} is used to investigate the sample. When the energy of incident infrared light is equal to the vibrational bond energy of the molecule, that energy is absorbed. Different bonds vibrate at different energies, which leads to the absorption of different wavelengths of IR radiation. The position (frequency or wavenumber) and intensity of these individual absorption bands compose the overall spectrum and generate a characteristic fingerprint of the molecule. In the spectrum, the peak positions present the structures of the molecules, the peak intensity is sensitive to the concentrations of molecules in a sample, and the peak widths are relevant to the chemical matrix of the sample (such as pH and hydrogen bonding).

This thesis used an attenuated total reflectance (ATR), an internal reflection-based method, FTIR spectrometer (PerkinElmer, spectrum 3/spotlight 400, US) is applied to investigate the gelation chemistry of BSFO precursors. The light energy is passed through an ATR sensor and reflected certain times, as shown in **Figure 3-10**. Therefore, any substance in direct contact with the sensor is investigated. A represented FTIR spectrum of BFO precursor is also plotted.

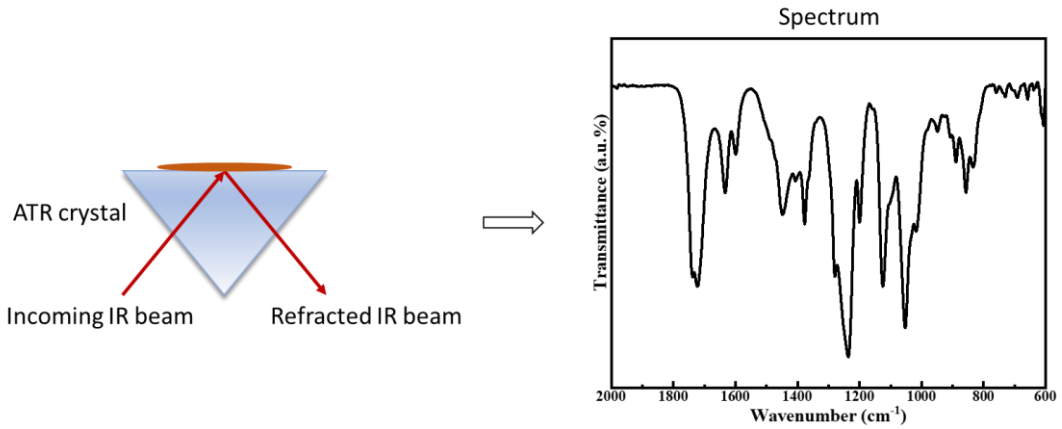

Figure 3-10. Schematic illustration of ATR FTIR and a collected spectrum of BFO precursor.

3.2.3 Microstructure and Elementary Composition Analysis

3.2.3.1 Scanning Electronic Microscopy (SEM)

SEM is a widely used technique for material microstructure analysis. A focused beam of electrons interacts with atoms in the material. The produced secondary electrons or back-scattered electrons are captured by the detector and thus provide information on both topography and composition. [140]

Nova NanoSEM 450 (FEI, US) is used to investigate the cross-sectional microstructure and estimate the thickness of the as-grown films. The samples are simply cut into two pieces from the backside using a diamond pen. Prior to the SEM analysis, a thin carbon conductive layer is coated, and a conductive carbon tape is utilized to maintain high conductivity and fix the samples onto the specimen stage. A secondary electron mode is adopted to acquire the cross-sectional information of films.

3.2.3.2 Wavelength Dispersive Spectrometer (WDS)

Field-emission SEM- electron probe microanalyzer (EPMA) hyperprobe (JEOL JXA-8500F, JEOL, Japan) is a powerful microanalytical instrument. The area-specific quantitative elemental analysis is down to the sub-micron level. [141] The EPMA is fitted with four WDS. The concentration of the elements with atomic number $Z \geqslant 4$ can be detected and measured with detection limit of often < 0.05%. Due to the fitted Schottky field-emission gun, low-kV work while retaining a stable and highly focused current (up to 100 nA) beam can be undertaken.

3.2.3.3 Transmission Electron Microscopy

TEM technique is conducted to realize a high resolution of up to atom level for material microstructure and crystal structure (crystal diffraction patterns). The electron beam transmits through an ultrathin specimen and interacts with the atoms.

For the investigation of the crystal structure in the film/substrate interface or phase boundary of films, a high-resolution TEM (HR-TEM) is applied to acquire the periodic structural information of the materials on an atomic scale.

TEM CM200 (Philips, Netherlands) and HR-TEM (2200, JEOL, Japan) are used for TEM analysis of BSFO thin film. BSFO/LSMO//LAO (001) film cross-section samples that are

approximately 100 nm thick are prepared using a focused ion beam (FIB, Auriga, Zeiss, Germany).

3.2.4 Scanning Probe Microscopy

3.2.4.1 Atomic Force Microscopy (AFM)

AFM is a non-optical surface interrogation technique, which consists of a cantilever (to which a sharp tip on a micromachined silicon probe is attached), a laser source, and a quadrant photodiode detector. The working principle of AFM is depicted in **Figure 3-11(a)**. When scanning, the tip is located on the surface of the targeted sample. The produced elastic force between the tip and the sample results in a deflection towards or away from the surface. A focused laser beam on the top surface of the cantilever monitors the change of deflection. After the laser is reflected off the cantilever, a quadrant photodiode detector detects this reflected signal and converts it into digital information. Thus, a topography image is acquired.

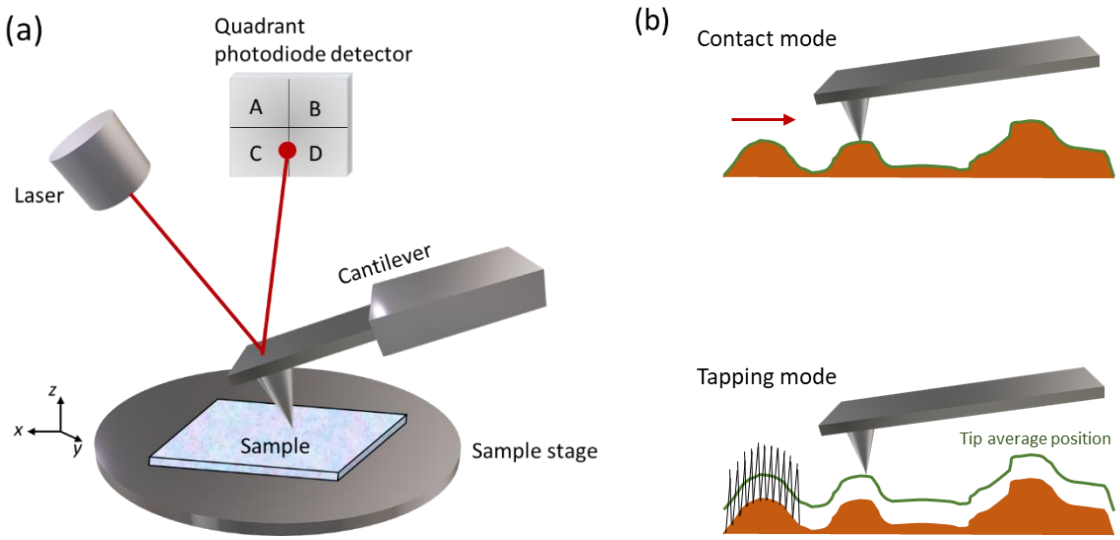

Figure 3-11. Schematic illustration of (a) AFM working principle and (b) two types of scanning mode. [142]

There are two common scanning modes of AFM: contact mode and tapping mode, [142] as shown in **Figure 3-11(b)**.

(1) Contact mode

In contact mode [143], the tip mechanically contacts with the sample surface during the whole scanning. As the scanner traces the tip traversing the sample, the repulsive contact force between the tip and sample leads to a bend of the cantilever, and thus accommodates

the changes in topography. To strengthen the deflection signal and avoid the sample damage, a cantilever with a low spring constant is often used for contact mode AFM. [144]

(2) Tapping mode

In tapping mode [143], the tip is oscillated up and down at or near its resonance frequency near the sample surface by applying a small sinusoidal voltage. The distance between tip and sample surface is controlled by keeping either the amplitude or the phase of the oscillating cantilever constant. Compared to the contact mode, a higher resolution is typically achieved in tapping mode because no lateral tip-sample forces exist in this technique. A cantilever with a high spring constant and high resonance frequency is often used to prevent the tip from getting stuck on the sample surface. [144]

3.2.4.2 Piezoresponse Force Microscopy

Piezoresponse force microscopy (PFM) is a variant of AFM which allows for imaging and manipulating ferroelectric domain structure by utilizing a conductive tip. During the scanning, an alternating current (AC) bias is applied to the tip and thus induces deformation in the film due to the converse piezoelectric effect. The amplitude and phase of the AC response bias of the film are then demodulated by a lock-in amplifier. In this way, topography, amplitude, and phase images can be collected simultaneously with high resolution. The amplitude and phase images demonstrate the piezoelectric deformation and polarization direction of the films, respectively.

The domain polarization of ferroelectric films has both the out-of-plane (OP) and in-plane (IP) vectors. They can be detected by corresponding vertical PFM (VPFM) and lateral PFM (LPFM) modes, respectively. As shown in **Figure 3-12 (a) and (b)**, the quadrant photodiode detector is divided into A, B, C, and D four parts. The output of the center position of the detector is 0 V. The movement of the laser spot leads to a radial distance from this center position and, thus, results in a linear increase in the magnitude of voltage. The vertical deflection is defined as [(A+B)-(C+D)]/(ABCD), which monitors the vertical displacement of the cantilever during the scanning. Similarly, the lateral deflection defined as [(B+D)-(A+C)]/(ABCD) tracks the torsional bending of the cantilever. The scan directions of the tip (applied in this thesis) and corresponding polarization component directions (OP and IP vectors) are shown in **Figure 3-12 (c)**.

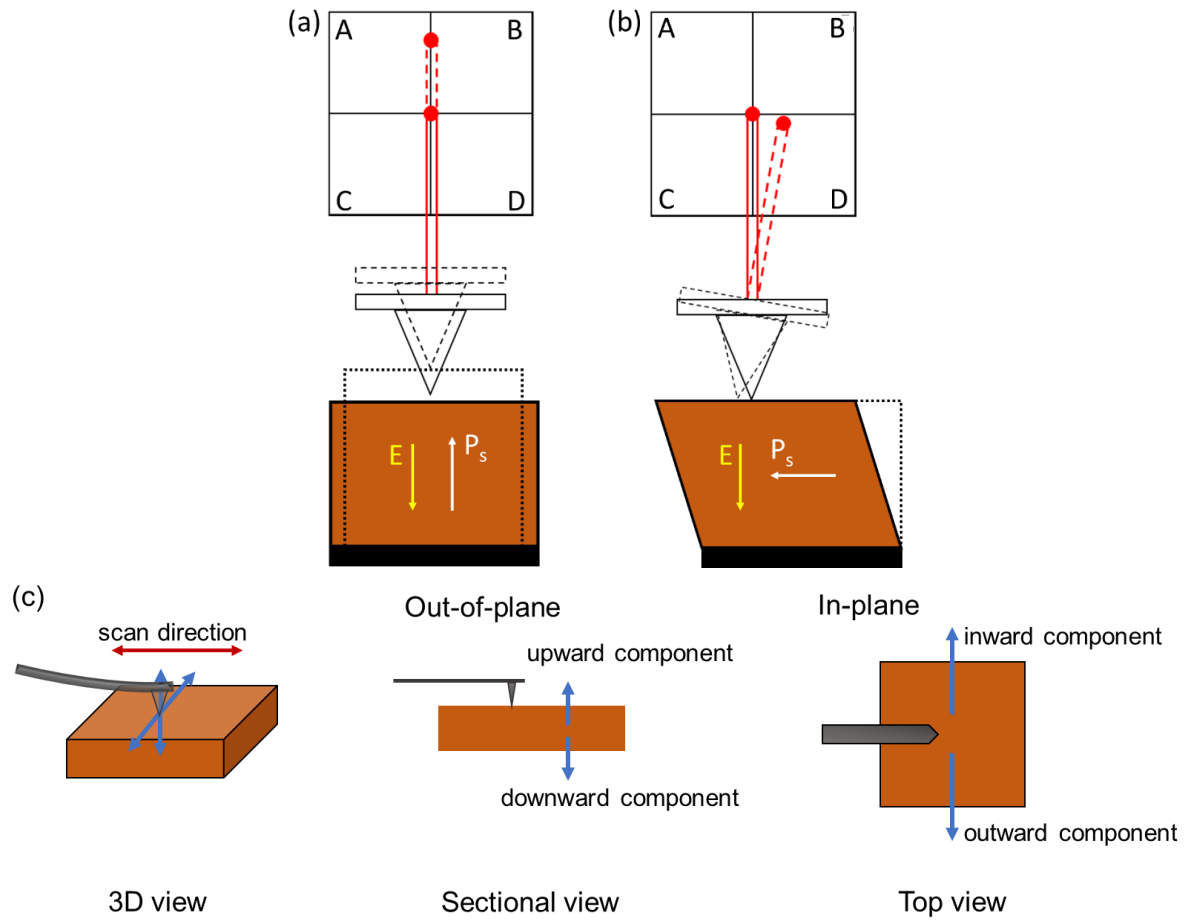

Figure 3-12. Schematic illustration of (a) vertical and (b) lateral PFM mode, [145] (c) schematic images of the scan direction of the tip and the polarization component directions (shown as the blue arrows)

3.2.4.3 Dual AC Resonance Tracking (DART) PFM

DART is a resonance-enhanced PFM technique, which facilitates the measurement of weak piezoresponses of materials, like thin film and avoids its breakdown.

In DART mode, two excitation frequencies (f_1 and f_2) are used as input feedback, which yields two amplitudes (A_1 and A_2). The difference between two the frequencies is typically larger than $2BW$ (BW is the imaging bandwidth with the order of 1kHz). [146] Since the potential of the cantilever is oscillated at a sum of two voltages with frequencies at or near the resonance, the amplitudes of A_1 and A_2 are close to $A_r/2$ (A_r is the amplitude at the resonance). Therefore, the continuous adjustment of the frequency of AC voltage is achieved by controlling the amplitude difference ratio of the two frequencies. Typically, a zero value of the amplitude difference (i.e., A_1 and A_2 coincide) is chosen (not a requirement of the technique) as the set point.

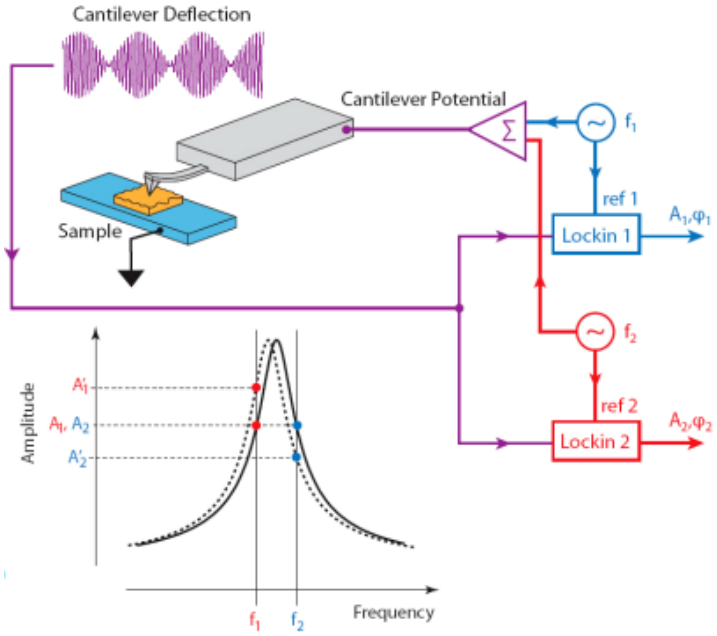

Figure 3-13. Schematic diagram of principle of the DART PFM. [146]

3.2.4.4 Domain Switching

To characterize the electromechanical properties of thin films, an external direct current (DC) (higher than the coercive voltage of the materials) can be applied to induce domain switching during PFM scanning.

In this thesis, the external voltage is applied from the sample to the tip. The domains are written by applying a positive DC bias in a 3 µm × 3 µm region and a negative DC bias in a 1 µm × 1 µm inside of it. The DC bias is applied to the sample when the probe scans the sample, and it has to be higher than the coercive voltage to cause fully domain switching. After writing, a PFM scan in a 5 µm × 5 µm region is collected under a reading AC bias. Thus, the domains are switched up by the positive bias and switched downwards by the negative bias, as shown in **Figure 3-14(a)**. **Figure 3-14(b)** shows the representative amplitude and phase images of BFO film when DC bias is applied.

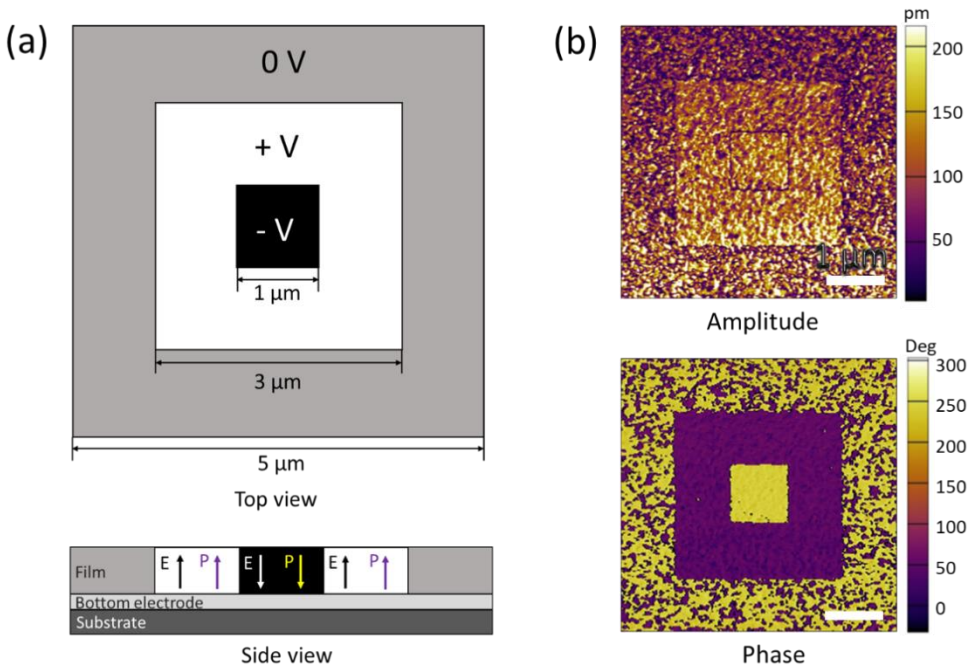

Figure 3-14. (a) Schematic illustration of the domain written pattern, (b) amplitude and phase images after domain writing with +6 V/-6 V bias (bias are applied from the sample to tip).

3.2. ferroelectric PFM Amplitude and Phase Hysteresis Loops

PFM amplitude-voltage butterfly loop and phase-voltage hysteresis loop are used to verify the ferroelectricity and estimate the coercive voltage of the ferroelectric films by switching spectroscopy (SS)-PFM. [145] During the SS-PFM measurement, a triangle square waveform bias is applied, which consists of a stepwise increasing DC voltage and a superimposition of an AC voltage, as shown in **Figure 3-15(a)**. The DC bias is used to reverse the domains, and the AC bias is used to amplify the piezoelectric signal. The loops at two states with “on” (DC loading) and “off” (no DC loading) are simultaneously collected. In the “on” state, hysteresis-like loops have also been observed in some non-ferroelectric materials due to the electrostatic effect. [147] Thus, to reduce the interference between electrostatic effect and piezoelectric response, the signal at the “off” state is usually adopted. Typical phase and amplitude loops of BFO/LSMO//LAO are shown in **Figure 3-15(b)**. By landing the probe directly on the surface of the films or on the top electrode, both the nanoscale and global domain switching behavior can be observed.

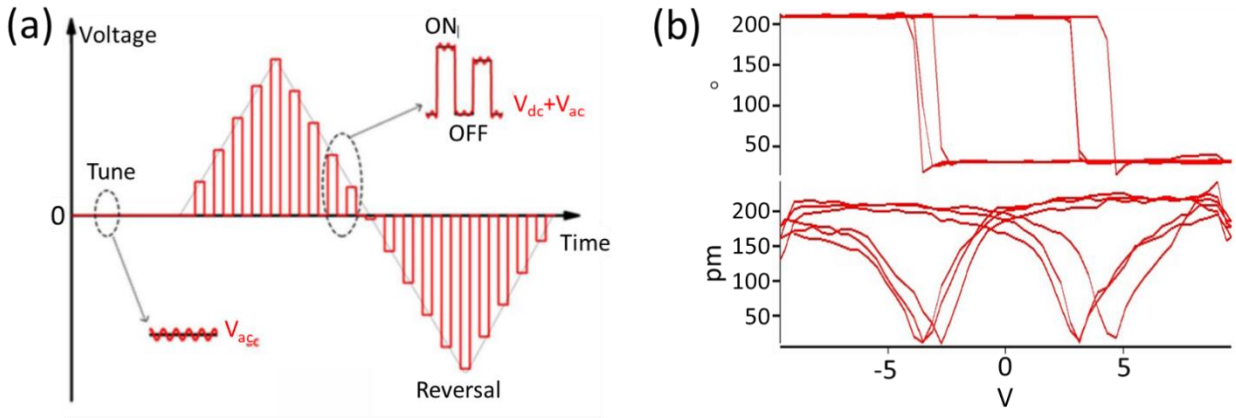

Figure 3-15. (a) Schematic illustration of the waveform loaded during SS-PFM [148], (b) typical phase and amplitude loops.

3.2.4.6 Conductive Atomic Force Microscopy (CAFM)

CAFM is another variant of AFM, which allows for the investigation of the conductivity behavior of films. The voltage difference between probe and sample surface leads to the current flow. Therefore, an electrical current map of the surface profile can be constructed. In addition, an I-V curve can also be collected in spectroscopic mode.

(1) Current mapping

During the scanning, a DC bias is applied from the bottom electrode to the sample. The mobile electrons driven by the electric field are then collected by the probes. Thus, a current map is acquired to show the conductivity of each pixel of the scanned area.

(2) I-V measurement

The probe is landed on a selected point of the sample surface. A triangular waveform voltage is then applied to study the conductivity as a function of the voltage. In this thesis, Asylum Cypher PFM is used for all measurements. The conductive Pt/Cr-coated silicon cantilevers (multi75E-G, BudgetSensors, Bulgaria) are applied for all data collection.

3.2.5 Electrical Properties Measurements

A probe workstation is used for the macroscope electrical properties tests, including ferroelectric polarization hysteresis loops and I-V curves measurements. Two probes are connected to the top electrode (Pt) and bottom electrode (LSMO) of the films, respectively to form a circuit.

(1) Ferroelectric polarization hysteresis loop measurement

The ferroelectric polarization-electric field (P-E) hysteresis loop is one of the most prominent features of ferroelectric materials. The reversely switchable polarization results in this hysteresis loop under an external electric field.

A Radiant Ferroelectric Tester (Radiant Technologies, inc., New Mexico, US) is used for the ferroelectric polarization hysteresis loop measurement, which is based on a Sawyer-Tower circuit, as shown in **Figure 3-16(a)**. A triangular voltage driven from the top electrode and returned from the bottom electrode at 10kHz is employed for the collection of hysteresis loops. **Figures 3-16(b) and (c)** give the driven triangular voltage function and a representative P-E loop of BSFO film with x = 0.10.

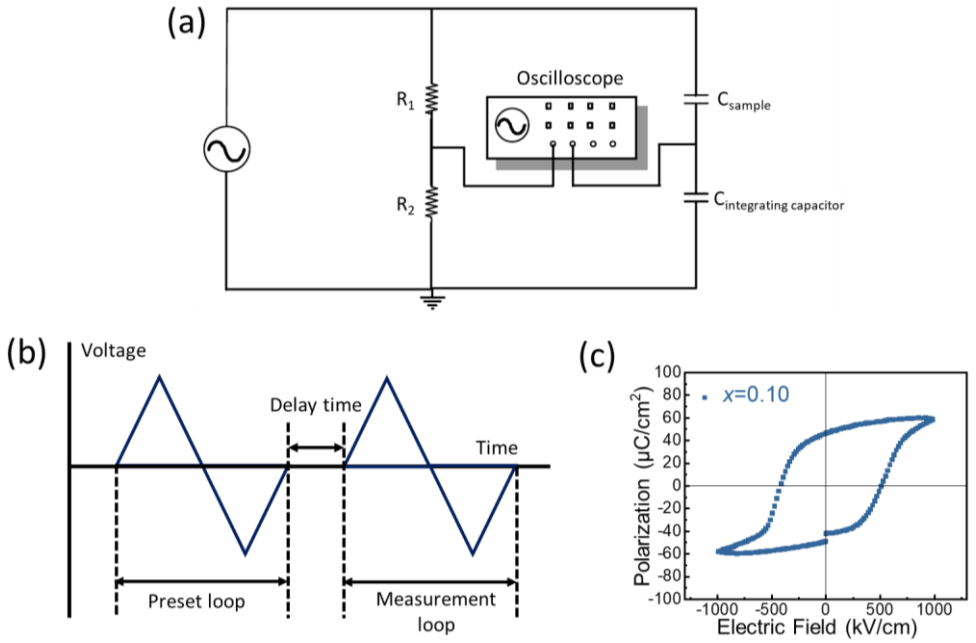

Figure 3-16. (a) Schematic illustration of Sawyer Tower circuit and (b) triangular sweep voltage for P-E loop measurements [149], and (c) example of P-E loop collected from BSFO/LSMO//LAO films.

(2) Macroscale I-V tests

Macroscale I-V curves (i.e., leakage current curves) display the resistivity of measured films. During the tests, an external voltage is applied from the top electrode to the bottom electrode through the films. The collected current signal is from the bulk film (the top electrode covered area), which represents the global conductivity behavior of the measured film. It is distinguished from the local I-V detected by CAFM, where the tip is directly landed on the sample surface.

A Keithley SourceMeter (Keithley 2400, Tektronix, US) is applied to collect the I-V curves (i.e., leakage current curves). A triangular sweep voltage, as shown in **Figure 3-17**, is applied to obtain the resistance of the films.

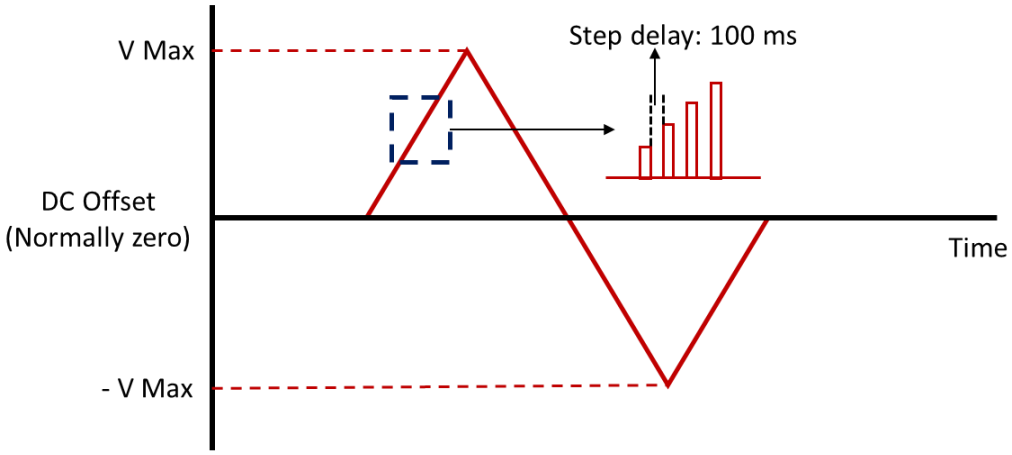

Figure 3-17. Triangular sweep voltage for macroscale I-V measurement.

3.3 Summary

This chapter first describes the methodologies of precursor solution preparation, film deposition, and top electrodes fabrication, then outlines the characterization techniques and their working principles, which includes the following:

(1) XRD technique: $\vartheta/2\vartheta$ scan for phase composition and crystal structure, pole figures and RSM for the orientation of films.
(2) Raman spectrometer for the phase composition alternation.
(3) FTIR for gelation chemistry process of precursor solutions.
(4) Electronic Microscopy: SEM for the thickness of films, WDS for elementary composition, and TEM for the cross-sectional microstructure and the epitaxial growth of films.
(5) Scanning probe microscopy: PFM for topography, domain structure, SS-PFM for local hysteresis behavior, CAFM for the conductivity of films, I-V for the nanoscale resistance as a function of voltage.
(6) Ferroelectric tester and Keithley SourceMeter for macro ferroelectricity and leakage current behavior, respectively.

In subsequent chapters, the above-mentioned techniques are employed for films preparation and characterization.

Chapter 4. Phase Fractions Tuning of Chemical Solution Deposition-Derived Mixed-Phase Bismuth Ferrite Thin Films

In this chapter, we report a detailed investigation of the phase development of chemical solution deposition (CSD)-derived mixed-phase $BiFeO_3$ (BFO) thin films. The number of spin-coated layers, the concentration of the applied precursors, and the heat treatment process (heating temperature and dwell time) have been systematically studied to understand their effects on the phase fraction and crystallographic structure composition. This will enable a full understanding of the phase behavior of this system and allow precise tuning and manipulation of the mixed-phase component.

4.1 Introduction

BFO is a popular multiferroic material that has been widely studied in thin-film form for applications in nonvolatile memories, [150-153] sensors, [154-156] and photovoltaics. [157-162] This is primarily driven by its attractive physical properties, such as large switchable spontaneous polarization, [10, 163, 164] strong electromechanical response, [9, 165] bandgap tuneability, [166] and rich phase diagrams. [9, 167-169] In the bulk, BFO forms in the R3c space group, but a strong in-plane (IP) compressive epitaxial strain can stabilize a novel tetragonal-like (T') polymorph. [135, 170] Using this idea, Zeches et al. demonstrated a 'strain-induced morphotropic phase boundary (MPB)' in BFO thin films. [9] In particular, they showed how misfit strain and external electric field can be used to tune the rhombohedral-like (R') and T' phase fractions. Termed as 'mixed-phase BFO', this material system has been found, both experimentally and theoretically, to have a giant-electric-field induced strain, as well as various other emergent properties. [164, 171-175]

To date, mixed-phase BFO thin films have been predominantly realized by physical vapor deposition (PVD) techniques, such as molecular beam epitaxy (MBE), [9] pulsed laser deposition (PLD), [70, 176] and magnetron sputtering deposition. [177] Such mixed-phase BFO films typically exhibit a topography wherein the R'-phase manifests as striations embedded in the T'-phase matrix. [9, 70, 169, 178] This spatially inhomogeneous distribution of the individual polymorphs could lead to a nonuniform electromechanical response. Furthermore, these phase boundaries have been associated with intrinsically high

conductivity, [179, 180] which could hinder their use in practical applications.

We recently reported that mixed-phase BFO thin films synthesized by chemical CSD have an entirely different microstructure when compared to the more common PLD-grown films. [14] In contrast to the continuous growth of PLD, CSD growth occurs through a deposition-nucleation-crystallization-relaxation process. [32, 115, 181] Due to this, the R' phase is nucleated and grows at the interface or in the film bulk away from the interface during the whole sintering procedures, and the T' phase is formed at the interface due to the heterogeneous nucleation at first and then partially relax to form the unstrained R' phase several unit cells above the interface. As a result, CSD-derived mixed-phase BFO films possess a nanoscale mixture of the T'-phase homogeneously distributed within the R' parent phase throughout the film volume, and notably with no distinct interphase boundary. [14] This nanoscale mixture results in a broad R' peak and relatively sharp T' peak when probed by X-ray diffraction (XRD) reciprocal space map (RSM) near the (00*l*) reflection. This is in strong contrast with the well-known striped topography for PLD-derived mixed-phase BFO films. [135] For films grown by PLD, at the growth temperature of ~ 600-700 °C, the film comprises only the T' phase. During cooling to room temperature, relaxed R' phases form, and in the process induce tilted phases which traverse the thickness of the film. As a consequence, the (00*l*) RSM for a PLD-grown mixed-phase BFO film reveals not only sharp T' and R' phases peaks, but more importantly, additional wing peaks arising from the tilted phases. We believe the lack of such structural interphase boundaries and wings in the (001) RSM for CSD-derived films are critical differences that must not be overlooked.

In CSD, the film is prepared by depositing a precursor on the substrate, followed by spin coating and heat treatment. The film thickness can be flexibly controlled by the number of layers deposited [182] and the concentration of the applied precursors. In addition, both the spin coating and heat treatment processes have a significant bearing on the resultant film's microstructure and morphology, as well as its corresponding electrical properties. [115, 183, 184]

In this chapter, a series of mixed-phase BFO films are deposited on $LaAlO_3$ (LAO) substrates by adjusting the processing parameters of the CSD method. We show that the number of layers has a significant influence on the overall multilayer film phase and microstructure. The T'-phase volume fraction significantly decreases from 35% to 10% upon

increase from one layer (45 nm) to four layers (250 nm). Next, we focus on a 2-layer system with an inserted 5 nm thick conductive bottom electrode. The precursor concentration of the bottom layer and the heat treatment time-temperature dependence are further utilized to tune the mixed-phase fractions. The T'-phase fraction ranging from ~ 10% to ~ 38% can be still tailored in this 2-layer structure. An optimized mixed-phase BFO epitaxial film with a T'-phase fraction of 28% can be achieved in a 0.25 M/0.2 M configuration with a crystallization temperature of 640 ℃ and dwell time of 30 min.

4.2 Experimental Procedure

BFO thin films were deposited by CSD on (001)-oriented LAO (Shinkosha, Japan) substrates with or without a 5 nm-thick $La_{0.67}Sr_{0.33}MnO_3$ (LSMO), prepared by PLD (Neocera, US)) bottom electrode. The stoichiometric precursor solutions were prepared by dissolving bismuth nitrate pentahydrate ($Bi(NO_3)_3 \cdot 5H_2O$) and iron nitrate nonahydrate ($Fe(NO_3)_3 \cdot 9H_2O$) in 5 ml 2-MOE organic solvent, followed by adding 5 ml acetic anhydride. After constant stirring for one hour, a further 5 ml 2-MOE was added to dilute the solution to the desired concentration. The amounts of metal nitrates were adjusted to prepare 0.05 M, 0.1 M, 0.2 M, and 0.25 M BFO precursors. The composition of precursors is shown in **Table 4-1**. The above process was performed under constant stirring at room temperature to obtain a homogenous precursor.

Table 4-1. Composition of precursors solution

Concentration	$Bi(NO_3)_3 \cdot 5H_2O$	$Fe(NO_3)_3 \cdot 9H_2O$	2-MOE	Acetic anhydride
0.05 M	0.3638 g	0.3030 g	10 ml	5 ml
0.1 M	0.7276 g	0.6060 g	10 ml	5 ml
0.2 M	1.2120 g	1.4550 g	10 ml	5 ml
0.25 M	1.5150 g	1.8190 g	10 ml	5 ml

Then a small amount of BFO solution was dropped and spin-coated on a cleaned and preheated (~ 80 °C) LAO substrate with or without LSMO at 4000 rpm for 10 s. The following gelation and drying process was performed by heating the film in the air at 300 °C for 5 min. As-prepared gel films were rapidly heated by putting the samples into a 450 °C preheated tube furnace for 30 min (pyrolysis) and then annealed at a certain temperature (520 °C, 580 °C, 640 °C, 700 °C) for a certain time (10 min, 30 min, 50 min) (crystallization). Both pyrolysis and

crystallization heat treatment processes were performed in an oxygen atmosphere. An air quenching cooling process was conducted after each heat treatment.

Here, the effects of thickness and deposition process on the film phase configuration were systematically investigated:

(1) Effect of multilayer: Multilayer BFO thin films ranging from one to four layers were directly deposited on (001)-oriented LAO substrate to investigate the effect of film thickness on the phase composition and film morphology. We started the multilayer experiment using a 0.25 M precursor for single layer deposition. The whole deposition and heat treatment process was repeated from one to four times to achieve the desired thickness, as shown in **Table 4-2**.

Table 4-2. Processing parameters of multilayer BFO thin films

Layer numbers	Precursor concentration	Pyrolysis		Crystallization		Deposition times
		temperature	time	temperature	time	
One	0.25 M	450 °C	30 min	640 °C	30 min	**one**
Two	0.25 M	450 °C	30 min	640 °C	30 min	**two**
Three	0.25 M	450 °C	30 min	640 °C	30 min	**three**
Four	0.25 M	450 °C	30 min	640 °C	30 min	**four**

Next, we fix the film configuration as two-layer BFO thin films on LSMO//LAO (001) substrate and investigate the effect of precursor concentration and heating treatment on the film phase configuration, crystallographic structure, and domain structures. The related deposition process parameters are listed in **Table 4-3**.

(2) Effect of precursor concentration: To understand the effect of precursor concentration or the film thickness on the BFO phase configuration, precursors of different concentrations (x = 0.05 M, 0.1 M, 0.2 M, and 0.25 M) were applied for the first layer of the BFO thin film. To reduce the leakage current from the ultrathin film, we used a constant concentration of 0.25 M for the second layer.

(3) Effect of heating treatment: The annealing temperature (T = 520 ℃, 580 ℃, 640 ℃, and 700 ℃, and dwelling time (t= 10 min, 30 min, and 50 min), were further set up to tune the phase structure and properties of materials. The configuration of the two-layer thin film was fixed as 0.2 M BFO precursor solution for the first layer and 0.25 M one for the second layer.

Table 4-3. Processing parameters of precursor concentration(*x*), annealing temperature (*T*), and annealing time (*t*) dependent BFO thin films

Samples	Precursor concentration		Pyrolysis		Crystallization	
	First layer (*x)**	Second layer	temperature	time	**Temperature (*T*)**	**Time (*t*)**
1	**0.05 M**	0.25 M	450 °C	30 min	640 °C	30 min
2	**0.1 M**	0.25 M	450 °C	30 min	640 °C	30 min
3	**0.2 M**	0.25 M	450 °C	30 min	640 °C	30 min
4	**0.25 M**	0.25 M	450 °C	30 min	640 °C	30 min
5	0.2 M	0.25 M	450 °C	30 min	**520 °C**	30 min
6	0.2 M	0.25 M	450 °C	30 min	**580 °C**	30 min
7	0.2 M	0.25 M	450 °C	30 min	640 °C	**10 min**
8	0.2 M	0.25 M	450 °C	30 min	**640 °C**	**30 min**
9	0.2 M	0.25 M	450 °C	30 min	640 °C	**50 min**
10	0.2 M	0.25 M	450 °C	30 min	**700 °C**	30 min

Note: x* is the applied precursor concentration for the first layer

4.3 Results and Discussion

4.3.1 Multilayer Dependence

Film thickness plays a critical role in the films phase composition. [70, 176, 185] In CSD, the number of deposited layers is utilized to tune the film thickness and, thus its phase fraction and morphology. Hence, multilayer BFO films are first synthesized to understand how the layer number affects BFO phase configuration.

Multilayer BFO thin films are achieved by repeating the whole deposition process several (up to four) times with the precursor concentration of 0.25 M and annealing temperature of 640 °C for 30 min. The fabrication process details are given in **Table 4-2**.

First, the cross-sectional images of scanning electron microscopy (SEM) are used to check films thickness, as shown in **Figure 4-1**. The average thicknesses of different multilayer BFO//LAO thin films are approximately 40 nm for the 1-layer film, 80 nm for the 2-layer film, 145 nm for the 3-layer film, and 250 nm for the 4-layer film. This nonlinear increase in thickness as a function of layer number may be ascribed to the increasing surface roughness, and better wettability of each subsequent layer of the deposited BFO. This leads to a thicker precursor layer during the spin coating and thus thicker BFO layers. [186] Here, a dense

microstructure can be seen in 1- and 2-layer films. The nonpenetrating holes are observed in 3- and 4-layer samples, which may also lead to the nonlinear increase of the films thickness. In addition, no clear interface is found between each layer, indicating a high-quality epitaxial growth of multilayer BFO thin films by CSD. Additional details about epitaxial growth information will be investigated later.

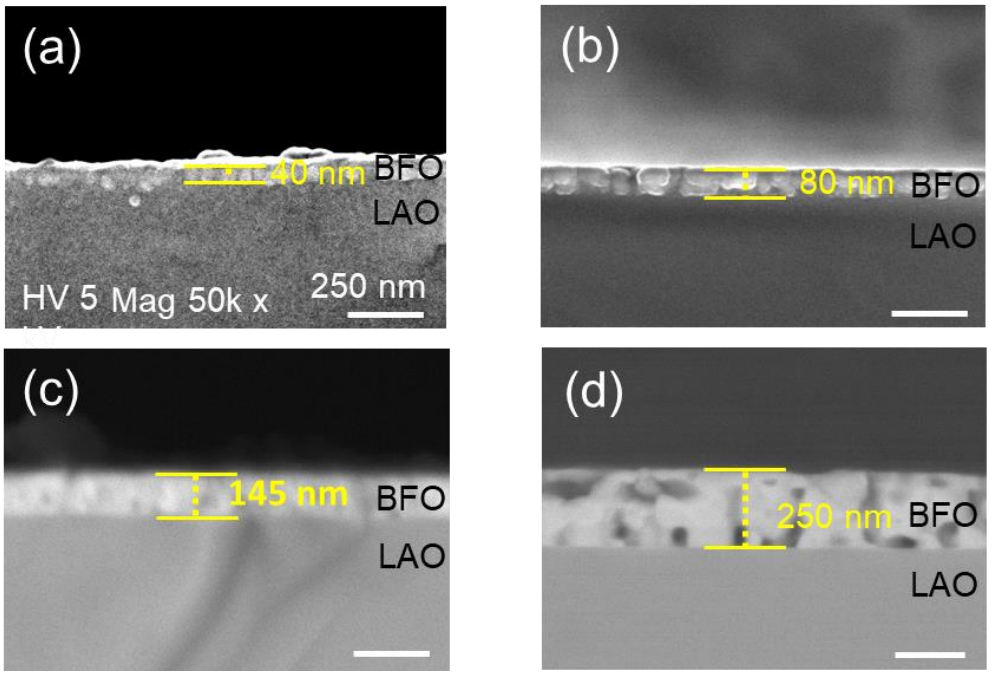

Figure 4-1. Cross-sectional FE-SEM images of BFO//LAO (001) films with (a) one-layer, (b) two-layer, (c) three-layer, and (d) four-layer configuration.

Next, we studied the surface topography, piezoresponse force microscopy (PFM) amplitude, and phase images (scan size of 1 µm × 1 µm) of the as-grown BFO//LAO thin films, as shown in **Figure 4-2**. Compared to PLD-derived BFO films, no typical striated morphology is observed (**Figure 4-2(a)**). The root-mean-square (RMS) surface roughness values of the four samples are 2.3 nm (1-layer), 2.4 nm (2-layer), 1.9 nm (3-layer), and 1.6 nm (4-layer), respectively. The out-of-plane (OP) PFM amplitude and phase images (with a scan size of 1 µm × 1 µm) are shown in **Figure 4-2(b)** and **(c)**. All films exhibit a mosaic-like polydomain structure as seen by the dual contrast. The yellow and purple domains correspond to downward and upward polarizations, respectively. This polydomain configuration is similar to that observed for CSD-derived pure rhombohedral (R)-phase BFO thin films. [182] There is no correlation between the film grain structure and the domain patterns, indicating a heterostructure of the films. Some white particles are observed on the surface of the single layer film showing low

PFM amplitude. Note there is no detectable impurity or other oriented phases of one-layer BFO thin film according to XRD results (**Figure 4-3**), which indicates these particles are also (00l)-oriented BFO phase. With the second layer deposited on top of the first layer, homogenous BFO thin films with no particles are obtained. This is because these oriented BFO particles in the first layer seed the epitaxial nucleation of the second layer, [187, 188] consistent with the above SEM results.

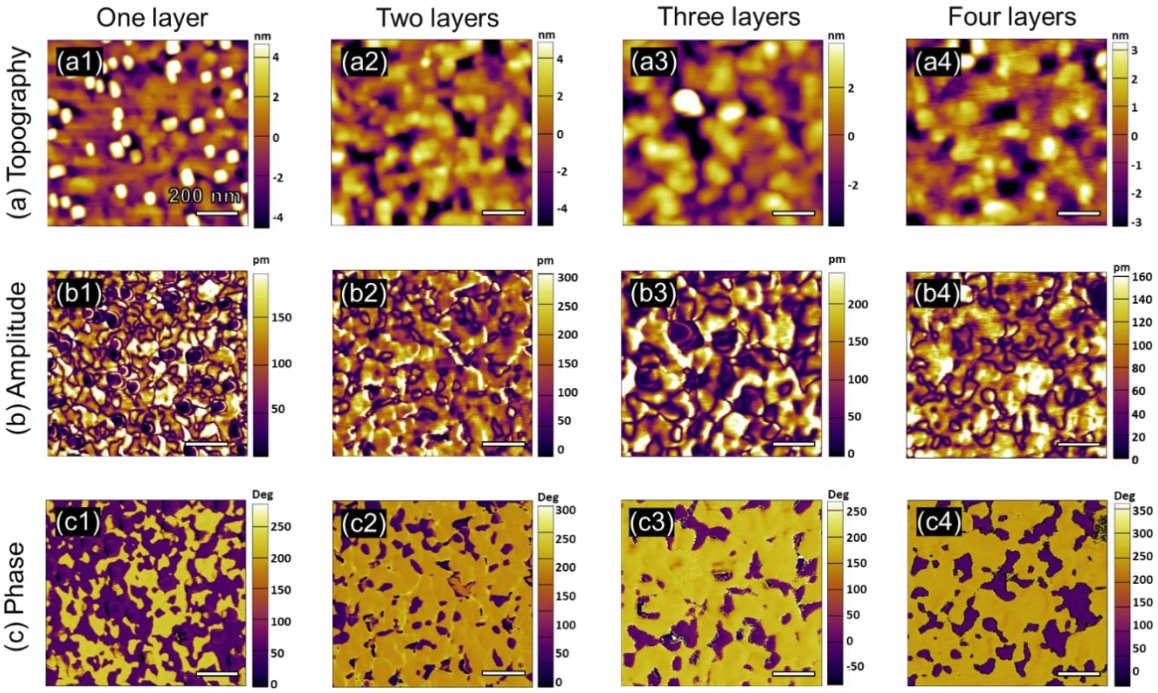

Figure 4-2. (a) Topography, OP PFM (b) amplitude, and (c) phase images (scan size of 1 µm × 1 µm) of BFO//LAO films with one-layer, two-layer, three-layer, and four-layer configurations.

The variation of phase structure composition with increasing BFO layer number is investigated using XRD ϑ-2ϑ scans, as shown in **Figure 4-3(a)**. Note that (001)-oriented BFO thin films with T'- and R'-phase are obtained for all samples. No misorientation or impurity phases are detected for films with thickness up to 145 nm (three-layer BFO). However, when the film thickness increases to 250 nm (4-layer), an extra peak at 32.1° is observed, which could be attributed to a small amount of (110) BFO or Bi_2O_3 phases. The extracted OP lattice constants of the T'- and R'-phase of BFO from the (00*l*) peak are plotted in **Figure 4-3(b)** and listed in **Table 4-3**. With increasing film thickness, the OP lattice parameters of R'-BFO shows a slightly increasing trend with an average value of 3.956 ±0.006 Å. However, the OP lattice parameters of the T'-phase decrease from 4.578 Å to 4.571 Å when the film thickness is

increased from 40 nm to 80 nm. This remains constant when the film thickness is increased to 145 nm. When the film thickness is further increased to 250 nm, a sharp drop in the T'-BFO OP lattice parameter to 4.528 Å is observed. This is attributed to a large epitaxial strain relaxation in thick films, [123, 185, 189] which may also lead to the misoriented (110) BFO formation or relate to the Bi_2O_3 impurity phase.

Figure 4-3(c) presents the T' and R' fractions as a function of layer number/thickness for the four samples. Here, the R' and T' fractions are calculated based on the integrated peak area of (00*l*) BFO. [133] The R'-phase BFO is the main component with a composition of over 65% in all samples. Upon increasing film layer number, the content of T'-phase BFO decreases, and correspondingly, that of R'-phase increases. The T'-phase fractions of 45 nm (one-layer), 80 nm (two-layer), 145 nm (three-layer), and 250 nm(four-layer) films are 35%, 30%, 15%, and 10%, respectively. This trend is likely due to the fact that the phase structure of a given layer is strongly dependent on the crystallographic structure of the preceding layer in the CSD process. Thus, with the decreasing of T'-phase fraction and the change of the IP lattice parameters from the bottom layer, the average OP parameters of T'-phase drop significantly with increasing layer number (i.e., increasing film thickness).

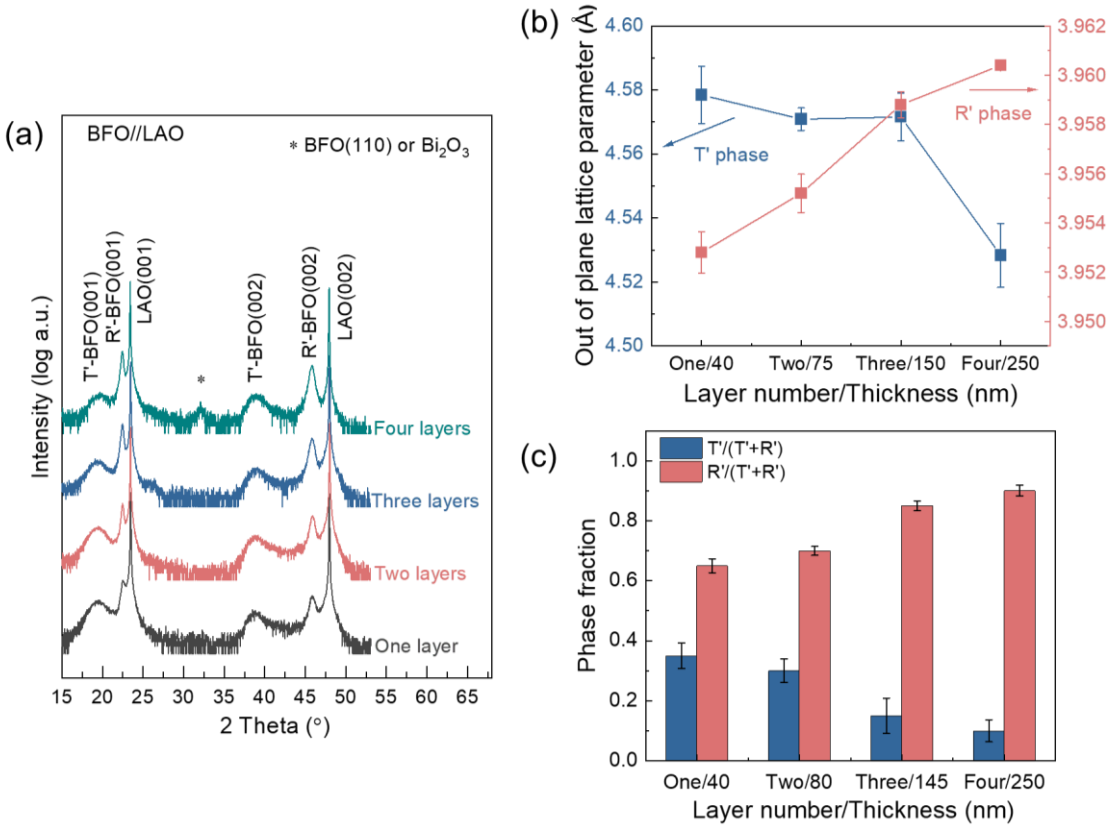

Figure 4-3. (a) X-ray ϑ-2ϑ diffraction patterns of BFO//LAO (001) films with one-layer (35% T'-BFO, black), two-layer (30% T'-BFO, red), three-layer (15% T'-BFO, blue), and four-layer (10% T'-BFO, green) configuration; (b) the extracted OP lattice parameters from the (00*l*) peaks of T'- and R'-phase BFO; and (c) the derived R' and T' fractions by according peak area.

Table 4-4. Extracted peak positions and the corresponding d-spacing, OP compressive strain parameters from (001) peaks.

Number of layers	2 Theta(deg)-(001)			d-spacing (Å)-(001)			Out-of-plane compressive strain
	T'-BFO	R'-BFO	LAO	T'-BFO	R'-BFO	LAO	
One	19.372	22.481	23.441	4.578	3.952	3.792	-15.6%
Two	19.441	22.461	23.461	4.562	3.955	3.7888	-15.2%
Three	19.421	22.461	23.481	4.567	3.955	3.7856	-15.3%
Four	19.721	22.431	23.421	4.498	3.960	3.7952	-13.6%

Raman spectroscopy measurements are carried out to further understand the changes in phase composition of BFO//LAO films as a function of film thickness. The acquired Raman spectrum is the superposition of signatures from the LAO substrate and BFO thin films, as shown in **Figure 4-4**. The phonon Raman active modes for R and T BFO are $4A_1$+9E and 13A'+14A'', respectively. Here, we exclude the analysis of the peaks located at 124, 153, 270, 278, and 488 cm^{-1}, which are produced by the strong LAO substrate, because it is difficult to

distinguish the contribution of the BFO phases from these five intensive peaks. The other discernable peaks are labeled and listed in **Table 4-5**. There are three intense bands at 140 (R-A_1), 171 (R-A_1), and 218 (T-A'') cm^{-1} observed after the deposition of BFO thin films. The former two peaks correspond to the active modes of the R' phase (labelled in orange dash) and the latter one suggests T'-phase (labelled in purple dash) structure. In particular, the two typical bands at 140 (R-A_1 phase mode) and 218 cm^{-1} (T-A' phase mode) become sharper with the increasing film thickness, indicating the accumulation of the two phases composition.

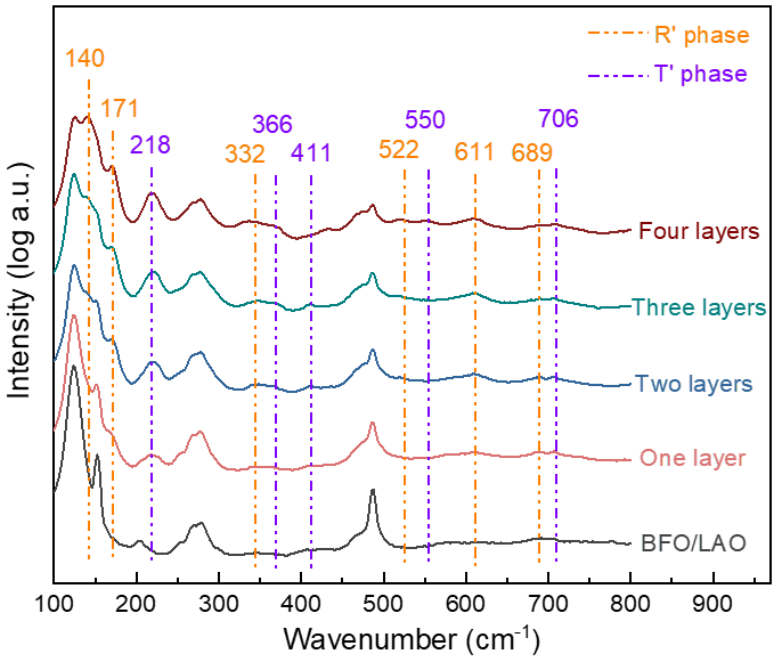

Figure 4-4. Raman spectra of LAO (001) substrate (black) and BFO//LAO (001) thin films with one-layer (red), two-layer (blue), three-layer (green), and four-layer (wine) configuration.

Table 4-5. Room temperature phonon modes at peak frequencies with symmetry assignment of T' phase and R' phase in BFO//LAO (001) thin films.

Peak position (wavenumber/cm^{-1})									
140	171	218	332	366	411	522	550	611	702
R-A_1	R-A_1		R-A_1			R-E		R-E	
		T-A''		T-E	T'_{tilt}-A		T-A'		T-A'

Based on the above results, the phase composition of multilayer BFO films strongly depends on the number of layers (i.e., total thickness). This is understandable from the reduced influence of the substrate strain for thicker films, thus reducing the T'-phase fraction. In the CSD process, film thickness can be also controlled by the applied precursor

concentration. Therefore, next, we explored the influence of bottom layer precursor concentration on the phase component of 2-layer BFO/LSMO//LAO thin films. Here, to facilitate electrical property characterization, a 5 nm thick LSMO layer is used as the bottom electrode, which will be discussed in **Chapter 5**.

4.3.2 Precursor Concentration Dependence

To study the effect of bottom layer thickness on the two-layer BFO system, we prepared precursors with different BFO concentrations (i.e., 0.05 M, 0.1 M, 0.2 M, and 0.25 M) for the bottom layer deposition. Following, a precursor of fixed concentration (0.25M) is deposited as the top layer for all films to promote a thicker film with higher resistance. Sample preparation details are given in **Table 4-1**. The estimated thickness of these four films is 48 nm (0.25 M/0.05 M), 56 nm (0.25 M/0.1 M), 72 nm (0.25 M/0.2 M), and 80 nm (0.25 M/0.25 M), respectively.

Figure 4-5(a) shows the XRD ϑ-2ϑ scans of the four samples. All the BFO films show only (00*l*) T'- and R'-BFO phases without other impurity peaks. As shown in **Figure 4-5(b)** and **Figure 4-5(c)**, with the slight increase of precursor concentration (thickness) from 0.05 M (48 nm) to 0.10 M (56 nm), the OP lattice parameters of T' and R' phases show a negligible increase with the average value of 4.558 ±0.002 Å and 3.956 ±0.001 Å, respectively. Correspondingly, the component of the T' phase increases slightly from 36% (0.05 M) to 38% (0.10 M). When rising the concentration to 0.20 M (72 nm), the OP lattice parameters of the T' and R' phases remain a minor increase to 4.562 Å and 3.958 Å, respectively. Meanwhile, the T'-phase component decreases to 28% due to the strain relaxation resulting from the increased thickness. As the film thickness keeps going to 80 nm using 0.25 M/0.25 M precursor, the further increased strain relaxation leads to the decrease of the OP parameters to 4.520 Å (T'-phase) and 3.954 Å (R'-phase), and the T'-phase component decreases to 19%. Note that this value is ~ 10% lower than that of two-layer (0.25 M, 0.25 M) BFO//LAO film, which is caused by partial strain relaxation of the inserted LSMO layer.

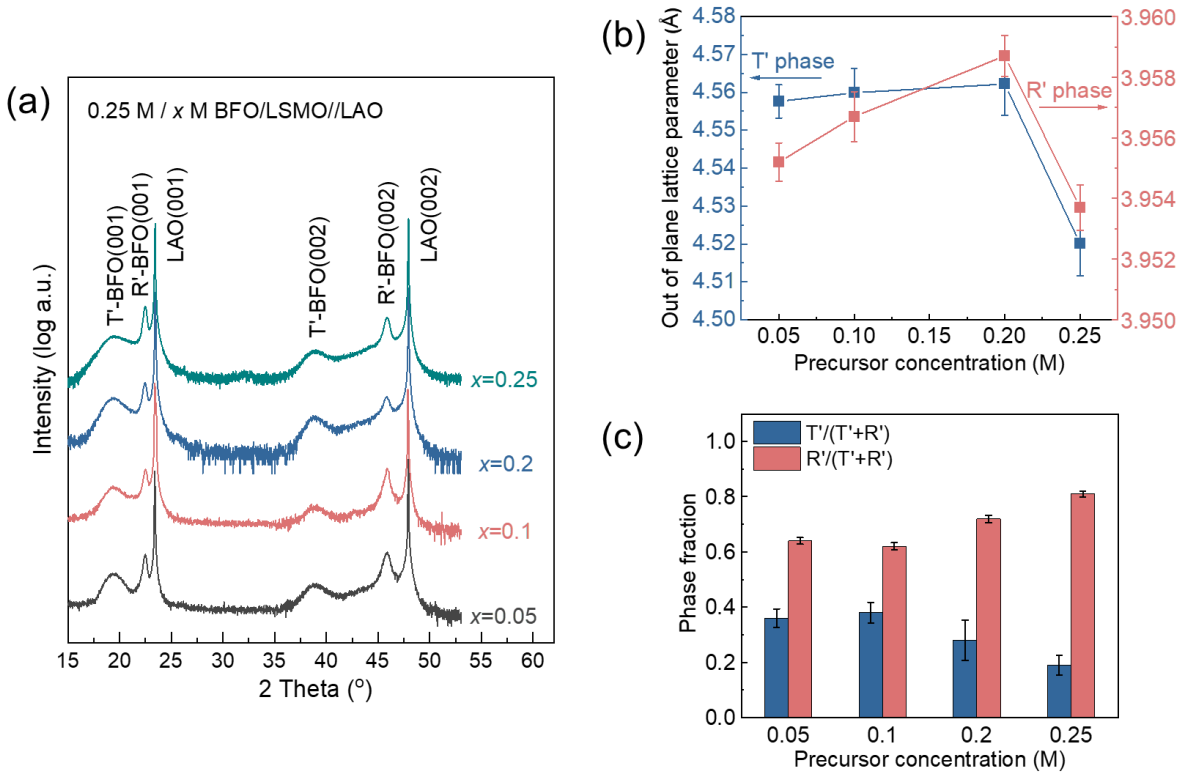

Figure 4-5. (a) X-ray ϑ–2ϑ diffraction patterns of the BFO/LSMO//LAO film annealed at 640 ℃ for 30 min with the applied concentration of the first layer of 0.05 (black), 0.1 (red), 0.2 (blue), and 0.25 (green); the (b) extracted OP lattice parameters from the (00l) peaks of T'- and R'-phase BFO; and the (c) R' and T' fractions derived by according peak area.

Figure 4-6 displays the surface topography, corresponding OP PFM amplitude and phase images (scan size of 1 μm × 1 μm) of the BFO/LSMO//LAO thin films. The films show a relatively smooth surface topography with the RMS surface roughness of 2.1 nm, 2.2 nm, 2.6 nm, and 1.1 nm, respectively. All the films show typical CSD-derived polydomain features with domain patterns independent of the topography in the as-grown state. While when the concentration of the first layer is lower, such as 0.05 M and 0.1 M, white particles are seen on the surface of the final 2-layer films. The corresponding XRD results show there are no extra peaks of impurity or other oriented phases. It is similar to the observed phenomenon in the above single layer BFO/LAO film, where the particles are allocated as the (001)-oriented BFO phase. When the concentration increases to 0.2 M and 0.25 M, homogenous BFO films with no particles are achieved. The uniform piezoresponse with a strong amplitude signal and clear domain walls is also shown.

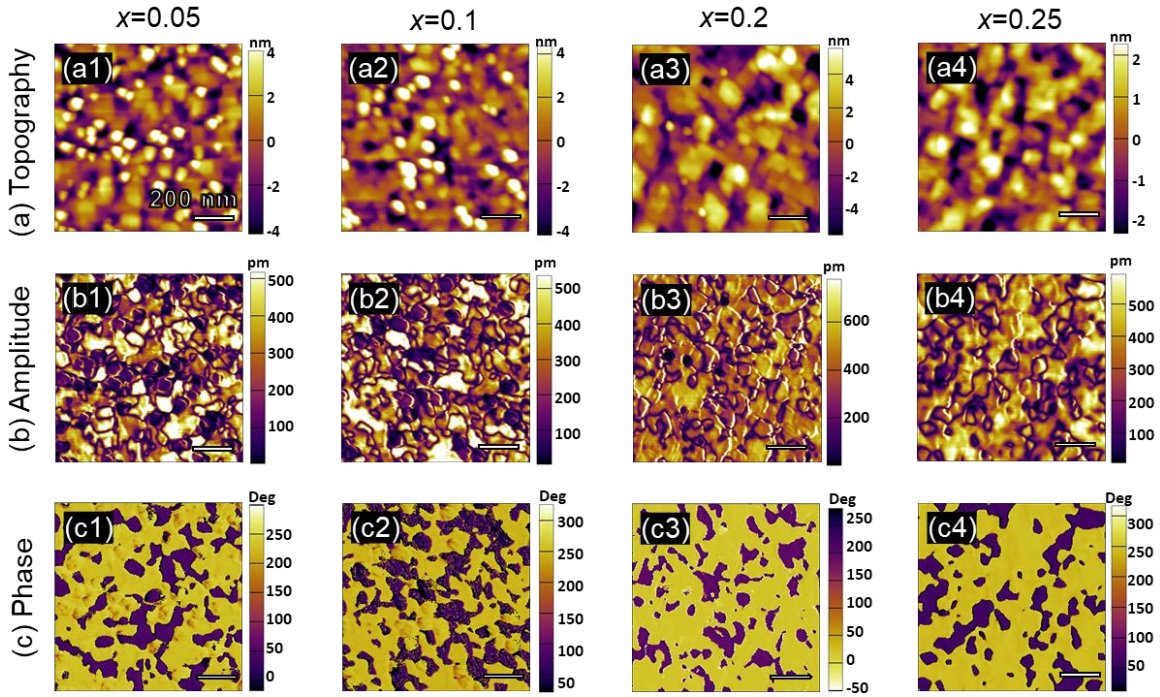

Figure 4-6. (a) Topography, OP PFM (b) amplitude, and (c) phase images (scan size of 1 µm × 1 µm) with the applied precursor concentration of the first layer of 0.05 M, 0.1 M, 0.2 M, and 0.25 M.

4.3.3 Heat Treatment Time-Temperature Dependence

Next, to study the effect of heat treatment processing on phase composition in the two-layer BFO/LSMO//LSO system, four 2-layer films are prepared by heating the films at 520˚C, 580˚C, 640˚C, and 700˚C for 30 min, respectively. An additional two samples heated at 640˚C for 10 min, and 50 min are also synthesized to understand the effects of heating dwell time. To compensate for the relaxation from the LSMO layer, the applied precursor for the bottom layer is adjusted to 0.2 M to maintain a relatively high T'-phase fraction (28%) and simultaneously a thicker film. The sample processing details for this sample set are listed in **Table 4-3**.

Figure 4-7(a) shows the XRD ϑ-2ϑ scans of the temperature dependent and dwell-time-dependent sample set. Only (00*l*) T'- and R'-BFO phases without other misorientation or impurity peaks are detected for the films with the temperature up to 640˚C. As shown in **Figure 4-7(b)**, when annealing temperature increases from 520 ˚C to 580 ˚C, the OP lattice parameters of T'-phase BFO stabilize at ~ 4.581 Å. Upon continuing increase of the temperature from 640˚C to 700 ˚C, a decreasing trend is displayed. The T'-phase component remains stable first

with a fraction of 27%-28% with the temperature from 520 ˚C to 640 ˚C, as shown in **Figure 4-7(c)**. When the temperature goes to 700˚C, the T'-phase fraction decreases to 8% and a slight peak (i.e., (110) BFO or Bi_2O_3 phase) appears due to the strain relaxation at high annealing temperatures. Thus, we conclude that to obtain pure phase BFO with high crystallinity, a heating temperature of 640˚C is optimal.

At this fixed heating temperature of 640˚C, when the dwell time decreases from 30 min to 10 min, the OP lattice parameters and the component of T'-phase BFO reduces from 4.562 nm to 4.511 nm and 28% to 10%, respectively. This is attributed to insufficient crystallization with shorter heating time. [131] On the other hand, upon increase of the heating time from 30 min to 50 min, there is a slight decrease in the T'-phase fraction due to the strain relaxation, however, negligible change in its OP lattice parameters. This suggests that a 30 min heating time is sufficient to realize a well-crystalized film.

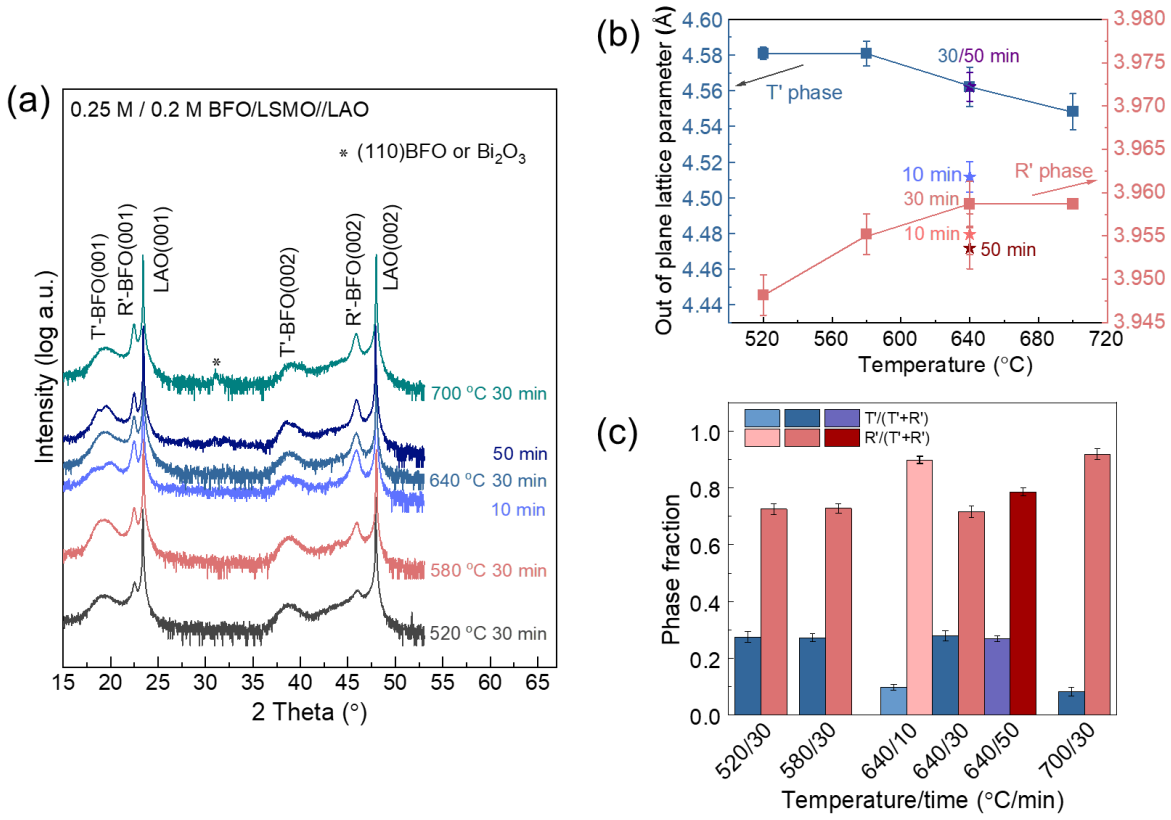

Figure 4-7. (a) X-ray ϑ–2ϑ diffraction patterns of the BFO/LSMO//LAO film annealed at 520 °C/30 min (black), 580 °C/30 min (red), 640 °C/10 min (shallow blue), 640 °C/30 min (blue), 640 °C/50 min (dark blue), and 700 °C/30 min (green); the (b) extracted OP lattice parameters from the (00l) peaks of T'- and R'-phase BFO; and the (c) R' and T' fractions derived by according peak area.

Figure 4-8 displays the surface topography, corresponding PFM amplitude, and phase images of the temperature-dependent BFO/LSMO//LAO thin films. All the films show a typical CSD-derived polydomain feature with domain patterns independent of the topography in the as-grown state. The films annealed at different temperatures of 520, 580, 640, and 700 °C show a relatively smooth surface topography with the RMS surface roughness (acquired from a scan size of 1 μm × 1 μm) of 0.7, 1.6, 2.6, and 1.9 nm, respectively. With the increasing temperature from 520 to 580, and to 640 °C, the morphology experiences a change from pebble-like shapes to jointed grain clusters, and to cubic shapes. This may be attributed to the higher activation energy at the higher crystallization temperature. [190] When the temperature is up to 700 ℃, white particles appear on the surface of the film showing low PFM amplitude, which may be allocated as (001)-oriented BFO phase and/or contributed from the other oriented BFO phase or impurity Bi_2O_3 (Where extra peaks from XRD results are shown in the film in **Figure 4-7**).

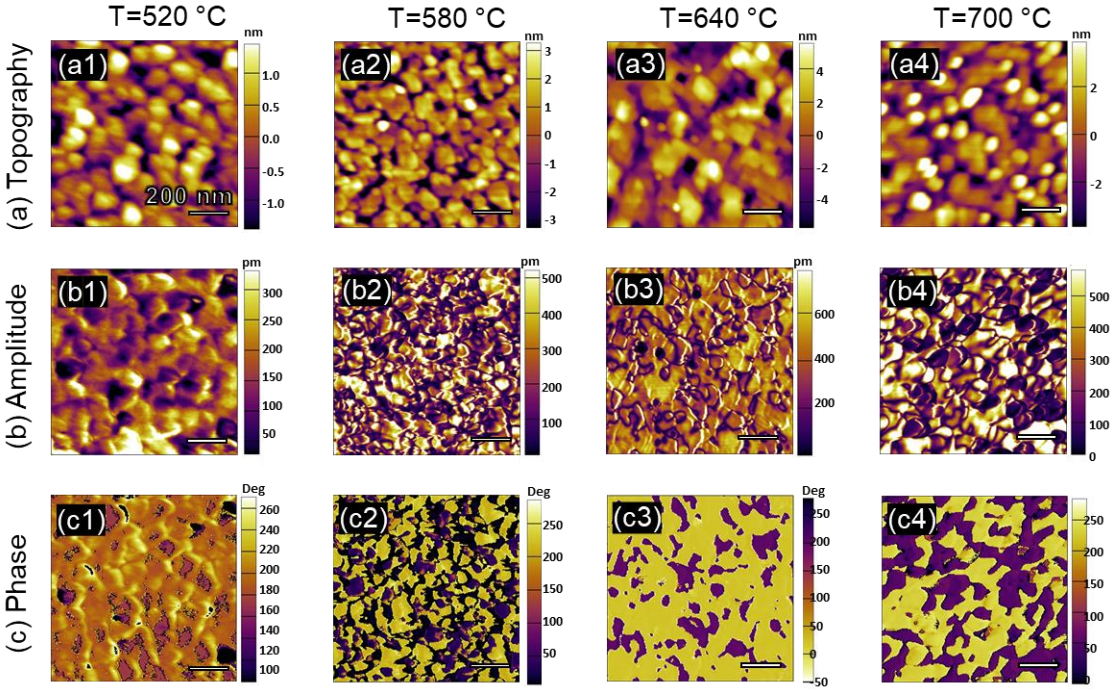

Figure 4-8. (a) Topography, OP PFM (b) amplitude, and (c) phase images (scan size of 1 μm × 1 μm) of BFO/LSMO//LAO films with crystallization temperatures of 520, 580, 640, and 700 °C for 30 min.

Figure 4-9 shows the surface topography and corresponding OP PFM amplitude and phase images of dwell time-dependent BFO/LSMO//LAO films. With the increasing heating time, the films become denser and the morphology changes from pebble-like shapes (10 min)

to cubic (30 min) and then changes to irregular shapes with indistinct boundaries (50 min). This is due to the additional thermal energy from longer crystallization dwell time, which causes grain growth. The RMS surface roughness values for the three samples are 2.0 nm, 2.6 nm, and 0.9 nm, respectively over the area of 1 µm x 1 µm. With the dwelling time going to 50 min, the domain phase becomes fuzzy, which indicates the non-unique polarization at the domain boundaries within the resolution of PFM.

It is suggested that both crystallization temperature and dwell time can obviously affect the surface microstructure and grain shapes, as well as the domain structure.

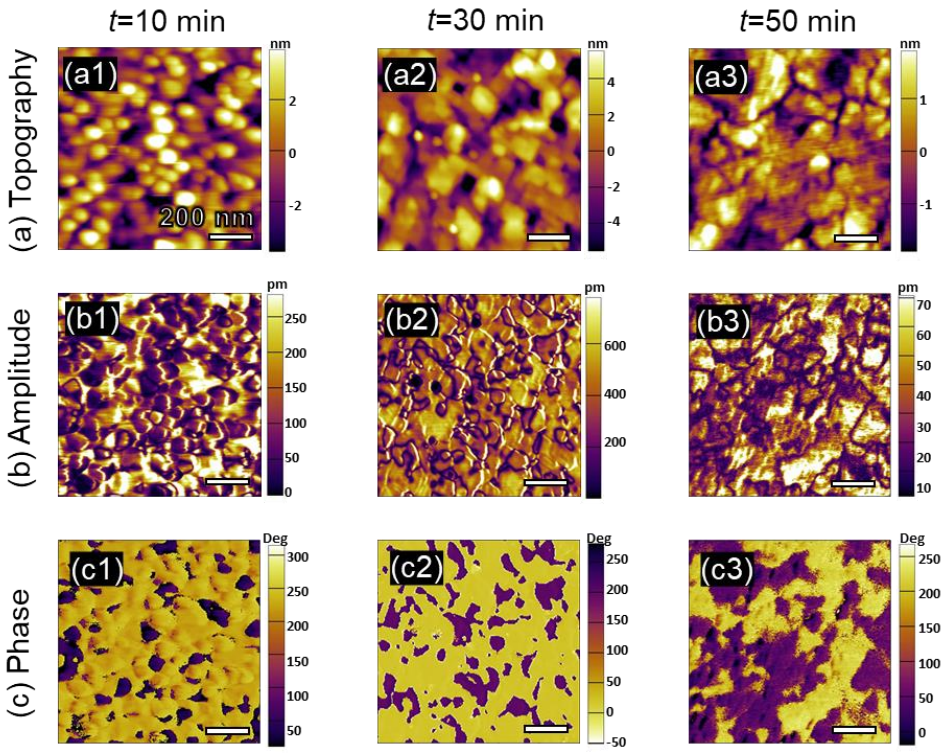

Figure 4-9. (a) Topography, OP PFM (b) amplitude, and (c) phase images (scan size of 1 µm × 1 µm) of BFO/LSMO//LAO films with crystallization dwell time of 10 min, 30 min, 50 min at the crystallization temperature of 640 °C.

Based on the above results, the tuning of T'-phase fractions ranging from 8% to 28% in a two-layer system is successfully realized through the concentration of the applied precursor and heat treatment process (crystallization temperature and dwell time). Next, we explored the crystallographic structures of the as-grown CSD-derived mixed BFO films.

4.3.4 Crystallographic Structure

To investigate the texture of the R' and T' structures of these mixed-phase BFO films, XRD

pole figures of the films with T' phase fractions of 10%, 18%, and 28% are collected first, as shown in **Figure 4-10**. All films show a single spot at the origin with the 2ϑ fixed at 19.3° corresponding to the T'-BFO {001} plane, which indicates the [001] oriented growth of the T' phase. Fourfold symmetry spots with the 2ϑ of 30.31° and 31.97° corresponding to T'- and R'-BFO {101} planes, respectively, demonstrate a cube-on-cube epitaxial growth of both the T' and R' phases in these films.

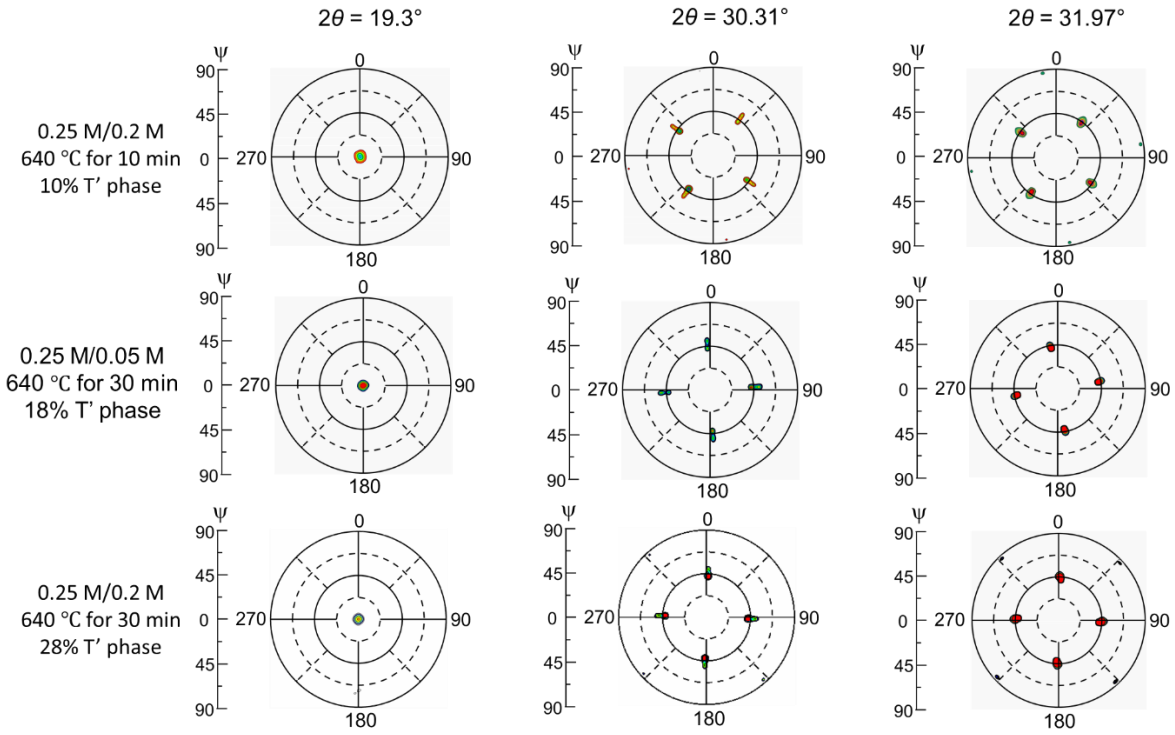

Figure 4-10. Pole figures with the 2ϑ value fixed at 19.3°, 30.31°, and 31.97 of two-layer BFO/LSMO//LAO (001) film with different T'-phase fractions.

The epitaxial growth of 28% T'-BFO (0.25 M/0.2 M with the crystallization temperature of 640℃ for 30 min) is further confirmed through a symmetric RSM near the (001) reflection measurements (**Figure 4-11**). The broad R' peak and a relatively sharp T' peak indicate the mosaic R' phase and much smaller T' phase crystallite size. While this RSM pattern is different from the PLD- or MBE-derived mixed-phase BFO, whose peaks are more complicated (i.e., often with sharp T' and R' phases) and additional triclinic phases. Thus, the CSD method nucleates a new T'-R' mixed phase, which may induce different physical properties compared to the PVD-derived films.

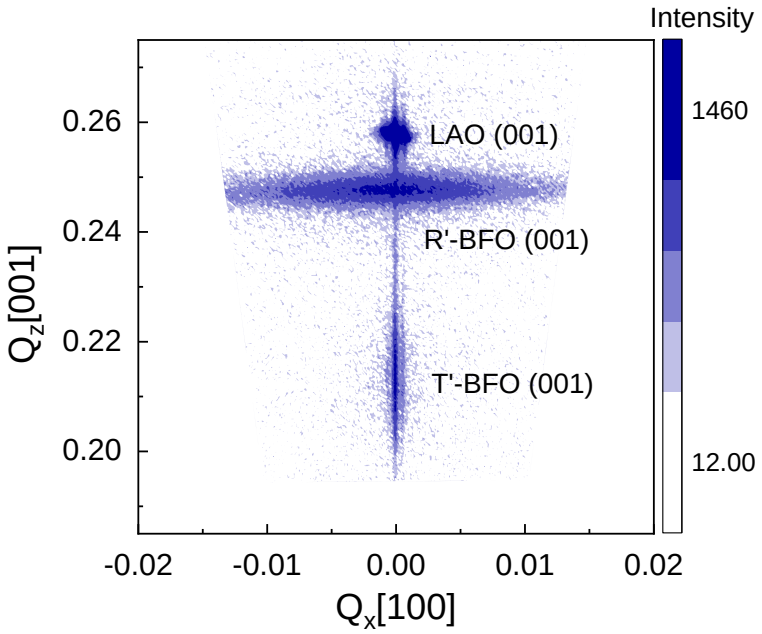

Figure 4-11. Symmetric RSM along (001) direction of two-layer BFO/LSMO//LAO (001) film annealed at 640 °C for 30 min.

The cross-sectional transmission electron microscopy (TEM) images are also conducted to investigate the crystallographic structure of this multilayer BFO/LSMO//LAO thin film, as shown in **Figure 4-12**. **Figure 4-12(a)** shows that the BFO thickness is approximately 80 nm thick. This is consistent with the SEM result of the two-layer BFO//LAO sample. The high-resolution TEM image in **Figure 4-12(b)** shows no evidence for an interfacial region about halfway through the film thickness, indicating a high-quality epitaxial growth of multilayer BFO thin films. A closer inspection of **Figure 4-12(c)** verifies a pseudomorphic BFO film on the LSMO buffer layer. This confirms that the bottom layer (either LSMO or strained BFO layer) can provide the necessary strain for the epitaxial growth of the upper layer through this CSD technique.

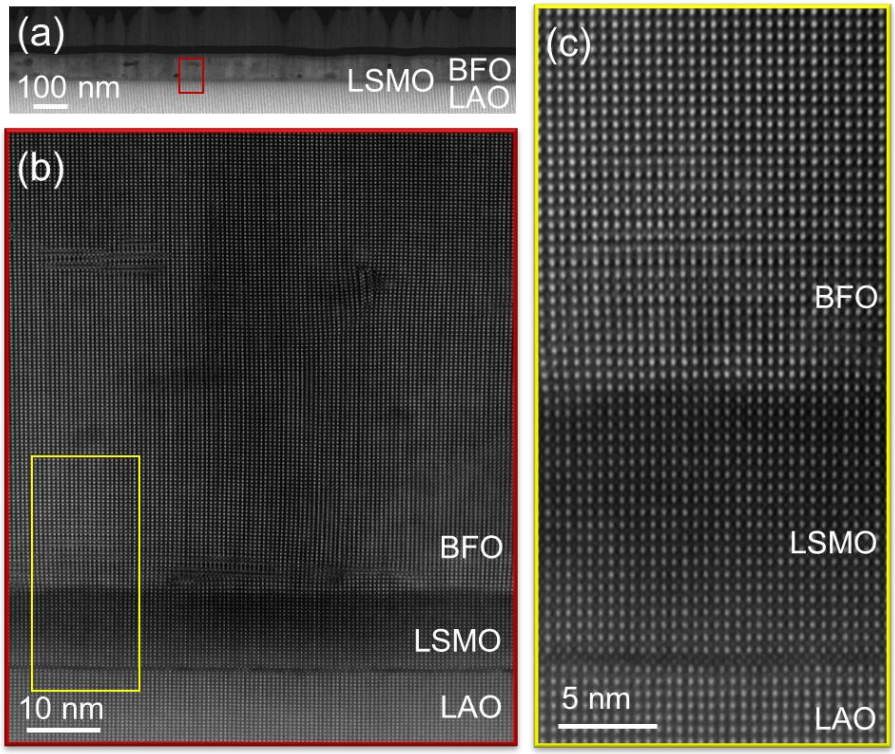

Figure 4-12. Cross-sectional TEM images of (a) a wide area, (b) zoom-in high-resolution image of a red rectangle region, and (c) yellow rectangle region of a two-layer BFO/LSMO//LAO (001) film with an annealing temperature of 640 °C for 30 min.

4.4 Summary

(1) In summary, (001)-oriented epitaxial mixed-phase BFO films are prepared through the CSD method. The tuning of phase fraction is successfully achieved by controlling the preparation process via the below step: the phase composition and microstructure are first tuned through the number of layers deposited. A T'-phase fraction ranging from 35% (one-layer, 45 nm) to 10% (four-layer, 250 nm) is achieved in multilayer BFO//LAO films.

(2) Subsequently, a two-layer BFO is fixed with a 5 nm thick LSMO bottom electrode inserted between BFO and LAO substrate. we further utilized the concentration of the applied precursor and heat treatment process (crystallization temperature and dwell time) to tailor their phase composition. The T'-phase fraction changing from 8% to 38% is successfully realized. The PFM results show a typical polydomain structure in these as-prepared CSD-derived BFO films.

(3) Last, we investigate the crystallographic structure of these mixed-phase BFO films.

The high-quality BFO films with (001)-oriented epitaxial growth are confirmed by the pole figure, RSM, and TEM techniques.

Through the optimization, a high T’-phase fraction of 28% mixed-phase BFO films with a thickness of 72 nm is obtained by annealing the film at 640 ℃ for 30 min.

Chapter 5. Leakage Current Behavior of Chemical Solution Deposition-derived Mixed-Phase Bismuth Ferrite Thin Films

In the previous chapter, mixed-phase $BiFeO_3$ (BFO) films are optimized through the tuning of the films thickness (the number of layers deposited and the concentration of precursor solution) and the heat treatment process (crystallization temperature and dwell time). In this chapter, the effects of films fraction on the ferroelectric characteristics, leakage current density and conduction mechanisms are further studied. The domain configuration and switching performance is studied using piezoresponse force microscopy (PFM), and the local polarization dependent conduction behavior is collected by conductive atomic force microscopy (CAFM). The effect of the phase fraction on the electrical leakage characteristics is also inspected. In addition, the conduction mechanism evolution with the magnitude of the external electric field and the phase fraction are investigated to reveal the role of the tetragonal-like (T') phase in the leakage behavior. This work, in turn, guides the precise design of the mixed phase component for improved electrical performance in mixed phase BFO films.

5.1 Introduction

Mixed-phase BFO with the coexistence of rhombohedral-like (R') and T' phase has proven to show a superior electromechanical response. [9] The measurable displacements of the surface driven by the reversible conversion between T' and R' phases across a morphotropic phase boundary (MPB) makes mixed-phase BFO of great interest for probe-based storage and actuator applications. [9] However, the large leakage current is a challenge for its applications. It is reported that the oxygen vacancies and Fe^{2+} ions, as well as the parasitic phases, are the main sources of the BFO films leakage. Two approaches that are usually applied to reduce the leakage current are (1) doping in A-site or/and B-site, and (2) modifying the synthesis conditions. For example, the La, Sm, Dy, Gd substitution for Bi^{3+} [8, 191-193] and Mn, Co, Cr, Ti substitution for Fe^{3+} ion [173, 194-196], or the co-substitution with Ce and Mn, [197] La and Mn, [198] Ti and Zn [199] were utilized to reduce the high leakage current and thus improve the ferroelectric properties. For undoped BFO, the optimization of the fabrication process is critical to efficient electrical performance. So far, many endeavors have been devoted to improving the leakage issues and the functionality of pure rhombohedral (R)-phase BFO films

by optimizing growth temperature [200], oxygen pressure [201], and nonstoichiometry [202]. The conduction mechanism has also been widely investigated. [105, 203, 204] However, rare studies are reported on how the leakage behavior and conduction mechanism are affected by the phase fraction variation in mixed-phase BFO films.

In this chapter, a systematical investigation of the ferroelectric domain switching and leakage current behavior is conducted. We show that a mixed-phase BFO film annealing at 640 °C for 30 min (28% T′-phase) has the lowest leakage current. In contrast to the observed bulk-limited Ohmic conduction mechanism or space-charge-limited-conduction (SCLC) mechanism in R′-phase and 10% T′-phase BFO thin films, this high T′-phase mixed-phase film shows a leakage mechanism that is strongly dependent on the magnitude of the applied field. At the low electric fields (280 kV/cm at negative bias, 470 kV/cm at positive bias), it is an interface-limited Schottky emission, which changes to SCLC when the field increases to 1065 kV/cm (at negative bias)/1435 kV/cm (at positive bias).

5.2 Experimental Procedure

Detailed information about the fabrication process of mixed-phase BFO films is described in the experimental procedure part of **Chapter 4**. The summarized samples information is listed in **Table 5-1**. For all the samples, the bottom electrode of 5 nm thick $La_{0.67}Sr_{0.33}MnO_3$ (LSMO) was prepared by pulsed laser deposition (PLD) (Neocera, US)) for the purpose of electrical property characterization. In addition, a two-layer pure R'-phase film, as a reference sample, was deposited on $SrTiO_3$ (STO) (001) substrate with 20 nm-thick LSMO as the bottom electrode.

Table 5-1. Summary of the fabrication parameters of mixed-phase BFO/LSMO//LAO films.

Samples	Precursor concentration		Pyrolysis		Crystallization		T'-phase fraction
	First layer (*x)**	Second layer	temperature	time	**Temperature (*T*)**	**Time (*t*)**	
1	**0.05 M**	0.25 M	450 °C	30 min	640 °C	30 min	38%
2	**0.1 M**	0.25 M	450 °C	30 min	640 °C	30 min	36%
3	**0.2 M**	0.25 M	450 °C	30 min	640 °C	30 min	28%
4	**0.25 M**	0.25 M	450 °C	30 min	640 °C	30 min	19%
5	0.2 M	0.25 M	450 °C	30 min	**520 °C**	30 min	27%
6	0.2 M	0.25 M	450 °C	30 min	**580 °C**	30 min	27%
7	0.2 M	0.25 M	450 °C	30 min	640 °C	**10 min**	10%
8	0.2 M	0.25 M	450 °C	30 min	**640 °C**	**30 min**	28%
9	0.2 M	0.25 M	450 °C	30 min	640 °C	**50 min**	27%
10	0.2 M	0.25 M	450 °C	30 min	**700 °C**	30 min	8%

Note: x* is the applied precursor concentration for the first layer, *T* is the annealing temperature, and *t* is the annealing time

5.3 Results and Discussion

5.3.1 Precursor Concentration Dependence

The domain structure evolution under an external electric field in ferroelectrics can be directly imaged using the PFM technique. A small Direct current (DC) voltage is utilized to induce local polarization reversal, effectively as a localized poling process. Thus, the 180° polarization, oriented upward or downward can be achieved by applying positive or negative DC bias through the bottom electrode toward the PFM probe.

The domains of 0.25 M/ *x* M BFO/LSMO//LAO (LAO: $LaAlO_3$) films are switched upwards on 3 μm × 3 μm (outer box) and downwards on 1 μm × 1 μm (inner box) square regions under +6 V) and -6 V, respectively. The corresponding PFM out-of-plane (OP) amplitude and phase images after switching are shown in **Figure 5-1(a)** and **(b)**. The enhanced amplitude is observed at either switched areas in all samples. Compared to the pristine domain region, nearly all domains written with +6 V/ -6 V are poled-up (purple color)/ down (yellow color), according to the phase images. These results indicates that the domains in all above mixed-phase BFO films can be completely switched under an external voltage of ±6 V.

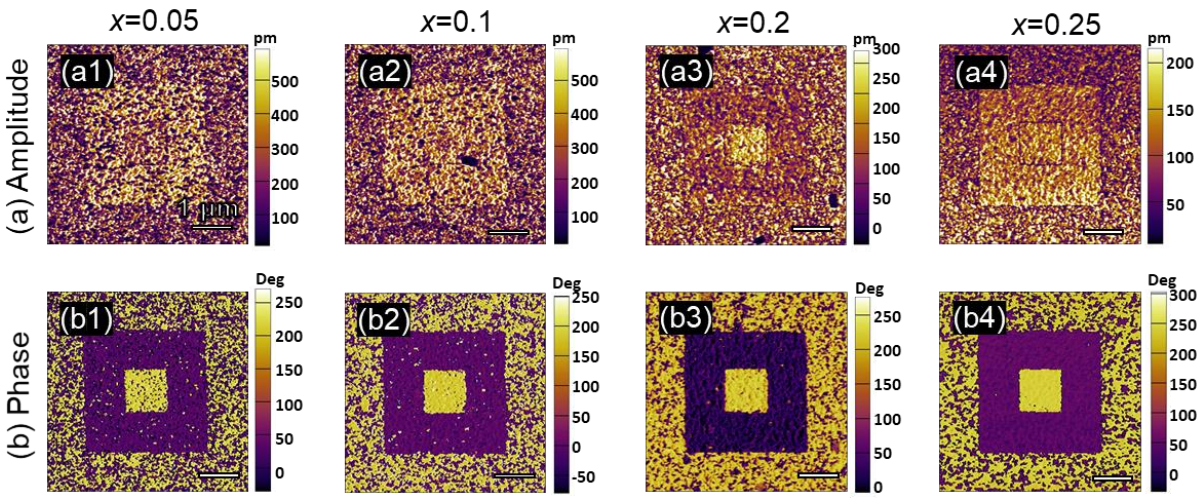

Figure 5-1. PFM OP (a) amplitude and (b) phase images (scan size of 5 μm × 5 μm) after domain switching of BFO/LSMO//LAO films with the applied precursor concentration of the first layer of 0.05 M, 0.1 M, 0.2 M, and 0.25 M. The applied switching DC bias is +6 V (3 μm × 3 μm, purple regions: poled-up)/−6 V (1 μm × 1 μm, yellow regions: poled-down).

However, BFO films often show high leakage current due to the oxygen vacancies. [199, 205] Thus, it is imperative to investigate the effects of the applied electric field on the electrical properties of thin films. Semi-log curves of current density versus electric field (*J-E*) are acquired for all samples, as shown in **Figure 5-2**. In general, the leakage current decreases with increasing thickness. For a thickness of 72 nm (0.2 M), the value of the leakage current density of BFO thin films is lower than 0.1 A/cm^2 under an electric field ranging from -500 kV/cm to +500 kV/cm. The 0.25 M / 0.25 M (80 nm) sample also shows relatively low leakage at the low electric field, while its T'-phase fraction is low (19%).

On the other hand, the samples prepared with the 0.05 M (48 nm) and 0.1 M (56 nm) precursor concentration for the bottom layer show a comparatively higher current density, which can be attributed to their higher T'-phase fraction (~ 37%) and/or lower film thickness.

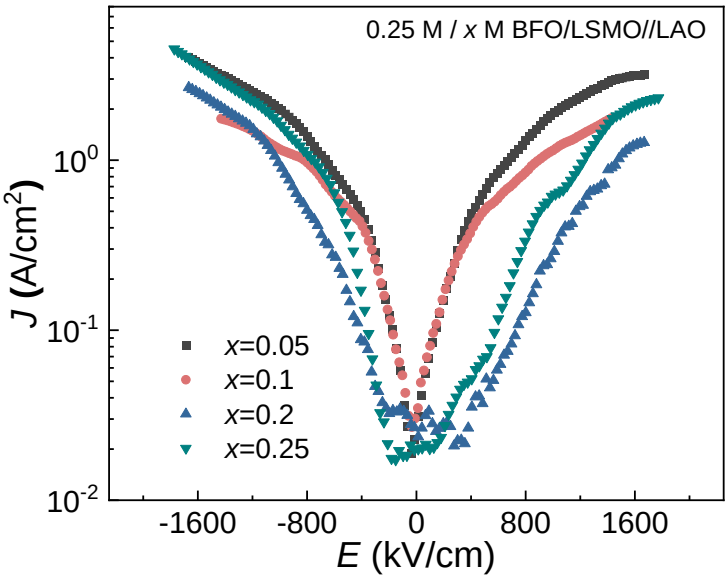

Figure 5-2. Leakage current density-electric field (J-E) curves in semi-log scales of BFO/LSMO//LAO (001) films annealed at 640 °C for 30 min with the applied first layer concentration of 0.05 (black square), 0.1 (red dot), 0.2 (blue upward triangle), and 0.25 (green downward triangle).

For the above-described four films, the 2-layer film with a 0.25 M / 0.2 M configuration shows the lowest current density, and simultaneously sustains a relatively higher T'-phase fraction. Because a higher T'-phase fraction can generate an enhanced electromechanical response, and for applications, low leakage is also desired, this film appears to have the required physical responses for nanoscale devices. However, the results on these four samples also highlight that a trade-off of properties would be inevitable because the T'-phase fraction (which is dependent on thickness) and the thickness itself both influence the leakage and the electromechanical response.

5.3.2 Heat Treatment Time-Temperature Dependence

Thus, we focus on the above-optimized film configuration (0.25 M/ 0.2 M) and investigate the role of heat treatment processing on the electrical properties. Four films heated at 520 °C, 580 °C, 640 °C, and 700 °C for 30 min, and additional two samples heated at 640 °C for 10 min, and 50 min are explored, respectively. The processing parameters and corresponding T'-phase fraction are listed in **Table 5-1**.

The ferroelectric nature of these heating temperature-dependent (520 °C, 580 °C, 640 °C, and 700 °C) BFO thin films are confirmed through domain switching using PFM. As shown in

Figure 5-3(a) and **(b)**, the high amplitude signal and clear dual color contrast are observed at both the switched upwards (purple region, outer box, 3 µm × 3 µm) and downwards (yellow region, inner box, 1 µm × 1 µm) areas for all samples, which indicates a full domain switching under the external +6 V/ -6 V DC bias.

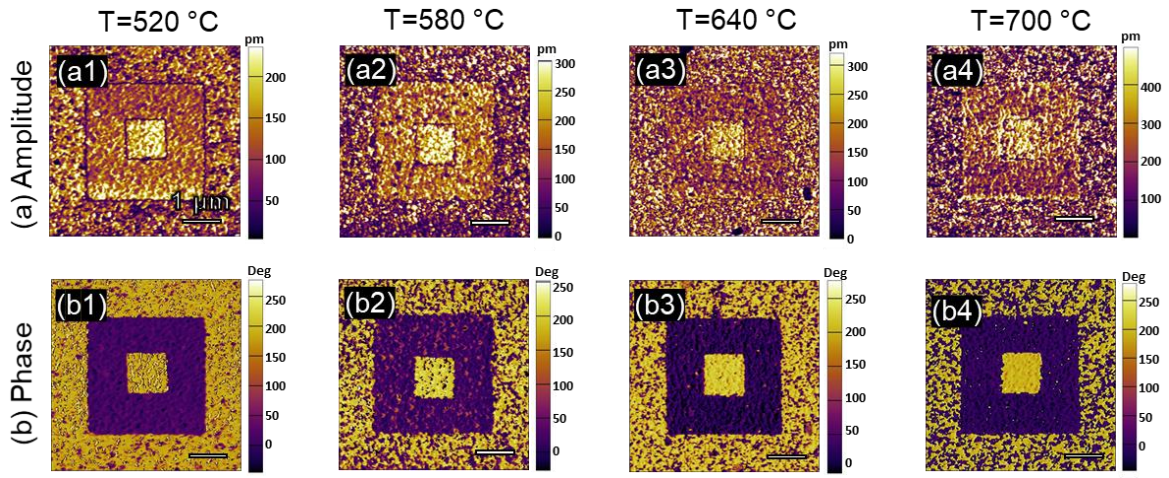

Figure 5-3. PFM OP (a) amplitude and (b) phase images (scan size of 5 µm × 5 µm) after domain switching of BFO/LSMO//LAO films with crystallization temperatures of 520, 580, 640, and 700 °C for 30 min. The applied switching DC bias is +6 V (3 µm × 3 µm, purple regions: poled-up)/−6 V (1 µm × 1 µm, yellow regions: poled-down).

Figure 5-4 shows the domain switching behavior in the mixed-phase BFO films with different dwell durations (10 min, 30 min, and 50 min). The written voltages of +6 V/+6 V/+9.6 V and -6 V/-6 V/-9.6 V are required to fully switch the domains upwards and downwards respectively (applying through the bottom electrode), for dwelling time of 10 min, 30 min, and 50 min. The increased written voltage in the mixed-phase BFO film with the extension the dwell time to 50 min may be attributed to the increased point defects [206] at the domain wall that pins the domain wall rotation [153, 207].

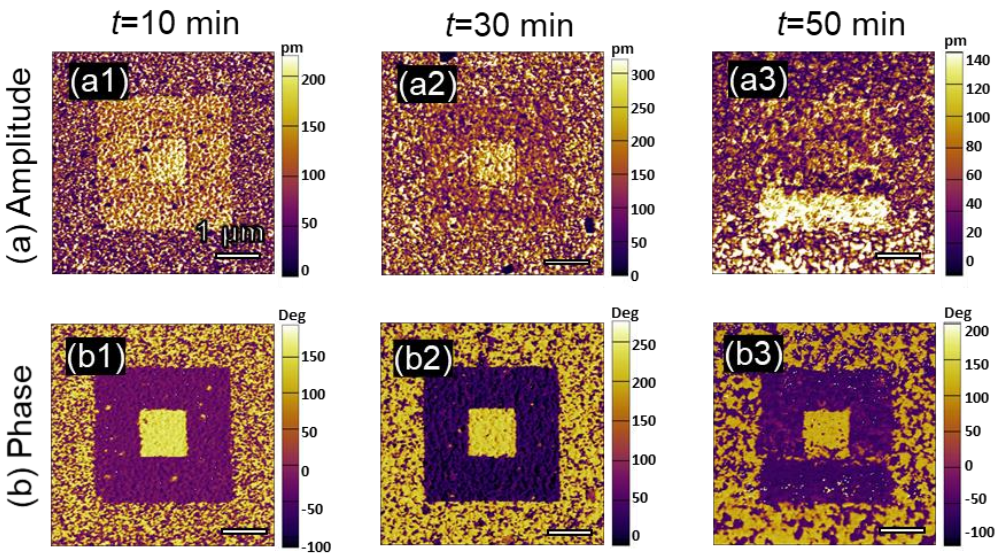

Figure 5-4. PFM OP (a) amplitude and (b) phase images (scan size of 5 μm × 5 μm) after domain switching of BFO/LSMO//LAO films annealed at 640 °C with dwell time of 10 min, 30 min, and 50 min, respectively. The applied switching DC bias is +6/9.6 V (3 μm × 3 μm, purple regions: poled-up)/−6/9.6 V (1 μm × 1 μm, yellow regions: poled-down).

Next, we focus on the investigation of the effects of the electric field on the electrical properties of these samples. Semi-log curves of current density versus electric field (*J-E*) are shown in **Figure 5-5 (a)** and **(b)**. First, a significantly higher leakage current density is observed for the BFO thin films annealed at 520 °C. With the temperature increased to 580 °C and above, the leakage current density of BFO thin films decreases by an order magnitude at fields exceeding 100 kV/cm. This behavior may be attributed to the improved crystallinity with the increasing temperature. [131] Particularly at high electric field, the leakage current density curves of BFO film with the crystallization temperatures of 580 °C, 640 °C, and 700 °C are saturated and overlapped. This implies a common conduction mechanism in this region. The conduction mechanism details are discussed later. We note that despite the low T'-BFO phase fraction (18%) of film annealed at 700 °C, it shows higher conductivity than the sample annealed at 640 °C. This observation can be ascribed to the misorientation (110)-BFO phase or the high conductive Bi_2O_3 impurity phase formed at higher temperature during annealing. [208]

At a fixed heating temperature of 640 °C, the BFO thin film has the lowest leakage current when the heating time is 30 min. With shorter heating times, the resulting film has insufficient crystallinity. When the dwell time is significantly increased, the Bi deficiency and surface defects may increase.

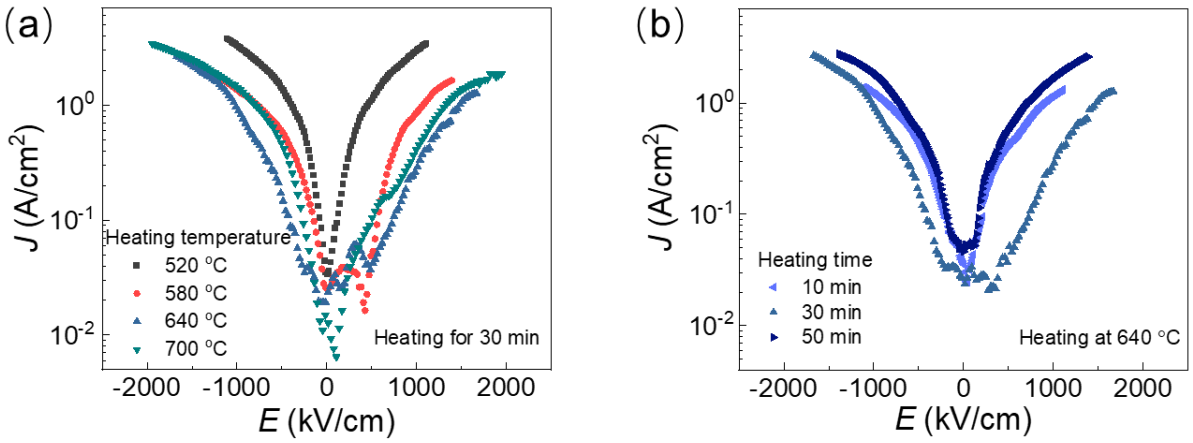

Figure 5-5. Leakage current density–electric field (J–E) curves in semi-log scales of BFO/LSMO//LAO samples (a) at the various crystallization temperatures of 520 °C (black square), 580 °C (red dot), 640 °C (blue upward triangle), and 700 °C (green downward triangle) for 30 min; and (b) at the 640 °C with the various crystallization dwell time of 10 min (light blue leftward triangle), 30 min (blue upward triangle), and 50 min (weight blue rightward triangle).

Based on the results of the studies described above, two-layer epitaxial mixed-phase BFO films are optimized by heating at 640 °C for 30 min in an oxygen atmosphere. This optimal film yields the highest resistivity (leakage current $\leqslant$ 0.1 A/cm^2 at E $\leqslant$ 500 kV/cm) with a T'-phase fraction of 28%. This is at least two orders of magnitude lower than that of 70 nm thick ALD-grown polycrystalline BFO films [201] and is comparable to 200 nm PLD-derived pure R-BFO thin films [195] under the same external electric field.

5.3.3 Electrical Properties and Conductivity Mechanisms.

The local current behavior of three samples with the T'-phase fraction of 10% (0.25 M / 0.2 M, heated at 640 °C for 10 min), 18% (0.25 M / 0.05 M, heated at 640 °C for 30 min), and 28% (0.25 M / 0.2 M, heated at 640 °C for 30 min) is characterized by CAFM. Here, the bias is applied through LSMO bottom electrode to BFO thin film.

As shown in **Figure 5-6**, OP PFM topography, amplitude, and phase images are mapped after the films are polarized by $\pm$6 V bias. Following, the current maps are acquired by scanning the switched regions with an applied DC bias of +2.1 V. There is no discernible change in the topography after the polling process. The respectively increased amplitude and two-color contrast in the amplitude and phase maps confirm the ferroelectric nature of as-prepared mixed-phase films. The corresponding CAFM images display a clearly opposite

contrast that the poled-up domain areas (right side, under +6 V poling bias) have a higher conductivity than the poled-down domain areas (left side, under –6 V poling bias) in all films. Among them, the films with lower T'-phase fraction of 10% and 18% show almost the same current amplitude (i.e., around 46 pA) at the poled-up domain region, while when the T'-phase fraction increases to 28%, the current at the poled-up area slightly increases to 55 pA. This increased conduct current at the high T'-phase fraction can be attributed to the reported higher conductivity at the R'- and T'-phase boundary in BFO compared to pure R'-phase BFO. [209]

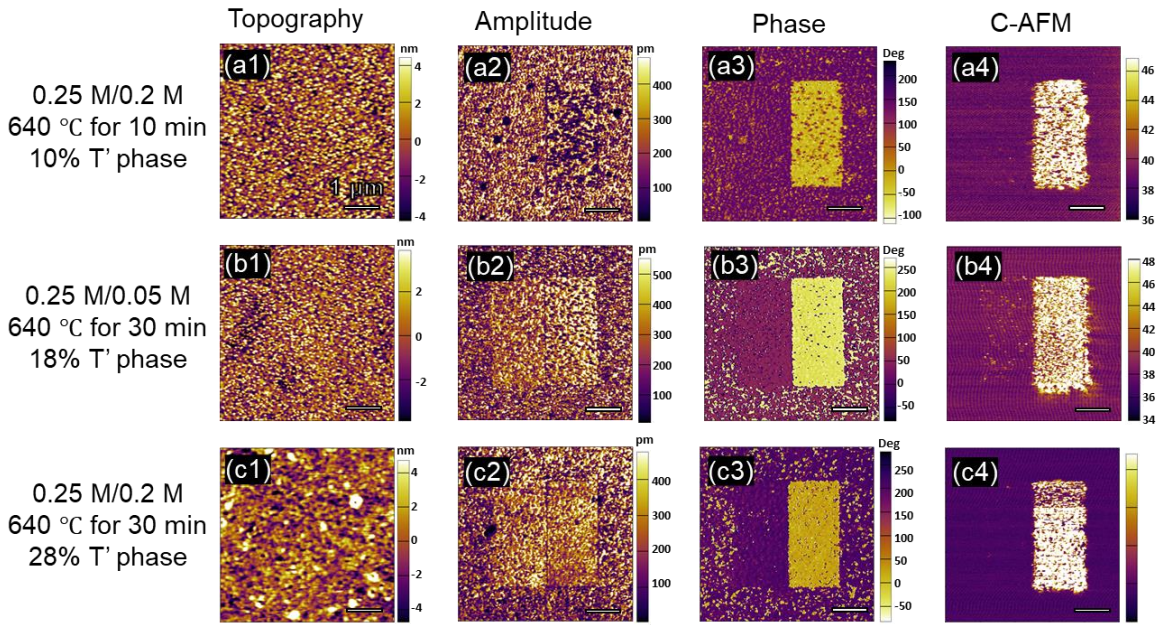

Figure 5-6. OP PFM topography, amplitude, phase, and CAFM images with 2.1 V bias applied after the films are polarized by ±6 V bias of the (a) 10%, (b) 18%, and (c) 28% T'-phase BFO/LSMO//LAO thin films. The applied switching DC bias is −6 V (left side: 1.5 µm × 3 µm, purple regions: poled-down)/+6 V (right side: 1.5 µm × 3 µm, yellow regions: poled-up).

To understand this polarization-dependent conductive behavior, next, we focus on the optimized two-layer BFO/LSMO//LAO mixed-phase film (i.e., 28% T'-phase film) and study its local and global conduction mechanisms.

Local I-V curves of the film with the domain polarization states of as-grown (outside black square), poled-down (left blue rectangle), and poled-up (right red rectangle) are collected by CAFM to explore the local conductive mechanism of polarized domains. The sweep bias for I-V measurement starts from 0 V and the sweep direction is indicated by red arrows in **Figure 5-7**. Among the three polarization states, the poled-up state shows the highest leakage current

with a maximum value of around 4 nA. This is twice that of an as-grown state (maximum value ~ 2 nA), and 10 times larger than that of poled-down domain areas (maximum value ~ 400 pA). The largest leakage current of the poled-up region is consistent with the CAFM mapping result, where the poled-up domain shows higher conductivity.

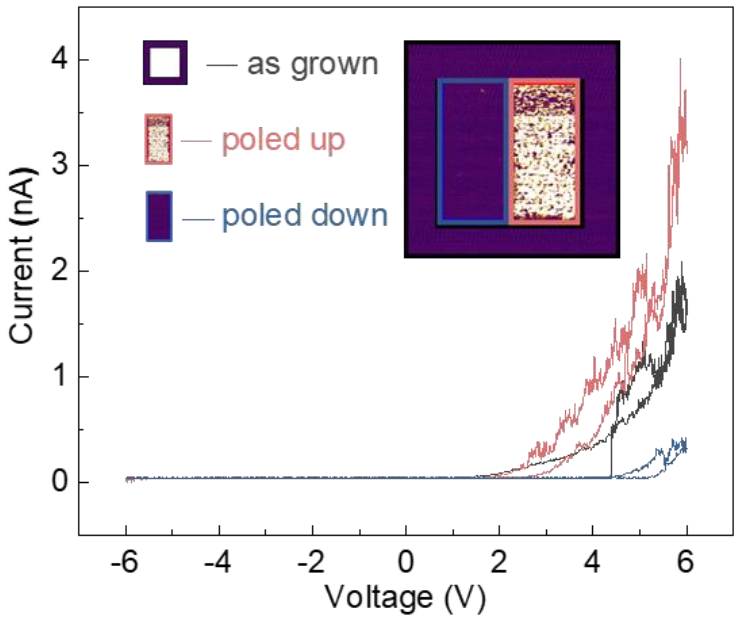

Figure 5-7. Local I–V curves of as-grown (black), poled-up (red), and poled-down (blue) areas with 2.1 V bias applied after the films are polarized by ±6 V bias of the 28% T'-phase BFO/LSMO//LAO thin films with the crystallization temperature of 640 °C and dwell time of 30 min. The applied switching DC bias is −6 V (left side: 1.5 µm × 3 µm, purple regions: poled down)/+6 V (right side: 1.5 µm × 3 µm, yellow regions: poled up). The red arrows indicate the sweep bias direction from 0 → +6 → 0 → −6 → 0 V.

Additionally, all curves show an asymmetric forward diode-like behavior under sweep bias of ±6 V. That is, high current is only observed under positive bias. This suggests a local polarization-orientation-dependent conductivity behavior of the film. A redistribution of the charge carriers (holes and oxygen vacancies) is induced due to polarization reversal, which results in the surface potential difference between the poled-up and poled-down areas of thin films. [210] The resulting energy difference change at the interface between the BFO thin film and LSMO further leads to a modulation of the barrier height. [202, 211] When the domains polarization is switched upward (under positive bias via LSMO), the negative charges accumulate in the BFO at the BFO/LSMO interface, which leads to a strong electron carries depletion (hole accumulation) inside the ultrathin LSMO layer (5 nm), as shown in **Figure 5-8**. A concomitant large upward band bending inside the LSMO at the BFO/LSMO interface is

produced. The applied positive DC bias at the LSMO reduces the barrier height and width, which allows current flow. In addition, under positive bias, both the holes migration from LSMO to BFO and the movement of electrons from Pt to BFO determines the magnitude of the current. Here, holes and electrons are the majority carriers in this PLD-derived LSMO (P-type) and metal Pt respectively, which also accelerates the current flow. Thus, a higher conductivity is observed when the domain polarization is poled up. [212, 213] On the other hand, in the poled-down region (under negative bias via LSMO), the holes are depleted inside the LSMO layer at the BFO/LSMO interface (**Figure 5-8(b)**). The accompanying downward band bending increases the barrier height between BFO and LSMO, which impairs the movement of electrons and holes between BFO and LSMO, thus leading to a high resistivity behavior.

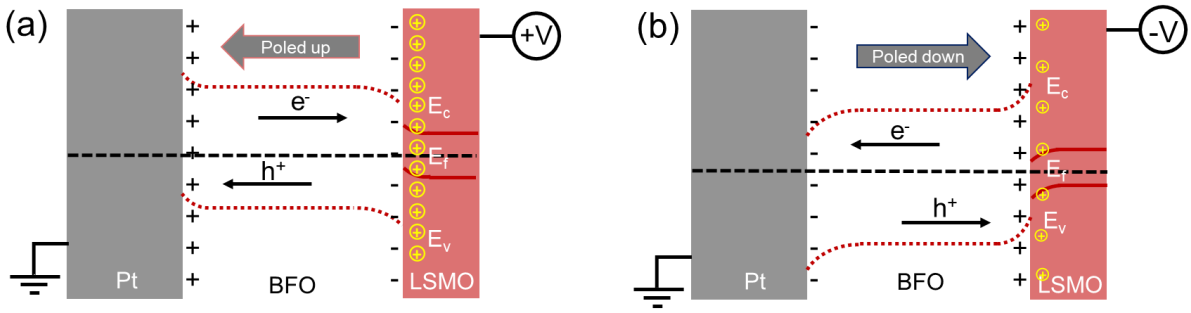

Figure 5-8. Energy band diagrams for (a) poled-up and (b) poled-down regions.

The local CAFM and I-V behavior is similar to a previous study on the R-phase BFO with a 5 nm LSMO bottom electrode. [212] However, the I-V behavior collected by the CAFM technique is limited to a local region and thus is difficult to explain the conduction mechanism of the homogenous mixed phase. To solve this problem, next, we study and analyze the global I-V behavior and conduction mechanism for the mixed-phase film with a square top electrode (23 μm × 23 μm).

The I-V and current density (J)-electric field (E) curves of the as-grown film are shown in **Figure 5-9(a)** and **(b)**. Note, here the bias is applied from Pt top electrode to BFO thin film with the LSMO bottom electrode connecting to the ground (as shown in the inset sketch in **Figure 5-9(a)**) (i.e., opposite to local I-V characterization). Thus, here the current increases relatively faster in the negative bias region (poled-up) than that in the positive bias region (poled-down). In addition, a much higher applied external bias is needed to trigger the current. The resultant leakage current is three orders of magnitude higher than the local I-V measurements. Thus, the diode feature of the global I-V is not as clear as the local I-V in **Figure 5-7**.

The asymmetry of I-V and J-E curves of the 28% T'-phase BFO thin film suggests that different conduction mechanisms may be at play for the positive and negative bias. Therefore, we consider the conduction mechanisms for positive and negative bias separately in the following fittings. We fit the data using three common considered leakage mechanisms for BFO thin films: Schottky emission, bulk-limited SCLC, and PF emission mechanisms. Schottky emission is an interface-limited conduction mechanism, which depends on the electrical properties at the electrode-dielectric interface. A Schottky barrier is formed due to the different Fermi levels between metal and semiconductor or insulator. The thermally or field activated electrons travel through this barrier resulting in Schottky emission. [214, 215] SCLC is a bulk-limited conduction determined by the electrical properties of the dielectric film itself. When charges are injected into the film from the electrode at a rate faster than that they travel through the film, space charge formation is impeded and leads to an SCLC mechanism. [196, 216] PF emission is another bulk-limited conduction governed by a consecutive hopping of charge carriers between defect traps with localized states. [105, 194] For our I-V curves, fitting with the PF mechanism does not yield satisfactory results (not shown here), therefore we focus on Schottky emission and SCLC mechanisms.

For Schottky emission (**Equation 5-1**), restricted by the extracted refractive index n with the theoretical value of 2.5 (calculated from the ideal optical dielectric permittivity $K=n^2=6.25$ for BFO), the fitting curves should show a linear fitting of ln(J) vs $E^{0.5}$ with a slope of ~ 0.204. According to **Equation 5-2**, to fit the SCLC mechanism, a linear fitting of ln(J) vs ln(E) with a slope of ~ 2 should be observed. At the very low electric field region (< ~ 250 kV/cm), the film shows high resistivity both at the negative and positive bias. The I-V curves displays a P-N or Schottky-diode-like feature where the onset of conduction occurs at 280 kV/cm (negative) and 470 kV/cm (positive). Above the onset electric field, more injected electrons participate in the conduction and a Schottky conduction mechanism appears with the slope of linear fitting of ln(J) vs $E^{0.5}$ of 0.197 (negative) and 0.202 (positive). The correspondingly derived K values are 6.71 (negative) and 6.38 (positive), which agree well with the expected K value of 6.25 based on the refractive index as described above. Thus, a Schottky emission conduction mechanism dominates this electric field region. For negative bias, the conduction mechanism changes to bulk-limited SCLC when the electric field increases above 1065 kV/cm. In contrast, for positive bias, it remains a Schottky emission conduction mechanism until the higher electric field region (~ 1435 kV/cm).

The change in conduction mechanism from Schottky to SCLC at a higher electric field can be attributed to impaired interface-limited effects. Upon increase of the applied voltage, a larger number of injected charge carriers from the electrode are captured by the holes at the interface, weakening interface-limited effects and inducing bulk-limited SCLC mechanism. The increase of the initial electric field for SCLC (E_2) at positive bias is due to the increased energy difference of the conduction band between BFO and LSMO. Upon increasing the electric field, the enhanced ferroelectric polarization assists hole depletion at the LSMO/BFO interface. Thus, a further downward bending is induced. In addition, as electrons are minority carriers in p-type LSMO bottom electrode, [217] this leads to relatively low injection efficiency from LSMO to BFO. Therefore, a higher electric field is needed to induce the conduction behavior transition from Schottky to the SCLC mechanism.

Here, in as-prepared 28% T'-phase BFO thin films (**Figure 5-9**), Schottky emission governs the I-V characteristic at the low electric field region, but the role is weakened at a higher electric field as the bulk-limited SCLC works afterwards. This is different from the most reported SCLC-predominant or PF emission-predominant conductive mechanism in R-phase BFO. [105, 194, 204, 216, 217]

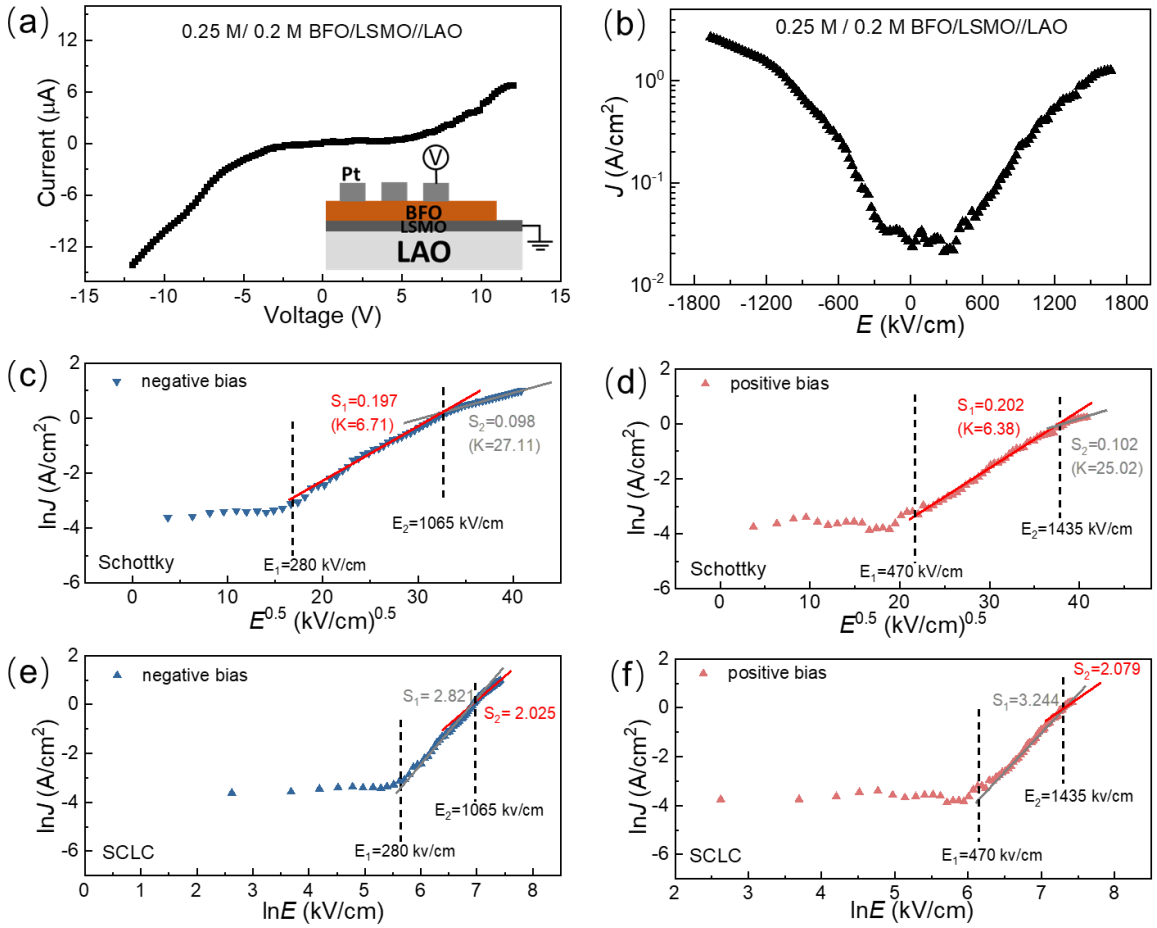

Electric field	Negative part	Positive part
Low field	Schottky	Schottky
High field	SCLC	Schottky

The relation between current density (J) and voltage (V) of these mechanisms is as follows:

Schottky emission: $J_s = AT^2 exp - \left[\frac{F}{k_B T} - \frac{1}{k_B T}\sqrt{\frac{q^3 V}{4\pi\varepsilon_0 K d}}\right]$ **Equation 5-1**

SCLC: $J_{SCLC} = \frac{9\mu\varepsilon_r\varepsilon_0 V^2}{8d^3}$ **Equation 5-2**

m - charge carrier mobility; e_r - relative dielectric permittivity; e_0 - permittivity of free space; V - applied voltage;

d - film thickness; A- Richardson constant; T - temperature; F - height of the Schottky barrier;

q - elementary charge; k_B - Boltzmann constant; K - optical dielectric constant;

Figure 5-9. (a) I-V curves, inset shows the sketch of the set-up for the I-V measurements; (b) corresponding semi-log J-E curves; fitting curves by (c)(d) the Schottky emission mechanism, and (e)(f) SCLC for negative (blue) and positive (wine) electric field, respectively, of 28% T'-phase BFO/LSMO//LAO thin film. Summary of leakage current mechanisms at different electric fields.

To further explore the T'-phase role on the effect of films' leakage conduction behavior, the corresponding leakage conduction mechanism of a reference pure R'-BFO film (BFO/LSMO//STO) (the X-ray diffraction (XRD) ϑ-2ϑ scan is plotted in **Figure 5-10**, and Only R'-phase BFO is detected) and a 10% T'-phase mixed-phase BFO/LSMO//LAO (annealing at 640 °C for 10 min sample) are fitted by SCLC mechanism in **Figure 5-11**. At both negative and positive bias, pure R'-BFO film shows an Ohmic conduction with the slope of linear fitting of ln(J) vs ln(E) of ~ 1 at a low electric field. With the increase of the electric field, the strong injection carriers filled up the traps and the SCLC mechanism starts to participate in the conduction, which leads to the slope value of ~ 1.5 lower than the slope (~ 2) of SCLC conduction. This is attributed to the taps-filled limit (TFL) SCLC. The BFO film with a lower T'-phase fraction (10%) also shows a similar conduction behavior that the slope value is ~1.6 in a high electric field. It is different from the optimal high T'-phase BFO film with a T'-BFO fraction of 28%.

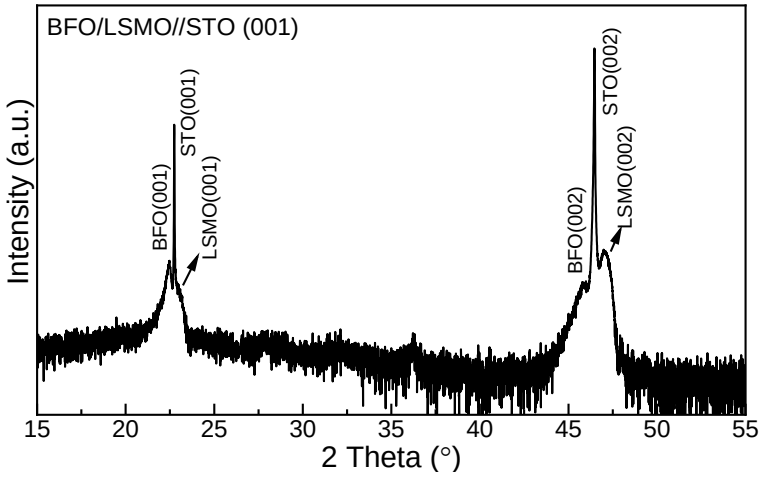

Figure 5-10. X-ray ϑ-2ϑ diffraction patterns of BFO/LSMO//STO (001) films.

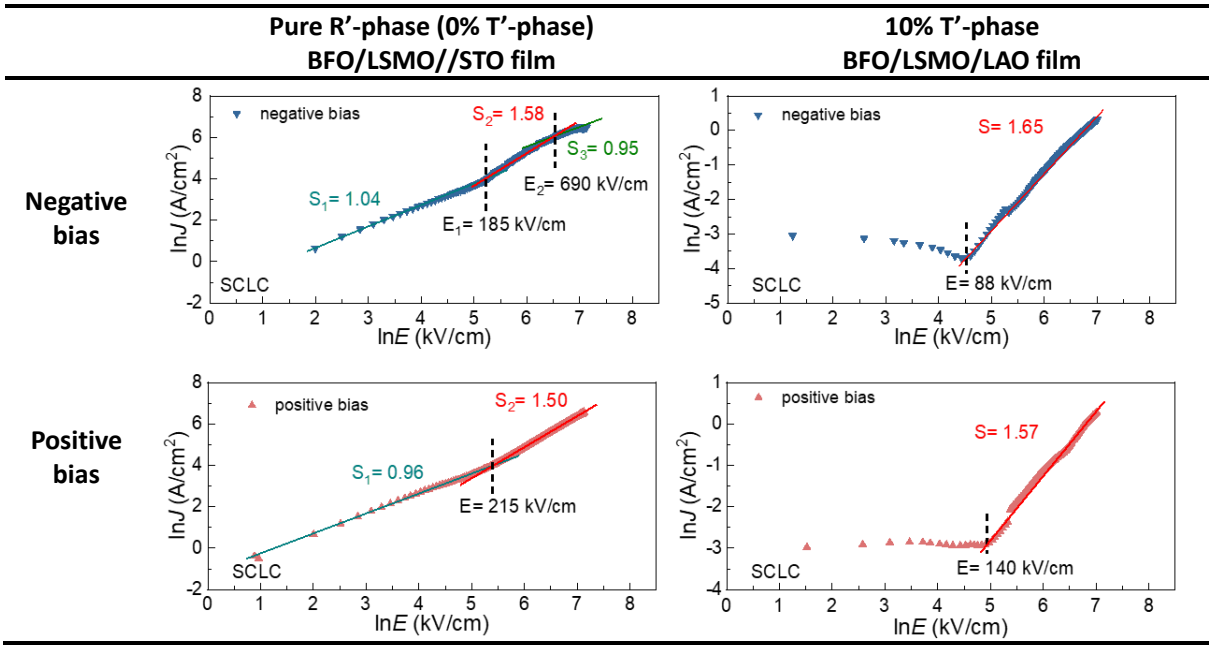

Figure 5-11. Fitting curves of J–E data to Ohmic/SCLC at negative (blue) and positive (wine) electric field, respectively, of pure R' BFO/LSMO//STO and 10% T'-phase BFO/LSMO//LAO thin film with heating at 640 °C for 10 min.

The I-V mechanisms of these three films (0% T'-phase, 10% T'-phase and 28% T'-phase BFO thin films) at different electric fields are summarized in **Table 5-2**. The leakage behavior shows a conduction mechanism transition from a bulk-limited (Ohmic or SCLC) to an interface-limited (Schottky) conduction with the increase of T'-phase fraction. This may be attributed to the Schottky barrier height increase with the increasing T'-phase fraction in mixed-phase BFO films, where an enlarged band gap is induced due to this strained T'-phase structure. [173, 218] This could be also related to the oxygen octahedral tilt and, further, the variation of the bond angle and orbital overlapping from this strained nonequilibrium T'-BFO. Besides, strain gradients at the R'-T' phase boundaries can also redistribute the nonequilibrium carriers excited by external stimuli, such as the photon. [219] As a result, the charge carriers transport behavior in strained BFO film can be different from the relaxed counterpart. Thus, the barrier height and the charge carriers' mobility behavior in T'-BFO at the interface are different from those in the R'-phase when applying an external electric field.

Table 5-2. Summary of Leakage Current Mechanisms at Different Electric Fields of Three BFO Thin Films.

Electric field		0% T'-phase BFO/LSMO//STO	10% T'-phase BFO/LSMO//LAO_10 min	28% T'-phase BFO/LSMO//LAO_30 min
Negative bias	Low field	Ohmic	-	Schottky
	High field	SCLC	SCLC	SCLC
Positive bias	Low field	Ohmic	-	Schottky
	High field	SCLC	SCLC	Schottky

5.4 Summary

In this chapter, the domain switching and leakage current behavior of mixed-phase BFO films with different T'-phase fractions has been investigated.

(1) The domains of all mixed-phase films are successfully switched under the externally applied voltage.

(2) The optimized film with the T'-phase fraction of ~ 28% shows the best leakage characteristic with the maximum leakage current of 0.1 A/cm up to field strengths of 500 kV/cm. The film also displays a polarization-orientation dependent conduction with poled-up (polarization pointing away from the lower electrode) domains showing higher conductivity.

(3) Compared to the bulk-limited Ohmic or SCLC-predominant conductive mechanism in pure R'-phase and 10% T'-phase BFO thin films, mixed-phase films with a high T'-phase fraction of 28% show an interface-limited Schottky emission to bulk-limited SCLC mechanism predominates leakage current transition with the electric field increase.

These findings suggest that chemical solution deposition (CSD) can provide a flexible way to fabricate BFO films with tailored phase composition and hence engineered electrical properties.

Chapter 6. Precursor Gelation Chemistry, Phase Structure and Ferroelectricity of Chemical Solution Deposition-Derived Sm-Doped Bismuth Ferrite Thin Films: The Role of Sm

This chapter reveals the precursor gelation chemistry and crystallization behavior, as well as the phase structure and the electrical performance transition of the Sm substituted $BiFeO_3$ (BFO) films. It lays a foundation for the understanding of the complex phase composition for the subsequent chapters, where both the strain and site engineering are utilized to prepare BFO films.

6.1 Introduction

Chemical substitution is a common way to induce the morphotropic phase boundary (MPB) in perovskite systems. It has been widely used to tailor films phase compositions [38, 40] and modify their electrical properties [100, 205, 220]. Unlike the "strain-induced MPB" mentioned in the previous chapter, where the rhombohedral-like (R') and tetragonal-like (T') phases coexist, rare earth (RE, such as La, Sm, and Dy) substituted BFO thin films can generate an intriguingly structural transformation from a ferroelectric rhombohedral (R) to paraelectric orthorhombic (O) phase with the doping amount variation. [8, 192]

Chemical solution deposition (CSD), as a feasible and cost-efficient deposition method, has attracted significant interest from an industrial perspective. It includes four steps: (1) precursor preparation, (2) precursor deposition on selected substrates, (3) low-temperature gelation, and (4) high-temperature pyrolysis and sintering. [115] CSD makes the in-situ monitoring of each step possible. This provides an opportunity to investigate and understand the effects of the RE element doping on both the molecular network during the gelation process and phase structure evolution during the crystallization process. In addition, the CSD can offer accurate control of the precursor composition, and thus realize fine-tuned structure and functional properties of the ultimate films. To date, most efforts on CSD-derived doped films are devoted to improving their leakage issue or modifying the multiferroic properties, while what happens during the gelation process is rarely given the attention it deserves.

This chapter first reports the influence of the rare earth Sm dopant on the gelation chemistry of BFO precursors. The polymeric functional groups of the starting precursors are

investigated by Fourier transformation infrared spectroscopy (FTIR) technique. The FTIR patterns of 0.25 M $Bi_{1-x}Sm_xFeO_3$ (BSFO, *x* is the doping ratio of Sm) precursors with *x* = 0, 0.05, 0.10, 0.14, 0.16, 0.18, and 0.22 are acquired to investigate the role of Sm composition. The FTIR analysis of raw chemicals (2-MOE, acetic anhydride, metal nitrates), the mixture of 2-MOE and acetic anhydride, and metal nitrate precursors are collected as references. To investigate the gelation chemistry of the Sm-doped BFO, around 0.1 ml precursor (BSFO solution with *x* = 0.14) is dropped onto a glass substrate. A uniformly coated layer is realized by inclining the substrate to a certain degree. After heating at 90 ℃ for a set time, a series of FTIR patterns are collected. Then in-situ high-temperature X-ray diffraction (XRD) is performed on the $Bi_{0.9}Sm_{0.10}FeO_3$/LSMO//STO (001) (LSMO: $La_{0.67}Sr_{0.33}MnO_3$, STO: $SrTiO_3$) to investigate the phase formation and development with the rising and cooling temperature. Consequently, crystallized BSFO films with *x* = 0, 0.05, 0.10, 0.14, and 0.15 are prepared. The phase structure and domain structure, as well as ferroelectric properties and leakage behaviors evolution as a function of Sm substitution, are investigated.

6.2 Experimental Procedure

Stoichiometric precursor solutions of BSFO (*x* =0, 0.05, 0.10, 0.14, 0.16, 0.18 and 0.22) were prepared to study the influence of the A-site Sm substitution on the gelation process. The recipe of the precursors is shown in **Table 6-1**. BSFO precursors were made by dissolving $Bi(NO_3)_3{\cdot}5H_2O$, $Sm(NO_3)_3{\cdot}6H_2O$, and $Fe(NO_3)_3{\cdot}9H_2O$ in 2-MOE and acetic anhydride organic solvents. In addition, as shown in **Table 6-2**, a set of solutions (i.e., without any metal nitrate, or with a single metal nitrate) were also investigated to serve as a reference.

Table 6-1. Composition of 0.25 M BSFO precursor solutions with different Sm content

$Bi_{1-x}Sm_xFeO_3$	$Bi(NO_3)_3{\cdot}5H_2O$	$Sm(NO_3)_3{\cdot}6H_2O$	$Fe(NO_3)_3{\cdot}9H_2O$	2-MOE	Acetic anhydride
***x* = 0**	0.00375 mol	-	0.00375 mol	10 ml	5 ml
***x* = 0.05**	0.00356 mol	0.00019 mol	0.00375 mol	10 ml	5 ml
***x* = 0.10**	0.00338 mol	0.00038 mol	0.00375 mol	10 ml	5 ml
***x* = 0.14**	0.00323 mol	0.00053 mol	0.00375 mol	10 ml	5 ml
***x* = 0.16**	0.00315 mol	0.00060 mol	0.00375 mol	10 ml	5 ml
***x* = 0.18**	0.00308 mol	0.00068 mol	0.00375 mol	10 ml	5 ml
***x* = 0.22**	0.00292 mol	0.00083 mol	0.00375 mol	10 ml	5 ml

Table 6-2. Composition of mixture solutions of 2-MOE and acetic anhydride, bismuth nitrate, samarium nitrate, iron nitrate, and formed $Bi_{0.86}Sm_{0.14}FeO_3$ precursors.

	$Bi(NO_3)_3 \cdot 5H_2O$	$Sm(NO_3)_3 \cdot 6H_2O$	$Fe(NO_3)_3 \cdot 9H_2O$	2-MOE	Acetic anhydride
Mixture solution	-	-	-	10 ml	5 ml
$Bi(NO_3)_3$ precursor	0.00323 mol	-	-	10 ml	5 ml
$Sm(NO_3)_3$ precursor	-	0.00053 mol	-	10 ml	5 ml
$Fe(NO_3)_3$ precursor	-	-	0.00375 mol	10 ml	5 ml
$Bi_{0.86}Sm_{0.14}FeO_3$ precursor	0.00323 mol	0.00053 mol	0.00375 mol	10 ml	5 ml

BSFO precursors with x = 0, 0.05, 0.10, 0.14, and 0.15 were deposited on STO (001) substrate with a 20 nm thick LSMO bottom electrode. BSFO solution was dropped and spin-coated on a cleaned and preheated STO substrate. The consequent gelation, heat treatment processes (pyrolysis and crystallization), and the quenching cooling process are similar with the fabrication process of the previous BFO/LSMO//LAO films in **Chapter 4** and **Chapter 5**. The whole deposition and heat treatment process was repeated twice to achieve the desired thickness (~ 80 nm).

6.3 Results and Discussion

6.3.1 Gelation Chemistry

6.3.1.1 FTIR Analysis of BSFO Precursors as a Function of Sm Doping

Figure 6-1(a) shows the molecular structure of the BSFO precursors as a function of the Sm doping ratio. There is no detectable influence on the peak position with the increasing Sm ratio. Nevertheless, at the wavenumber ranging from 1800 to 1660 cm^{-1} (as denoted by the red rectangle box in **Figure 6-1(a)**), a variation of the peak intensities at 1737 cm^{-1} (C=O stretch bond in ester RCOOR', noted as I_1) and 1724 cm^{-1} (C=O stretch bond in acetic acid CH_3COOH, noted as I_2) can be observed. To have a clear view of these two peaks alternations, an enlarged image is shown in **Figure 6-1(b)**. The ratio of the two peaks remains nearly instant at ~ 1.02 ($\pm$ 0.01) with the Sm composition reaching up to 0.10. When the Sm amount is increased to 0.14 and 0.16, the peak intensity ratio goes up from ~ 1.022 to ~ 1.026. When Sm reaches x = 0.18 and 0.22, the peak intensity ratio returns to ~ 1.019 and ~ 1.000, respectively. The peak intensity and the corresponding intensity ratio are listed in **Table 6-3**. A further close-up inspection of the peak intensity and the plot of the intensity ratio of I_1/I_2 as a function of Sm

composition is shown in the inserted images **in Figure 6-1 (b)**. The change of the intensity ratio indicates that the Sm introduction has an influence on the competition reactions between the reactions: formation of ester and acetic acid, and thus the gelation chemistry behavior. This may lead to the different phase structure and electrical properties of the ultimate films.

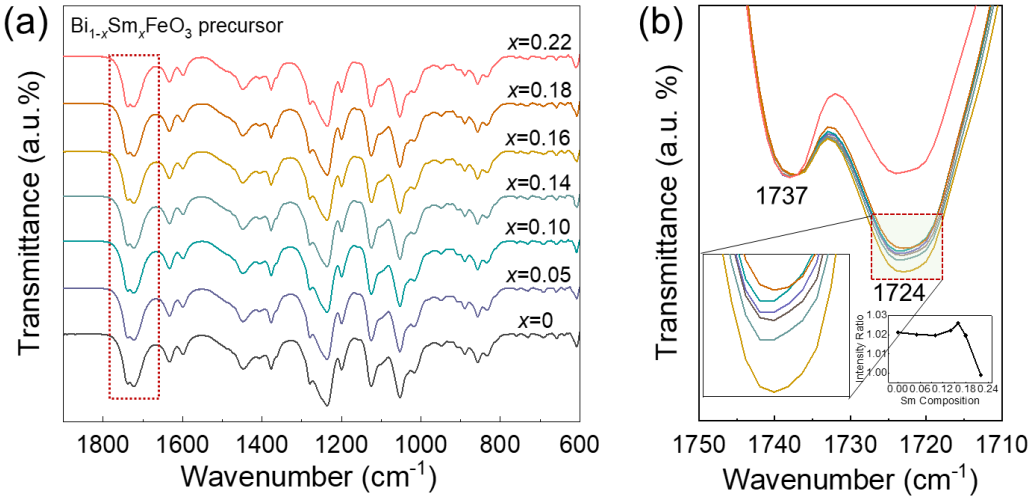

Figure 6-1. (a) FTIR spectra of BSFO (*x* = 0, 0.05, 0.10, 0.14, 0.16, 0.18, and 0.22) precursors as a function of Sm doping content at room temperature, and (b) close-up inspection of FTIR spectra with the wavenumber ranging from 1664 to 1800 cm^{-1}. The inserted images are an enlarged view of the peaks at 1724 cm^{-1} (left) and the plot of intensity ratio variation as a function of Sm composition (right).

Table 6-3. Intensity ratio of FTIR analysis with the peak position at 1737 and 1724 cm^{-1}.

$Bi_{1-x}Sm_xFeO_3$	*x* = 0	*x* = 0.05	*x* = 0.10	*x* = 0.14	*x* = 0.16	*x* = 0.18	*x* = 0.22
I_1 (λ_1=1737 cm^{-1})	60.52	60.34	60.77	60.36	59.85	59.89	60.42
I_2 (λ_2=1724 cm^{-1})	59.27	59.11	59.58	59.03	58.35	58.76	60.44
Intensity ratio (I_1/I_2)	1.021	1.020	1.020	1.022	1.026	1.019	1.000

*1737 cm^{-1} => C=O stretch bond in ester (RCOOR'); 1724 cm^{-1} => C=O stretch bond in acetic acid (CH_3COOH)

6.3.1.2 FTIR Analysis of Organic Solvents

To understand the underlying reaction mechanism during the precursor preparation process, FTIR patterns of 2-MOE, acetic anhydride, and the mixture of 2-MOE and acetic anhydride solvents are carried out, as shown in **Figure 6-2(a)**. It shows that the FTIR pattern of a mixed 2-MOE and acetic anhydride solvent is a simple superposition of these two individual chemicals, and no additional absorption peak is formed. In the 1650 to 1900 cm^{-1} wavelength range, only the intensity of two absorption peaks (C=O stretch bond in acetic anhydride) decreases (**Figure 6-2(b)**). It indicates that there is no chemical reaction, or the reaction is quite slow at room temperature within the organic solvent.

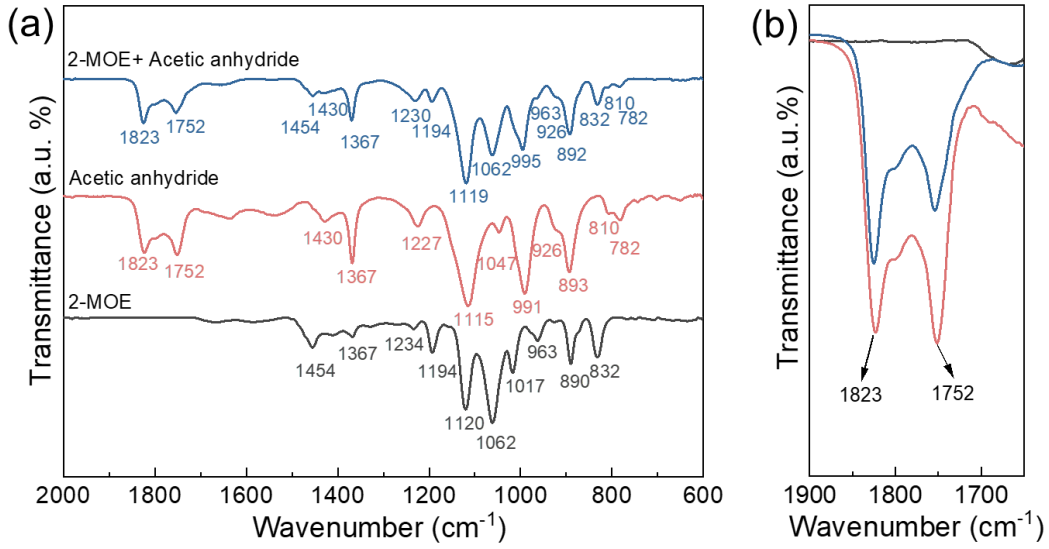

Figure 6-2. (a) FTIR analysis of 2-MOE, acetic anhydride, and mixture of 2-MOE and acetic anhydride solutions at room temperature, (b) close-up inspection of FTIR spectra with the wavenumber ranging from 1650 to 1900 cm^{-1}.

6.3.1.3 FTIR Analysis of Individual Metal Nitrate

Next, the FTIR patterns of raw metal nitrate chemicals (i.e., bismuth nitrate pentahydrate, samarium nitrate hexahydrate, and iron nitrate nonahydrate) are collected as the references, as shown in **Figure 6-3**. The characteristic peaks attributed to water of crystallization are located in the range from 1670 to 1600 cm^{-1}. The peaks assigned to the vibration of NO^{3-} are listed in **Table 6-4**.

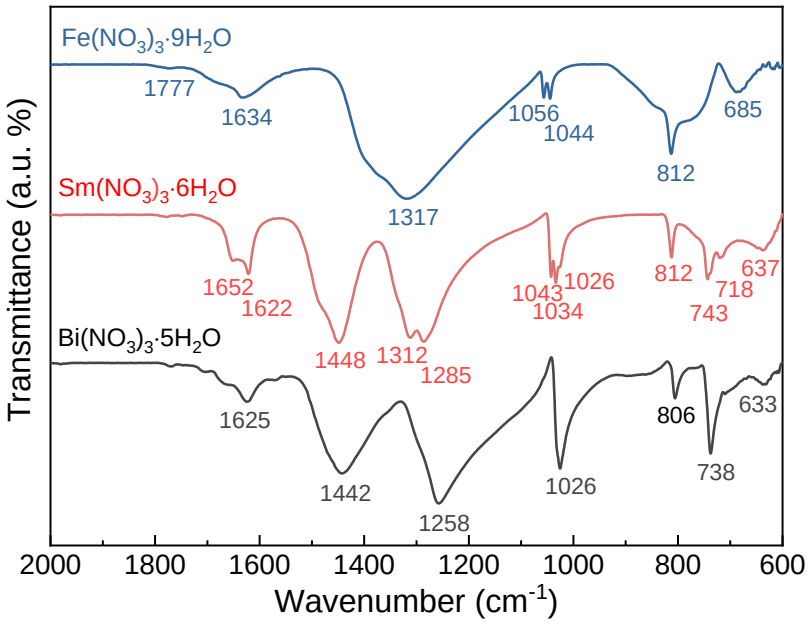

Figure 6-3. FTIR analysis of bismuth nitrate pentahydrate, samarium nitrate hexahydrate, and iron nitrate nonahydrate at room temperature.

Table 6-4. Summary of FTIR patterns of raw metal nitrate chemicals.

Functional groups	Water of crystallization	NO^{3-}
Wavenumber (cm^{-1})	1670 - 1600	1810 - 1730 (weak and sharp), 1450 - 1300 (strong and board), 1060 - 1020 (weak and sharp), 850 - 800 (sharp), and 770 - 715 (weak)

6.3.1.4 FTIR Analysis of Single Meta Nitrate and BSFO (with *x* = 0.14) Precursors

Then we focus on the gelation of BSFO (*x* = 0.14) precursor and compare its FTIR spectra with single metal nitrates precursors (i.e., a mixture of bismuth nitrate/samarium nitrate/iron nitrate with 2-MOE and acetic anhydride). The composition of every applied precursor is listed in **Table 6-2** and the corresponding functional groups in FTIR patterns are summarized in **Table 6-5**.

As shown in **Figure 6-4(a)**, the FTIR spectrum of $Bi_{0.86}Sm_{0.14}FeO_3$ precursor is a superposition of the spectra of bismuth nitrate, samarium nitrate, iron nitrate precursors. Compared to the FTIR spectrum of the mixture of the 2-MOE and acetic anhydride, bismuth nitrate and iron nitrate precursors display obvious change at the 1900 to 1550 cm^{-1} wavelength range as shown in **Figure 6-4(b)**. This can be attributed to the below reactions:

(1) Esterification in bismuth nitrate and iron nitrate precursors

The peaks at 1823 and 1752 cm^{-1} (corresponding to the C=O stretch bond in the $(CH_3CO)_2O$ structure in the mixture of 2-MOE and acetic anhydride solution) disappear. The new peaks at 1742 cm^{-1} (corresponding to the C=O stretch bond in ester RCOOR') and at 1721 cm^{-1} (corresponding to the C=O stretch bond in acetic acid CH_3COOH) are formed. The derived intensity ratio of these two peaks is less than 1 due to the introduction of sufficient $Bi(NO_3)_3{\cdot}5H_2O$ and $Fe(NO_3){\cdot}9H_2O$. These reactions have been summarized in **Equation 6-1** and **Equation 6-2**. The reaction between acetic anhydride and the water of crystallization (**Equation 6-1**) releases appreciable heat, which can promote the esterification reaction between 2-MOE and the formed CH_3COOH (**Equation 6-2**).

(2) Esterification in samarium nitrate precursors

Meanwhile, peaks in the range of 1670-1600 cm^{-1} (corresponding to the water of crystallization in the metal nitrates) are still detectable. When adding a small amount of $Sm(NO_3)_3{\cdot}6H_2O$ (14%), the intensity of the peak at 1823 cm^{-1} decreases and the peak at 1752 cm^{-1} disappears, with new peaks emerging at 1740 and 1725 cm^{-1}. The remaining peak at 1826

cm^{-1} is because of the exhaustion of water of crystallization from the samarium nitrate, which leads to the incomplete reaction among H_2O, acetic anhydride, and 2-MOE. The undetectable characteristic absorption peak of water of crystallization further confirms it.

In addition, we notice that the intensity ratio between newly formed 1740 and 1725 cm^{-1} is greater than 1 when adding samarium nitrate, which is different from bismuth and iron nitrate precursors. It confirms that different metal cations show a reaction selectivity to promote hydrolysis reaction or esterification reaction. This may be related to the electronegativity difference among them, where Sm has the lower electronegativity of 1.17 and Bi and Fe shows the closer electronegativity of 2.02 and 1.83, respectively. A higher electronegativity of the metallic ion is responsible for a higher yield of ester. [221]

(3) Esterification in $Bi_{0.86}Sm_{0.14}FeO_3$ precursor

The introduction of the electronegativity of the metallic ion into the molecular networks can lead to a shift of the peaks to the higher frequency, shown as the closer inspection with the ranging from 1150 to 1350 cm^{-1} in **Figure 6-4(c)**. The peaks attributed to CH_2 wagging vibration and C-O stretch bond in generic R-O-R' shift from 1230 to 1235 cm^{-1} and from 1194 to 1199 cm^{-1}, respectively. Here, a reaction shown as **Equation 6-3** may occur, that metal coordination complex is possibly formed due to the metal nitrates reacting with the 2-MOE and the formed acetic anhydride.

$(CH_3CO)_2O+H_2O \leftrightarrow 2CH_3COOH$ ($\Delta H<0$ exothermic reaction) **Equation 6-1**

$CH_3OCH_2CH_2OH+CH_3COOH \leftrightarrow CH_3OCH_2CH_2OOCCH_3+H_2O$ **Equation 6-2**

$M(NO_3)_3+xCH_3OCH_2CH_2OH+(3-x)CH_3COOH \leftrightarrow M(OCH_2CH_2OCH_3)_x(OOCCH_3)_{3-x}+3HNO_3$
(where $x \leq 3$, M = Bi^{3+}, Sm^{3+}, or Fe^{3+}) **Equation 6-3**

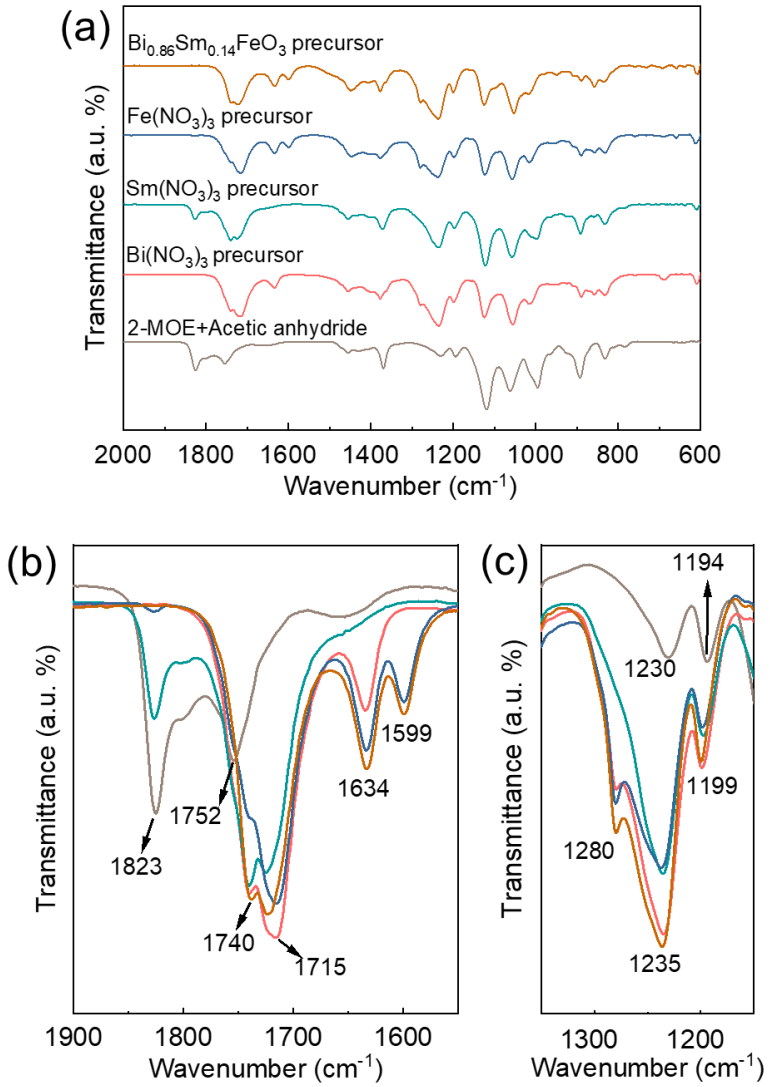

Figure 6-4. (a) FTIR analysis of mixture of 2-MOE and acetic anhydride, after adding metal nitrate in the mixture of 2-MOE and acetic anhydride solutions, and $Bi_{0.86}Sm_{0.14}FeO_3$ precursor at room temperature, and the close-up inspection with the wavenumber ranging from (b) 1550 to 1900 cm^{-1} and (c) 1150 to 1350 cm^{-1}.

Table 6-5. Summary of FTIR patterns of the mixture of 2-MOE and acetic anhydride, after adding metal nitrate in mixture of 2-MOE and acetic anhydride solutions, and $Bi_{0.86}Sm_{0.14}FeO_3$ precursor.

Functional groups	Wavenumber (cm^{-1})
C=O stretch bond in $(CH_3CO)_2O$	1823
C=O stretch bond in $(CH_3CO)_2O$	1752
C=O stretch bond in ester (RCOOR')	1740
C=O stretch bond in acetic acid (CH_3COOH)	1715
H_2O	1634
H_2O	1599
CH_2 twisted vibration	1280
CH_2 wagging vibration	1235/1230
C-O stretch bond in generic R-O-R'	1199/1194

6.3.1.5 Temperature-Dependent FTIR Analysis of BSFO (with *x* = 0.14) Precursor

Next, we investigate the $Bi_{0.86}Sm_{0.14}FeO_3$ precursor chemistry during heating at 90 ℃. As shown in **Figure 6-5(a)**, a noticeable change in the FTIR spectrum is observed after 120 s. In particular, a minor change is observed in the 1640 -1800 cm^{-1} range (**Figure 6-5(b)**) with the increasing heating time before gelation. It shows a gradual increase in the ratio of peaks intensity between the wavenumber at 1740 cm^{-1} (C=O stretch bond in ester (RCOOR')) and 1722 cm^{-1} (C=O stretch bond in acetic acid (CH_3COOH)). It indicates that a higher temperature can promote the esterification reaction. When the gelation occurs, a clear change in the FTIR patterns shape is shown. A sharp decrease of the intensity and change of the intensity ratio of these two peaks appear and the peaks positions shift to the lower value. Another closer inspection with the range of 950-1200 cm^{-1} displays the similar behavior with the peaks at 1099 cm^{-1} (corresponding to the C-O bond in -**C**H_2-**O**-M), 1053 cm^{-1} (corresponding to the C-O stretch bond in CH_2-**C**H_2-**O**H), and 1017 cm^{-1} (corresponding to the C-O stretch bond in general) shifted to lower value with the increasing time at 90 ℃ before gelation. An exception is that the peak at 1124 cm^{-1} (C-O stretch bond in a generic R-O-R') shows an opposite shift to a higher value. After the gelation with the heating time of 120 s, the FTIR patterns show an obvious decrease in the intensity of peaks at 1125 and 1048 cm^{-1} and an increase in the intensity of the peak at 1011 cm^{-1}. The slight shift of these peaks before gelation is possible due to the further reaction between metal nitrates, 2-MOE, and acetic acid (**Equation 6-3**) at the high temperature, where the formed HNO_3 can be removed and thus promote the reaction forward. The obvious change of the FTIR patterns after gelation indicates the following primary condensation reaction, as shown in **Equation 6-4**.

$$n[M(OCH_2CH_2OCH_3)_x(OOCCH_3)_y] \rightarrow$$
$$(CH_3OCH_2CH_2O)_xCH_3COO)_{y-1}M[OM(CH_3COO)_{n-2}OM(OCH_2CH_2OCH_3)_{x-1}(OOCCH_3)_y +$$
$$n\text{-}1\left[CH_3COOCH_2CH_2OCH_3\right] \quad (\text{where } x + y \leq 3,\ M = Bi^{3+},\ Sm^{3+},\ \text{or } Fe^{3+}) \qquad \textbf{Equation 6-4}$$

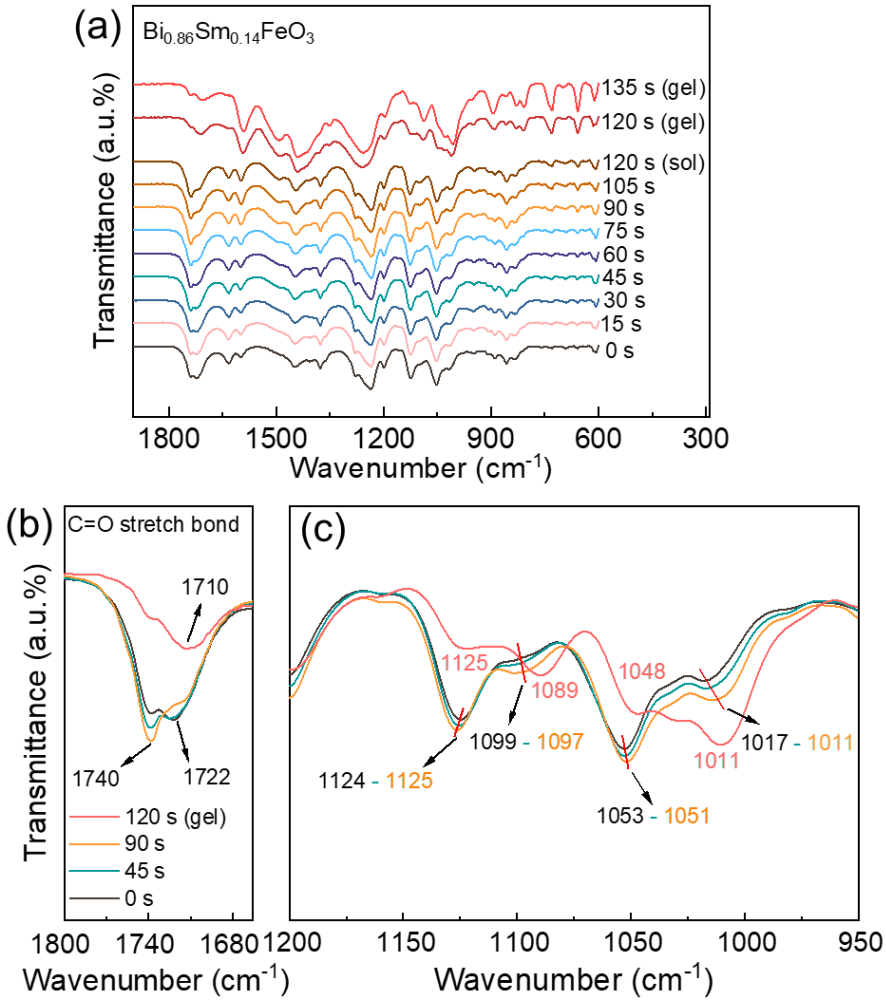

Figure 6-5. FTIR analysis of (a) the gelation process of $Bi_{0.86}Sm_{0.14}FeO_3$ precursor with heating at 90 ℃ for different time, and the close-up inspection with the wavenumber ranging from (b) 1660 to 1800 cm^{-1}, and (c) 950 to 1200 cm^{-1}.

In the subsequent pyrolysis (~ 450 ℃) and crystallization (~ 640 ℃) processes, the organic substances will be decomposed and removed. The residual material consists of a molecular skeleton formed by -M-O- bonds. These -M-O- networks are converted to the desired perovskite BSFO structure at a proper high-temperature sintering step.

6.3.2 Structure and Ferroelectricity of Crystallized Films

6.3.2.1 Temperature-Dependent Phase Development of BSFO (*x* = 0.10) Film

Temperature-dependent in-situ XRD diffractions of $Bi_{0.90}Sm_{0.10}FeO_3$ are first collected to understand the BSFO phase evolution during the crystallization process. The 0.25 M BSFO with *x* = 0.10 precursor is spin-coated on the bare STO substrate. This as-prepared sample is heated from room temperature to 750 ℃ at a heating rate of 30 ℃·min^{-1} and subsequently cooled

down to room temperature at a cooling rate of 60 ℃·min^{-1}. XRD patterns are collected at various temperatures as shown in **Figure 6-7(a)**. At each acquired temperature, 2 min interval is kept for temperature stabilization. The (001) peak intensities and out-of-plane (OP) lattice parameters of R'-BSFO and STO substrate as a function of temperature are plotted in **Figure 6-7(b) and (c)**. When the temperature is below 450 ℃, no R'-BSFO phase is detected. Upon heating to 500 ℃, a weak R'-BSFO starts to appear. With the increasing temperature, the peak intensity of R'-BSFO gradually increases due to the sustaining crystallization. During cooling, the peak intensity keeps relatively stable. The peak intensity of STO, as a reference, remains unchanged during the whole process of the temperature variation, which further confirms that the peak intensity change of R'-BSFO is from the temperature-induced crystallization behavior. Due to thermal expansion, the OP lattice parameter of STO shows a slightly increasing during the heating process and goes down back to 3.905 Å when cooling down to room temperature. For R'-BSFO, its OP lattice parameter shows an increase from 500 ℃ to 600 ℃ and remains relatively stable at 3.964 Å with heating up to 750 ℃. Upon cooling, it shows a sharp increase from 700 ℃ to 450 ℃ and then decreases to ~ 3.973 Å at room temperature. This abnormal increase during the cooling process may be attributed to the compressive strain released by the obvious lattice contraction of the STO from 700 ℃ to 450 ℃. When continuing to cool down, a slight relaxation occurs that leads to a slight decrease of the R'-BSFO lattice.

Based on the above in-situ temperature-dependent XRD results, we find that the temperature for pyrolysis cannot be beyond 450 ℃. Otherwise, a nucleation of the R'-phase BSFO will appear. It also indicates that a temperature higher than 500 ℃ is needed for the crystallization.

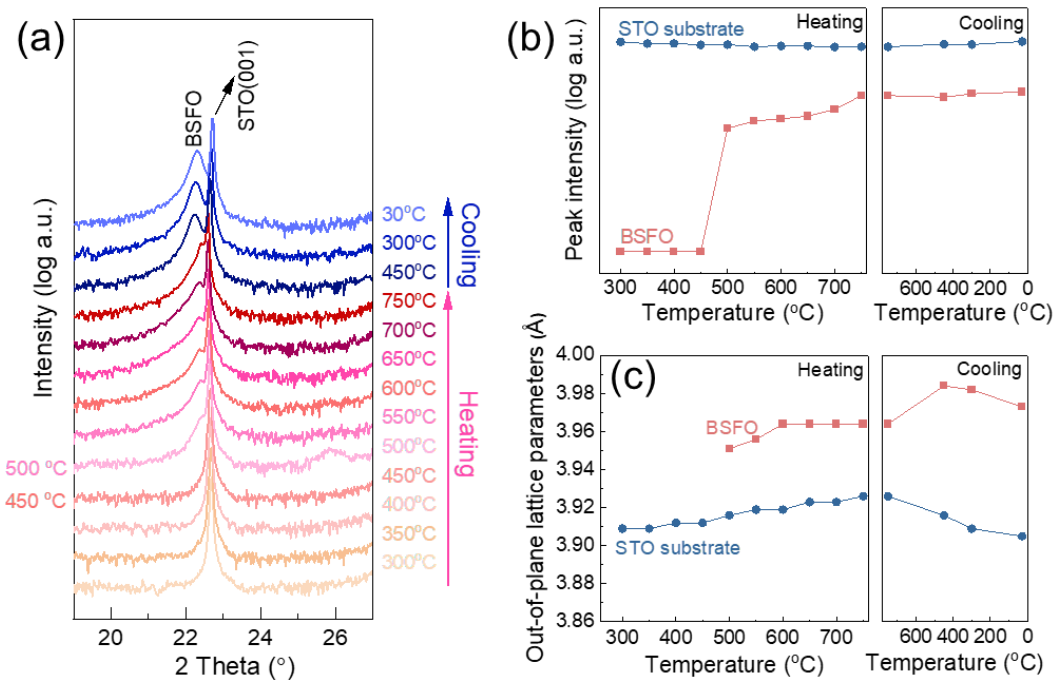

Figure 6-6. (a) XRD ϑ–2ϑ scans around the (001) reflection of a $Bi_{0.9}Sm_{0.1}FeO_3$/LSMO//STO (001) film heated acquired at different temperatures from ambient to 750 ℃, followed by cooling to room temperature, and (b) (001) peak intensity and (c) the corresponding derived OP lattice parameters both of BSFO and STO as a function of the heating and cooling process.

6.3.2.2 Crystal Structure of BSFO (*x* = 0, 0.05, 0.10, 0.14 and 0.15) Films

BSFO (*x* = 0, 0.05, 0.10, 0.14, and 0.15) thin films are prepared on STO substrate with the 20 nm LSMO as the bottom electrode. The corresponding XRD ϑ–2ϑ scans are plotted in **Figure 6-7**. (001)-oriented R'-BFO (or BSFO) films are obtained for all compositions. In addition, insignificant amounts of (110) and (111)-oriented BFO and impurity phases of α-Bi_2O_3 and $Bi_2Fe_4O_9$ are detected. At *x* = 0, there are two weak peaks at 2θ= 25.9° and 29.5°, which are attributed to α-Bi_2O_3 and (111) BFO phases, respectively. When the Sm composition is increased to 0.05 and 0.10, the amount of α-Bi_2O_3 and (111) BFO phases slightly increases and the impurity phase of $Bi_2Fe_4O_9$ appears. With further increasing Sm to 0.14 and 0.15, (110) oriented BFO is formed. The formation of these undesirable phases may be caused by the A-site Sm introduction, which leads to the Bi^{3+} ion leftover. The smaller radius of Sm may disturb the pristine crystalline structure, resulting in the strain relaxation, and further form the (110)- and (111)- oriented BFO phases.

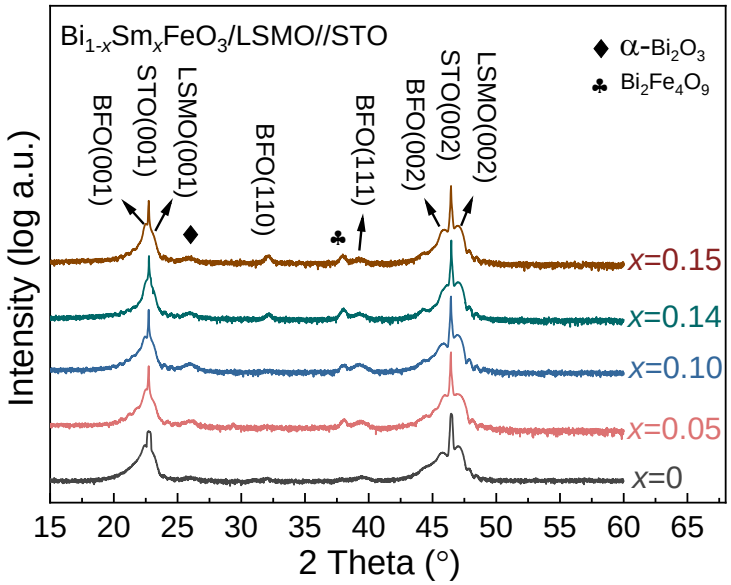

Figure 6-7. X-ray ϑ–2ϑ diffraction patterns of BSFO/LSMO//STO (001) with x = 0, 0.05, 0.10, 0.14 and 0.15.

Symmetrical 2D reciprocal space maps (RSMs) are collected to investigate the phase change of as-prepared BSFO films, as shown in **Figure 6-8(a)-(e)**. For all films, two fundamental peaks are observed with the center position of Q_z at 0.2565 1/nm and 0.5125 1/nm. The corresponding OP lattice parameters are 3.90 Å and 1.95 Å, respectively, which are attributed to the (001) and (002) peaks of the STO substrate. It is difficult to distinguish BSFO, STO, and LSMO phases in these 2D RSM mappings due to their similar lattice parameters. Thus, a close-up inspection of the RSM scan around the (002) reflection of BFO with x = 0 is taken, as shown in **Figure 6-8(ai)**. A clear peak split resulted from the (002) plane of BFO (Q_z= 0.5052 1/nm, d_{002}= 1.98 Å), STO (Q_z= 0.5125 /nm, d_{002}= 1.95 Å), and LSMO (Q_z= 0.5166 1/nm, d_{002}= 1.94 Å) is observed. The center position of Q_x= 0 of all these phases confirms a high quality of (001)-oriented growth of BSFO films. Another two peaks with Q_z= 0.2920 1/nm (d= 3.42 Å) and 0.4365 1/nm (d= 2.29 Å) are also detected, which correspond to the impurity phase of α-Bi_2O_3 and (111)-BFO, respectively. The streaky peaks observed in several BSFO films are the result of the polycrystal Pt/Ti top electrodes (50 nm/ 5nm thick), which are deposited for the purpose of electrical property characterizations.

In addition, extra diffraction ½ and/or ¼ spots (denoted by the green circle and red square boxes, respectively) appear for x = 0.10, 0.14 and 0.15 films. The ½ superstructure sports, corresponding to the ½ {010} reflection, arise from the unit cell doubling along the in-plane (IP) direction as compared to the R'-BFO lattice. [192] It has been reported that films

showing ½ {010} spots are (pseudo) orthorhombic structural phases with the dimension of the unit cell of $\sqrt{2}a_{pc} \times \sqrt{2}a_{pc} \times 2a_{pc}$ (a_{pc} is the lattice parameter of the pseudocubic perovskite). [15] The ¼ {011} spots are reported to result from the antiparallel cation displacements along the [011] direction due to the substitution. [8, 15, 220] With the further increase of Sm amount to *x* = 0.15, ¼ spots are getting weak and almost undetectable. Notice, we find that ½ spots are not observed at *x* = 0.14, we infer that it could be screened by the streaky line induced by the polycrystal Pt/Ti top electrodes, as mentioned above. Thus, the Sm doping induces a phase transition from ferroelectric R' to paraelectric O phases at the *x* = 0.10, which is lower than that of *x* = 0.14±0.015 reported in pulsed laser deposition (PLD)-derived BSFO films [7].

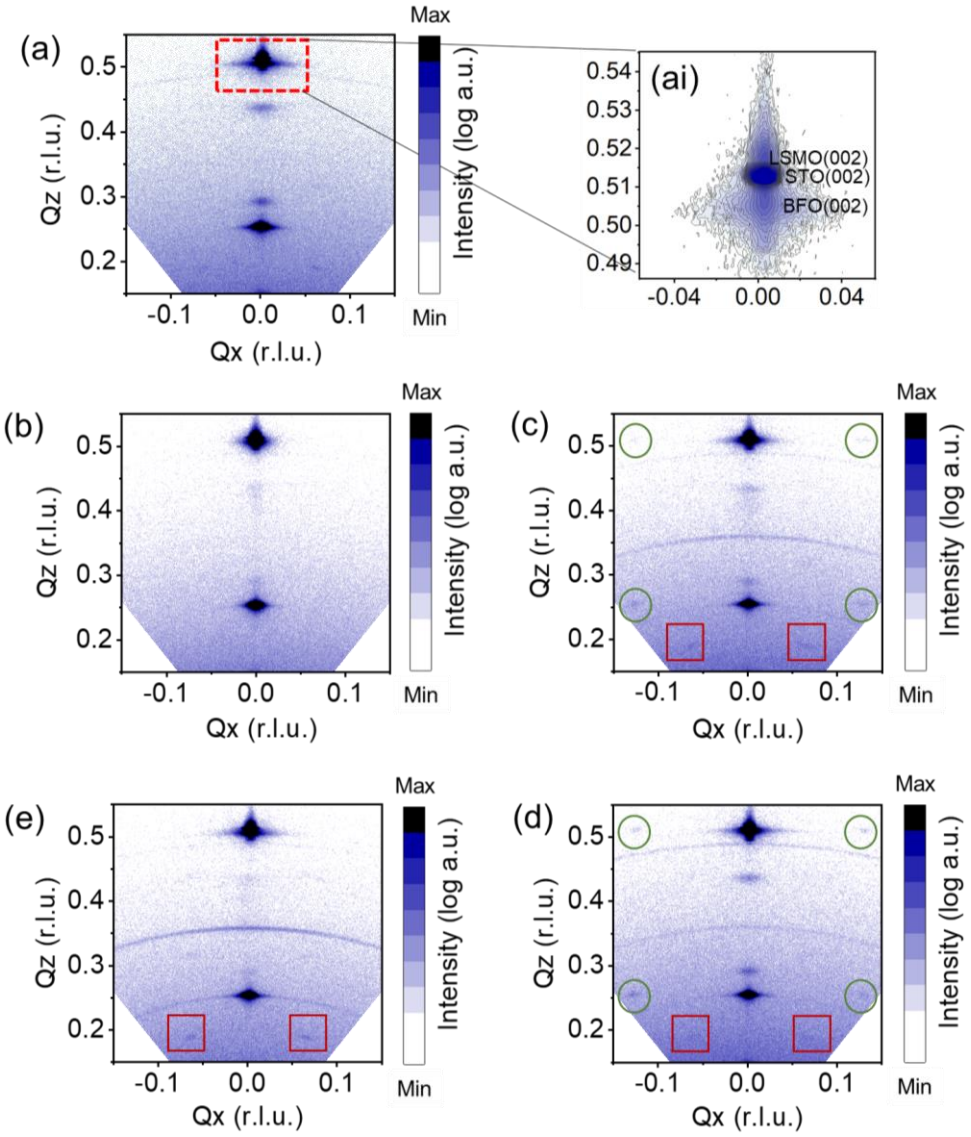

Figure 6-8. 2D RSMs of BSFO films with *x* = (a) 0, (b) 0.05, (c) 0.10, (d) 0.14, and (e) 0.15; (ai) the close-up inspection of the dash square of BFO (*x* = 0).

6.3.2.3 Domain Structure of BSFO (*x* = 0, 0.05, 0.10, 0.14 and 0.15) Films

The topography and domain structure evolution of BSFO films is investigated by piezoresponse force microscopy (PFM). The surface topography, as shown in **Figure 6-9 (a1) - (a5)**, displays a uniform distribution of round shape grains for all five compositions. The root-mean-square (RMS) roughness values are 2.318 nm, 0.760 nm, 2.040 nm, 2.100 nm, and 1.038 nm, respectively.

To elucidate the piezoelectric response and domain orientation, both the OP and IP amplitude and phase of all films are collected with the scanning area of 1 μm × 1 μm, as shown in **Figure 9 (b1-b5)-(e1-e5)**. There is no coupling between the domain structure and the surface topography. When the Sm doping amount is low (*x* = 0 and *x* = 0.05), both the OP and IP amplitude images show high magnitude with the maximum value of 500 (OP)/200 (IP) and 200 (both OP and IP) a.u., respectively. With the increase of Sm to *x* = 0.10, a relatively high amplitude is still attained (maximum magnitude of 80 (OP) and 140 (IP)). With the continuous increase of Sm composition to *x* = 0.14 and 0.15, the amplitude value decreases (lower than 100 for both OP and IP). The domain walls are transferred from clear lines to blurry ones with Sm doping. This decrease in the amplitude with the increasing Sm content can be attributed to the generated structure transition at *x* = 0.10, where the antiferroelectric and paraelectric phases form. Weak or lack of ferroelectricity of the formed antiferroelectric or paraelectric phases leads to smaller or zero piezoelectric response, and, thus, a reduced trend of amplitude from *x* = 0.10.

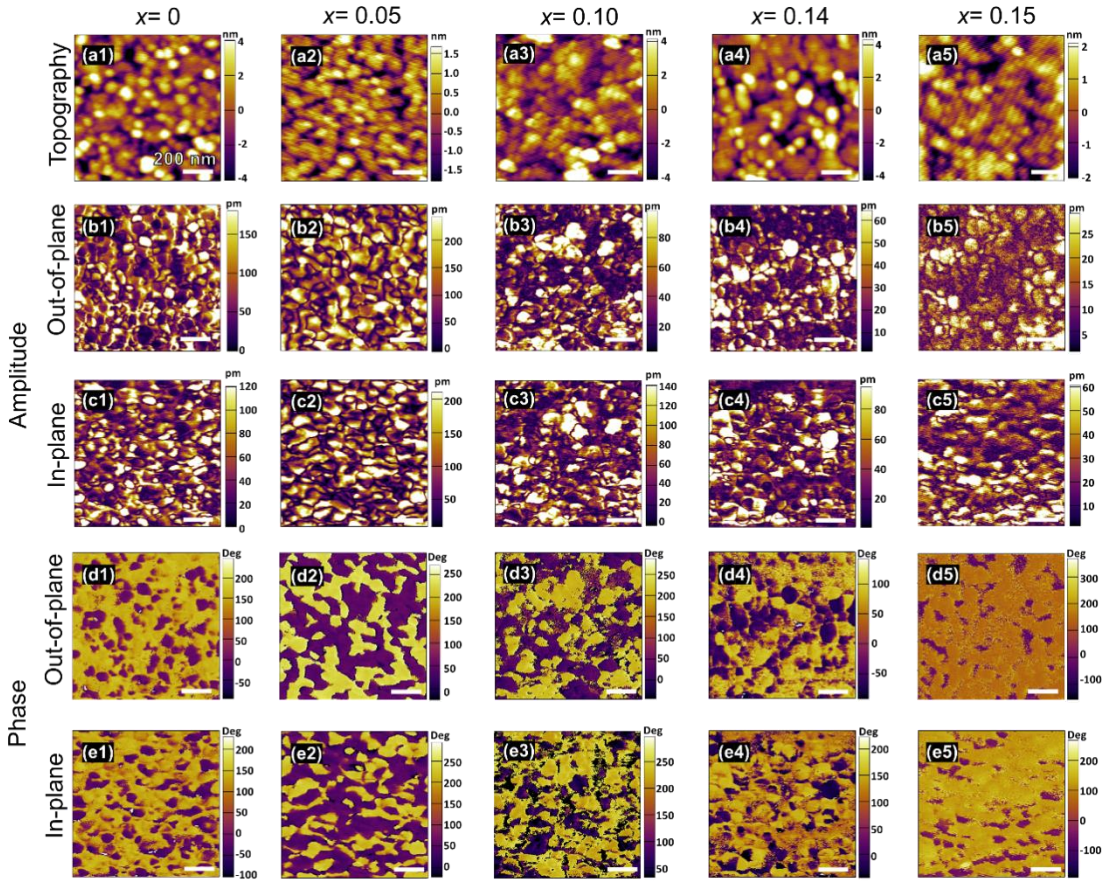

Figure 6-9. (a) Topography, (b) (c) PFM amplitude, (d) (e) phase (both OP and IP) images of BSFO films with *x* = 0, 0.05, 0.10, 0.14, and 0.15.

All the phase images exhibit obvious 180° contrast, as demonstrated through the two distinguished colors. The corresponding phase distribution images of both OP and IP domains are extracted by using the PFM software package and shown in **Figure 6-10 (a1-a5)-(b1-b5)**. The two peaks represent two polarization directions with 180° contrasts. The left/right peak represents the upward (outward)/downward (inward) polarizations (i.e., the purple regions/yellow regions) along OP (IP) directions. For the undoped BFO (*x* = 0) and low doped BSFO with *x* = 0.05, the upward (outward) and downward (inward) components of polarization vectors are equally distributed with close areas of two peaks. With the increase of Sm doping (*x* = 0.10 and 0.14), the downward (inward) component starts to predominate. When the Sm dopant increases to 0.15, the film almost shows a monodomain-like structure with a slight component of upward (outward) polarizations.

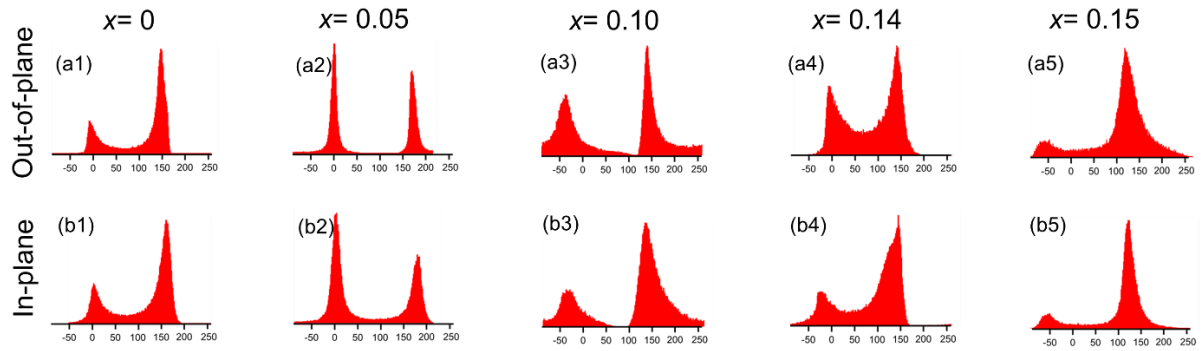

Figure 6-10. (a) OP and (b) IP phase distribution histograms (extracted from Figure 6-9 (d) and (e) phase images) of BSFO films with *x* = 0, 0.05, 0.10, 0.14, and 0.15.

The evolution of the domain structures is determined by the phase structure transition with the Sm doping. At *x*= 0 and 0.05, the ferroelectric R'-phase dominates. Thus, high piezoresponse is observed. The polarization of R'-phase points to <111> directions, which show equal components along both the OP and IP directions. With the increase of Sm doping to *x* = 0.10 and 0.14, the minority antiferroelectric phase with ¼ {011} spots and the paraelectric O phase with ½ {010} spots appear, which leads to the decrease of the PFM amplitude magnitude. When the Sm amount reaches 0.15, the increased paraelectric O phase results in a monodomain-like state.

6.3.2.4 Ferroelectricity Evolution of BSFO (*x* = 0, 0.05, 0.10, 0.14, and 0.15) Films

Polarization-electric field (P-E) hysteresis loops of BSFO (*x* = 0, 0.05, 0.10, 0.14, and 0.15) films are acquired to explore the ferroelectricity evolution with the Sm substitution. In the undoped BFO and low Sm-doped BSFO (*x* = 0.05 and 0.10), the films cannot reach full saturation as the PE loops acquired displays leakage current features, as shown in **Figure 6-11 (a)-(c)**. This serious leakage issue may result from the existing impurity phases (α-Bi_2O_3, $Bi_2Fe_4O_9$). In addition, the relatively thin value of thickness ~ 80 nm also decreases the resistivity of films. An improved trend of the ferroelectric properties with the increase of Sm doping can be still observed. When the Sm ratio is increased to 0.14, a square P-E loop is obtained with the $2P_r$ of 70 μC/cm^2 and $2E_c$ of 1180 kV/cm in **Figure 6-11 (d)**. With the further increase of Sm ratio to 0.15, a slightly distorted P-E loop is shown with the $2P_r$ of 62 μC/cm^2 and $2E_c$ of 1370 kV/cm. This loop distortion indicates an electric-field-induced paraelectric O to ferroelectric transition. Note that this phase transition only happens near the phase transition composition. [192] The transition composition (*x* = 0.15) of the macroscopic

ferroelectricity is higher than that of phase structure transition (x = 0.10) from the 2D RSMs results. It may be due to the minority antiferroelectric and paraelectric O phases in BSFO films with x = 0.10 and 0.14, which is not sufficient to induce a ferroelectric property transition at a macroscale. In addition, this distorted polarization hysteresis loop curve at x = 0.15 is found not change its shape over 1 year. Further even after applying several tens of switching cycles, no detectable changes in the loop shape can be observed. Thus, the domain pinning effect induced pinched response can be excluded here.

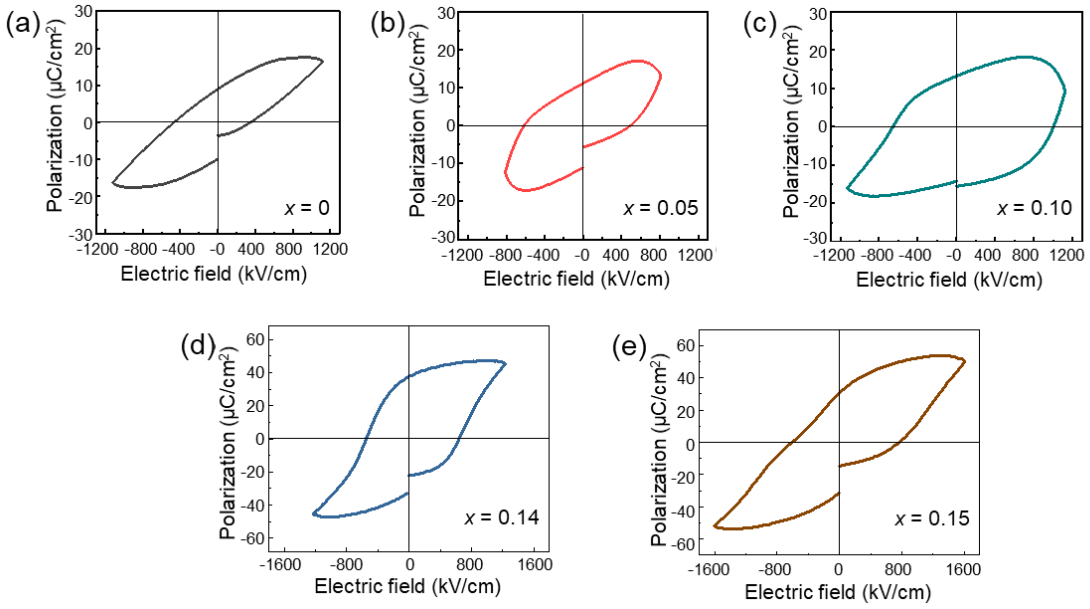

Figure 6-11. Ferroelectric polarization hysteresis loops of BSFO/LSMO//STO (001) films with x = (a)0, (b) 0.05, (c) 0.10, (d) 0.14, and (d) 0.15, measured at room temperature with a frequency of 10 kHz.

Hence through site engineering, a structural phase transition and ferroelectricity evolution are successfully achieved. The improved ferroelectricity at higher Sm doping composition can be attributed to the improved leakage behavior by suppression of oxygen vacancies. [72, 222] In addition, MPB effects also play important role in enhancing the BSFO thin film performance, when the coexistence of different crystal structure phases makes the domain rotation easier at the external stimulus. [16]

6.4 Summary

The non-aqueous Sm-substituted BFO precursors are prepared for the deposition of BSFO films. The molecular chemical structure evolution with the Sm composition is

investigated using FTIR. The gelation chemistry of the Sm-substituted BFO precursor with x = 0.14 is explored during the low-temperature heating process. It is found that the metal cation species show different promotion effects for hydrolysis reaction or esterification reaction. The metal coordination complexes are first developed by the reactions among the 2-MOE, formed acetic acid, and the metal nitrate during the precursor preparation. The consequent condensation reaction between these coordination complexes under the low-temperature heating further leads to gel films formation.

Subsequent investigation of the crystal structure and domain feature on the deposited BSFO films demonstrates a homogeneous R-BFO film with a typical polydomain structure. The paraelectric O phase and antipolar phase start to form at x = 0.10. The domain walls of films become fuzzy with the increase of the Sm ratio. In addition, the Sm substitution affects the polarization vectors distribution. The ferroelectric properties of BSFO film are greatly improved by the Sm doping. At x = 0.14, a fully developed polarization hysteresis loop is acquired. When the further increase of Sm composition to 0.15, a slightly distorted PE loop is observed.

In brief, the Sm substitution in the A-site in BFO influences the precursor gelation chemistry, as well as the phase structure and electrical properties of BFO films. The work in this chapter paves a road to understanding the complex phase transition under both strain engineering and site engineering.

Chapter 7. Chemical Solution Deposition-Derived Sm-Doped Bismuth Ferrite Thin Films: Crystallographic Structure Evolution

In the previous chapters, the phase composition and ferroelectric properties of mixed-phase $BiFeO_3$ (BFO) films stabilized on $LaAlO_3$ (LAO) substrate (strain engineering), and $Bi_{1-x}Sm_xFeO_3$ (BSFO) (site engineering) on $SrTiO_3$ (STO) substrates are studied respectively. In this chapter, the synergetic effects of both strain engineering and site engineering on the crystalline structure transition of BFO films are investigated. A series of techniques, such as X-ray diffraction (XRD), Raman spectra, 2D XRD, and wavelength dispersive spectrometer (WDS), are carried out to understand the complex phase structure evolution of BSFO as a function of Sm substitution. This chapter lays the foundation for the understanding of the enhanced piezoelectricity and ferroelectricity properties observed at the morphotropic phase boundary (MPB), which are discussed in **Chapter 8**.

7.1 Introduction

The anomalous enhancement of electromechanical properties at an MPB primarily stems from the phase structure alternation. Chemical substitution [8, 223] and epitaxial strain [9, 189] are two common ways to construct the MPB in BFO films. So far, most studies focus on the effect of either the strain or the chemical pressure on the phase structure and piezoelectric properties of BFO thin films are on those made by the pulsed laser deposition (PLD) technique. [8, 15, 100] In contrast, the phase evolution of chemical solution deposition (CSD) derived BFO thin films when strain and chemical pressure are applied simultaneously remains unexplored.

In this chapter, we combine both the strain and site engineering to create a complex mixed phase (coexistence of tetragonal-like (T')- rhombohedral-like (R')- orthorhombic (O) phases) [9] in Sm-doped BFO thin films. Ferroelectric R to paraelectric O phase transition is expected in these BSFO films through the tuning of the Sm doping ratio[7, 8]. A series of Sm-doped BFO thin films are deposited on LAO (001) substrates. The compressive misfit strain (-4.4%) imposed by LAO substrate and the A-site chemical pressure induced by smaller Sm^{3+} ion substitution provide a complex phase configuration in BFO. With the Sm substitution in the A-

site, a phase transition from mixed T'-R' to T'-R'-O, and to T'-O phases is achieved in this BSFO/LAO system. We show that Sm doping in A-site can affect the local strain state, and thus the phase structure configuration. At a lower concentration of the Sm substitution ($x \leq 0.14$), the increased T' phase is favored to compensate for the gradually increased compressive strain induced by chemical pressure. With the further increase of Sm composition from x = 0.16 to x = 0.22, the T' phase starts to relax, while the O phase is formed to accommodate this large chemical pressure with the appearance of the superstructure of ½ spots.

7.2 Experimental Procedure

BSFO (x =0, 0.05, 0.10, 0.14, 0.16, 0.18 and 0.22) thin films were deposited by CSD process on LAO (001) substrate with a 5 nm thick $La_{0.67}Sr_{0.33}MnO_3$ (LSMO) buffer layer as a bottom electrode. The stoichiometric precursor solutions were prepared by dissolving $Bi(NO_3)_3{\cdot}5H_2O$, $Sm(NO_3)_3{\cdot}6H_2O$ and $Fe(NO_3)_3{\cdot}9H_2O$ in 2-MOE organic solvent. The detailed precursor parameters are given in **Chapter 6**. Then a small amount of BSFO solution was dropped and spin-coated on a cleaned and preheated LAO substrate. The following gelation process, pyrolysis, and sintering procedures are the same as those used for the preparation of BSFO/LSMO//STO films in **Chapter 6**. The whole deposition and heat treatment process was repeated four times to achieve the desired thickness, here.

7.3 Results and Discussion

7.3.1 Topography of BSFO Thin Films

The piezoresponse force microscopy (PFM) topography images of BSFO/LSMO//LAO films with the Sm doping ratio of 0, 0.05, 0.10, 0.14, 0.16, 0.18 and 0.22 are shown in **Figures 7-1(a)-(g)**. All films show a relatively smooth surface with root-mean-square (RMS) surface roughness of 2.2 nm (x = 0), 1.7 nm (x = 0.05), 2.1 nm (x = 0.10), 0.8 nm (x = 0.14), 1.1 nm (x = 0.16), 0.9 nm (x = 0.18), 0.5 nm (x = 0.22), respectively. For the films with Sm ratio from 0 to 0.14, the films show a relatively similar microstructure that large grains (~ 80 nm in size) accompanied by small ones are observed. When the Sm ratio is beyond 0.16, the grain size decreases to ~ 30 nm (x = 0.16) and ~ 20 nm (x = 0.18 and 0.22), respectively. This change in grain size suggest a phase transition may occur at the Sm composition between 0.14 and 0.16.

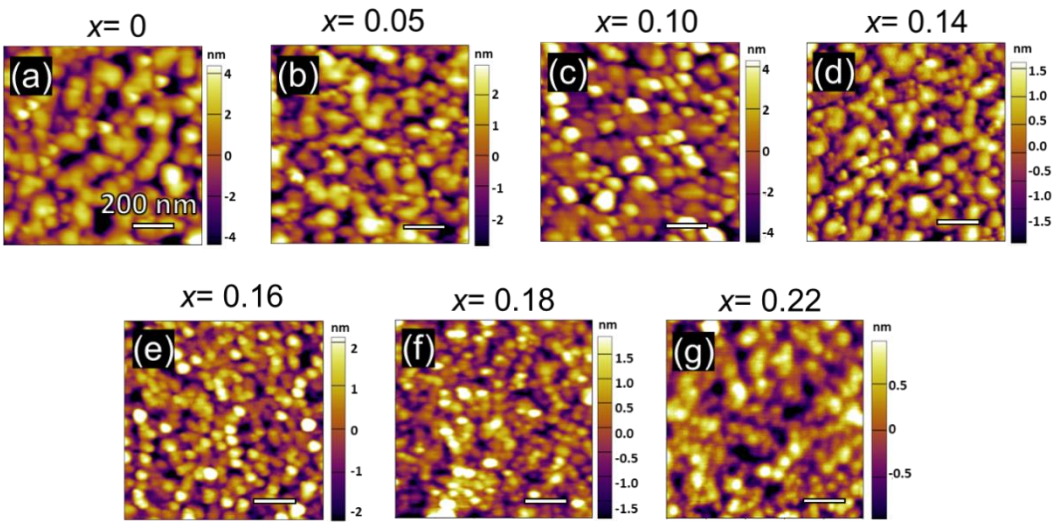

Figure 7-1. PFM topography of BSFO/LSMO//LAO with *x* = (a) 0, (b) 0.05, (c) 0.10, (d) 0.14, (e) 0.16, (f) 0.18 and (g) 0.22 films.

7.3.2 Chemical Composition of BSFO Thin Films

Next, we investigate the chemical composition of as-prepared BSFO films by WDS. As shown in **Table 7-1**, the theoretical value of the Sm doping ratio is consistent with the experimental doped ratio (i.e., the ratio of Sm/Fe), yet with Bi deficiency in all Sm-doped films. The undoped BFO shows a ~ 30% Bi deficiency, which is consistent with the reported PLD-derived BFO films made with the Bi/Fe stoichiometric target [202]. With the Sm substitution ratio increased from 0.05 to 0.14 in the A-site, the Bi deficiency decreases from 27% to 24%. When the Sm substitution ratio increases to 0.18 and 0.22, the Bi deficiency further decreases to ~ 23% and ~ 19%, respectively. It indicates that the Sm substitution in A-site plays an important role in limiting the Bi evaporation.

Table 7-1. Composition of BSFO/LSMO//LAO thin films by WDS.

	$Bi_{1-x}Sm_xFeO_3$/LSMO//LAO thin films					
x	**Bi (atom%)**	**Sm (atom%)**	**Fe (atom%)**	**Sm/(Bi+Sm)**	**Sm/Fe**	**(Bi+Sm)/Fe**
0	6.7657	-	9.5075	-	-	0.71
0.05	5.5407	0.5877	8.3950	0.10	0.07	0.73
0.10	3.9947	0.6733	6.3410	0.14	0.11	0.74
0.14	5.3774	1.2727	8.7020	0.19	0.14	0.76
0.16	2.5704	0.7250	4.4803	0.22	0.16	0.74
0.18	5.3121	1.7206	9.1350	0.24	0.18	0.77
0.22	6.2590	2.5401	10.8448	0.29	0.23	0.81

As mentioned in **Chapter 2.1.2**, Goldschmidt's tolerance factor (*t*) is an indicator of the stability and distortion of the perovskite ABO_3 crystal structure. [224] It can be used to predict the preferentially formed structure.

Based on the above WDS results, the theoretical and experimental values of the chemical composition of BSFO films, as well as the corresponding Goldschmidt's tolerance factor (*t*) parameters are listed in **Table 7-2**. The theoretical *t* value shows a slightly decreasing trend with the increase of Sm doping composition. The experimental *t* value presents a different trend. It increases slightly from 0.8240 to 0.8438 with the Sm doping ratio from 0 to 0.14, and decreases to 0.8338 at the Sm ratio of 0.16, and then starts to increase again to 0.8650 at the Sm ratio of 0.22. This decrease at x = 0.16 may also be related to the structural transition. It has been reported that when the *t* value lies between 0.71 and 0.9, both R and O phases can be stabilized. [224]

Table 7-2. Goldschmidt's tolerance factor (*t*) and the composition from WDS of BSFO (x =0, 0.05, 0.10, 0.14, 0.16, 0.18, and 0.22) films.

Theoretical composition	*t* theory value	Real composition by WDS	*t* reality value
$BiFeO_3$	0.8591	$Bi_{0.71}FeO_3$	0.8240
$Bi_{0.95}Sm_{0.05}FeO_3$	0.8579	$Bi_{0.66}Sm_{0.07}FeO_3$	0.8315
$Bi_{0.90}Sm_{0.10}FeO_3$	0.8567	$Bi_{0.63}Sm_{0.11}FeO_3$	0.8352
$Bi_{0.86}Sm_{0.14}FeO_3$	0.8557	$Bi_{0.62}Sm_{0.14}FeO_3$	0.8438
$Bi_{0.84}Sm_{0.16}FeO_3$	0.8551	$Bi_{0.58}Sm_{0.16}FeO_3$	0.8338
$Bi_{0.82}Sm_{0.18}FeO_3$	0.8547	$Bi_{0.58}Sm_{0.19}FeO_3$	0.8471
$Bi_{0.78}Sm_{0.22}FeO_3$	0.8537	$Bi_{0.58}Sm_{0.23}FeO_3$	0.8650

7.3.3 Crystalline Structure Evolution of BSFO Thin Films

XRD is utilized to understand the evolution of crystalline structure as a function of Sm substitution in BSFO/LSMO//LAO (001) films. A series of ϑ-2ϑ scans of BSFO films with various compositions are shown in **Figure 7-2(a)**. (001)-oriented BFO or BSFO films with T' and R' phases are detected in all samples, while the T'-BFO (001) peak intensity shows a decreasing trend with the increasing Sm doping ratio. Extra peaks at 2ϑ= 31° and 32° are detected in undoped BFO film (x =0), corresponding to a small amount of $Bi_2Fe_4O_9$ and (110)-oriented BFO phases, respectively. The formation of the iron-rich impurity phase of $Bi_2Fe_4O_9$ is due to the loss of Bi at the high-temperature heating process, as mentioned above. The BFO (110) may be formed due to the strain relaxation in the thicker films (4-layer, 250 nm).

After introducing Sm to the A-site, the $Bi_2Fe_4O_9$ phase disappears. However, a new impurity phase of Bi_2O_3 starts to form at the 2ϑ= 26°. It indicates that the Sm introduction can effectively suppress Bi evaporation and leads to the Bi-rich impurity phase of Bi_2O_3. **Figure 7-2(b)** shows the corresponding ϑ-2ϑ scans around the (002) LAO Bragg reflection for all films. The out-of-plane (OP) lattice parameters determined by the $(002)_{pc}$ reflection are plotted in **Figure 7-2(c)**. The corresponding 2ϑ and OP lattice parameter values are listed in **Table 7-3**.

The coexistence of T'-and R'-phase peaks at 2ϑ= 39° and 46°, respectively, confirms the mixed-phase configuration. The R'-phase peaks of Sm-substituted films demonstrate a gradual shift of the $(002)_{pc}$ reflections toward the higher 2ϑ side as the Sm substitution increased up to 22%. Particularly, an abnormal shift to the lower 2ϑ angle is observed at the Sm composition of 14%, as indicated by the red dash arrows in **Figure 7-2(b)**. The $(002)_{pc}$ reflections of T'-phase BFO initially show a shift towards the higher 2ϑ direction when the Sm composition increases to 10%, and remain constant afterwards, as marked by the violet dash arrows in **Figure 7-2(b)**. Correspondingly, we see a gradual decrease in d_{002} of the R' phase in BSFO from 3.95 Å for 0% to 3.90 Å for 22%, while the highest value of 3.96 Å at 14% in **Figure 7-2(c)**. The d_{002} of the T' phase decreases from 4.64 Å to 4.58 Å from 0% to 10% and stabilizes at 4.58 Å with the continuous increase of the Sm composition to 22%. This abrupt change at x = 0.14 indicates the strain variation and/or phase component change in films.

A broad shoulder peak close to R'-BFO (002) is detected, as indicated by the red arrow in **Figure 7-2(b)**. This shoulder peak gets broader with increasing Sm doping ratio, indicating Sm composition dependence. Note that the typical O phase in BFO films induced by A-site substitution reported by previous research [8] cannot be distinguished from the R' phase by just using ϑ-2ϑ scan due to their relatively similar lattice parameters. Thus, a detailed investigation into the phase structure using advanced XRD and other sensitive techniques is required to be carried out to further understand of the complex structural transition in as-prepared Sm-doped BFO films.

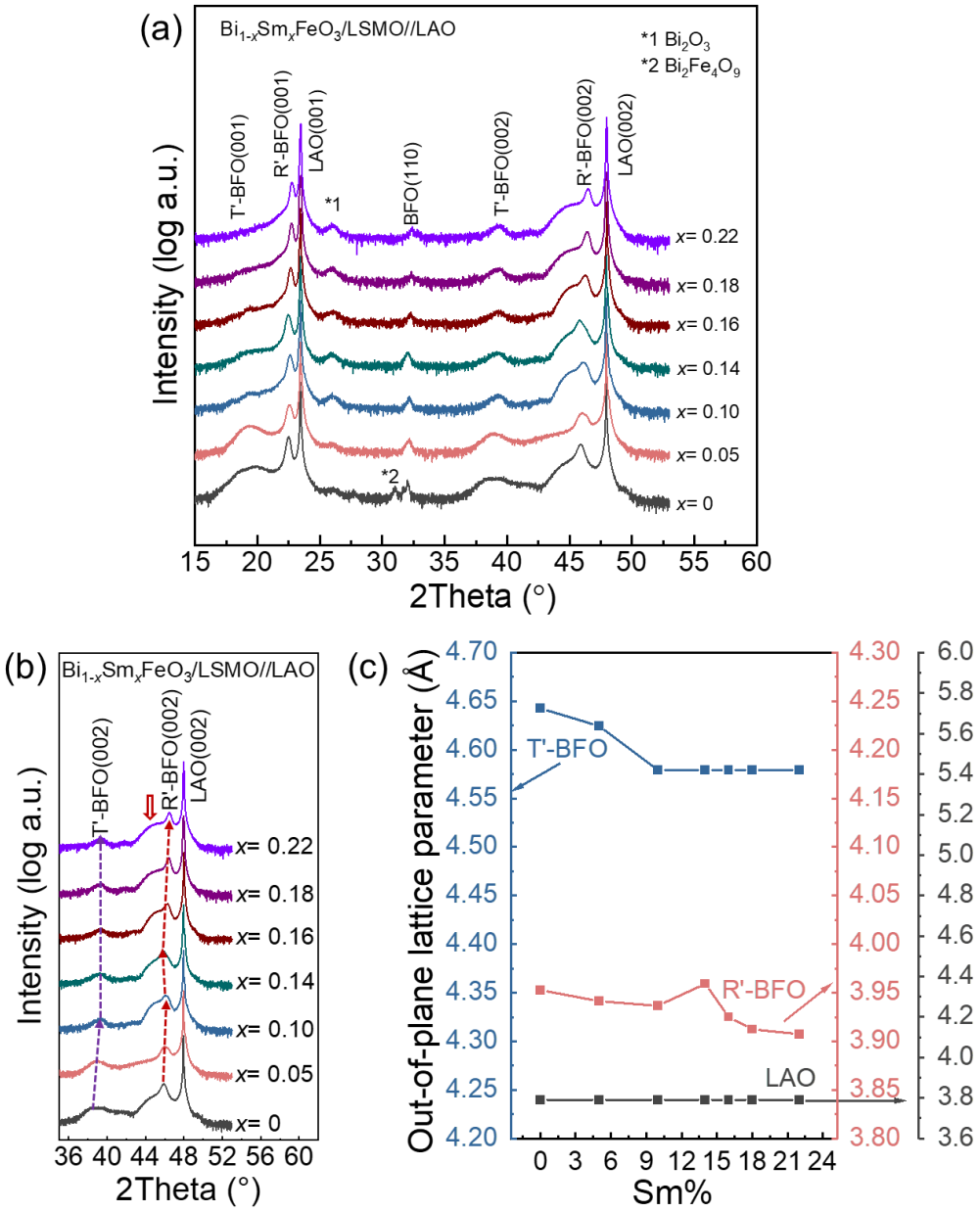

Figure 7-2. (a) ϑ-2ϑ scans, (b) close inspection at around LAO (002) diffraction and (c) the derived OP lattice parameters from (002) peaks of BSFO (x =0, 0.05, 0.10, 0.14, 0.16, 0.18, and 0.22) films.

Table 7-3. 2ϑ values and the derived OP lattice parameters of T'-BFO (002), R'-BFO (002), and LAO (002) peaks of BSFO (x =0, 0.05, 0.10, 0.14, 0.16, 0.18, and 0.22) films.

$Bi_{1-x}Sm_xFeO_3$	2 Theta(°)-(002)			d-spacing (Å)-(002)		
	T'-BFO	R'-BFO	LAO	T'-BFO	R'-BFO	LAO
***x* = 0**	38.76	45.88	47.96	4.6427	3.9526	3.791
***x* = 0.05**	38.92	46.02	47.96	4.6244	3.9412	3.791
***x* = 0.10**	39.32	46.08	47.96	4.5792	3.9364	3.791
***x* = 0.14**	39.32	45.80	47.96	4.5792	3.9592	3.791
***x* = 0.16**	39.32	46.22	47.96	4.5792	3.9251	3.791
***x* = 0.18**	39.32	46.38	47.96	4.5792	3.9123	3.791
***x* = 0.22**	39.32	46.44	47.96	4.5792	3.9075	3.791

The texture of the R' and T' structures in BSFO (with x = 0.10 and 0.16) films is studied by XRD pole figures, as shown in **Figure 7-3**. The pole figure images for T'-BFO {101} and R'-BFO {101} planes of $Bi_{0.90}Sm_{0.10}FeO_3$ and $Bi_{0.84}Sm_{16}FeO_3$ films are collected with 2ϑ value fixed at 30.31°, and 31.97°. Fourfold symmetry spots are observed for both planes in both films. It suggests cube-on-cube epitaxial growth of both the T' and R' phases in these two films. Here, splits of the T'-BFO {101} peaks with the deviation of the center peak position of △ψ(psi) = 3° and △ϕ(phi) = 6° are observed, as shown by the double arrows in **Figure 7-3(a)**. These splits may be induced by the triclinic phases (Tri-1 and Tri-2), where ± 2.7° and ±1.5° tilt angles are determined along [100] (or [010]) direction, respectively, in previous PLD-derived BFO films. [225]

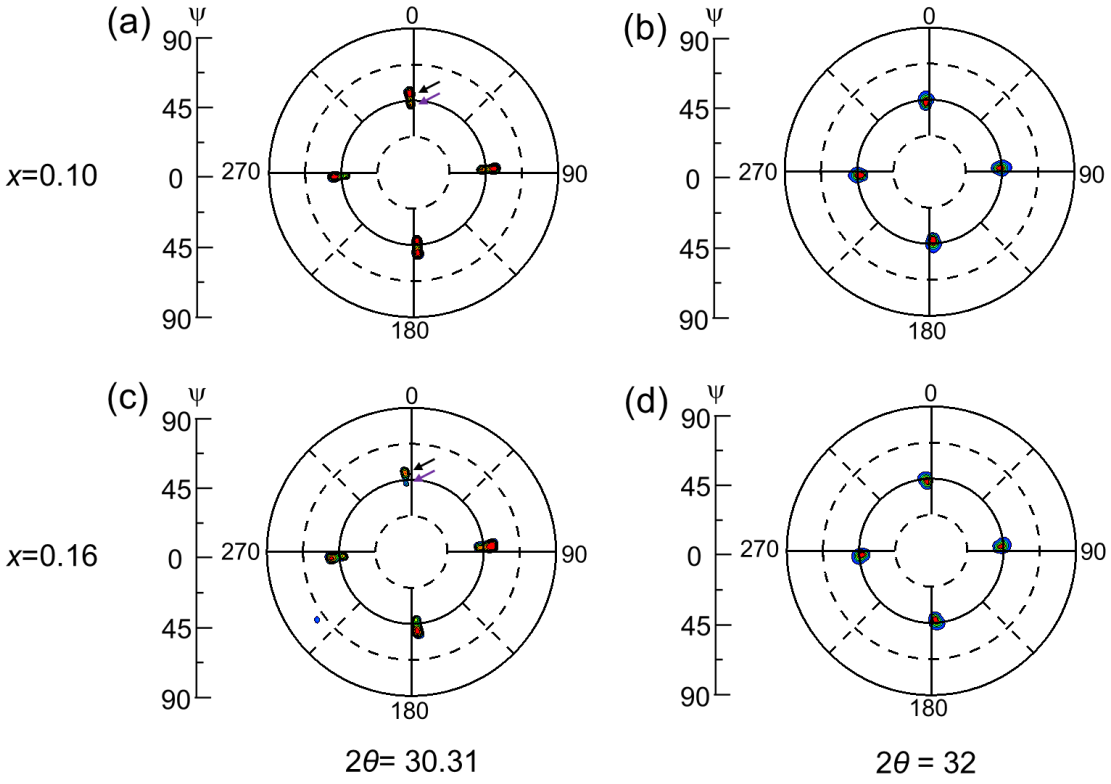

Figure 7-3. Pole figures with 2ϑ value fixed at 30.31°, and 31.97° of (a) (b) $Bi_{0.90}Sm_{10}FeO_3$ and (c) (d) $Bi_{0.84}Sm_{16}FeO_3$ films.

Raman scattering has proved to be a powerful method to study the ferroelectric phase structures because it has a high sensitivity to the soft modes that drive the structural distortion. Group theory predicts that the R' phase (belongs to R3c space group) yields 13 Raman active phonon modes ($4A_1$+9E), [3] high-symmetry T' phase (belongs to P4mm) yields

8 Raman active phonon modes ($3A_1+B_1+4E$), [2, 4] the O phase can yield 24 Raman active phonon modes ($7A_g+7B_{g1}+5B_{g2}+5B_{g3}$). [5] Raman spectra of all the BSFO/LSMO//LAO films are collected in a normal backscattering geometry (**Figure 7-4**) with the wavenumber ranging from 100 cm^{-1} to 900 cm^{-1}.

As shown in **Figure 7-4(a)**, three strong peaks at 123, 151, and 487 cm^{-1} allocated to the LAO substrate are observed in all films. The increased width of the peaks at ~ 280 (orange region) and ~ 620 cm^{-1} (green region) indicates a softening of phonon modes. In addition, the peak (at ~ 620 cm^{-1}) shifts to the lower frequency with the increasing Sm composition, as marked by the red dash arrow. This "red shift" suggests the existence of a gradual strain relaxation in the IP direction. All these variations indicate the change in the phase structures with the Sm substitution.

To identify the detailed evolution of the phase structure, Raman spectra of BSFO with *x* =0 and 0.22 are fitted and decomposed into Gaussian components, as shown in **Figure 7-4(b)**. There are 10 peaks with the frequency of 139, 171, 218, 273, 286, 344, 365, 470, 524, and 616 cm^{-1} in undoped BFO films. Among them, six peaks at 139, 171, 273, 286, 524, and 616 are assigned to A_1-1, A_1-2, E-3, E-4, E-8, and E-9 modes of the R' phase, respectively. Another four peaks at 218, 344, 365, and 470 cm^{-1} are assigned to A_1-3, B, and the two E modes of the T' phase, respectively. With the introduction of Sm, peaks at 139 (A_1-1 mode of R' phase) and 171 cm^{-1}(A_1-2 mode of the R' phase) disappear. In addition, the Raman modes at 218, 365, and 470 cm^{-1} assigned to the T' phase also disappear, while two new peaks at 410 and 632 cm^{-1} are formed. The peaks at 286, 324, and 508 cm^{-1} shows increased intensity, which indicates a greater tilt of the FeO_6-octahedra accompanying the polar cation displacements. The frequency of the corresponding Raman active mode is summarized in **Table 7-4**. Although it is difficult to identify the R and O phases due to their close Raman active modes, Raman results confirm that Sm substitution in the A-site can lead to the strain variation and crystal structure evolution.

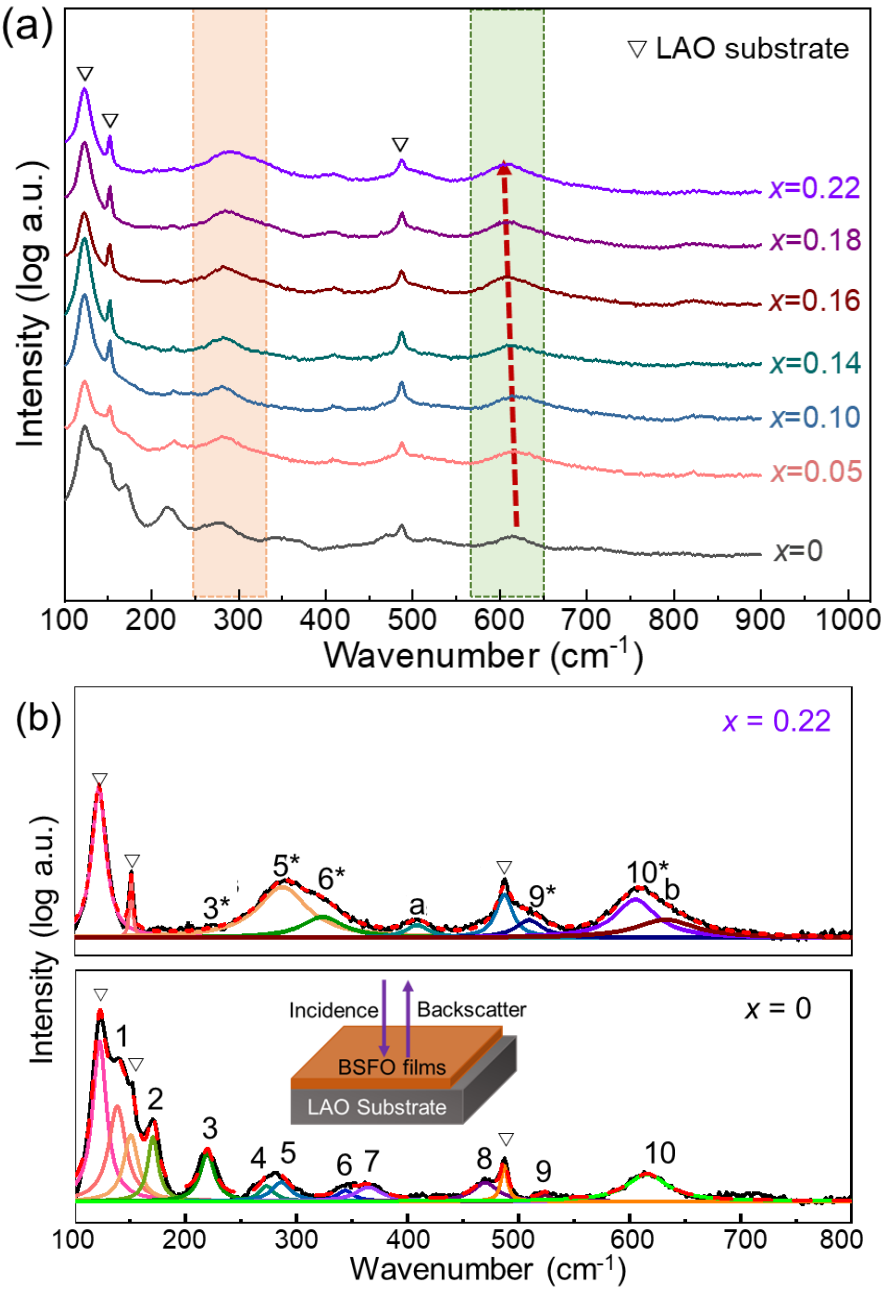

Figure 7-4. (a) Raman spectra of BSFO (*x* =0, 0.05, 0.10, 0.14, 0.16, 0.18, and 0.22) films, and (b) the peak fitting plots of BSFO with *x* =0 (down) and 0.22 (up) films, the inserted picture is the geometry of Raman tests.

Table 7-4. Raman frequencies (cm^{-1}) values of Rhombohedral (R3c), Tetragonal (P4mm), and Orthorhombic (Pnma) perovskite structure, as well as BSFO (*x* =0, 0.05, 0.10, 0.14, 0.16, 0.18, and 0.22) films, respectively.

	Raman active models																							
R3c[1-3] ($4A_1$+9E)	E-1	A_1-1	A_1-2	A_1-3	E-2	E-3	E-4	E-5	E-6	E-7	A_1-4	E-8	E-9											
	72	140	172	221	262	275	307	345	369	429	472	521	615											
P4mm[4] ($3A_1$+B+4E)	E	A_1-1	A_1-2	A_1-3	E	B	E	E																
	126	130	156	206	245	333	454	531																
Pnma[5] ($7A_g$+$7B_{1g}$+$5B_{2g}$+$5B_{3g}$)	A_g	B_2g	A_g	B_3g	B_2g	B_1g	A_g	B_2g	B_1g	A_g	B_1g	B_3g	B_3g	B_2g	A_g	B_1g	A_g	B_2g	B_3g	A_g	B_2g	B_1g	B_3g	B_2g
	104	137	147	145	162	181	223	285	288	304	342	363	390	393	407	413	466	470	476	524	583	593	610	617
x =0	▽	1	▽	2	3	4	5	6	7	-	8	▽	9	10										
	123	139	151	171	218	273	286	344	365	-	470	487	524	616										
	-	R	-	R	T	R	R	T	T	-	T	-	R	R										
x =0.22	▽	-	▽	-	3*	-	5*	6*	-	a	-	▽	9*	10*	b									
	123	-	152	-	218	-	286	324	-	410	-	487	508	603	632									
	-	-	-	-	T	-	R/O	T	-	R/O	-	-	R/O	R/O	R/O									

Next, 2D reciprocal space map (RSM) images are taken around the LAO (002) reflection to further elucidate the structural evolution of BSFO films as a function of Sm content, as shown in **Figures 7-5(a)-(g)**. For pure BFO (x = 0) and low doping content (x = 0.05 and 0.10) BSFO films, only (002) reflections from the LAO substrate, R' and T'-BFO phase are observed. Here, a streaky peak (denoted by the orange arrow) attributed to the Pt/Ti top electrodes (50 nm/ 5nm thick) is observed in several BSFO films. These top electrodes are deposited for the purpose of electrical properties characterizations (discussed in **Chapter 8**).

With the Sm doping content increased to 0.14, ½ {010} diffraction spots (denoted by red squares) begin to appear in addition to the fundamental spots. As mentioned in **Chapter 6**, the presence of ½ {010} spots indicates the formation of (pseudo) orthorhombic structural phases. Note that the same phase transition happened at x = 0.10 in strain-free BSFO (BSFO/LSMO//**STO**) films. On the other hand, ¼ {011} spots, representing the antipolar phase appearance, which are observed in BSFO/LSMO//**STO** samples, are missing here in the BSFO/LSMO//**LAO** films. These differences demonstrate that compressive strain affects the phase configuration in Sm-doped mixed-phase BFO films.

The normalized intensity ratios of ½ superstructure spots, R' and T' phases are further plotted to understand the phase transition with the Sm substitution in strained BFO films, as shown in **Figure 7-5(h)**. When the Sm doping ratio increases from 0 to 0.10, the intensity of R'(002) peak dramatically decreases from 0.973 to 0.942. In contrast, the intensity of T'(002) peak shows a clear increase trend from 0.026 to 0.058. At x = 0.14, the ½ spots emerge with the intensity ratio of 0.017, the intensity of R'(002) further decreases to 0.921, and T'(002) peak increases to 0.061, respectively. When the Sm composition is further increased to x = 0.22, the ½ spots get stronger and reach the highest intensity ratio of 0.05. Meanwhile, the intensity ratio of T'(002) peak decreases from 0.055 (x = 0.16) to 0.045 (x = 0.22), while the intensity ratio of R'(002) peaks decrease slowly from 0.909 (x = 0.16) to 0.905 (x = 0.18), and remains at 0.905 with x = 0.22.

For BSFO/LSMO//**STO** films the structural transition from R' to O phase starts at x = 0.10, while for BSFO/LSMO//**LAO** films the corresponding phase transition happens at x = 0.14 This difference can be attributed to the strained T' phase in Sm-doped mixed-phase BFO films on LAO substrate. The initial lower chemical pressure produced by Sm doping plays a similar role with the compressive strain from the LAO substrate to facilitate the T'-BFO formation and

leads to the insufficient formation energy for O phase nucleation. This can be confirmed by the increased intensity of the T' phase with the increase of the Sm ratio from 0 to 0.10 (**Figure 7-5(h)**). The R to O+T phase transition found in Pr and Nd-doped BFO films on LAO [226] also proved that the RE doping can induce the T phase. Thus, the lack of the ¼ spots should be attributed to alternation of the localized strain state due to the T'-phase existence, which leads to the absence or trace amounts of antipolar phases existence that is beyond the 2D XRD sensitivity. The change of BSFO phase boundary composition with substrate selection indicates we successfully realize the MPB adjustment through misfit strain and chemical pressure.

According to the above results, in BSFO/LSMO//**LAO** films, Sm substitution with $x \leq 0.10$ promotes the formation of the T' phase due to the chemical pressure provided by the smaller radium of Sm^{3+} ion (1.28 Å) compared to A-site Bi^{3+} (1.36 Å). [192] With Sm ratio increased to $x = 0.14$ and above, the O phase starts to form because of the higher chemical pressure of Sm substitution. [8, 220] This releases most of the chemical pressure, thus decreasing the T'-phase fraction. Since the T'-phase fraction of BSFO (at $x = 0.22$) is still higher than that of undoped BFO film, where the peak intensity of the T' phase of $Bi_{0.78}Sm_{0.22}FeO_3$ is stronger than that of BFO.

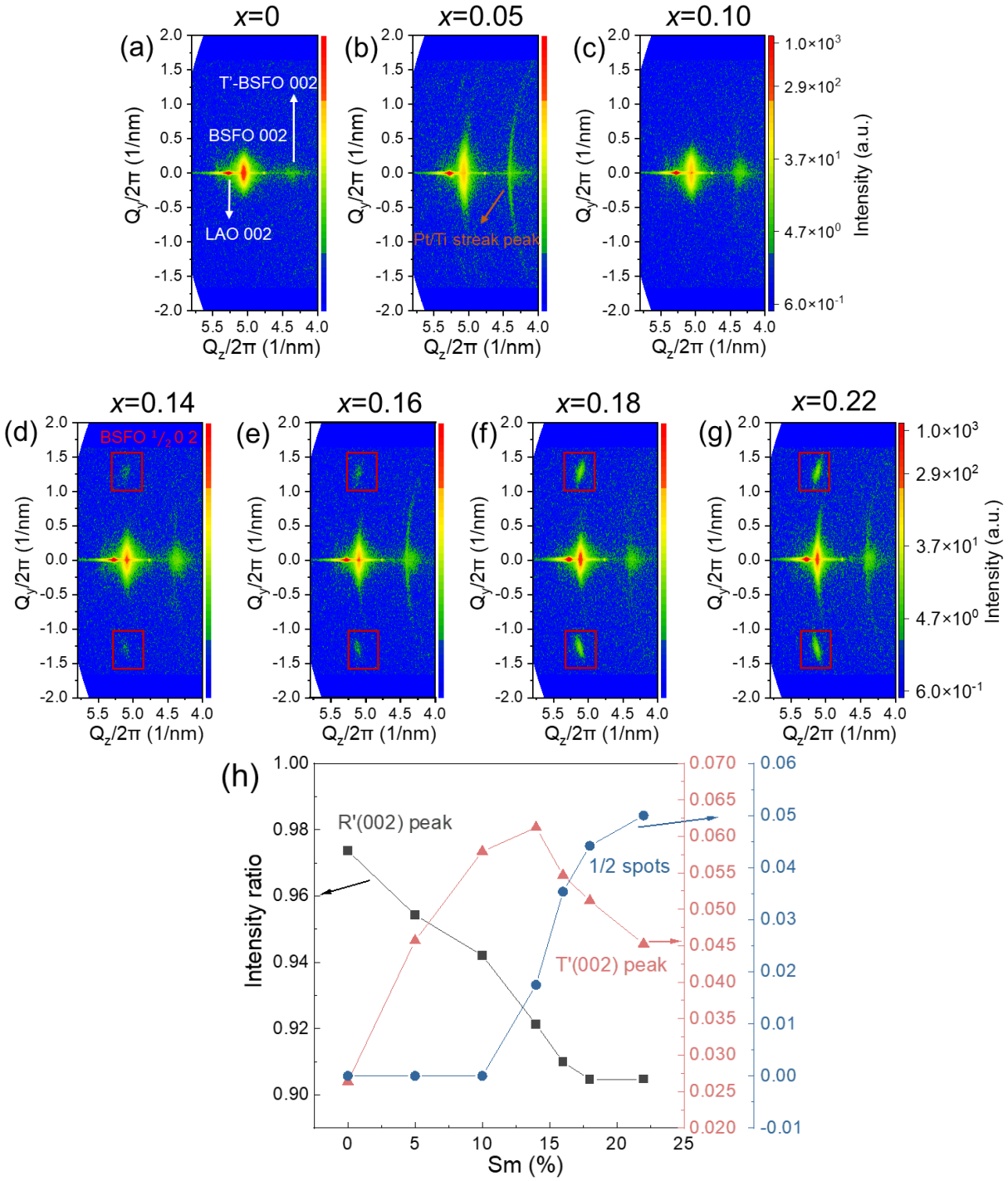

Figure 7-5. 2D XRD RSMs of BSFO films with *x* = (a) 0, (b) 0.05, (c) 0.10, (d) 0.14, (e) 0.16, (f) 0.18, and (g) 0.22; and (f) intensity ratio of R'(002), T'(002), and ½ spots (from (½ 0 2) peak).

7.4 Summary

Phase evolution of BSFO films as a function of the Sm doping composition is investigated. Compared to the strain-free BSFO system (on STO substrate), in this chapter, an LAO substrate is used to provide compressive strain to stabilize the T' phase in BSFO system.

(1) The topography of BSFO films displays an obvious change at *x*= 0.16.

(2) The chemical composition study shows that these CSD-derived BSFO films are Bi deficiency. Sm doping can suppress Bi evaporation.

(3) The crystal structure investigation shows that the T’ phase is obtained in all BSFO films. With the Sm substitution, the OP lattice parameters of both R’ and T’ phases decrease, except for an abnormal increase of the R’ phase at *x* = 0.14. The epitaxial growth of BSFO films is confirmed by pole figures.

(4) 2D RSM images show ½ spots appearance from *x* = 0.14 and get stronger with the increasing Sm content. In addition, the content of Sm substitution has an influence on the phase configuration of the T’ and R’ phases. When the Sm content is from 0 to 0.14, the R’ phase fraction decreases and correspondingly T’-phase fraction increases. When the Sm content is further increased, T’-phase fraction starts to decrease and the decrease of the R’-phase fraction gets slow.

These findings suggest that a complex phase structure of BFO films is obtained by combing site engineering and strain engineering. A structural evolution as a function of Sm is observed with an MPB may lie at 0.14, which is expected to arise a corresponding ferroelectricity transition.

Chapter 8. Chemical Solution Deposition-Derived Sm-Doped Mixed-Phase Bismuth Ferrite Thin Films: Ferroelectric Domain and Functional Properties Evolution

In the previous chapter, we analyze the crystallographic structural evolution of Sm-doped $BiFeO_3$ (BFO) films deposited on $LaAlO_3$ (LAO) substrate. A complex phase transition from the tetragonal-like (T')-rhombohedral-like (R') phases, to T'-R'-orthorhombic (O), and then to T'-O phases as a function of Sm composition is observed. In this chapter, we link these changes in the phase structures to their functional properties, including the domain structure, piezoelectric and ferroelectric properties, as well as conductivity and resistive switching behaviors.

8.1 Introduction

The structural transition at morphotropic phase boundary (MPB) can generate interesting functional properties. [39, 40] In BFO films, enhanced electromechanical response is realized at a "strain-induced MPB". [9] In rare earth substituted BFO, an electric-field-induced ferroelectricity transition is observed at a MPB composition. [8] Here, we introduce various phase configurations in BSFO/LSMO//LAO (BSFO: $Bi_{1-x}Sm_xFeO_3$, LSMO: $La_{0.67}Sr_{0.33}MnO_3$) system through the synergetic effects of strain and site engineering. Novel functional properties are expected in this complex MPB with the coexist of T'-R'-O phases (as demonstrated in **Chapter 7**). Multiple polarization directions due to the coexistence of these different phases provide versatile paths for domain reversal, and, thus, affect ferroelectric behavior as well as piezoresponse. [38-40] In addition, the intrinsic Bi deficiency of these as-prepared chemical solution deposition (CSD)-derived BSFO films (confirmed by the wavelength dispersive spectrometer (WDS) characterization in the previous chapter) may also influence their conductivity behavior. [202] Thus, next, we focus on the study of the electrical properties of BSFO/LSMO//LAO films.

Piezoresponse force microscopy (PFM) is first utilized to characterize its domain structure and piezoelectric properties. Then conductive atomic force microscopy (CAFM) is applied to investigate the polarization reversal relevant conductive behavior transition with the Sm substitution. The coexistence of multiple phases due to the Sm doping ($x \leqslant 0.16$) leads to an

enhanced domain switching ability and thus, higher conductivity at the upward polarization regions (polarization direction away from the bottom electrode). In addition, a concomitant evolution of the ferroelectric properties with the structural phase transition is also found. Typical room-temperature polarization hysteresis loops are obtained, and they exhibit a transition from single ferroelectric (FE) square-shaped to a slightly distorted double hysteresis loop with the Sm^{3+} doping content increasing from 0.14 to 0.16. It indicates the presence of an electric-field-induced phase transition from paraelectric to ferroelectric. The high remanent polarization with $2P_r$ of 103 μC/cm^2 at x =0.14 is achieved. Last, the effect of phase transition on the leakage current behavior is also revealed. Different types of resistive switching behavior are demonstrated with the increase of Sm composition.

8.2 Experimental Procedure

The fabrication process of mixed-phase BSFO/LSMO//LAO (001) (x =0, 0.05, 0.10, 0.14, 0.16, 0.18, and 0.22) films is described in **Chapter 7.2**. The summarized samples information including the fabrication parameters, chemical composition, as well as the occurrence of superstructure ½ spots, is listed in **Table 8-1**.

Table 8-1. Summary of the fabrication parameters and samples information of mixed-phase BSFO/LSMO//LAO films.

$Bi_{1-x}Sm_xFeO_3$	Precursor concentration	Layer number	Pyrolysis		Crystallization	
			temperature	time	Temperature	Time
	0.25 M	four	450 °C	30 min	640 °C	30 min
	Theoretical composition		Real composition		½ spots	
***x* = 0**	$BiFeO_3$		$Bi_{0.71}FeO_3$		-	
***x* = 0.05**	$Bi_{0.95}Sm_{0.05}FeO_3$		$Bi_{0.66}Sm_{0.07}FeO_3$		-	
***x* = 0.10**	$Bi_{0.90}Sm_{0.10}FeO_3$		$Bi_{0.63}Sm_{0.11}FeO_3$		-	
***x* = 0.14**	$Bi_{0.86}Sm_{0.14}FeO_3$		$Bi_{0.62}Sm_{0.14}FeO_3$		√	
***x* = 0.16**	$Bi_{0.84}Sm_{0.16}FeO_3$		$Bi_{0.58}Sm_{0.16}FeO_3$		√	
***x* = 0.18**	$Bi_{0.82}Sm_{0.18}FeO_3$		$Bi_{0.58}Sm_{0.19}FeO_3$		√	
***x* = 0.22**	$Bi_{0.78}Sm_{0.22}FeO_3$		$Bi_{0.58}Sm_{0.23}FeO_3$		√	

8.3 Results and Discussion

8.3.1 Domain Structure

PFM is applied to understand the evolution of domain structure and domain reversal of BSFO (*x* =0, 0.05, 0.10, 0.14, 0.16, 0.18, and 0.22) films as a function of Sm substitution. **Figure 8-1** displays the out-of-plane (OP) (vertical) PFM amplitude and phase images of as-grown BSFO films as well as the images after poling with applied direct current (DC) bias of ±6 V. The undoped BFO films exhibit a mosaic-like polydomain structure as seen by the dual contrast in **Figure 8-1(b1)**, where the yellow and purple domains correspond to downward and upward polarization directions, respectively. With the increase of Sm doping composition, the as-grown OP PFM amplitude and phase images indicate changes from a polydomain structure to a monodomain-like state with the domain walls getting blurry. The amplitude images show a decreased trend of the magnitude. This can be attributed to the smaller radius of Sm^{3+} (1.28 Å) compared to Bi^{3+} (1.36 Å) and the weaker electronegativity of Sm than Bi, which weakens ferroelectric polarization. [215] The local domain switching behavior is shown in **Figure 8-1(c1)-(c7) and (d1)-(d7)**, that the ferroelectric domains can be easily switched under an applied electrical field with the domain poled-up/down at the +6/-6 V bias, respectively.

With the increasing Sm doping composition from 0 to 0.16, both poled-up and poled-down areas exhibit significantly enhanced amplitude. This can be attributed to the rich multiple domain variants provided by the complex mixed-phase structure in BSFO films. [69] As found in **Chapter 7**, the phase structure goes through an evolution from T'-R' mixed phase to the coexistence of T'-R'-O phases and then to a T'-O mixed phase with the A-site substitution by Sm. It indicates that the Sm doping leads to a transition from a ferroelectric R dominated state to a paraelectric O dominated state. There are 6, 8, and 12 possible spontaneous polarization vectors along <001>, <111>, and <110> directions in T', R', and O phase, respectively. The multiphase coexistence can provide multiple rotated paths and leads to a reduced energy barrier for the polarization reversal, which could contribute to an enhanced switched amplitude characteristic under the external electric field. When the Sm composition reaches 0.18, the poled-up area shows a high amplitude, while the poled-down one demonstrates a low amplitude. When the Sm composition increases to 0.22, the phase and amplitude contrasts of switched domains become very weak. At such a high concentration

of Sm doping, the paraelectric O phase (no ferroelectricity) becomes dominant, although the existence of the minority T'-BFO phase can still show ferroelectricity under the external electric field.

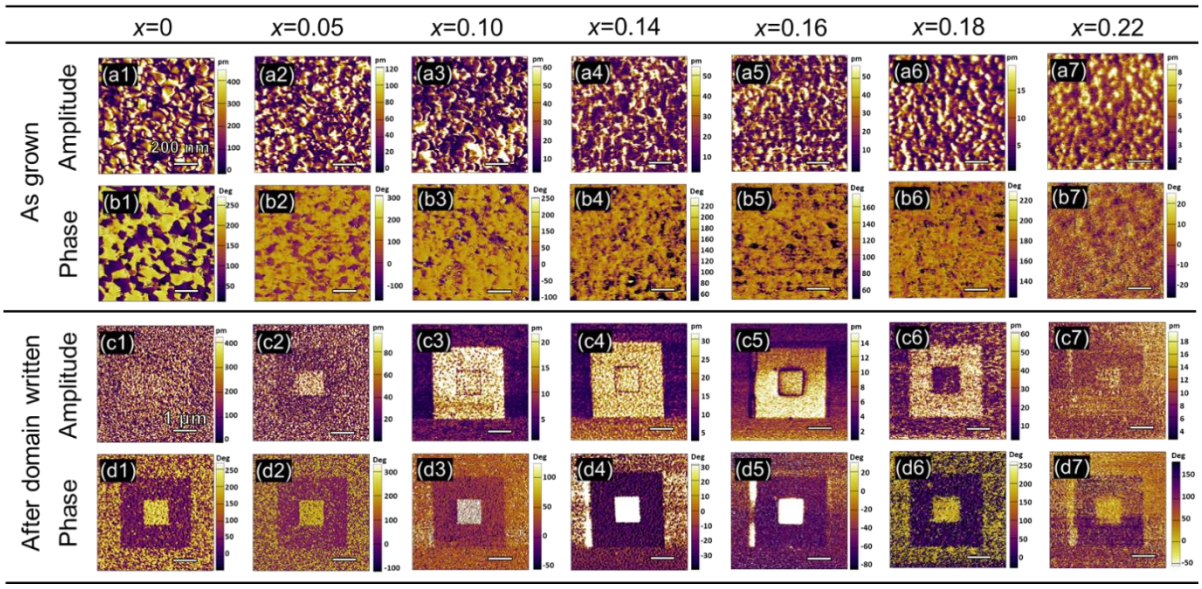

Figure 8-1. OP PFM amplitude, and phase images (scan size of 1 μm × 1 μm), as well as the amplitude and phase images (scan size of 5 mm × 5 mm) after domain switching of BSFO (*x* =0, 0.05, 0.10, 0.14, 0.16, 0.18, and 0.22) films. The applied switching DC bias is +6 V (3 μm × 3 μm, poled-up)/-6 V (1 mm × 1 mm, poled-down).

To further investigate the microscale piezoelectric properties of BSFO films, the switching spectroscopy (SS)-PFM is used to analyze the local domain switching behavior with the tip landed directly on the surface of the film. **Figure 8-2(a)-(g)** displays the PFM amplitude hysteresis loops of BSFO films. The corresponding coercive voltage ($2V_c$) and maximum amplitude as a function of Sm composition are plotted in **Figure 8-2(h).** With the increase of the Sm ratio from 0 to 0.18, the coercive voltage ($2V_c$) reduced from 9.0 V to 3.3 V. As reported in a previous investigation, Sm doping can lower the coercive voltage of BFO films, mainly contributed by increased anisotropy of spontaneous polarization. [16, 72] However, at 0.22 composition, the $2V_c$ bounces back to 5.0 V. This is because of the weak ferroelectricity from the minority T' phase and the predominant paraelectric O phase. The nonpolar O phase without any piezoelectric effect, as a result, leads to the impedance of the domain switching of the T' phase under an external electric field.

Similarly, the amplitude also gradually decreased with the increasing Sm doping composition. It is consistent with the above PFM amplitude changes in **Figure 8-1(a1)-(a7)**.

However, this SS-PFM is limited to a local region and thus is not sufficient to explain the macroscale piezoelectric behavior. Therefore, we explored the "global" domain switching with the tip landing on the top electrode.

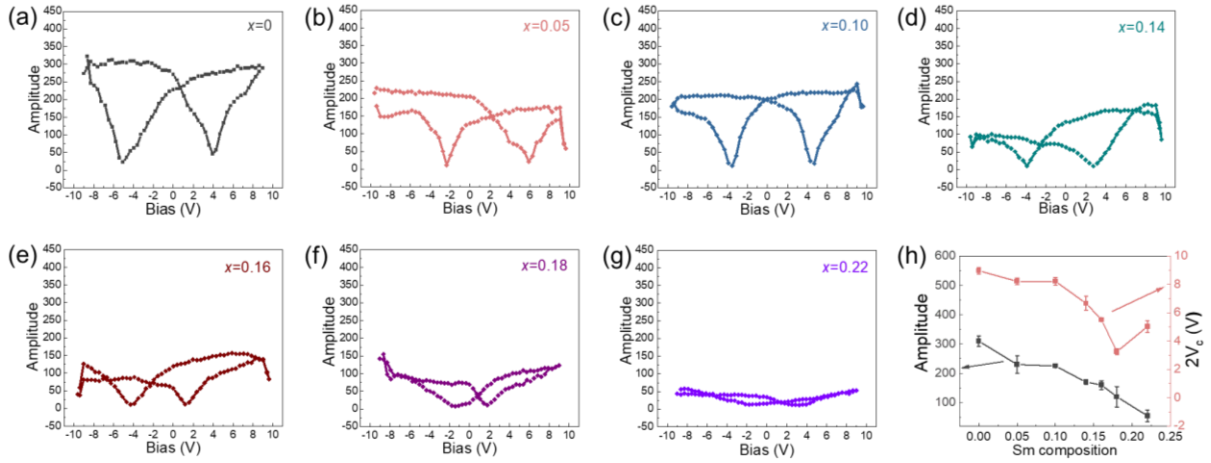

Figure 8-2. Local amplitude hysteresis loops of BSFO with *x* = (a) 0, (b) 0.05, (c) 0.10, (d) 0.14, (e) 0.16, (f) 0.18 and (g) 0.22 films; and (h) maximum amplitude and coercive voltage ($2V_c$) as a function of the Sm doping composition.

The typical global butterfly-hysteresis loops of the as-grown BSFO films and corresponding coercive voltage and maximum amplitude variation with the Sm composition are shown in **Figure 8-3(a)-(h)**. With the increase of Sm substitution, the piezoresponse amplitude increases to the maximum value up to ~ 370 a.u. at x = 0.14, and then drops gradually below ~ 150 a.u. at x = 0.18. When x = 0.22, a collapsed hysteresis loop is obtained with decreasing amplitude. The enhanced piezoelectric performance at x = 0.14 can be contributed to the R'-T'-O MPB, where the O phase starts to form with the featured ½ spots appearance in 2D reciprocal space maps (RSMs) (seen **Figure 7-5 in Chapter 7**). When crossing this boundary and continuously increasing the Sm amount, the paraelectric O phase becomes predominant and leads to the amplitude decrease (x = 0.18), as well as the paraelectric switching behavior at x =0.22 under an external field. The global coercive voltage ($2V_c$) enhances from 7.6 V to 9 V when the Sm substitution increases from 0 to 0.10, and reaches to the maximum value of ~ 10 V at x = 0.14 and 0.16. Then $2V_c$ value drops to 8 V at x = 0.18. It is incompatible with the local results and the reported lowering coercive voltage effect with the Sm substitution. This abnormal increased coercive voltage near the MPB composition (x =0.14) may be ascribed to the decrease of the grain size, where the domain wall motions are inhibited [227, 228].

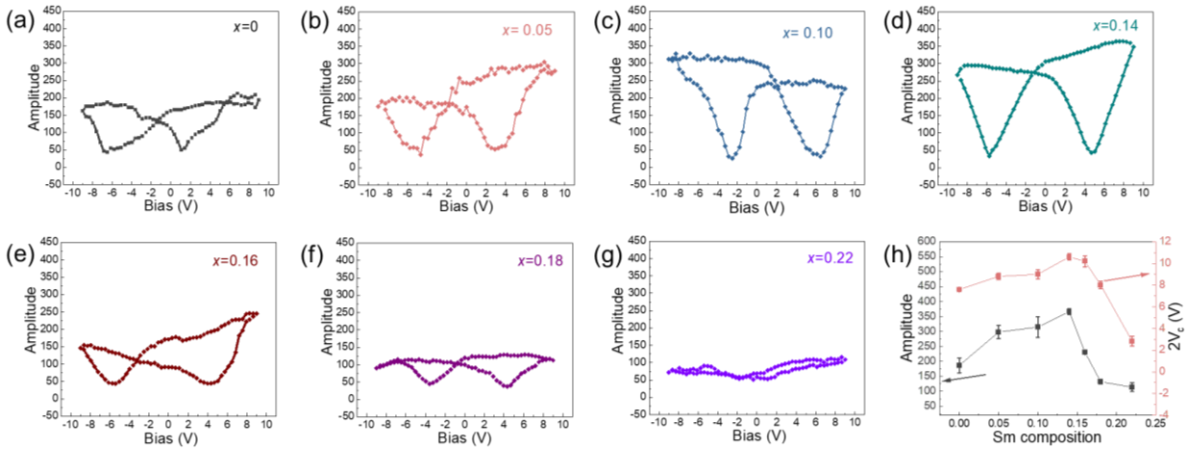

Figure 8-3. Global amplitude hysteresis loops of BSFO with *x* = (a) 0, (b) 0.05, (c) 0.10, (d) 0.14, (e) 0.16, (f) 0.18 and (g) 0.22 films; and (h) maximum amplitude and coercive voltage ($2V_c$) as a function of Sm doping composition.

Figures 8-4(a) and (b) show the local and global phase-voltage hysteresis loops of BSFO films, respectively. Square-shape hysteresis loops are observed for all local measurements of BSFO films. For global measurements through top electrodes, square hysteresis loops are only observed for BSFO films with the $x \leqslant 0.16$. When $x = 0.18$, the hysteresis loop starts to distort. With further increasing the *x* to 0.22, an obvious collapse of the hysteresis loop is obtained, which indicates the disappearance of the ferroelectricity. This is the result of the crystallographic structural transition driven by the Sm substitution (discussed in **Chapter 7**), where mixed ferroelectric T' and R' phases are stable with the $x \leqslant 0.10$, and a small amount of O phase starts to form at $x = 0.14$, while R' and T' phases still dominate. With the further increase of Sm composition, the paraelectric O phase dominates, which leads to the collapse of the hysteresis loop.

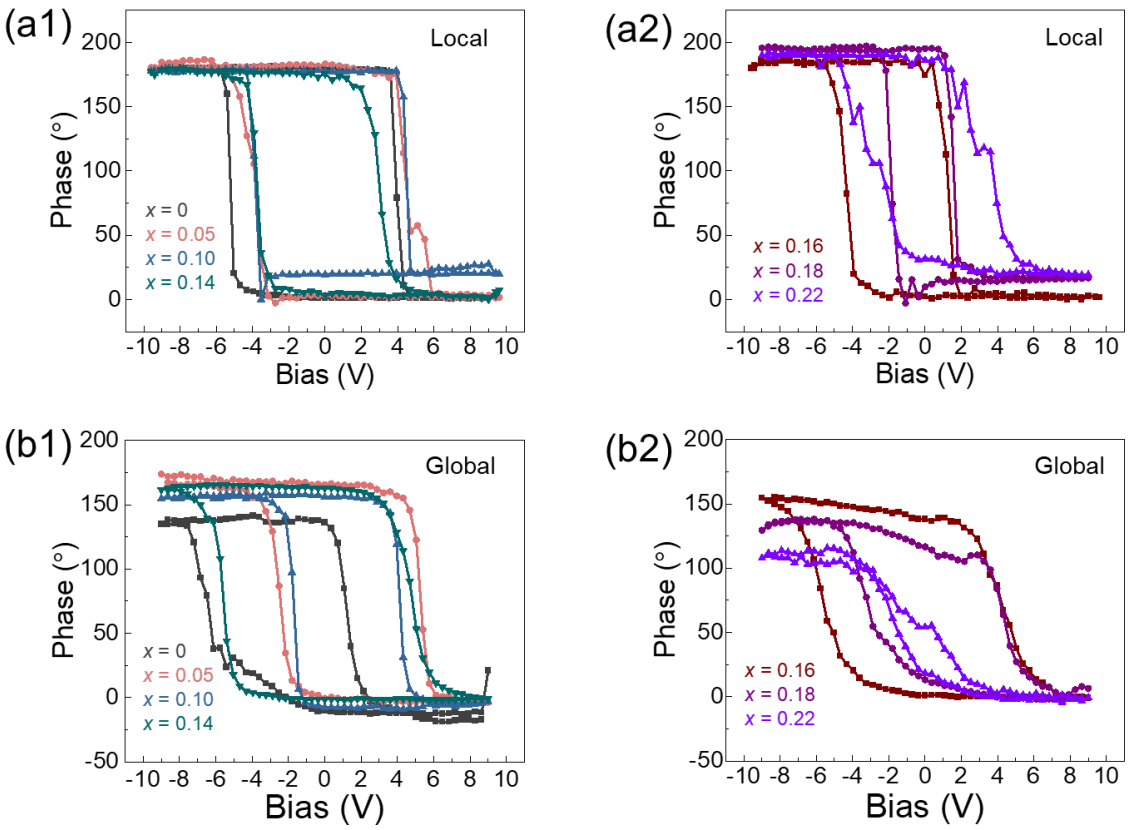

Figure 8-4. (a1) and (a2) Local and (b1) and (b2) global phase hysteresis loops of BSFO with *x* = 0, 0.05, 0.10, 0.14, 0.16, 0.18 and 0.22 films.

8.3.2 Ferroelectric Properties

Figure 8-5(a)-(e) exhibits the typical ferroelectric hysteresis loops of all BSFO films at room temperature with the frequency of 10 kHz. The extracted remanent polarization ($2P_r$) and coercive electric field ($2E_c$) as a function of Sm composition are plotted in **Figure 8-5(f)**.

The pristine mixed-phase BFO film with $x = 0$ shows an unsaturated polarization-electric field (P-E) loop **(Figure 8-5(a))**. This indicates the BFO film suffers from high leakage current, which is due to the Bi deficiencies and oxygen vacancies [195, 229]. Sm dopants enable the suppression of the formation of oxygen vacancy by compensating for Bi loss, and, therefore, diminish leakage issue [230, 231]. As shown in **Figure 8-5(b)**, even with a small amount of Sm substitution of 0.05, a square-shaped hysteresis loop of $Bi_{0.95}Sm_{0.05}FeO_3$ film is formed with $2P_r$ of ~ 73 μC/cm^2 and $2E_c$ of ~ 860 kV/cm. When the Sm dopants increases to 0.10, a fully developed P-E loop with $2P_r$ of ~ 95 μC/cm^2 and $2E_c$ of ~ 940 kV/cm is collected. Continuing increasing the Sm amount to 0.14, the $2P_r$ increases slightly up to ~ 103 μC/cm^2, and $2E_c$ decreases by 200 kV/cm to ~ 740 kV/cm.

At the x = 0.16, a distorted double hysteresis loop appeared with the $2P_r$ remaining ~ 95 μC/cm^2 and $2E_c$ of ~ 605 kV/cm, suggesting an electric-field-induced paraelectric O phase to ferroelectric rhombohedral (R) phase transition. When the Sm ratio crossed this phase boundary at x = 0.18 and x =0.22, spindle-like shape of P-E loops are acquired. This is because that excess Sm substitution further prompts the structure transition to the paraelectric O phase. Meanwhile, due to the remaining ferroelectric T' phase, the $2P_r$ and $2E_c$ in P-E loops at x = 0.18 and 0.22 are nonzero **(Figure 8-5(f) and (g))**. It is consistent with the X-ray diffraction (XRD) and PFM results. Thus, the combination of the chemical pressure induced by A-site substitution and compressive strain provided by the substrate stabilizes various phase structure and yield diverse electrical properties at different Sm contents. That is a mixed-phase transition from T'-R' to T'-R'-O and then to T'-O, and it ensued electrical properties evolution from a ferroelectric to a paraelectric characteristics with the Sm substitution.

Here, we noticed that the MPB of as-fabricated CSD-derived mixed-phase BSFO films on LAO substrate is located at x = 0.16, which is 2% higher than the reported pulsed laser deposition (PLD)-derived BSFO films on $SrTiO_3$ (STO) [15]. This is attributed to the extrinsic compressive strain from the LAO substrate, which stabilizes T phase BFO and suppresses the O phase formation. [69, 232] Thus, a higher Sm doping content is needed to trigger the phase transition.

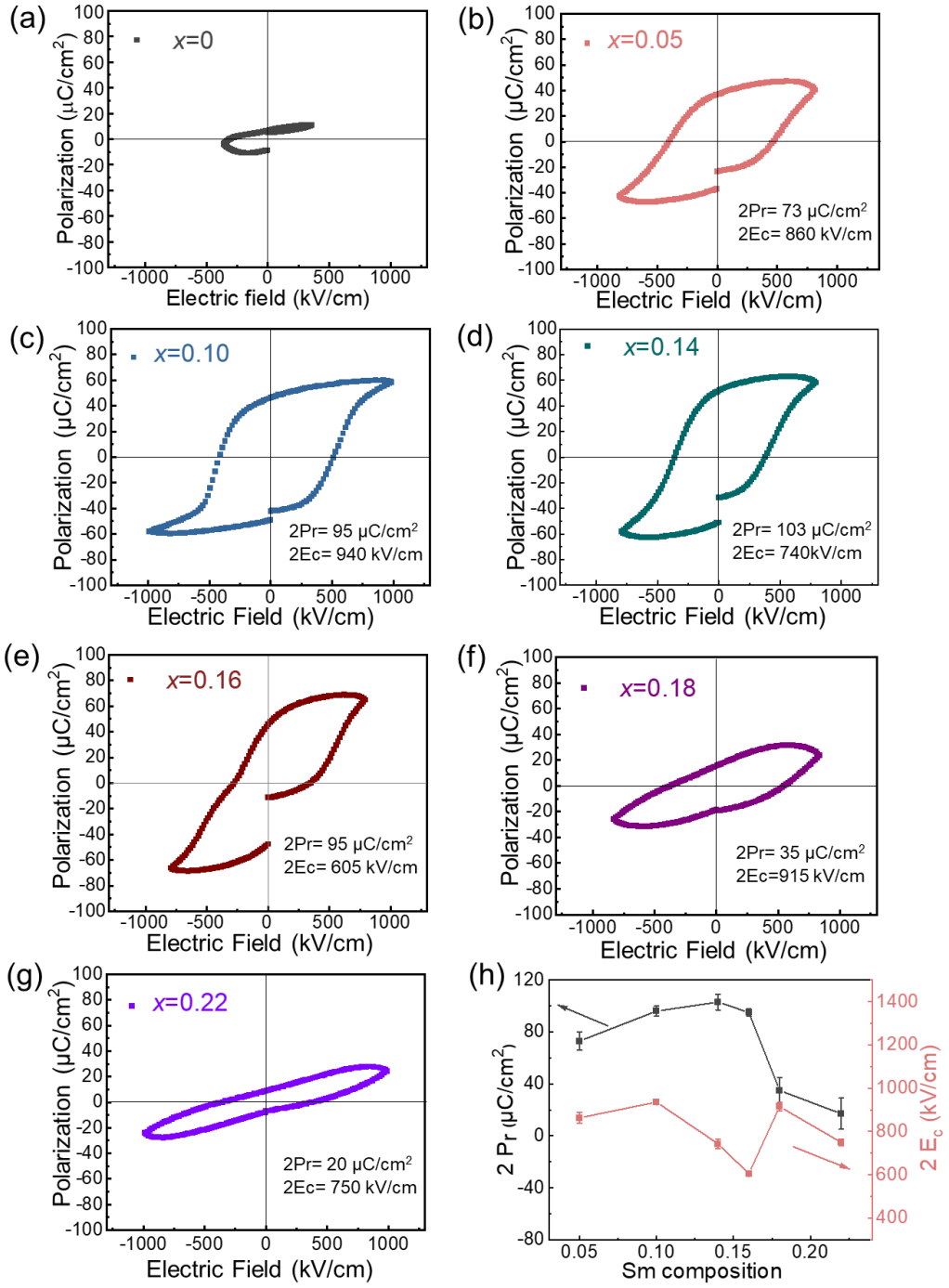

Figure 8-5. Ferroelectric P-E hysteresis loops of BSFO with *x* = (a) 0, (b) 0.05, (c) 0.10, (d) 0.14, (e) 0.16, (f) 0.18, and (g) 0.22 thin films measured with a frequency of 10 kHz at room temperature, and (h) $2P_r$ and $2E_c$ as a function of Sm doping composition.

8.3.3 Conductivity Behavior

Next, the effects of the phase transition and domain configuration induced on film conductivity behavior are also investigated by CAFM. **Figure 8-6** shows the current maps of switched regions, and the schematic energy band variation with the polarization states.

The applied minimum reading DC bias for CAFM scanning of BSFO films are 2.6 V (x = 0), 2.4 V (x = 0.05), 2.4 V (x = 0.10), 2.3 V (x = 0.14), and 2.3 V (x = 0.16), respectively. The CAFM images of upwards and downwards domains show clear contrast (i.e., higher conductivity at the poled-up domain areas (right side, under +8 V poling bias), and lower conductivity at the poled-down domain areas (left side, under -8 V poling bias)). It is similar to our previous study on both the pure R-phase BFO and mixed T'-R' phases BFO films. [212, 233] Nevertheless, for Sm composition at 18% and 22%, no polarization-orientation-dependent conductivity behavior is observed even at the DC bias up to 3.8 V and 5.8 V, respectively.

This polarization related conductivity behavior for BSFO (x = 0, 0.05, 0.10, 0.14, and 0.16) can be attributed to the redistribution of the charge carriers (oxygen vacancies and released electrons) induced by the polarization reversal. At the virgin state, there is no net polarization and, thus, no modulation of the energy barrier height, as shown in **Figure 8-6(d)**. The barrier heights at both interfaces are sufficiently high to forbid the charge carrier's movement and high resistive behavior is displayed. At the poled-up or poled-down domain areas, in **Figure 8-6(e) and (f)**, upward or downward band bending inside the LSMO at the BFO/LSMO interface is produced, which could reduce/increase the barrier height and thus allows/impairs the current flow. A detailed explanation can be seen in our previous report. [233]

In addition, with the increasing Sm doping composition from 0 to 0.16, dipoles are easier to rotate under the external electric field due to the phase configuration evolution from R'-T' to R'-T'-O mixed-phase in BSFO films. This can lead to a much higher interface potential, and, thus, an increased concentration of the holes and electrons accumulation inside LSMO at LSMO/BFO interface and Pt at Pt/BFO interface. Therefore, the higher composition of Sm is, the more downward band bending is induced at the poled-up domain regions. As a result, decreasing reading bias is needed to trigger this higher conductivity behavior at the polarization upward areas with increasing Sm composition. However, when continuing increasing the Sm composition to 0.18 and 0.22, nearly all the ferroelectric R' phases develop into nonpolar paraelectric O phase which has non polarization reversal under the external electric field. Even though there is still a minority T' phase, the produced poled dipoles are too weak to realize the sufficient band bending. Thus, the poled area at both positive and negative bias shows the same high resistivity behavior as the as-grown state. Hence, we realize the control of the conductive behavior through phase configuration transition induced by the Sm doping composition.

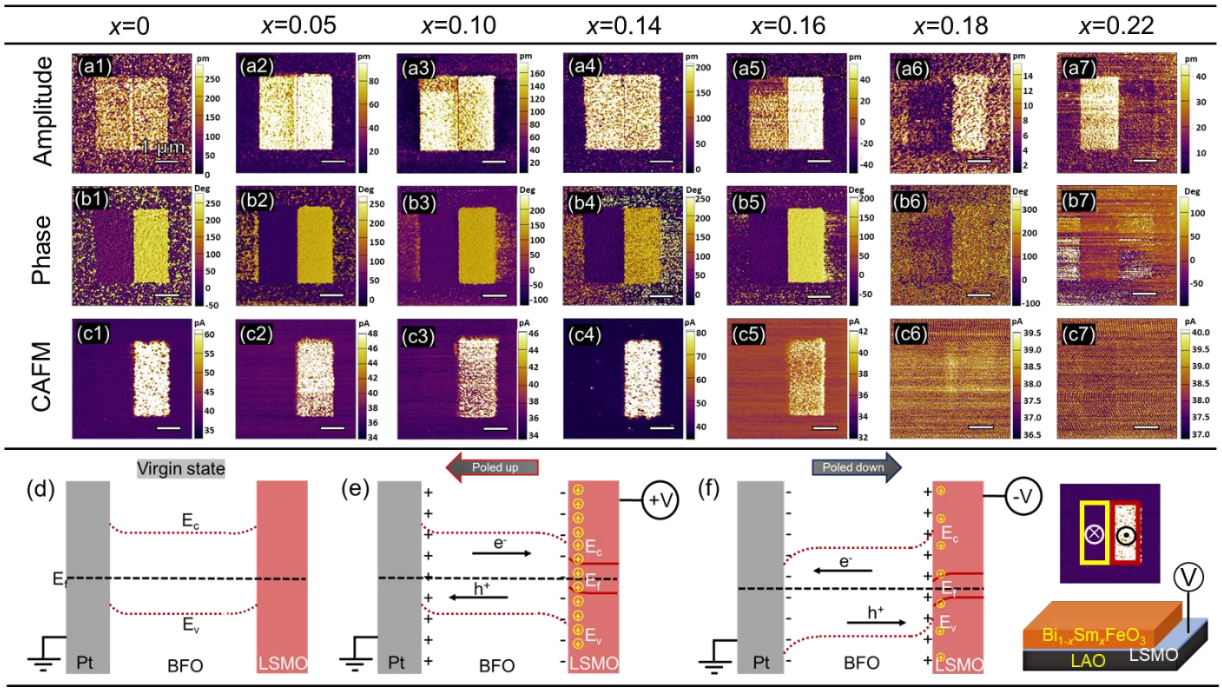

Figure 8-6. OP PFM (a) amplitude, (b) phase, and (c) CAFM images of BSFO with *x* = 0, 0.05, 0.10, 0.14, 0.16, 0.18 and 0.22 films, Schematic energy band diagrams for (d) virgin, (e) poled up, (f) poled down states and (g) CAFM measurement setup and the polarization direction indication (yellow box: poled-down; red box: poled-up).

Lastly, the leakage current behaviors of BSFO films are investigated to illuminate the role of Sm substitution on film conductivity. **Figure 8-7 (a)-(g)** shows the current density versus electric field (i.e., J-E) curves with the applied maximum sweeping voltage of 20 V (800 kV/cm). The bias is applied from the Pt top electrode to the films with the LSMO bottom electrode connecting to the ground, as shown in **Figure 8-7(h)**. No distinctive leakage variation is observed with the magnitude of the current density of all films stable at the range between 10 and 10^2 A/cm^2 under the maximum electric field of 800 kV/cm. The purple arrows indicate the sweeping direction.

We observed that there is a change of the resistance state as a function of the Sm composition under the applied electric field sweeping 0-> $+E_{max}$ -> 0 -> $-E_{max}$. Here, we categorized the resistance change in two different types with varying Sm dopant ratios: (1) Type 1 (at *x* = 0 and 0.05): “high resistance state (HRS) -> low resistance state (LRS) -> HRS -> LRS”, and (2) Type 2 ($x \geqslant 0.10$): “HRS -> LRS -> LRS -> HRS”.

Type 1 represents forward diode-like rectifying characteristic. The open curves indicate a reverse diode behavior. [213] Type 2 is a typical bipolar resistive switching behavior. [234] In particular, the transitional state can be observed at *x* = 0.10, where a cross of the J-E curve

occurs from LRS-> HRS -> LRS-> HRS at the negative part is observed, as shown in **Figure 8-7(c)** (denoted as “Intermediate”).

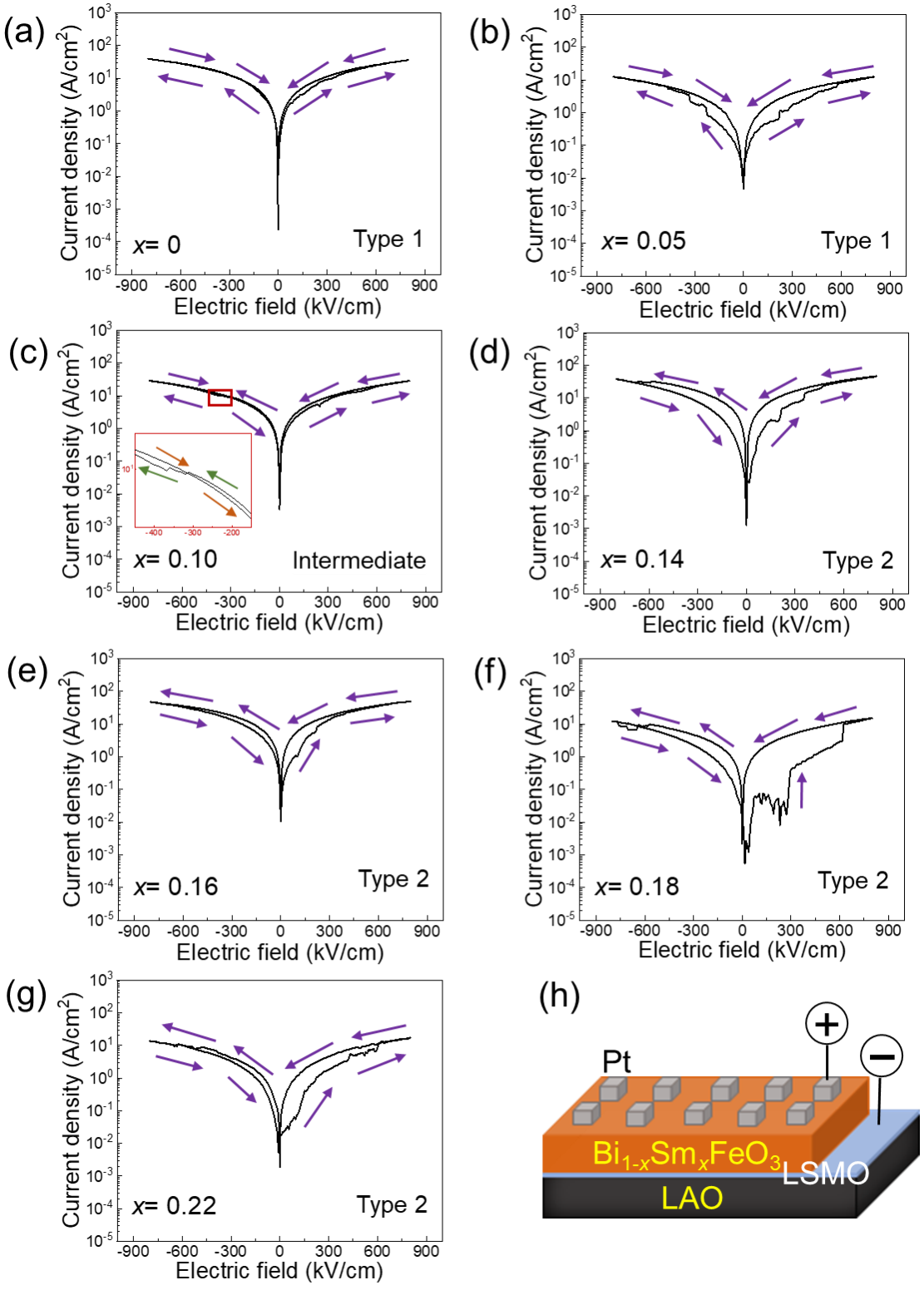

Figure 8-7. Typical I-V curves of BSFO/LSMO//LAO (001) films with *x* = (a) 0, (b) 0.05, (c) 0.10, (d) 0.14, (e) 0.16, (f) 0.18, and (g) 0.22 measured at different electric fields, (h) the setup for the I-V measurements.

Polarization-mediated and defect-dominated mechanisms are the two main pathways reported to explain the resistive switching phenomenon in ferroelectric heterostructures. [235, 236] Both mechanisms modulate the potential profile of a Schottky-like barrier formed at the Pt/BFO and/or LSMO/BFO interface. [235] As proved from the WDS results in **Chapter 7 and Table 8-1**, our as-prepared BSFO films are Bi deficient, which leads to the increase of the valence of Fe ions and confers p-type characteristics to $Bi_{1-x-\delta}Sm_xFeO_3$ films (δ represents the Bi deficiency).

In pure BFO (x = 0) and low doping BSFO (x = 0.05) films, there is a high concentration of bismuth vacancies (V_{Bi}''') with Bi deficiency of 30%, which can induce plenty of mobile positive holes $h^{\bullet}$. Thus, the films show defect-dominated resistive switching behavior. When a positive voltage is applied from the top electrode Pt, the positive charged $h^{\bullet}$ will move and accumulate at the BFO/LSMO interface. This leads to an enrichment region of holes or oxygen vacancies (p-type semiconductor) near the BFO/LSMO interface and an enrichment region of electrons or bismuth vacancies (n-type semiconductor) near the Pt/BFO interface. The BFO/LSMO heterostructures consequently show an HRS to LRS when the applied voltage from 0 -> $+V_{max}$ ->0. When an opposite voltage is applied, the distribution of defects (i.e., bismuth vacancies, holes, or oxygen vacancies and electrons) recovers to the initial state. Hence, an HRS is observed. With further applied a negative voltage, an opposite p-n junction is formed due to the redistribution of the defects, which leads to an LRS. Therefore, a type 1 current flow with the HRS->LRS->HRS->LRS is formed. [235]

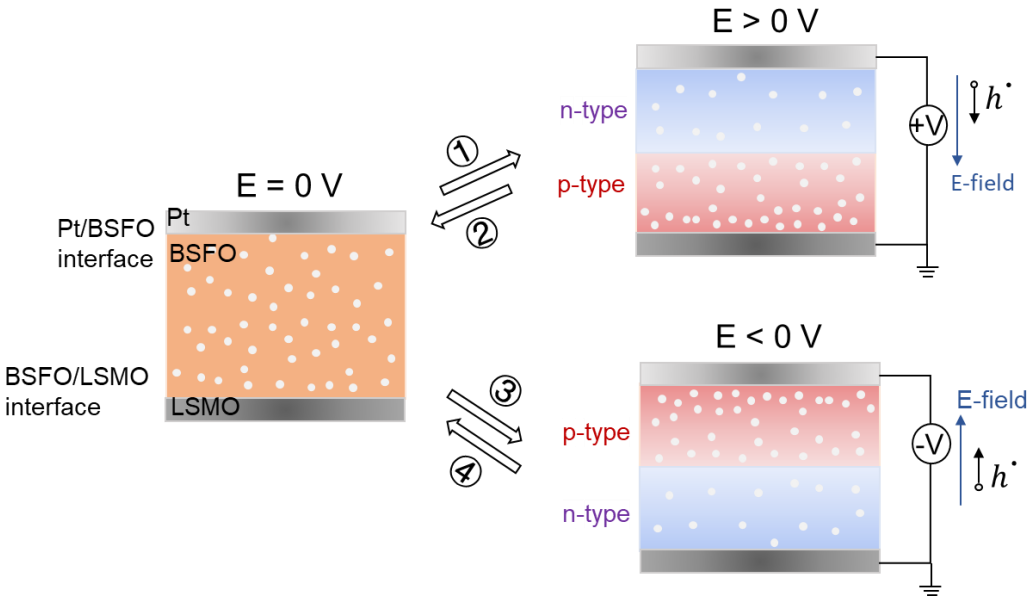

Figure 8-8. Schematic of resistive switching mechanism with the migration of defects under the applied electric field. The numbers indicate the direction of the applied voltage: ① 0 -> + V_{max}, ② + V_{max} -> 0, ③ 0 -> - V_{max}, ④ - V_{max} -> 0.

As Sm substitution is increased, not only the Bi volatilization is suppressed, but also the ability of the polarization reversal is enhanced due to the multiphase coexistence. Hence, the polarization plays a dominant role in the switching behavior. The resistive switching happens as follows:

Under positive voltage from 0 -> +V_{max}, the induced poled-down polarization leads to the upward band bending at the interface of BSFO/LSMO, which increases the Schottky barrier height and, thus, an HRS. With the decrease of the applied positive voltage from +V_{max} to 0 V, the Schottky barrier height decreases and leads to an LRS obtained. When a negative voltage is applied from 0 -> -V_{max}, a reduced Schottky barrier height is achieved due to the downward band bending induced from the upward polarization. Hence, an LRS is retained. With the gradual decline of the negative voltage, an HRS is detected.

Thus, type 2 current flow with the HRS->LRS->LRS->HRS is attained. Note that both the defects and polarization reversal attribute to the resistive switching behavior in all BSFO films. At a lower concentration of Sm substitution, defects dominate. When there is a high amount of Sm substitution, it is polarization-dominated.

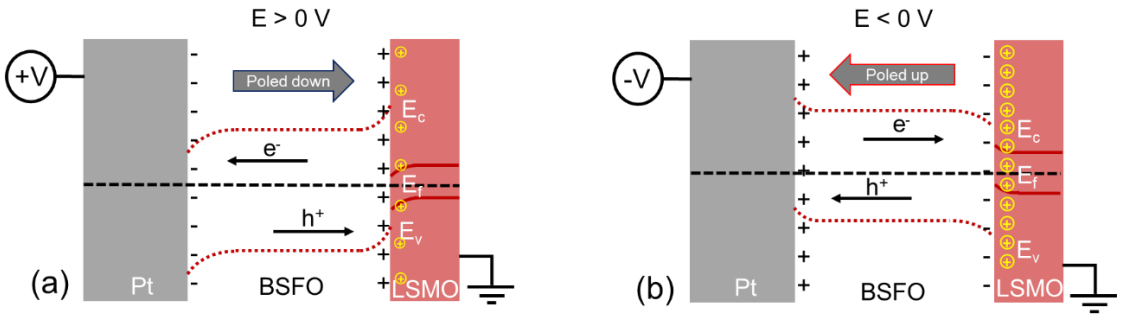

Figure 8-9. Schematic of resistive switching mechanism with the band diagram alternation under the (a) forward bias and (b) reverser bias.

8.4 Summary

The evolution of domain structure, electrical properties (including piezoelectric properties, conductivity behavior, as well as ferroelectric properties) of BSFO films as a function of Sm substitution is found. An MPB located between 0.14 and 0.16 is achieved, which is higher than the MPB composition at x = 0.14 in the compressive strain-free PLD-derived BSFO on STO.

(1) The A-site substitution with smaller Bi^{3+} leads to a decrease of PFM amplitude magnitude. While an enhanced domain switching behavior is attained with $x \leqslant 0.16$. Beyond MPB composition (x = 0.18 and 0.22), weak ferroelectricity is still observed in paraelectric O phase predominant films due to the existence of a minority ferroelectric T' phase.

(2) A transition from a single ferroelectric square-shaped hysteresis loop to a slightly distorted double (antiferroelectric like) hysteresis loop is induced with the Sm^{3+} doping content increasing from 0.14 to 0.16.

(3) Poled-up domains (polarization direction away from the bottom electrode) show higher conductivity before the MPB composition. In addition, the reading bias needed to trigger the higher conductivity in the poled-up regions is lowered with the increasing Sm substitution.

(4) A transition of the current flow under the external bias from "HRS->LRS->HRS->LRS" to "HRS->LRS->LRS->HRS" is observed due to the competition of the defects and the polarization state predominant on the Schottky barrier height.

The synergetic effect of chemical pressure and compressive strain grants BFO films versatile phase structures and thus, functional physical properties. These findings suggest that a complex phase configuration at an MPB can be constructed to introduce multifunctional physical properties.

Chapter 9. Summary of the Thesis and Future Work

9.1 Summary

In this thesis, the phase structure and electrical properties of chemical solution deposition (CSD) fabricated $BiFeO_3$ (BFO) films are studied using strain and site engineering. The film's strain engineering properties are investigated by comparing films fabricated on two different substrates viz. $SrTiO_3$ (STO) (001) and $LaAlO_3$ (LAO) (001) respectively. The -4.4% in-plane compressive epitaxial strain imposed by the LAO substrate can stabilize a tetragonal-like (T') phase, which is absent for films made on STO. Site engineering is investigated by comparing the effects of with and without A-site substitution with Sm. The chemical pressure of A-site substitution with Sm leads to a deformation of the crystal structure from rhombohedral (R) phase to orthorhombic (O) phase. The ensuing structural-transition-induced morphotropic phase boundary (MPB) effect is observed. The evolution of the crystal structure, domain feature, and ferroelectric properties and leakage current behaviors have been studied by X-ray diffraction (XRD), piezoresponse force microscopy (PFM) techniques as well as polarization-electric field (P-E) and I-V hysteresis techniques.

The significant findings are summarized below:

(1) Phase-pure epitaxial BFO films with a homogeneous mixed-phase structure are synthesized on (001)-oriented LAO substrates. The phase development of the BFO thin film and its leakage current characteristics have been systematically investigated as functions of thickness (number of spin-coated layers and precursor concentration) and the heat treatment process (heating temperature and dwell time). The results show that the T′-phase fraction changes dramatically from 35% (45 nm thick single layer) to 10% (250 nm thick four-layer film). In a two-layer film (80 nm) configuration, the T′-phase fraction is further tuned. When annealing at 640 °C for 30 min, this mixed-phase BFO film, despite its high T′-phase fraction (28%), shows the lowest leakage current (<0.1 A/cm^2 at <500 kV/cm), comparable to 200 nm pulsed laser deposition (PLD)-grown pure R-BFO thin films. In contrast to the observed bulk-limited Ohmic or space-charge-limited-conduction (SCLC)-predominant mechanism in pure R′-phase and low T′-phase-fraction BFO thin films, the high T′-phase fraction

(28%) mixed-phase BFO film displays an interface-limited Schottky emission to an SCLC mechanism transition with increasing the electric field. (The results are included in **Chapter 4 and Chapter 5**) (Published as Jinling Zhou et al. Tuning Phase Fractions and Leakage Properties of Chemical Solution Deposition-Derived Mixed-Phase $BiFeO_3$ Thin Films. *ACS Applied Electronic Materials*, 2020, **2**: 4099-4110.)

(2) RE element Sm is introduced into the BFO lattice. In this work, STO substrates which have a close lattice parameter with BFO, are chosen to minimize the mismatch strain effect on the phase composition. First, the gelation chemistry of the Sm added BFO precursors is investigated. The species of metal cations affect the reaction rate between hydrolysis reaction and esterification reaction, and thus, determine the gelation process. The crystalized $Bi_{1-x}Sm_xFeO_3$ (BSFO) films demonstrated a R phase structure with a typical polydomain feature. The paraelectric O phase and antipolar phase began to form from x = 0.10. The Sm doping greatly improved the ferroelectricity of BFO films. At x = 0.14, a well-developed polarization hysteresis loop is acquired. When the further increase of Sm composition to 0.15, we see the onset of a double hysteresis with a slightly distorted PE loop. (The results are included in **Chapter 6**)

(3) Sm-doped BFO films are deposited on LAO substrates. The synergetic effect of the compressive strain and chemical pressure provides a complex phase evolution in BSFO/LSMO//LAO (LSMO: $La_{0.67}Sr_{0.33}MnO_3$) system. 2D XRD maps show ½ spots appearance from x = 0.14, indicating the O phase existence, and get stronger with the increasing Sm content. In addition, the content of Sm substitution has an influence on the phase configuration of the T' and rhombohedral-like (R') phases. When the Sm content increases from 0 to 0.14, the R'-phase fraction decreases and correspondingly T'-phase fraction increases. When we further increased the Sm content, the T'-phase fraction started to decrease and the decrease of R'-phase fraction became slow. Thus, we infer that a structural transition from T'-R' to T'-R'-O, and then to T'-O phase as a function of Sm composition. (The results are included in **Chapter 7**)

(4) The evolution of domain structure, electrical properties (including piezoelectric properties, conductivity behavior, as well as ferroelectric properties) of BSFO/LSMO//LAO films as a function of Sm substitution is further studied. An MPB located between 0.14 and 0.16 is achieved. This is higher than the MPB composition at x = 0.14 (±0.015) in the compressive strain-free PLD-derived BSFO on STO. [192] The A-site substitution with smaller Bi^{3+} leads to a decrease of PFM amplitude magnitude. While an enhanced domain switching behavior is attained with $x \leqslant 0.16$. Beyond MPB composition (x = 0.18 and 0.22), weak ferroelectricity is still observed in paraelectric O phase predominated films due to the existence of a minority ferroelectric T' phase. A transition from a single ferroelectric square-shaped hysteresis loop to a slightly distorted double hysteresis loop is induced with the Sm^{3+} doping content increasing from 0.14 to 0.16. Poled-up domains (polarization direction away from the bottom electrode) show higher conductivity with $x \leqslant 0.16$. In addition, the reading bias needed to trigger the higher conductivity in the poled-up regions is lowered with the increasing Sm substitution. A transition of the current flow under the external bias from "high resistance state (HRS)-> low resistance state (LRS)->HRS->LRS" to "HRS->LRS->LRS->HRS" is observed due to the competition of the defects and the polarization state predominated on the Schottky barrier height. (The results are included in **Chapter 8**)

The successfully design of the crystal structure of BFO films offers an exciting tuning strategy for perovskite oxide films and thus their multifunctional properties through the CSD method.

9.2 Suggestions for Future Work

A detailed study on the tuning of the phase structure of BFO films using strain engineering or/and site engineering and an understanding of the relationship between the structural development and the evolution of electrical properties are presented. The findings of this work provide meaningful guidance for the tailoring of the multifunctional properties of perovskite oxides films through the design of phase composition. Based on these results, the following warrant further investigation.

(1) It has been demonstrated that the introduction of both epitaxial compressive strain and Sm substitution can stabilize the complex multiple phases and induce phase transition. These closely abutting areas of different phases usually exist only under differing electrical or mechanical boundary conditions. It is likely at these boundaries non-trivial topological defects, including vortices (antivortices), bubble domains, and flux-closure domains exist. [237] Therefore, PFM and transmission electron microscopy (TEM) techniques to further investigate the polarization configuration at the multiphase BSFO samples may produce exciting new results.

(2) Superlattices, where periodical arrays of two or more types of perovskite compounds are stacked, may yield phases and properties due to interface coupling that may not exist in the constituent parents. Here, we can use the CSD method to achieve the alternating growth of dielectric (STO) and ferroelectric (BSFO) layers, or even achieved graded compositions as shown by Bastani et al [238]. The interaction between these neighboring layers is expected to lead to the continuous tailoring of the domains, and improved dielectric permittivity and electromechanical coefficients, as well as possibly multiferroic behavior.

(3) Flexible piezoelectric thin films are currently highly pursued in areas, such as biomedicine and wearable electronics. The deposition of the BSFO thin films can be also extended onto the flexible substrates through the CSD method. An initial attempt to deposit BFO films onto flexible Mica substrates showed high-quality as-prepared BFO/Mica films. Next, the RE doping can be further introduced into the system to realize its functional properties.

References

[1] M. N. Iliev, M. V. Abrashev, D. Mazumdar, V. Shelke and A. Gupta, Polarized Raman Spectroscopy of Nearly Tetragonal $BiFeO_3$ Thin Films, *Physical Review B*, 2010, **82**(1): 014107.

[2] H. M. Tütüncü and G. P. Srivastava, Electronic Structure and Lattice Dynamical Properties of Different Tetragonal Phases of $BiFeO_3$, *Physical Review B*, 2008, **78**(23): 235209.

[3] Y. Yang, J. Y. Sun, K. Zhu, Y. L. Liu and L. Wan, Structure Properties of $BiFeO_3$ Films Studied by Micro-Raman Scattering, *Journal of Applied Physics*, 2008, **103**(9): 093532.

[4] M. K. Singh, S. Ryu and H. M. Jang, Polarized Raman Scattering of Multiferroic $BiFeO_3$ Thin Films with Pseudo-Tetragonal Symmetry, *Physical Review B*, 2005, **72**(13): 132101.

[5] M. V. Abrashev, M. N. Iliev, H. -G. Lee, Popov, V. N., Y. Y. Sun, C. Thomsen, R. L. Meng, and C. W. Chu, Raman Spectroscopy of Orthorhombic Perovskitelike $YMnO_3$ and $LaMnO_3$, *Physical Review B*, **57**(5): 2872.

[6] D. Sando, A. Barthelemy and M. Bibes, $BiFeO_3$ Epitaxial Thin Films and Devices: Past, Present and Future, *Journal of Physics: Condensed Matter*, 2014, **26**(47): 473201.

[7] S. Fujino, M. Murakami, V. Anbusathaiah, S. H. Lim, N. Valanoor, C. J. Fennie, M. Wuttig, L. Salamanca-Riba and I. Takeuchi, Combinatorial Discovery of A Lead-Free Morphotropic Phase Boundary in A Thin-Film Piezoelectric Perovskite, *Applied Physics Letters*, 2008, **92**(20): 202904.

[8] D. Kan, L. Pálová, V. Anbusathaiah, C. J. Cheng, S. Fujino, N. Valanoor, K. M. Rabe and I. Takeuchi, Universal Behavior and Electric-Field-Induced Structural Transition in Rare-Earth-Substituted $BiFeO_3$, *Advanced Functional Materials*, 2010, **20**(7): 1108-1115.

[9] R. J. Zeches, M. D. Rossell, J. X. Zhang, A. J. Hatt, Q. He, C. H. Yang, A. Kumar, C. H. Wang, A. Melville, C. Adamo, G. Sheng, Y. H. Chu, J. F. Ihlefeld, R. Erni, C. Ederer, V. Gopalan, L. Q. Chen, D. G. Schlom, N. A. Spaldin, L. W. Martin and R. Ramesh, A Strain-Driven Morphotropic Phase Boundary in $BiFeO_3$, *Science*, 2009, **326**(5955): 977-980.

[10] J. Wang, J. B. Neaton, H. Zheng, N. Valanoor, S. B. Ogale, B. Liu, D. Viehland, V. Vaithyanathan, D. G. Schlom, U. V. Waghmare, N. A. Spaldin, K. M. Rabe, M. Wuttig and R. Ramesh, Epitaxial $BiFeO_3$ Multiferroic Thin Film Heterostructures, *Science*, 2003, **299**(5613): 1719-1722.

[11] N. Deepak, P. Carolan, L. Keeney, P. F. Zhang, M. E. Pemble and R. W. Whatmore, Bismuth Self-Limiting Growth of Ultrathin $BiFeO_3$ Films, *Chemistry of materials*, 2015, **27**(19): 6508-

6515.

[12] Y.-H. Lee, J.-M. Wu and C.-H. Lai, Influence of La Doping in Multiferroic Properties of $BiFeO_3$ Thin Films, *Applied Physics Letters*, 2006, **88**(4): 042903.

[13] H. W. Chang, F. T. Yuan, K. T. Tu, Y. C. Lo, S. Y. Tu, C. R. Wang, A. B. Yang, C. S. Tu, S. U. Jen and W. C. Chang, Effect of Ba Substitution on The Multiferroic Properties of $BiFeO_3$ Films on Glass Substrates, *Journal of Applied Physics*, 2015, **117**(17): 17C734.

[14] Q. Zhang, H.-H. Huang, D. Sando, M. Summers, P. Munroe, O. Standard and N. Valanoor, Mixed-Phase Bismuth Ferrite Thin Films by Chemical Solution Deposition, *Journal of Materials Chemistry C*, 2018, **6**: 2882-2888.

[15] C. J. Cheng, D. Kan, S. H. Lim, W. R. McKenzie, P. R. Munroe, L. G. Salamanca-Riba, R. L. Withers, I. Takeuchi and N. Valanoor, Structural Transitions and Complex Domain Structures Across A Ferroelectric-to-Antiferroelectric Phase Boundary in Epitaxial Sm-Doped $BiFeO_3$ Thin Films, *Physical Review B*, 2009, **80**(1): 014109.

[16] W. Sun, J.-F. Li, Q. Yu and L.-Q. Cheng, Phase Transition and Piezoelectricity of Sol–Gel-Processed Sm-Doped $BiFeO_3$ Thin Films on Pt(111)/Ti/SiO_2/Si Substrates, *Journal of Materials Chemistry C*, 2015, **3**(9): 2115-2122.

[17] D. Damjanovic, Ferroelectric, Dielectric and Piezoelectric Properties of Ferroelectric Thin Films and Ceramics, *Reports on Progress in Physics*, 1998, **61**: 1267–1324.

[18] S. C. Abrahams, S. K. Kurtz and P. B. Jamieson, Atomic Displacement Relationship to Curie Temperature and Spontaneous Polarization in Displacive Ferroelectrics, *Physical Review*, 1968, **172**(2): 551-553.

[19] J. B. Neaton, C. Ederer, U. V. Waghmare, N. A. Spaldin and K. M. Rabe, First-Principles Study of Spontaneous Polarization in Multiferroic $BiFeO_3$, *Physical Review B*, 2005, **71**(1): 014113.

[20] Z. Sroubek, Mechanism of Negative Ion Emission from Surfaces of Ferroelectrics, *Surface Science*, 2012, **606**(15-16): 1327-1330.

[21] L. Jin, F. Li and S. Zhang, Decoding The Fingerprint of Ferroelectric Loops: Comprehension of The Material Properties and Structures, *Journal of the American Ceramic Society*, 2014, **97**(1): 1-27.

[22] J. Valasek, Piezo-Electric and Allied Phenomena in Rochelle Salt, *Physical Review*, 1921, **17**(4): 475-481.

[23] E. J. Baran, Structural Chemistry and Physicochemical Properties of Perovskite-Like

Materials, *Catalysis today*, 1990, **8**(2): 133-151.

[24] D. Ricinschi, K. Y. Yun and M. Okuyama, A Mechanism for The 150 μC cm^{-2} Polarization of $BiFeO_3$ Films Based on First-Principles Calculations and New Structural Data, *Journal of Physics: Condensed Matter*, 2006, **18**(6): L97-L105.

[25] J. Young and J. M. Rondinelli, Atomic Scale Design of Polar Perovskite Oxides without Second-Order Jahn–Teller Ions, *Chemistry of materials*, 2013, **25**(22): 4545-4550.

[26] S. Luo and W. A. Daoud, Recent Progress in Organic–Inorganic Halide Perovskite Solar Cells: Mechanisms and Material Design, *Journal of Materials Chemistry A*, 2015, **3**(17): 8992-9010.

[27] T. Minemoto, Perovskite Solar Cells, Available from: http://www.ritsumei.ac.jp/se/r-e/takakuralab/html_storage/intro_perov2015.html.

[28] V. M. Goldschmidt, The Laws of Crystal Chemistry, *Naturwissenschaften*, 1926, **14**: 477-485.

[29] P. Marton, I. Rychetsky and J. Hlinka, Domain Walls of Ferroelectric $BaTiO_3$ within The Ginzburg-Landau-Devonshire Phenomenological Model, *Physical Review B*, 2010, **81**(14): 144125.

[30] V. Boddu, F. Endres and P. Steinmann, Molecular Dynamics Study of Ferroelectric Domain Nucleation and Domain Switching Dynamics, *Scientific Reports*, 2017, **7**(1): 806.

[31] D. Li and D. A. Bonnell, Controlled Patterning of Ferroelectric Domains: Fundamental Concepts and Applications, *Annual Review of Materials Research*, 2008, **38**(1): 351-368.

[32] Q. Zhang, D. Sando and N. Valanoor, Chemical Route Derived Bismuth Ferrite Thin Films and Nanomaterials, *Journal of Materials Chemistry C*, 2016, **4**(19): 4092-4124.

[33] Y. A. Genenko, J. Glaum, M. J. Hoffmann and K. Albe, Mechanisms of Aging and Fatigue in Ferroelectrics, *Materials Science and Engineering: B*, 2015, **192**: 52-82.

[34] H. W. Jang, D. Ortiz, S.-H. Baek, C. M. Folkman, R. R. Das, P. Shafer, Y. Chen, C. T. Nelson, X. Pan, R. Ramesh and C.-B. Eom, Domain Engineering for Enhanced Ferroelectric Properties of Epitaxial (001) $BiFeO_3$ Thin Films, *Advanced Materials*, 2009, **21**(7): 817-823.

[35] J.-W. Lee, C.-S. Park, M. Kim and H.-E. Kim, Effects of Residual Stress on The Electrical Properties of PZT Films, *Journal of the American Ceramic Society*, 2007, **90**(4): 1077-1080.

[36] S. Dussan, A. Kumar, J. F. Scott and R. S. Katiyar, Effect of Electrode Resistance on Dielectric and Transport Properties of Multiferroic Superlattice: A Impedance Spectroscopy Study, *AIP Advances*, 2012, **2**(3): 032136.

[37] B. Jaffe, R. S. Roth and S. Marzullo, Piezoelectric Properties of Lead Zirconate-Lead Titanate Solid-Solution Ceramics, *Journal of Applied Physics*, 1954, **25**(6): 809-810.

[38] D. Damjanovic, A Morphotropic Phase Boundary System Based on Polarization Rotation and Polarization Extension, *Applied Physics Letters*, 2010, **97**(6): 062906.

[39] H. Fu and R. E. Cohen, Polarization Rotation Mechanism for Ultrahigh Electromechanical Response in Single-Crystal Piezoelectrics, *Nature*, 2000, **403**: 281-283.

[40] M. Ahart, M. Somayazulu, R. E. Cohen, P. Ganesh, P. Dera, H. K. Mao, R. J. Hemley, Y. Ren, P. Liermann and Z. Wu, Origin of Morphotropic Phase Boundaries in Ferroelectrics, *Nature*, 2008, **451**(7178): 545-548.

[41] B. Jaffe, W. R. Cook and H. Jaffe, Piezoelectric Ceramics, 1971.

[42] B. Noheda, Structure and High-Piezoelectricity in Lead Oxide Solid Solutions, *Current Opinion in Solid State and Materials Science*, 2002, **6**: 27-34.

[43] B. Noheda, D. E. Cox, G. Shirane, R. Guo, B. Jones and L. E. Cross, Stability of The Monoclinic Phase in The Ferroelectric Perovskite $PbZr_{1-x}Ti_xO_3$, *Physical Review B*, 2000, **63**(1): 014103.

[44] D. Viehland, Symmetry-Adaptive Ferroelectric Mesostates in Oriented $Pb(BI_{1/3}BII_{2/3})O_3$–$PbTiO_3$ Crystals, *Journal of Applied Physics*, 2000, **88**(8): 4794-4806.

[45] Y. M. Jin, Y. U. Wang, A. G. Khachaturyan, J. F. Li and D. Viehland, Conformal Miniaturization of Domains with Low Domain-Wall Energy: Monoclinic Ferroelectric States near The Morphotropic Phase Boundaries, *Physcial Review Letters*, 2003, **91**(19): 197601.

[46] A. M. Glazer, P. A. Thomas, K. Z. Baba-Kishi, G. K. H. Pang and C. W. Tai, Influence of Short-Range and Long-Range Order on The Evolution of The Morphotropic Phase Boundary in $Pb(Zr_{1-x}Ti_x)O_3$, *Physical Review B*, 2004, **70**(18): 184123.

[47] K. I. Park, S. Xu, Y. Liu, G. T. Hwang, S. J. Kang, Z. L. Wang and K. J. Lee, Piezoelectric $BaTiO_3$ Thin Film Nanogenerator on Plastic Substrates, *Nano Letters*, 2010, **10**(12): 4939-4943.

[48] T. R. Shrout and S. Zhang, Lead-Free Piezoelectric Ceramics: Alternatives for PZT?, *Journal of Electroceramics*, 2007, **19**(1): 113-126.

[49] Y.-J. Dai, X.-W. Zhang and K.-P. Chen, Morphotropic Phase Boundary and Electrical Properties of $K_{1-x}Na_xNbO_3$ Lead-Free Ceramics, *Applied Physics Letters*, 2009, **94**(4): 042905.

[50] Y. Saito, H. Takao, T. Tani, T. Nonoyama, K. Takatori, T. Homma, T. Nagaya and M. Nakamura, Lead-Free Piezoceramics, *Nature*, 2004, **432**(2013): 81-84.

[51] J. König, B. Jančar and D. Suvorov, New $Na_{0.5}Bi_{0.5}TiO_3$-$NaTaO_3$-Based Perovskite Ceramics,

Journal of the American Ceramic Society, 2007, **90**(11): 3621-3627.

[52] H. Irie, M. Miyayama and T. Kudo, Structure Dependence of Ferroelectric Properties of Bismuth Layer-Structured Ferroelectric Single Crystals, *Journal of Applied Physics*, 2001, **90**(8): 4089-4094.

[53] X. Xie, Z. Zhou, R. Liang and X. Dong, Significantly Enhanced Piezoelectric Performance in $Bi_4Ti_3O_{12}$-based High-Temperature Piezoceramics via Oxygen Vacancy Defects Tailoring, *Journal of Materiomics*, 2021, **7**(1): 59-68.

[54] C.-M. Wang and J.-F. Wang, Aurivillius Phase Potassium Bismuth Titanate: $K_{0.5}Bi_{4.5}Ti_4O_{15}$, *Journal of the American Ceramic Society*, 2008, **91**(3): 918-923.

[55] Y. Chen, D. Liang, Q. Wang and J. Zhu, Microstructures, Dielectric, and Piezoelectric Properties of W/Cr Co-Doped $Bi_4Ti_3O_{12}$ Ceramics, *Journal of Applied Physics*, 2014, **116**(7): 074108.

[56] W. Jiang, W. Cao, X. Yi and H. Chen, The Elastic and Piezoelectric Properties of Tungsten Bronze Ferroelectric Crystals $(Sr_{0.7}Ba_{0.3})_2NaNb_5O_{15}$ and $(Sr_{0.3}Ba_{0.7})_2NaNb_5O_{15}$, *Journal of Applied Physics*, 2005, **97**(9): 094106.

[57] P. K. Panda and B. Sahoo, PZT to Lead Free Piezo Ceramics: A Review, *Ferroelectrics*, 2015, **474**(1): 128-143.

[58] D. Lebeugle, D. Colson, A. Forget, M. Viret, P. Bonville, J. F. Marucco and S. Fusil, Room-Temperature Coexistence of Large Electric Polarization and Magnetic Order in $BiFeO_3$ Single Crystals, *Physical Review B*, 2007, **76**(2): 024116.

[59] N. A. Spaldin, M. Fiebig and M. Mostovoy, The Toroidal Moment in Condensed-Matter Physics and Its Relation to The Magnetoelectric Effect, *Journal of Physics: Condensed Matter*, 2008, **20**(43): 434203.

[60] I. Sosnowska, T. P. Neumaier and Steichele E., Spiral Magnetic Ordering in Bismuth Ferrite, *Solid State Physics*, 1982, **15**(23): 4835-4846.

[61] C. Ederer and N. A. Spaldin, Weak Ferromagnetism and Magnetoelectric Coupling in Bismuth Ferrite, *Physical Review B*, 2005, **71**(6): 060401.

[62] Y.-H. Chu, L. W. Martin, M. B. Holcomb and R. Ramesh, Controlling Magnetism with Multiferroics, *Materials Today*, 2007, **10**(10): 16-23.

[63] J. Wu, Z. Fan, D. Xiao, J. Zhu and J. Wang, Multiferroic Bismuth Ferrite-Based Materials for Multifunctional Applications: Ceramic Bulks, Thin Films and Nanostructures, *Progress in Materials Science*, 2016, **84**: 335-402.

[64] M. Bibes and A. Barthélémy, Multiferroics: Towards Amagnetoelectric Memory, *Nature materials*, 2008, **7**(6): 425-426.

[65] P. Ravindran, R. Vidya, A. Kjekshus, H. Fjellvåg and O. Eriksson, Theoretical Investigation of Magnetoelectric Behavior in $BiFeO_3$, *Physical Review B*, 2006, **74**(22): 224412.

[66] S. Hiromi, H. Naganuma and S. Okamura, Optical Properties of Multiferroic $BiFeO_3$ Films, in *Materials Science - Advanced Topics*, 2013, **Chapter 2**: 35-61.

[67] R. Palai, R. S. Katiyar, H. Schmid, P. Tissot, S. J. Clark, J. Robertson, S. A. T. Redfern, G. Catalan and J. F. Scott, *β* Phase and *γ–β* Metal-Insulator Transition in Multiferroic $BiFeO_3$, *Physical Review B*, 2008, **77**(1): 014110.

[68] D. Lebeugle, D. Colson, A. Forget and M. Viret, Very Large Spontaneous Electric Polarization in $BiFeO_3$ Single Crystals at Room Temperature and Its Evolution under Cycling Fields, *Applied Physics Letters*, 2007, **91**(2): 022907.

[69] Z. Chen, Z. Luo, C. Huang, Y. Qi, P. Yang, L. You, C. Hu, T. Wu, J. Wang, C. Gao, T. Sritharan and L. Chen, Low-Symmetry Monoclinic Phases and Polarization Rotation Path Mediated by Epitaxial Strain in Multiferroic $BiFeO_3$ Thin Films, *Advanced Functional Materials*, 2011, **21**(1): 133-138.

[70] D. Mazumdar, V. Shelke, M. Iliev, S. Jesse, A. Kumar, S. V. Kalinin, A. P. Baddorf and A. Gupta, Nanoscale Switching Characteristics of Nearly Tetragonal $BiFeO_3$ Thin Films, *Nano Letters*, 2010, **10**(7): 2555-2561.

[71] A. R. Damodaran, E. Breckenfeld, A. K. Choquette and L. W. Martin, Stabilization of Mixed-Phase Structures in Highly Strained $BiFeO_3$ Thin Films via Chemical-Alloying, *Applied Physics Letters*, 2012, **100**(8): 082904.

[72] D. Kan, V. Anbusathaiah and I. Takeuchi, Chemical Substitution-Induced Ferroelectric Polarization Rotation in $BiFeO_3$, *Advanced Materials*, 2011, **23**(15): 1765-1769.

[73] D. Sando, Strain and Orientation Engineering in ABO_3 Perovskite Oxide Thin Films, *Journal of Physics: Condensed Matter*, 2022, **34**(15): 153001.

[74] L. Yan, H. Cao, J. Li and D. Viehland, Triclinic Phase in Tilted (001) Oriented $BiFeO_3$ Epitaxial Thin Films, *Applied Physics Letters*, 2009, **94**(13): 132901.

[75] F. Yan, M.-O. Lai, L. Lu and T. J. Zhu, Enhanced Multiferroic Properties and Valence Effect of Ru-Doped $BiFeO_3$ Thin Films, *The Journal of Physical Chemistry C*, 2010, **114**(15): 6994-6998.

[76] W.-H. Kim and J. Y. Son, The Effects of La Substitution on Ferroelectric Domain Structure and Multiferroic Properties of Epitaxially Grown $BiFeO_3$ Thin Films, *Applied Physics Letters*,

2013, **103**(13): 132907.

[77] Z. Zhong, Y. Sugiyama and H. Ishiwara, Large Remanent Polarization in Sm-Substituted $BiFeO_3$ Thin Film Formed by Chemical Solution Deposition, *Japanese Journal of Applied Physics*, 2010, **49**(4): 041502.

[78] Z. Hu, M. Li, J. Liu, L. Pei, J. Wang, B. Yu and X. Zhao, Structural Transition and Multiferroic Properties of Eu-Doped $BiFeO_3$ Thin Films, *Journal of the American Ceramic Society*, 2010, **93**(9): 2743-2747.

[79] M. Li, Z. Hu, L. Pei, J. Liu, J. Wang, B. Yu and X. Zhao, Multiferroic Properties of Rare-Earth Eu and Nd Doped $BiFeO_3$ Thin Films, *Ferroelectrics*, 2011, **410**(1): 3-10.

[80] Y. Wang and C.-W. Nan, Effect of Tb Doping on Electric and Magnetic Behavior of $BiFeO_3$ Thin Films, *Journal of Applied Physics*, 2008, **103**(2): 024103.

[81] C. Chen, Z. Liu, G. Wang and X. Feng, Fabrication and Characterization of Compositionally Graded $Bi_{1-x}Gd_xFeO_3$ Thin Films, *Materials Science-Poland*, 2014, **32**(3): 498-502.

[82] Z. Quan, W. Liu, H. Hu, S. Xu, B. Sebo, G. Fang, M. Li and X. Zhao, Microstructure, Electrical and Magnetic Properties of Ce-Doped $BiFeO_3$ Thin Films, *Journal of Applied Physics*, 2008, **104**(8): 084106.

[83] K. Brinkman, T. Iijima, K. Nishida, T. Katoda and H. Funakubo, The Influence of Acceptor Doping on The Structure and Electrical Properties of Sol-Gel Derived $BiFeO_3$ Thin Films, *Ferroelectrics*, 2007, **357**(1): 35-40.

[84] Y. J. Kim, J. W. Kim and S. S. Kim, Frequency Dependent Ferroelectric and Electrical Properties of (Ho, Ni) Co-Doped $BiFeO_3$ Thin Films, *Journal of Sol-Gel Science and Technology*, 2013, **66**(1): 38-42.

[85] J. M. Luo, S. P. Lin, Y. Zheng and B. Wang, Nonpolar Resistive Switching in Mn-Doped $BiFeO_3$ Thin Films by Chemical Solution Deposition, *Applied Physics Letters*, 2012, **101**(6): 062902.

[86] J.-Z. Huang, Y. Wang, Y. Lin, M. Li and C. W. Nan, Effect of Mn Doping on Electric and Magnetic Properties of $BiFeO_3$ Thin Films by Chemical Solution Deposition, *Journal of Applied Physics*, 2009, **106**(6): 063911.

[87] Y. Wang, A Giant Polarization Value in Bismuth Ferrite Thin Films, *Journal of Alloys and Compounds*, 2011, **509**(41): L362-L364.

[88] H. Hojo, K. Onuma, Y. Ikuhara and M. Azuma, Structural Evolution and Enhanced Piezoresponse in Cobalt-Substituted $BiFeO_3$ Thin Films, *Applied Physics Express*, 2014, **7**(9):

091501.

[89] G. N. Sharma, S. Dutta, A. Pandey, S. K. Singh and R. Chatterjee, Microstructure and Improved Electrical Properties of Ti-Substituted $BiFeO_3$ Thin Films, *Materials Research Bulletin*, 2017, **95**: 223-228.

[90] J. K. Kim, S. S. Kim, W.-J. Kim, A. S. Bhalla and R. Guo, Enhanced Ferroelectric Properties of Cr-Doped $BiFeO_3$ Thin Films Grown by Chemical Solution Deposition, *Applied Physics Letters*, 2006, **88**(13): 132901.

[91] S. K. Singh, H. Ishiwara and K. Maruyama, Room Temperature Ferroelectric Properties of Mn-Substituted $BiFeO_3$ Thin Films Deposited on Pt Electrodes Using Chemical Solution Deposition, *Applied Physics Letters*, 2006, **88**(26): 262908.

[92] S. K. Singh, H. Ishiwara, K. Sato and K. Maruyama, Microstructure and Frequency Dependent Electrical Properties of Mn-Substituted $BiFeO_3$ Thin Films, *Journal of Applied Physics*, 2007, **102**(9): 094109.

[93] P. Sharma and V. Verma, Structural, Magnetic and Electrical Properties of La and Mn Co-Substituted BFO Samples Prepared by The Sol–Gel Technique, *Journal of Magnetism and Magnetic Materials*, 2015, **374**: 18-21.

[94] W. Zhou, H. Deng, H. Cao, J. He, J. Liu, P. Yang and J. Chu, Effects of Sm and Mn Co-Doping on Structural, Optical and Magnetic Properties of $BiFeO_3$ Films Prepared by A Sol–Gel Technique, *Materials Letters*, 2015, **144**: 93-96.

[95] V. Verma, Structural, Electrical and Magnetic Properties of Rare-Earth and Transition Element Co-Doped Bismuth Ferrites, *Journal of Alloys and Compounds*, 2015, **641**: 205-209.

[96] X. Yan, G. Tan, W. Liu, H. Ren and A. Xia, Structural, Electric and Magnetic Properties of Dy and Mn Co-Doped $BiFeO_3$ Thin Films, *Ceramics International*, 2015, **41**(2): 3202-3207.

[97] J. Rout and R. N. P. Choudhary, Structural Phase Transition and Multiferroic Properties of $Bi_{0.8}A_{0.2}Fe_{0.8}Mn_{0.2}O_3$ (A = Ca, Sr), *Indian Journal of Physics*, 2017, **92**(5): 575-585.

[98] J. Liu, M. Li, Z. Hu, L. Pei, J. Wang, X. Liu and X. Zhao, Effects of Ion-Doping at Different Sites on Multiferroic Properties of $BiFeO_3$ Thin Films, *Applied Physics A*, 2010, **102**(3): 713-717.

[99] G. S. Arya, R. K. Kotnala and N. S. Negi, Enhanced Magnetic and Magnetoelectric Properties of In and Co Codoped $BiFeO_3$ Nanoparticles at Room Temperature, *Journal of Nanoparticle Research*, 2013, **16**(1): 2155.

[100] C.-J. Cheng, D. Kan, V. Anbusathaiah, I. Takeuchi and N. Valanoor, Microstructure-Electromechanical Property Correlations in Rare-Earth-Substituted $BiFeO_3$ Epitaxial Thin Films

at Morphotropic Phase Boundaries, *Applied Physics Letters*, 2010, **97**(21): 212905.

[101] C.-J. Cheng, A. Y. Borisevich, D. Kan, I. Takeuchi and N. Valanoor, Nanoscale Structural and Chemical Properties of Antipolar Clusters in Sm-Doped $BiFeO_3$ Ferroelectric Epitaxial Thin Films, *Chemistry of materials*, 2010, **22**(8): 2588-2596.

[102] F.-C. Chiu, A Review on Conduction Mechanisms in Dielectric Films, *Advances in Materials Science and Engineering*, 2014, **2014**: 1-18.

[103] C.-F. Chung, J.-P. Lin and J.-M. Wu, Influence of Mn and Nb Dopants on Electric Properties of Chemical-Solution-Deposited $BiFeO_3$ Films, *Applied Physics Letters*, 2006, **88**(24): 242909.

[104] C. Wang, M. Takahashi, H. Fujino, X. Zhao, E. Kume, T. Horiuchi and S. Sakai, Leakage Current of Multiferroic $(Bi_{0.6}Tb_{0.3}La_{0.1})FeO_3$ Thin Films Grown at Various Oxygen Pressures by Pulsed Laser Deposition and Annealing Effect, *Journal of Applied Physics*, 2006, **99**(5): 054104.

[105] G. W. Pabst, L. W. Martin, Y.-H. Chu and R. Ramesh, Leakage Mechanisms in $BiFeO_3$ Thin Films, *Applied Physics Letters*, 2007, **90**(7): 072902.

[106] D. H. Lowndes, D. B. Geohegan, A. A. Puretzky, D. P. Norton and C. M. Rouleau, Synthesis of Novel Thin-Film Materials by Pulsed Laser Deposition, *Science*, 1996, **273**(5277): 898-903.

[107] P. R. Willmott and J. R. Huber, Pulsed Laser Vaporization and Deposition, *Reviews of Modern Physics*, 2000, **72**(1): 315-328.

[108] P. J. Kelly and R. D. Arnell, Magnetron Sputtering: A Review of Recent Developments and Applications, *Vacuum*, 2000, **56**(3): 159-172.

[109] D. J. Eaglesham, Semiconductor Molecular-Beam Epitaxy at Low Temperatures, *Journal of Applied Physics*, 1995, **77**(8): 3597-3617.

[110] A. C. Jones, Molecular Design of Improved Precursors for The MOCVD of Electroceramic Oxides, *Journal of Materials Chemistry*, 2002, **12**(9): 2576-2590.

[111] A. Huang, A. D. Handoko, G. K. L. Goh, P. K. Pallathadka and S. Shannigrahi, Hydrothermal Synthesis of (00l) Epitaxial $BiFeO_3$ Films on $SrTiO_3$ Substrate, *CrystEngComm*, 2010, **12**(11): 3806.

[112] I. A. Velasco-Davalos, M. Moretti, M. Nicklaus, C. Nauenheim, S. Li, R. Nechache, C. Gomez-Yanez and A. Ruediger, Polar Properties of Hydrothermally Synthesized $BiFeO_3$ Thin Films, *Applied Physics A*, 2013, **115**(3): 1081-1085.

[113] I. A. Velasco-Davalos, F. Ambriz-Vargas, G. Kolhatkar, R. Thomas and A. Ruediger, Synthesis of $BiFeO_3$ Thin Films on Single-Terminated Nb: $SrTiO_3$ (111) Substrates by Intermittent Microwave Assisted Hydrothermal Method, *AIP Advances*, 2016, **6**(6): 065117.

[114] X. Qi, J. Dho, M. Blamire, Q. Jia, J.-S. Lee, S. Foltyn and J. L. MacManus-Driscoll, Epitaxial Growth of $BiFeO_3$ Thin Films by LPE and Sol–Gel Methods, *Journal of Magnetism and Magnetic Materials*, 2004, **283**(2-3): 415-421.

[115] R. W. Schwartz, Chemical Solution Deposition of Perovskite Thin Films, *Chemistry of materials*, 1997, **9**: 2325-2340.

[116] J. Fukushima, K. Kodaira and T. Matsushita, Preparation of Ferroelectric PZT Films by Thermal Decomposition of Organometallic Compounds, *Journal of materials science*, 1984, **19**(2): 595-598.

[117] K. D. Budd, S. K. Dey and D. A. Payne, Sol-Gel Processing of $PbTiO_3$, $PbZrO_3$, PZT, and PLZT Thin Films, 1985, University of Illinois, Urbana, Illinois 61801, USA.

[118] G. Teowee, K. McCarthy, F. McCarthy, T. J. Bukowski, T. P. Alexander and D. R. Uhlmann, Dielectric and Ferroelectric Properties of Sol-Gel Derived $BiFeO_3$ Films, *Integrated Ferroelectrics*, 2006, **18**(1-4): 329-337.

[119] C. Gutiérrez-Lázaro, I. Bretos, R. Jiménez, J. Ricote, H. E. Hosiny, D. Pérez-Mezcua, R. J. Jiménez Rioboó, M. García-Hernández, M. L. Calzada and R. Riman, Solution Synthesis of $BiFeO_3$ Thin Films onto Silicon Substrates with Ferroelectric, Magnetic, and Optical Functionalities, *Journal of the American Ceramic Society*, 2013, **96**(10): 3061-3069.

[120] S. Gupta, M. Tomar, V. Gupta, A. R. James, M. Pal, R. Guo and A. Bhalla, Optimization of Excess Bi Doping to Enhance Ferroic Orders of Spin Casted $BiFeO_3$ Thin Film, *Journal of Applied Physics*, 2014, **115**(23): 234105.

[121] Y. Nakamura, S. Nakashima and M. Okuyama, Influences of Surface Texture and BiFe Ratio on Electric Properties of $BiFeO_3$ Thin Films Prepared by Chemical Solution Deposition, *Japanese Journal of Applied Physics*, 2008, **47**(9): 7250-7253.

[122] X. Tang, J. Dai, X. Zhu, J. Lin, Q. Chang, D. Wu, W. Song, Y. Sun and X. Tan, Thickness-Dependent Dielectric, Ferroelectric, and Magnetodielectric Properties of $BiFeO_3$ Thin Films Derived by Chemical Solution Deposition, *Journal of the American Ceramic Society*, 2012, **95**(2): 538-544.

[123] Y. Wang, Y. Lin and C.-W. Nan, Thickness Dependent Dize Dffect of $BiFeO_3$ Films Grown on $LaNiO_3$-Buffered Si Substrates, *Journal of Applied Physics*, 2008, **104**(12): 123912.

[124] Z. Lin, W. Cai, W. Jiang, C. Fu, C. Li and Y. Song, Effects of Annealing Temperature on The Microstructure, Optical, Ferroelectric and Photovoltaic Properties of $BiFeO_3$ Thin Films Prepared by Sol–Gel Method, *Ceramics International*, 2013, **39**(8): 8729-8736.

[125] J. K. Kim, S. S. Kim and W. J. Kim, Phase Developments, Microstructures, and Ferroelectric Properties of $BiFeO_3$ Thin Films Prepared by A Solution, *Integrated Ferroelectrics*, 2006, **76**(1): 103-109.

[126] V. R. Singh, A. Dixit, A. Garg and D. C. Agrawal, Effect of Heat Treatment on The Structure and Properties of Chemical Solution Processed Multiferroic $BiFeO_3$ Thin Films, *Applied Physics A*, 2007, **90**(1): 197-202.

[127] A. H. M. Gonzalez, A. Z. Simões, L. S. Cavalcante, E. Longo, J. A. Varela and C. S. Riccardi, Soft Chemical Deposition of $BiFeO_3$ Multiferroic Thin Films, *Applied Physics Letters*, 2007, **90**(5): 052906.

[128] A. Z. Simões, A. H. M. Gonzalez, L. S. Cavalcante, C. S. Riccardi, E. Longo and J. A. Varela, Ferroelectric Characteristics of $BiFeO_3$ Thin Films Prepared via A Simple Chemical Solution Deposition, *Journal of Applied Physics*, 2007, **101**(7): 074108.

[129] F. Tyholdt, S. Jørgensen, H. Fjellvåg and A. E. Gunnæs, Synthesis of Oriented $BiFeO_3$ Thin Films by Chemical Solution Deposition: Phase, Texture, and Microstructural Development, *Journal of Materials Research*, 2005, **20**(8): 2127-2139.

[130] M. I. Yanovskaya, I. E. Obvintseva, L. I. Solovyova, E. P. Kovsman, K. A. Vorotilov and V. A. Vasilyev, Alkoxy-Derived Ferroelectric PZT Films: The Effect of Lead Acetate Dehydration Techniques and Lead Content in The Electrochemically Prepared Solutions on The Properties of The Films, *Integrated Ferroelectrics*, 2006, **19**(1-4): 193-209.

[131] R. W. Schwartz, J. A. Voigt and B. A. Tuttle, Comments on The Effects of Solution Precursor Characteristics and Thermal Processing Conditions on The Crystallization Behavior of Sol-Gel Derived Lead Zirconate Titanate Thin Films, *Journal of Materials Research*, 1997, **12**(2): 444-456.

[132] J. Wu and J. Wang, Orientation Dependence of Ferroelectric Behavior of $BiFeO_3$ Thin Films, *Journal of Applied Physics*, 2009, **106**(10): 104111.

[133] A. Herklotz, S. F. Rus, N. Balke, C. Rouleau, E. J. Guo, A. Huon, S. Kc, R. Roth, X. Yang, C. Vaswani, J. Wang, P. P. Orth, M. S. Scheurer and T. Z. Ward, Designing Morphotropic Phase Composition in $BiFeO_3$, *Nano Letters*, 2019, **19**(2): 1033-1038.

[134] D. G. Schlom, L.-Q. Chen, C. J. Fennie, V. Gopalan, D. A. Muller, X. Pan, R. Ramesh and R. Uecker, Elastic Strain Engineering of Ferroic Oxides, *MRS Bulletin*, 2014, **39**(2): 118-130.

[135] D. Sando, B. Xu, L. Bellaiche and N. Valanoor, A Multiferroic on The Brink: Uncovering The Nuances of Strain-Induced Transitions in $BiFeO_3$, *Applied Physics Reviews*, 2016, **3**(1):

011106.

[136] Md. M. Bellah, S. M. Christensen and S. M. Iqbal, Nanostructures for Medical Diagnostics, *Journal of Nanomaterials*, 2012, **2012**: 1-21.

[137] M. Birkholz, Thin Film Analysis by X-Ray Scattering, 2005, WILEY-VCH Verlag GmbH & Co. KGaA, Weinheim.

[138] P. Rostron, S. Gaber and D. Gaber, Raman Spectroscopy, A Review, *International Journal of Engineering and Technical Research*, 2016, **6**(1): 50-64.

[139] A. R. Hinda, S. K. Bhargava and A. McKinnon, At the Solid/Liquid Interface: FTIR/ATR—the Tool of Choice, *Advances in Colloid and Interface Science*, 2001, **93**: 93-114.

[140] R. P. Apkarian W. L. Zhou, Z. L. Wang, and D. Joy, Fundamentals of Scanning Electron Microscopy, 2007, Springer New York, New York.

[141] A. Ul-Hamid, H. M. Tawancy, A.-R. I. Mohammed, S. S. Al-Jaroudi and N. M. Abbas, Quantitative WDS Analysis Using Electron Probe Microanalyzer, *Materials Characterization*, 2006, **56**(3): 192-199.

[142] The Opensource Handbook of Nanoscience and Nanotechnology, 2020, Available from: https://en.wikibooks.org/wiki/Nanotechnology.

[143] BudgetSensors Categories / AFM Probes, Available from: https://www.budgetsensors.com/afmprobes?gclid=CjwKCAiAvaGRBhBlEiwAiYyMN5I6XfDLcN0ks1XdETwAfOAWpMReb36g3x7ugOLiSDDcRQ-fR_tZxoCE5EQAvD_BwE.

[144] What is Atomic Force Microscopy (AFM), Available from: https://www.nanoandmore.com/what-is-atomic-force-microscopy.

[145] Piezoresponse Force Microscopy, Available from: https://www.wikiwand.com/en/Piezoresponse_force_microscopy.

[146] B. J. Rodriguez, C. Callahan, S. V. Kalinin and R. Proksch, Dual-Frequency Resonance-Tracking Atomic Force Microscopy, *Nanotechnology*, 2007, **18**(47): 475504.

[147] Y. Liu, Y. Sun, W. Lu, H. Wang, Z. Wang, B. Yu, T. Li and K. Zeng, Variation of Contact Resonance Frequency during Domain Switching in PFM Measurements for Ferroelectric Materials, *Journal of Materiomics*, 2020, **6**(1): 109-118.

[148] M.-H. Zhang, H. C. Thong, Y. X. Lu, W. Sun, J.-F. Li and K. Wang, (K,Na)NbO_3-based Lead-Free Piezoelectric Materials: An Encounter with Scanning Probe Microscopy, *Journal of the Korean Ceramic Society*, 2017, **54**(4): 261-271.

[149] M. Stewart, M. G. Cain and D. A. Hall, Ferroelectric Hysteresis Measurement & Analysis,

1999, National Physical Laboratory, Teddington, Middlesex, United Kingdom.

[150] R. Thomas, J. F. Scott, D. N. Bose and R. S. Katiyar, Multiferroic Thin-Film Integration onto Semiconductor Devices, *Journal of Physics: Condensed Matter*, 2010, **22**(42): 423201.

[151] H. Béa, M. Gajek, M. Bibes and A. Barthélémy, Spintronics with Multiferroics, *Journal of Physics: Condensed Matter*, 2008, **20**(43): 434221.

[152] P. Sharma, Q. Zhang, D. Sando, C. H. Lei, Y. Liu, J. Li, N. Valanoor and J. Seidel, Nonvolatile Ferroelectric Domain Wall Memory, *Science Advances*, 2017, **3**: 1-8.

[153] D. Zhang, D. Sando, P. Sharma, X. Cheng, F. Ji, V. Govinden, M. Weyland, N. Valanoor and J. Seidel, Superior Polarization Retention through Engineered Domain Wall Pinning, *Nature Communications*, 2020, **11**(1): 349.

[154] A. Khan, Z. Abas, H. S. Kim and I.-K. Oh, Piezoelectric Thin Films: An Integrated Review of Transducers and Energy Harvesting, *Smart Materials and Structures*, 2016, **25**(5): 053002.

[155] C. R. Bowen, H. A. Kim, P. M. Weaver and S. Dunn, Piezoelectric and Ferroelectric Materials and Structures for Energy Harvesting Applications, *Energy & Environmental Science*, 2014, **7**(1): 25-44.

[156] E. Aksel and J. L. Jones, Advances in Lead-Free Piezoelectric Materials for Sensors and Actuators, *Sensors*, 2010, **10**(3): 1935-1954.

[157] M. Alexe and D. Hesse, Tip-Enhanced Photovoltaic Effects in Bismuth Ferrite, *Nature Communications*, 2011, **2**: 256.

[158] S. M. Young, F. Zheng and A. M. Rappe, First-Principles Calculation of The Bulk Photovoltaic Effect in Bismuth Ferrite, *Physical Review Letters*, 2012, **109**(23): 236601.

[159] N. A. Spaldin, S.-W. Cheong and R. Ramesh, Multiferroics: Past, Present, and Future, *Physics Today*, 2010, **63**(10): 38-43.

[160] R. Moubah, O. Rousseau, D. Colson, A. Artemenko, M. Maglione and M. Viret, Photoelectric Effects in Single Domain $BiFeO_3$ Crystals, *Advanced Functional Materials*, 2012, **22**(22): 4814-4818.

[161] Y. Yuan, Z. Xiao, B. Yang and J. Huang, Arising Applications of Ferroelectric Materials in Photovoltaic Devices, *Journal of Materials Chemistry A*, 2014, **2**(17): 6027-6041.

[162] T. Choi, S. Lee, Y. J. Choi, V. Kiryukhin and S.-W. Cheong, Switchable Ferroelectric Diode and Photovoltaic Effect in $BiFeO_3$, *Science*, 2009, **324**(5923): 63-66.

[163] J. Li, J. Wang, M. Wuttig, R. Ramesh, N. Wang, B. Ruette, A. P. Pyatakov, A. K. Zvezdin and D. Viehland, Dramatically Enhanced Polarization in (001), (101), and (111) $BiFeO_3$ Thin Films

due to Epitiaxial-Induced Transitions, *Applied Physics Letters*, 2004, **84**(25): 5261-5263.

[164] J. X. Zhang, Q. He, M. Trassin, W. Luo, D. Yi, M. D. Rossell, P. Yu, L. You, C. H. Wang, C. Y. Kuo, J. T. Heron, Z. Hu, R. J. Zeches, H. J. Lin, A. Tanaka, C. T. Chen, L. H. Tjeng, Y. H. Chu and R. Ramesh, Microscopic Origin of The Giant Ferroelectric Polarization in Tetragonal-Like $BiFeO_3$, *Physical Review Letters*, 2011, **107**(14): 147602.

[165] B. Xiang, J. X. Zhang, Q. He, J. Seidel, R. J. Zeches, P. Yu, S. Y. Yang, C. H. Wang, Y.-H. Chu, L. W. Martin, A. M. Minor and R. Ramesh, Large Field-Induced Strains in A Lead-Free Piezoelectric Material, *Nature nanotechnology*, 2011, **6**: 98-102.

[166] D. Sando, C. Carrétéro, M. N. Grisolia, A. Barthélémy, N. Valanoor and M. Bibes, Revisiting The Optical Band Gap in Epitaxial $BiFeO_3$ Thin Films, *Advanced Optical Materials*, 2018, **6**(2): 1700836.

[167] H. M. Christen, J. H. Nam, H. S. Kim, A. J. Hatt and N. A. Spaldin, Stress-Induced $R–M_A–M_C–T$ Symmetry Changes in $BiFeO_3$ Films, *Physical Review B*, 2011, **83**(14): 144107.

[168] O. Diéguez, O. E. González-Vázquez, J. C. Wojdeł and J. Íñiguez, First-Principles Predictions of Low-Energy Phases of Multiferroic $BiFeO_3$, *Physical Review B*, 2011, **83**(9): 094105.

[169] D. Sando, F. Appert, B. Xu, O. Paull, S. R. Burns, C. Carrétéro, B. Dupé, V. Garcia, Y. Gallais, A. Sacuto, M. Cazayous, B. Dkhil, J. M. Le Breton, A. Barthélémy, M. Bibes, L. Bellaiche, N. Valanoor and J. Juraszek, A Magnetic Phase Diagram for Nanoscale Epitaxial $BiFeO_3$ Films, *Applied Physics Reviews*, 2019, **6**(4): 041404.

[170] H. Bea, B. Dupe, S. Fusil, R. Mattana, E. Jacquet, B. Warot-Fonrose, F. Wilhelm, A. Rogalev, S. Petit, V. Cros, A. Anane, F. Petroff, K. Bouzehouane, G. Geneste, B. Dkhil, S. Lisenkov, I. Ponomareva, L. Bellaiche, M. Bibes and A. Barthelemy, Evidence for Room-Temperature Multiferroicity in A Compound with A Giant Axial Ratio, *Physical Review Letters*, 2009, **102**(21): 217603.

[171] Q. He, Y. H. Chu, J. T. Heron, S. Y. Yang, W. I. Liang, C. Y. Kuo, H. J. Lin, P. Yu, C. W. Liang, R. J. Zeches, W. C. Kuo, J. Y. Juang, C. T. Chen, E. Arenholz, A. Scholl and R. Ramesh, Electrically Controllable Spontaneous Magnetism in Nanoscale Mixed Phase Multiferroics, *Nature Communications*, 2011, **2**: 225.

[172] D. Sando, Y. Yang, E. Bousquet, C. Carretero, V. Garcia, S. Fusil, D. Dolfi, A. Barthelemy, P. Ghosez, L. Bellaiche and M. Bibes, Large Elasto-Optic Effect and Reversible Electrochromism in Multiferroic $BiFeO_3$, *Nature Communications*, 2016, **7**: 10718.

[173] T. Young, P. Sharma, D. H. Kim, T. D. Ha, J.-Y. Juang, Y. H. Chu, J. Seidel, N. Valanoor, S. Yasui, M. Itoh and D. Sando, Structural, Magnetic, and Ferroelectric Properties of T-Like Cobalt-Doped $BiFeO_3$ Thin Films, *APL Materials*, 2018, **6**(2): 026102.

[174] P. S. Sankara Rama Krishnan, J. A. Aguiar, Q. M. Ramasse, D. M. Kepaptsoglou, W. I. Liang, Y. H. Chu, N. D. Browning, P. Munroe and N. Valanoor, Mapping Strain Modulated Electronic Structure Perturbations in Mixed Phase Bismuth Ferrite Thin Films, *Journal of Materials Chemistry C*, 2015, **3**(8): 1835-1845.

[175] C.-H. Chiu, W.-I. Liang, C.-W. Huang, J.-Y. Chen, Y.-Y. Liu, J.-Y. Li, C.-L. Hsin, Y.-H. Chu and W.-W. Wu, Atomic Visualization of The Phase Transition in Highly Strained $BiFeO_3$ Thin Films with Excellent Pyroelectric Response, *Nano Energy*, 2015, **17**: 72-81.

[176] A. R. Damodaran, S. Lee, J. Karthik, S. MacLaren and L. W. Martin, Temperature and Thickness Evolution and Epitaxial Breakdown in Highly Strained $BiFeO_3$ Thin Films, *Physical Review B*, 2012, **85**(2): 024113.

[177] T. C. Kim, S. Ojha, G. Tian, S. H. Lee, H. K. Jung, J. W. Choi, L. Kornblum, F. J. Walker, C. H. Ahn, C. A. Ross and D. H. Kim, Self-Assembled Multiferroic Epitaxial $BiFeO_3$–$CoFe_2O_4$ Nanocomposite Thin Films Grown by RF Magnetron Sputtering, *Journal of Materials Chemistry C*, 2018, **6**(20): 5552-5561.

[178] D. Sando, T. Young, R. Bulanadi, X. Cheng, Y. Zhou, M. Weyland, P. Munroe and N. Valanoor, Designer Defect Stabilization of The Super Tetragonal Phase in >70-nm-Thick $BiFeO_3$ Films on $LaAlO_3$ Substrates, *Japanese Journal of Applied Physics*, 2018, **57**(9): 0902B0902.

[179] K.-E. Kim, B.-K. Jang, Y. Heo, J. H. Lee, M. Jeong, J. Y. Lee, J. Seidel and C.-H. Yang, Electric Control of Straight Stripe Conductive Mixed-Phase Nanostructures in La-Doped $BiFeO_3$, *NPG Asia Materials*, 2014, **6**: 1-9.

[180] P. Sharma, Y. Heo, B.-K. Jang, Y. Liu, N. Valanoor, J. Li, C.-H. Yang and J. Seidel, Morphotropic Phase Elasticity of Strained $BiFeO_3$, *Advanced materials interfaces*, 2016, **3**: 1600033.

[181] L. W. Martin, Y. H. Chu and R. Ramesh, Advances in The Growth and Characterization of Magnetic, Ferroelectric, and Multiferroic Oxide Thin Films, *Materials Science and Engineering: R: Reports*, 2010, **68**(4-6): 89-133.

[182] Q. Zhang, N. Valanoor and O. Standard, Chemical Solution Deposition Derived (001)-Oriented Epitaxial $BiFeO_3$ Thin Films with Robust Ferroelectric Properties Using Stoichiometric Precursors (invited), *Journal of Applied Physics*, 2014, **116**(6): 066810.

[183] R. W. Schwartz, T. Schneller and R. Waser, Chemical Solution Deposition of Electronic Oxide Films, *Comptes Rendus Chimie*, 2004, **7**(5): 433-461.

[184] Q. Zhang, N. Valanoor and O. Standard, Epitaxial (001) $BiFeO_3$ Thin-Films with Excellent Ferroelectric Properties by Chemical Solution Deposition-The Role of Gelation, *Journal of Materials Chemistry C*, 2015, **3**(3): 582-595.

[185] C.-S. Woo, J. H. Lee, K. Chu, B.-K. Jang, Y.-B. Kim, T. Y. Koo, P. Yang, Y. Qi, Z. Chen, L. Chen, H. C. Choi, J. H. Shim and C.-H. Yang, Suppression of Mixed-Phase Areas in Highly Elongated $BiFeO_3$ Thin Films on $NdAlO_3$ Substrates, *Physical Review B*, 2012, **86**(5): 054417.

[186] M. N. Popescu, G. Oshanin, S. Dietrich and A. M. Cazabat, Precursor Films in Wetting Phenomena, *Journal of Physics: Condensed Matter*, 2012, **24**(24): 243102.

[187] Z. Jia, X. Wu, M. Zhang, J. Xu, N. Zhang and J. J. Liou, Study on Polarization Characteristics of $BiFeO_3$ Thin Films Prepared by Sol-Gel Spin-Coating Technology, *The European Physical Journal Applied Physics*, 2015, **71**(1): 10301.

[188] S.-H. Jo, S.-G. Lee and Y.-H. Lee, Ferroelectric Properties of PZT/BFO Multilayer Thin Films Prepared Using The Sol-Gel Method, *Nanoscale Research Letters*, 2012, **7**(54): 1-5.

[189] D. Kan and I. Takeuchi, Effect of Substrate Orientation on Lattice Relaxation of Epitaxial $BiFeO_3$ Thin Films, *Journal of Applied Physics*, 2010, **108**(1): 014104.

[190] C. Herring, Effect of Change of Scale on Sintering Phenomena, *Journal of Applied Physics*, 1950, **21**(4): 301-303.

[191] M. Khodabakhsh, C. Sen, H. Khassaf, M. A. Gulgun and I. B. Misirlioglu, Strong Smearing and Disappearance of Phase Transitions into Polar Phases due to Inhomogeneous Lattice Strains Induced by A-Site Doping in $Bi_{1-x}A_xFeO_3$ (A: La, Sm, Gd), *Journal of Alloys and Compounds*, 2014, **604**: 117-129.

[192] D. Kan, C.-J. Cheng, N. Valanoor and I. Takeuchi, Composition and Temperature-Induced Structural Evolution in La, Sm, and Dy Substituted $BiFeO_3$ Epitaxial Thin Films at Morphotropic Phase Boundaries, *Journal of Applied Physics*, 2011, **110**(1): 014106.

[193] G. D. Hu, X. Cheng, W. B. Wu and C. H. Yang, Effects of Gd Substitution on Structure and Ferroelectric Properties of $BiFeO_3$ Thin Films Prepared Using Metal Organic Decomposition, *Applied Physics Letters*, 2007, **91**(23): 232909.

[194] Z. Zhong and H. Ishiwara, Variation of Leakage Current Mechanisms by Ion Substitution in $BiFeO_3$ Thin Films, *Applied Physics Letters*, 2009, **95**(11): 112902.

[195] X. Qi, J. Dho, R. Tomov, M. G. Blamire and J. L. MacManus-Driscoll, Greatly Reduced

Leakage Current and Conduction Mechanism in Aliovalent-Ion-Doped $BiFeO_3$, *Applied Physics Letters*, 2005, **86**(6): 062903.

[196] X. H. Zhu, H. Béa, M. Bibes, S. Fusil, K. Bouzehouane, E. Jacquet, A. Barthélémy, D. Lebeugle, M. Viret and D. Colson, Thickness-Dependent Structural and Electrical Properties of Multiferroic Mn-Doped $BiFeO_3$ Thin Films Grown Epitaxially by Pulsed Laser Deposition, *Applied Physics Letters*, 2008, **93**(8): 082902.

[197] S. Gupta, M. Tomar and V. Gupta, Ferroelectric Photovoltaic Properties of Ce and Mn Codoped $BiFeO_3$ Thin Film, *Journal of Applied Physics*, 2014, **115**(1): 014102.

[198] J. Wu, J. Wang, D. Xiao and J. Zhu, Leakage Mechanism of Cation -Modified $BiFeO_3$ Thin Film, *AIP Advances*, 2011, **1**(2): 022138.

[199] G. D. Hu, S. H. Fan, C. H. Yang and W. B. Wu, Low Leakage Current and Enhanced Ferroelectric Properties of Ti and Zn Codoped $BiFeO_3$ Thin Film, *Applied Physics Letters*, 2008, **92**(19): 192905.

[200] D. H. Kuang, P. Tang, S. H. Yang and Y. L. Zhang, Effect of Annealing Temperatures on The Structure and Leakage Mechanisms of $BiFeO_3$ Thin Films Prepared by The Sol–Gel Method, *Journal of Sol-Gel Science and Technology*, 2014, **73**(2): 410-416.

[201] I. S. Golovina, M. Falmbigl, A. V. Plokhikh, T. C. Parker, C. Johnson and J. E. Spanier, Effect of Annealing Conditions on The Electrical Properties of ALD-Grown Polycrystalline $BiFeO_3$ Films, *Journal of Materials Chemistry C*, 2018, **6**(20): 5462-5472.

[202] A. Tsurumaki, H. Yamada and A. Sawa, Impact of Bi Deficiencies on Ferroelectric Resistive Switching Characteristics Observed at p-Type Schottky-Like Pt/$Bi_{1-\delta}FeO_3$ Interfaces, *Advanced Functional Materials*, 2012, **22**(5): 1040-1047.

[203] H. Yang, Y. Q. Wang, H. Wang and Q. X. Jia, Oxygen Concentration and Its effect on The Leakage Current in $BiFeO_3$ Thin Films, *Applied Physics Letters*, 2010, **96**(1): 012909.

[204] H. Yang, M. Jain, N. A. Suvorova, H. Zhou, H. M. Luo, D. M. Feldmann, P. C. Dowden, R. F. DePaula, S. R. Foltyn and Q. X. Jia, Temperature-Dependent Leakage Mechanisms of Pt/$BiFeO_3$/$SrRuO_3$ Thin Film Capacitors, *Applied Physics Letters*, 2007, **91**(7): 072911.

[205] W. Sun, Z. Zhou, J. Luo, K. Wang and J.-F. Li, Leakage Current Characteristics and Sm/Ti Doping Effect in $BiFeO_3$ Thin Films on Silicon Wafers, *Journal of Applied Physics*, 2017, **121**(6): 064101.

[206] X. Tang, X. Zhu, J. Dai, J. Yang, L. Chen and Y. Sun, Evolution of The Resistive Switching in Chemical Solution Deposited-Derived $BiFeO_3$ Thin Films with Dwell Time and Annealing

Temperature, *Journal of Applied Physics*, 2013, **113**(4): 043706.

[207] C. T. Nelson, P. Gao, J. R. Jokisaari, C. Heikes, C. Adamo, A. Melville, S.-H. Baek, C. M. Folkman, B. Winchester, Y. Gu, Y. Liu, K. Zhang, E. Wang, J. Li, L.-Q. Chen, C.-B. Eom, D. G. Schlom and X. Pan, Domain Dynamics During Ferroelectric Switching, *Science*, 2011, **334**: 968-971.

[208] H. Béa, M. Bibes, A. Barthélémy, K. Bouzehouane, E. Jacquet, A. Khodan, J. P. Contour, S. Fusil, F. Wyczisk, A. Forget, D. Lebeugle, D. Colson and M. Viret, Influence of Parasitic Phases on The Properties of $BiFeO_3$ Epitaxial Thin Films, *Applied Physics Letters*, 2005, **87**(7): 072508.

[209] J. Seidel, M. Trassin, Y. Zhang, P. Maksymovych, T. Uhlig, P. Milde, D. Kohler, A. P. Baddorf, S. V. Kalinin, L. M. Eng, X. Pan and R. Ramesh, Electronic Properties of Isosymmetric Phase Boundaries in Highly Strained Ca-Doped $BiFeO_3$, *Advanced Materials*, 2014, **26**(25): 4376-4380.

[210] L. Jiang, W. S. Choi, H. Jeen, S. Dong, Y. Kim, M. G. Han, Y. Zhu, S. V. Kalinin, E. Dagotto, T. Egami and H. N. Lee, Tunneling Electroresistance Induced by Interfacial Phase Transitions in Ultrathin Oxide Heterostructures, *Nano Letters*, 2013, **13**(12): 5837-5843.

[211] S. Hong, T. Choi, J. H. Jeon, Y. Kim, H. Lee, H. Y. Joo, I. Hwang, J. S. Kim, S. O. Kang, S. V. Kalinin and B. H. Park, Large Resistive Switching in Ferroelectric $BiFeO_3$ Nano-Island Based Switchable Diodes, *Advanced Materials*, 2013, **25**(16): 2339-2343.

[212] Q. Zhang, A. Rana, X. Liu and N. Valanoor, Electrode Dependence of Local Electrical Properties of Chemical-Solution-Deposition-Derived $BiFeO_3$ Thin Films, *ACS Applied Electronic Materials*, 2019, **1**(1): 154-162.

[213] C. Wang, K.-J. Jin, Z.-T. Xu, L. Wang, C. Ge, H.-B. Lu, H.-Z. Guo, M. He and G.-Z. Yang, Switchable Diode Effect and Ferroelectric Resistive Switching in Epitaxial $BiFeO_3$ Thin Films, *Applied Physics Letters*, 2011, **98**(19): 192901.

[214] B. Nagaraj, S. Aggarwal and R. Ramesh, Influence of Contact Electrodes on Leakage Characteristics in Ferroelectric Thin Films, *Journal of Applied Physics*, 2001, **90**(1): 375-382.

[215] R. T. Tung, The Physics and Chemistry of The Schottky Barrier Height, *Applied Physics Reviews*, 2014, **1**(1): 011304.

[216] H. Yang, H. Wang, G. F. Zou, M. Jain, N. A. Suvorova, D. M. Feldmann, P. C. Dowden, R. F. DePaula, J. L. MacManus-Driscoll, A. J. Taylor and Q. X. Jia, Leakage Mechanisms of Self-Assembled $(BiFeO_3)_{0.5}$:$(Sm_2O_3)_{0.5}$ Nanocomposite Films, *Applied Physics Letters*, 2008, **93**(14): 142904.

[217] F. Chen, Q. Z. Liu, H. F. Wang, F. H. Zhang and W. Wu, Polarization Switching and Fatigue

in $Pb(Zr_{0.52}Ti_{0.48})O_3$ Films Sandwiched by Oxide Electrodes with Different Carrier Types, *Applied Physics Letters*, 2007, **90**(19): 192907.

[218] C. Himcinschi, A. Bhatnagar, A. Talkenberger, M. Barchuk, D. R. T. Zahn, D. Rafaja, J. Kortus and M. Alexe, Optical Properties of Epitaxial $BiFeO_3$ Thin Films Grown on $LaAlO_3$, *Applied Physics Letters*, 2015, **106**(1): 012908.

[219] M. M. Yang, A. N. Iqbal, J. J. P. Peters, A. M. Sanchez and M. Alexe, Strain-Gradient Mediated Local Conduction in Strained Bismuth Ferrite Films, *Nature Communications*, 2019, **10**(1): 2791.

[220] D. Kan, C. J. Long, C. Steinmetz, S. E. Lofland and I. Takeuchi, Combinatorial Search of Structural Transitions: Systematic Investigation of Morphotropic Phase Boundaries in Chemically Substituted $BiFeO_3$, *Journal of Materials Research*, 2012, **27**(21): 2691-2704.

[221] A. M. B. Santos, M. Martinez and J. A. Mira, Comparison Study of Lewis Acid Type Catalysts on The Esterification of Octanoic Acid and n-Octyl Alcohol, *Chemical Engineer Technology*, 1996, **19**: 538-542.

[222] B. K. Vashisth, J. S. Bangruwa, A. Beniwal, S. P. Gairola, A. Kumar, N. Singh and V. Verma, Modified Ferroelectric/Magnetic and Leakage Current Density Properties of Co and Sm Co-Doped Bismuth Ferrites, *Journal of Alloys and Compounds*, 2017, **698**: 699-705.

[223] A. A. Heitmann and G. A. Rossetti, Thermodynamics of Ferroelectric Solid Solutions with Morphotropic Phase Boundaries, *Journal of the American Ceramic Society*, 2014, **97**(6): 1661-1685.

[224] A. Biswas and Y. H. Jeong, Strain Effect in Epitaxial Oxide Heterostructures, Available from: http://dx.doi.org/10.5772/intechopen.70125.

[225] Z. Chen, S. Prosandeev, Z. L. Luo, W. Ren, Y. Qi, C. W. Huang, L. You, C. Gao, I. A. Kornev, T. Wu, J. Wang, P. Yang, T. Sritharan, L. Bellaiche and L. Chen, Coexistence of Ferroelectric Triclinic Phases in Highly Strained $BiFeO_3$ Films, *Physical Review B*, 2011, **84**(9): 094116.

[226] N. T. Huong, S. Lee, T. S. Atabaev, M. Kurisu and N. H. Hong, Rare Earth-Doped $BiFeO_3$ Thin Films: Relationship between Structural and Magnetic Properties, *Advances in Condensed Matter Physics*, 2015, **2015**: 1-5.

[227] D. M. Marincel, H. Zhang, A. Kumar, S. Jesse, S. V. Kalinin, W. M. Rainforth, I. M. Reaney, C. A. Randall and S. Trolier-McKinstry, Influence of A Single Grain Boundary on Domain Wall Motion in Ferroelectrics, *Advanced Electronic Materials*, 2014, **24**: 1409–1417.

[228] C. A. Randall, N. Kim, J.-P. Kucera, W. Cao and T. R. Shrout, Intrinsic and Extrinsic Size

Effects in Fine-Grained Morphotropic-Phase-Boundary Lead Zirconate Titanate Ceramics, *Journal of American Ceramic Society*, 1998, **81**(3): 677-688.

[229] D. Hong, S. Yu and J. Cheng, Sm–Ti Co-Substituted $BiFeO_3$ Thin Films Prepared by Sol–Gel Technique, *Current Applied Physics*, 2011, **11**(3): S255-S259.

[230] F. Lin, Q. Yu, L. Deng, Z. Zhang, X. He, A. Liu and W. Shi, Effect of La/Cr Codoping on Structural Transformation, Leakage, Dielectric and Magnetic Properties of $BiFeO_3$ Ceramics, *Journal of materials science*, 2017, **52**(12): 7118-7129.

[231] N. Panwar, I. Coondoo, A. Tomar, A. L. Kholkin, V. S. Puli and R. S. Katiyar, Nanoscale Piezoresponse and Magnetic Studies of Multiferroic Co and Pr Co-Substituted BFO Thin Films, *Materials Research Bulletin*, 2012, **47**(12): 4240-4245.

[232] Y. Y. Liu, L. Yang and J. Y. Li, Strain-Engineered Orthorhombic-Rhombohedral Phase Boundary in Epitaxial Bismuth Ferrite Films, *Journal of Applied Physics*, 2013, **113**(18): 183524.

[233] J. Zhou, D. Sando, X. Cheng, Z. Ma, N. Valanoor and Q. Zhang, Tuning Phase Fractions and Leakage Properties of Chemical Solution Deposition-Derived Mixed-Phase $BiFeO_3$ Thin Films, *ACS Applied Electronic Materials*, 2020, **2**(12): 4099-4110.

[234] Q. Jin, C. Zheng, Y. Zhang, C. Lu, J. Dai and Z. Wen, Enhanced Resistive Memory in Nb-Doped $BaTiO_3$ Ferroelectric Diodes, *Applied Physics Letters*, 2017, **111**(3): 032902.

[235] Z. J. Wang and Y. Bai, Resistive Switching Behavior in Ferroelectric Heterostructures, *Small*, 2019, **15**(32): e1805088.

[236] C. H. Yang, J. Seidel, S. Y. Kim, P. B. Rossen, P. Yu, M. Gajek, Y. H. Chu, L. W. Martin, M. B. Holcomb, Q. He, P. Maksymovych, N. Balke, S. V. Kalinin, A. P. Baddorf, S. R. Basu, M. L. Scullin and R. Ramesh, Electric Modulation of Conduction in Multiferroic Ca-Doped $BiFeO_3$ Films, *Nature materials*, 2009, **8**(6): 485-493.

[237] R. S. Winkler, Y. Y. Zhang, Q. Zhang, Z. Wang, Y. M. Zhu, M. G. Han, D. G. Schlom and N. Valanoor, Electromechanical Manipulation of Topological Defects to Yield Giant Piezoelectric Response in Epitaxial Lead Zirconate Titanate Bilayers on Silicon, *Advanced Electronic Materials*, 2021, **7**(8): 2100195.

[238] Y. Bastani and N. Bassiri-Gharb, Enhanced Dielectric and Piezoelectric Response in PZT Superlattice-Like Films by Leveraging Spontaneous Zr/Ti Gradient Formation, *Acta Materialia*, 2012, **60**(3): 1346-1352.